# Modeling of Lithium-ion Battery Performance and Thermal Behavior in Electrified Vehicles

by

Ehsan Samadani

A thesis
presented to the University of Waterloo
in fulfillment of the
thesis requirement for the degree of
Doctor of Philosophy
in
Mechanical Engineering

Waterloo, Ontario, Canada, 2015

## AUTHOR'S DECLARATION

I hereby declare that this thesis consists of material which I mainly authored or co-authored. This is a true copy of the thesis, including any required final revisions, as accepted by my examiners. I understand that my thesis may be made electronically available to the public.

# Abstract

Electric vehicles (EVs) have received significant attention over the past few years as a sustainable and efficient green transportation alternative. However, severe challenges, such as range anxiety, battery cost, and safety, hinder EV market expansion. A practical means to reduce these barriers is to improve the design of the battery management system (BMS) to accurately estimate the battery state of charge (SOC) and state of health (SOH) in addition to communicating with other powertrain components. Along with a robust estimation strategy, a critical requirement in developing an efficient BMS is a high fidelity battery model to predict the battery voltage, SOC, and heat generation profile at various temperature and power demands. Such a model should also be able to capture battery degradation, which is a path-dependent parameter that affects the battery performance in terms of output voltage, power capability and heat generation. In this thesis, the Li-ion battery, a proven technology for electrified vehicles, is studied under different operation scenarios on a plug-in hybrid vehicle (PHEV). The following steps have been accomplished:

1- **Development of a data-driven battery thermal model**: A set of thermal characterization tests are conducted on Li-ion cells. Heat generation profiles of each battery are driven for a set of operating points including various ambient temperatures, states of charge (SOCs) and load profiles. A regression model is developed accordingly which is able to accurately predict the battery temperature during a driving or charging event. The model shows an average error of 4% in temperature predictions.

2- **Development of a data-driven battery performance model** for real-time on-board applications: An equivalent circuit model is developed based on the electrochemical impedance spectroscopy (EIS) tests. This model can precisely predict the battery operating voltage under various operating conditions. An overall 6% improvement is observed in voltage prediction compared to common models in the literature. Results also show, depending on the powertrain designer expected accuracy, that this model can be used to predict the battery internal resistance obtained from hybrid pulse power characterization (HPPC) tests.

3- **Battery degradation studies through field tests**: An electrified Ford Escape vehicle is tested through random and controlled driving and charging events and battery data is collected and analyzed to identify trends of degradation including capacity fade and power fade. A battery life model is recalibrated based on the measured battery capacities over the field test period. Although, data shortage and technical issues prevented this study from meeting its targeted scope, the presented analysis provides a pathway for future research.

4- **Battery lifetime modeling**: fuel consumption, all-electric range and battery capacity loss are simulated under various scenarios including different climate control loads, ambient conditions, powertrain architectures and battery preconditioning. To simulate the climate control loads impact, a vehicle cabin thermal model is developed that incorporates the ambient conditions to predict the temperature profile of the cabin and the cooling/heating load required to regulate the temperature. Accordingly, this load is translated into additional load on the battery, which enables assessment of its impacts on the battery life, fuel consumption and vehicle range.

## Acknowledgements

I would like to express my sincere gratitude to Prof. Fraser and Prof. Fowler, for their constant guidance, and support during the course of this research. I would also like to thank people at Burlington Hydro Co., Cross Chasm Co. and also my friends, Dr. Siamak Farhad, Satyam Panchal and Mehrdad Mastali for providing assistance and constructive feedback. Last but not least, my special gratitude to my lovely wife, Ensieh, for her continuous love and support during these years.

***To those who sacrificed to make this world a better place to live…***

# Table of Contents

AUTHOR'S DECLARATION ..... ii
Abstract ..... iii
Acknowledgements ..... v
Table of Contents ..... vii
List of Figures ..... xi
List of Tables ..... xv
1 Introduction ..... 1
1.1 Problem definition and research objectives ..... 4
1.1.1 Battery Performance Modeling ..... 4
1.1.2 Battery Thermal Characterization ..... 6
1.1.3 Battery Degradation ..... 7
1.1.4 Auxiliary Loads in EVs ..... 7
1.2 Document Organization ..... 8
2 Background and literature review ..... 10
2.1 Battery Elements and Specificationds ..... 10
2.1.1 Anode ..... 10
2.1.2 Cathode ..... 10
2.1.3 Electrolyte ..... 10
2.1.4 Separator ..... 11
2.2 Battery Gloassary ..... 11
2.2.1 Battery Management System ..... 11
2.2.2 State of Charge ..... 12
2.2.3 Depth of Discharge- ..... 12
2.2.4 C-rate ..... 12
2.2.5 Cell Capacity ..... 12
2.2.6 Cycle ..... 13
2.2.7 Cell Open Circuit Voltage ..... 13
2.2.8 Internal Resistance ..... 14

2.3 Electric Vehicles Battery Types ..... 16
2.4 Li-ion Cell Operation ..... 19
2.5 Battery Models ..... 21
2.5.1 Electrochemical Models ..... 21
2.5.2 Equivalent Circuit Models ..... 21
2.6 Battery Degradation Modeling ..... 25
2.7 Degradation Mechanisms of Li-ion Cells ..... 26
2.7.1 Degradation under Storage (i.e. Calendar Aging) ..... 26
2.7.2 Degradation during Cycling ..... 27
2.8 Accelerated Degradation during Cycling ..... 29
2.9 Duty cycle & Drive cycle ..... 32
2.10 PHEV and HEV Considerations ..... 33
3 Modeling of Battery Thermal Behavior and Performance ..... 36
3.1 Thermal Characterization ..... 36
3.1.1 Experimental setup ..... 37
3.1.2 Analysis of results ..... 41
3.2 Modeling of Battery Performnce Based on EIS Tests ..... 60
3.2.1 Experiment Setup and Tests Procedure ..... 61
3.2.2 Establishment of the Equivalent Circuit ..... 63
3.2.3 Parameters Fitting ..... 68
3.2.4 Determination of the Voltage Response in Time Domain ..... 70
3.2.5 Results and Discussion ..... 74
3.2.6 Impact of convection coefficient on the temperature profile ..... 82
3.3 Conclusions ..... 83
4 Battery Characterization through Field Tests ..... 85
4.1 Data Management System and Battery Packs ..... 86
4.2 Results and Analysis ..... 88
4.2.1 Individual Event Analysis ..... 88
4.2.2 Energy and Cost Analysis of EV-ACX 2.5 ..... 91

4.3 Vehicle Powertrain Modeling ..... 96
4.3.1 Estimation of the Battery OCV and Internal Resistance ..... 98
4.3.2 Model Testing and Validation ..... 101
4.3.3 Case study- Testing the proposed ECM with a Real-life drive cycle ..... 112
4.3.4 Overall Powertrain Efficiency of EV-ACX2.5 ..... 115
4.3.5 Energy Requirement of EV-ACX2.5 as a Fleet Vehicle ..... 117
4.3.6 Studies on Battery Degradation ..... 118
4.4 Conclusion ..... 132
5 Modeling of Battery Lifetime in Hybrid Vehicle Operation ..... 134
5.1 Range Anxiety and Auxiliary loads in PEVs ..... 134
5.2 Cabin Thermal Model ..... 135
5.3 Climate Scenarios ..... 140
5.4 Results- Thermal model and A/C impacts ..... 140
5.5 Vehicle Simulations ..... 142
5.5.1 CD range and Fuel consumption ..... 143
5.5.2 Degradation simulation ..... 145
5.6 Conclusions ..... 148
6 Conclusions and Recommendations ..... 150
6.1 Conclusions and Contributions ..... 150
6.1.1 Thermal studies ..... 150
6.1.2 EIS Tests and Modeling ..... 151
6.1.3 Field tests ..... 151
6.1.4 Vehicle lifetime studies ..... 153
6.2 Recommendations ..... 153
6.2.1 Thermal testing ..... 154
6.2.2 EIS testing ..... 154
6.2.3 Field testing ..... 155
6.2.4 Battery lifetime modeling ..... 156
References ..... 157

Appendix-A Statistical Analysis of Cell Temperature Distribution ..... 165
Appendix-B Derived Regression Models for the Circuit Parameters ..... 168
Appendix-C Modification on the driver model in Autonomie ..... 171
Appendix-D Monthly Report of EV-ACX2.5 ..... 172

# List of Figures

Figure1-1. Power flow in a series HEV powertrain [5] ..... 2
Figure1-2. Power flow in a parallel HEV powertrain [5] ..... 3
Figure1-3. Power flow in a series parallel HEV powertrain [5] ..... 3
Figure 2-1 Li-ion battery OCV variation against SOC [45] ..... 14
Figure 2-2 Lead acid battery OCV variation against SOC [46] ..... 14
Figure 2-3. Typical polarization of a battery [50] ..... 16
Figure 2-4. The Ragone plot of various cell types capable of meeting the requirements for EV applications [53] ..... 18
Figure 2-5. Comparison of suitable Li-ions for EV. The more the colored shape extends along a given axis, the better the performance in that direction [56] ..... 19
Figure 2-6.Charge and discharge process in Li-ion battery [58] ..... 20
Figure 2-7 Types of Li-ion cell formats: cylindrical, prismatic and pouch cell. ..... 20
Figure 2-8 Rint model equivalent circuit diagram ..... 22
Figure 2-9 RC model equivalent circuit diagram ..... 23
Figure 2-10 Thevenin model equivalent circuit diagram [66] ..... 23
Figure 2-11 DP model equivalent circuit diagram [65]. ..... 24
Figure 2-12 Expanded DP model equivalent circuit diagram ..... 24
Figure 2-13 EDP model components correlated with EIS results [19] ..... 25
Figure 2-14. The general shape for capacity versus cycle number [70]. ..... 27
Figure 2-15.Schematic of SEI film layer in Li-ion battery [71] ..... 28
Figure 2-16. Cycle life vs. ΔDoD curve for different battery cell chemistries[75] ..... 30
Figure 2-17. Example-Battery cell's temperature range for optimal cycle life [76] ..... 30
Figure 2-18. The accelerated capacity fading due to high temperatures [78] ..... 31
Figure 2-19- Schematic of a driving cycle broken down into a series of sequential isolated "driving pulses" or "micro trip" ..... 33
Figure 3-1: Battery cycling test bench ..... 38
Figure 3-2: Battery setup in thermal chamber ..... 39
Figure 3-3: Thermocouple placement on cell surface ..... 40
Figure 3-4: A two factor NFCD used for thermal studies ..... 41
Figure 3-5: $LiFePO_4$ Cell temperature changes during rest period at 23.75 °C- measured against fitted values ..... 45
Figure 3-6: $LiFePO_4$ cell temperature changes during discharge cycles ..... 46
Figure 3-7: $LiFePO_4$ cell temperature changes during charge cycles ..... 46
Figure 3-8: $LiMn_2O_4$ cell temperature changes during discharge cycles ..... 47

Figure 3-9: $LiMn_2O_4$ cell temperature changes during charge cycles ..... 47
Figure 3-10: $LiFePO_4$ cell cumulative heat during discharge cycles ..... 48
Figure 3-11: $LiFePO_4$ cell cumulative heat during charge cycles ..... 49
Figure 3-12: $LIMn_2O_4$ cell cumulative heat during discharge cycles ..... 49
Figure 3-13: $LiMn_2O_4$ cell cumulative heat during charge cycles ..... 50
Figure 3-14 Residuals showing a trend (variable variance) [88] ..... 57
Figure 3-15 Temperature profile of cell #1 ($LiFePO_4$) during discharge at 2.5 C-rate and 23.75 °C ambient ..... 58
Figure 3-16 Temperature profile of cell #1 ($LiFePO_4$) during discharge at 1.75 C-rate and 12.5 °C ambient ..... 58
Figure 3-17 Temperature profile of cell #1 (LiFePO4) under US06 profile and 12.5 °C ambient. 59
Figure 3-18 Temperature profile of cell #1 (LiFePO4) under US06 profile and 35 °C ambient .... 59
Figure 3-19: Experimental setup for the EIS test. ..... 62
Figure 3-20 EIS test results of battery #1 with $LiFePO_4$ cathode 12.5 °C ..... 64
Figure 3-21 EIS test results of battery #1 with $LiFePO_4$ cathode 23.75 °C ..... 64
Figure 3-22 EIS test results of battery #1 with $LiFePO_4$ cathode 35 °C ..... 65
Figure 3-23 EIS test results of battery #1 with $LiMn_2O_4$ ..... 65
Figure 3-24 EIS test results of battery #1 with $LiMn_2O_4$ ..... 66
Figure 3-25 EIS test results of battery #1 with $LiMn_2O_4$ ..... 66
Figure 3-26 Examples of the EIS plots showing two semicircles justifying the need for CPE element in the circuit structure ..... 67
Figure 3-27. Proposed equivalent circuit in frequency domain ..... 68
Figure 3-28. Simplification of the proposed circuit for time domain solution. ..... 68
Figure 3-29. Fitted values of R1 for battery #1 ..... 70
Figure 3-30 Fitted values of R1 for battery #2 ..... 70
Figure 3-31 : HPPC test- pulse power characterization profile ..... 75
Figure 3-32. Comparison of discharge resistances obtained from HPPC tests and modeling for the battery with LFP cathode at different temperatures. ..... 77
Figure 3-33. Comparison of the battery voltage obtained from the empirical model and experiment for the battery with LFP cathode at 35°C standard EPA drive cycles. ..... 78
Figure 3-34. Comparison of discharge resistances obtained from HPPC tests and modeling for the battery with composite LMO & NMC cathode at different temperatures. ..... 81
Figure 3-35 Simulation of temperature profile under EPA drive cycles; (1)-(3): Impact of convection coefficient on the temperature, (4) maximum temperature change as a function of convection coefficient ..... 83
Figure 4-1 Converted Ford Escape (EV-ACX2.5) ..... 87

Figure 4-2. integration of multiple batteries packs [110] ..... 87
Figure 4-3: Data recorder unit ..... 87
Figure 4-4: Data logger connection and shut down wire ..... 87
Figure 4-5: Drive cycle for longest recorded trip with EV-ACX2.5 ..... 88
Figure 4-6: Acceleration profile for longest recorded trip with EV-ACX2.5 ..... 88
Figure 4-7: Battery voltage profile for longest recorded trip with EV-ACX2.5 ..... 90
Figure 4-8: Battery current profile for longest recorded trip with EV-ACX2.5 ..... 90
Figure 4-9: Battery SOC profile for longest recorded trip with EV-ACX2.5 ..... 90
Figure 4-10: Battery temperature profile for longest recorded trip with EV-ACX2.5 ..... 91
Figure 4-11: ACX 2.5 November 2011 monthly report [111] ..... 94
Figure 4-12 Drivetrain configuration of the converted EV in PSAT [111] ..... 97
Figure 4-13 Top level of the battery model in PSAT ..... 97
Figure 4-14. Drive cycle #1 Synthesized for calibrating the battery model ..... 98
Figure 4-15: Sample battery pack voltage profile ..... 99
Figure 4-16: Comparison of OCVs estimated from the road test and measured after 2hr resting time. ..... 100
Figure 4-17: Internal resistance of the battery module derived from data of drive cycle #1 ..... 101
Figure 4-18: SOC versus time; obtained from the model and drive cycle #1 ..... 102
Figure 4-19: Power Flow into the Electric Motor, model and drive cycle #1 (first 8000 sec) ..... 103
Figure 4-20. Inputs and Outputs to the Electric Motor ..... 103
Figure 4-21. Vehicle Longitudinal Acceleration; drive cycle #1 (first 8000 sec) ..... 104
Figure 4-22: Drive cycle #2 used for testing the model ..... 104
Figure 4-23: SOC versus time; obtained from the model and field test related to drive cycle #2. ..... 105
Figure 4-24. Input Power from Electric Motor; Test Drive Cycle(Dec7-Part1) ..... 106
Figure 4-25. Vehicle Longitudinal Acceleration; Test Drive Cycle(Dec7-Part1) ..... 106
Figure 4-26: Drive cycle #3 ..... 107
Figure 4-27: Frequency of the Battery pack C-rates for the drive cycle #3 ..... 108
Figure 4-28: Battery SOC Validation Against drive cycle #3 ..... 109
Figure 4-29: Battery Model Validation against Test Data over Drive cycle #3 ..... 109
Figure 4-30: The coefficient of d(OCV)/dT versus SOC for the single cell of the battery back under study [48]. ..... 110
Figure 4-31: Reversible heat generated during drive cycle #3 ..... 111
Figure 4-32: Validation of the battery pack thermal model for drive cycle #3. ..... 112
Figure 4-33: Modeling error in predicting the battery pack temperature over drive cycle #3 ..... 112
Figure 4-34 Battery power profiles under test drive cycle operation ..... 113

Figure 4-35 Profile of battery current of the drive cycle #3 ..... 113
Figure 4-36 Battery SOC power profiles under test drive cycle operation..... 114
Figure 4-37 Profile of battery temperature during the tests drive cycle ..... 115
Figure 4-38 Tests drive cycle and relevant battery performance profiles ..... 115
Figure 4-39 Histogram of charge data (over Jan-Oct, 2012) ..... 119
Figure 4-40: Trips distance driven by EV-ACX2.5..... 120
Figure 4-41 selected drive cycles for comparing the polarization curves ..... 122
Figure 4-42 Battery polarization curve for three selected trips with EV-ACX2.5 ..... 123
Figure 4-43 Charge input over time for 10 similar charging events ..... 124
Figure 4-44 Energy discharged per km driven for 6 similar driving events ..... 125
Figure 4-45 Test plan provided that the vehicle is available for systematic usage ..... 127
Figure 4-46 ACX2.5 battery capacity profile during four months test ..... 129
Figure 4-47 Battery pack maximum and minimum temperature during each event (Over July-October) ..... 130
Figure 4-48 Simulated capacity fade using the calibrated life model ..... 132
Figure 5-1 Vehicle cabin and thermal loads acting on the cabin air..... 136
Figure 5-2 schematic of the AC system [118] ..... 136
Figure 5-3 Fuzzy controller to determine the blower mass flow rate ..... 139
Figure 5-4. Cabin temperature profile- Test derive cycle..... 141
Figure 5-5. Profile of cabin absolute humidity under test drive cycle..... 141
Figure 5-6. Profile of air flow through the blower..... 141
Figure 5-7. Profile of compressor current under test drive cycle..... 141
Figure 5-8 Graphical presentation of the EREV series architecture ..... 142
Figure 5-9 Graphical presentation of the pre-transmission parallel architecture ..... 143
Figure 5-10 AER results for different minimum SOC ..... 144
Figure 5-11 Battery temperature at the end of AER ..... 144
Figure 5-12 Series PHEV (EREV) CD range assumming 30% critical SOC ..... 145
Figure 5-13 Series PHEV (EREV) fuel consumption assumming 30% critical SOC ..... 145
Figure 5-14 Parallel PHEV CD range assumming 30% critical SOC ..... 145
Figure 5-15 Parallel PHEV fuel consumption assumming 30% critical SOC..... 145
Figure 5-16 Vehicle daily duty cycle assumed for simulations ..... 146
Figure 5-17 The test drive cycle collected from the converted EV road tests ..... 146
Figure 5-18 Annual battery capacity loss rate in the series PHEV..... 147
Figure 5-19 Battery capacity loss rate in the Parallel PHEV..... 148

# List of Tables

Table 2-1- Characteristics of battery types used in EVs [9] ..... 17
Table 2-2- Examples of different Li-ion batteries used in EVs [4] ..... 18
Table 3-1: Prismatic Pouch Cell Specifications ..... 37
Table 3-2: Resulting test points from NFCD ..... 40
Table 3-3 Electrical efficiency of the $LiFePO_4$ cell ..... 51
Table 3-4 Electrical efficiency of the $LiMn_2O_4$ cell ..... 52
Table 3-5: Thermal loss (%) of $LiFePO_4$ cell during discharge ..... 54
Table 3-6: Thermal loss (%) of $LiFePO_4$ cell during charge ..... 54
Table 3-7 Thermal loss (%) of $LiMn_2O_4$ cell during discharge ..... 54
Table 3-8 Thermal loss (%) of $LiMn_2O_4$ cell during charge ..... 55
Table 3-9 Results of regression analysis on the heat generation rate during discharge of $LiFePO_4$ cell ..... 56
Table 3-10 Results of regression analysis on the heat generation rate during charge of $LiFePO_4$ cell ..... 56
Table 3-11 Powertrain components specifications of the EREV modified Chevrolet Malibu used in the Autonomie model [45, 96] ..... 63
Table 3-12. Average and maximum errors of the proposed empirical model for voltage prediction of the battery with LFP cathode in various drive cycles over 90% to 10% SOC. ..... 80
Table 4-1 Data logging signals ..... 87
Table 4-2 Cycle details, November 25, 2011 ..... 89
Table 4-3: Acceleration comparison between Nov25 drive cycle and standard drive cycles ..... 89
Table 4-4: Energy and cost analysis of EV-ACX2.5 (October 2011-February 2012) ..... 92
Table 4-5: Distance travelled and energy consumption by fleet vehicles ..... 95
Table 4-6: Energy and cost comparison between EV-ACX2.5 and HEV#4 ..... 95
Table 4-7 Key specifications for the electrified Ford Escape ..... 97
Table 4-8 drive cycle #1 statistics ..... 98
Table 4-9: Statistics of test drive cycle #2 ..... 105
Table 4-10: Drive Cycle #3 Specification ..... 107
Table 4-11: Input and output of each component in the EV powertrain ..... 116
Table 4-12: Monthly efficiency of the EV-ACX2.5 powertrain ..... 117
Table 4-13: Energy saving of EV-ACX2.5 as a fleet vehicle based on the HEV drive cycles ..... 118
Table 4-14 Cost saving of EV-ACX2.5 as a fleet vehicle based on the HEV drive cycles ..... 118
Table 4-15 EV-ACX2.5 usage over January 2012- October 19, 2012 ..... 119
Table 4-16 Extraction of similar charge and driving events ..... 124

Table 4-17 Important parameters in the battery degradation field test ..... 126
Table 4-18 Capacity measurement, Dec.7, 2011 ..... 129
Table 4-19 Extended Ning life model [115] ..... 131
Table 4-20 Model parameters calibrated with road test data ..... 132
Table 5-1 Specifications of the variable speed electric compressor [120] ..... 137
Table 5-2 Baseline vehicle dimensions and thermodynamic properties assumed for simulation ..... 139
Table 5-3 Scenarios considered for simulating the temperature profile of vehicle cabin ..... 140
Table 5-4 Component specifications and model inputs used in the Autonomie model of EREV [96] ..... 143

# Chapter 1

# Introduction

Over the past few decades, increasing concern about the environmental impact and non-renewable infrastructure of fossil fuel-based transportation has highlighted the need for a long-term transition to sustainable energy alternatives [1]. Therefore, the automotive industry has observed a renewed interest in electricity as an automotive propulsion technology in the recent decade [2]. EVs and electrified (hybrid) vehicles are superior to conventional vehicles in the following areas [1, 3]:

1- Compared to an internal combustion engine (ICE) with about 20% energy efficiency, electric motors convert about 75% of the chemical energy stored in the battery into mechanical energy. Thanks to the regenerative braking system, which allows for energy recovery during braking, the efficiency of the electric traction system is further improved.
2- Electric motors require less maintenance compared to ICEs as they have fewer moving parts. Furthermore, electric motors are able to provide high torque at low speeds; making the multi-speed gearboxes unnecessary for certain EVs.
3- EVs offer a simple powertrain design, zero tailpipe emissions, and high efficiency on a tank-to-wheel basis.

However, due to their higher costs, limited range, charging concerns and grid impacts [4], hybridized powertrains combining multiple power sources have been introduced. The most common type of hybrid vehicles today utilizes an ICE with an electric propulsion system. Compared to conventional vehicles, hybrid vehicles benefit from a smaller engine (ICE) size which is allowed to run at its efficient operating range, have a regenerative braking system, and have no idling mode, which all result in improved energy efficiency and emissions. The third class of electrified vehicles is the plug-in hybrid electric vehicle (PHEV) which combines the

characteristics of an HEV and the capability of an EV to recharge its battery from the grid. Therefore, a PHEV can rely solely on the electricity while it is not range limited like an EV. In addition, waste engine heat can be used to regulate cabin temperature, which reduces the need for an electric motor and avoids extra load on the battery. P/HEVs' powertrain architecture can have a series, parallel or series-parallel design. In a series design, the traction power is provided to the wheels by the battery through the electric motor and the ICE charges the battery (through a generator) to maintain the battery state of charge (SOC) within a specified range. The power flow in a series design is shown in Figure1-1.

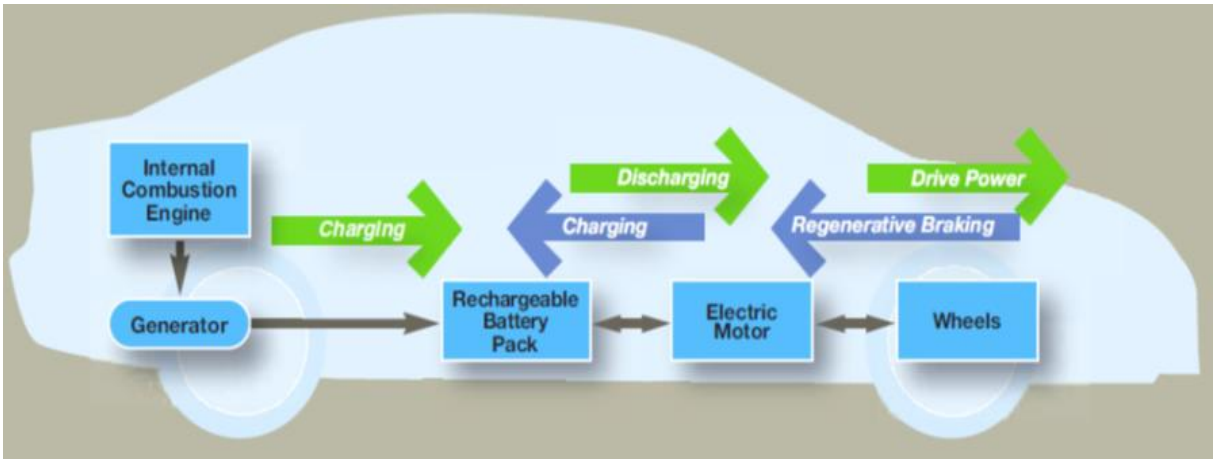


**Figure1-1. Power flow in a series HEV powertrain [5]**

In a parallel design, both the electric motor and ICE are mechanically connected to the wheel through a torque coupler. This design allows different operating modes: only electric (in which the ICE is disengaged from the coupler), only ICE (in which the electric motor freely spins), combined mode (in which the battery and ICE provide power) and, lastly, ICE being used for charging the battery in excess road load. Figure1-2 shows the power flow in the parallel design.

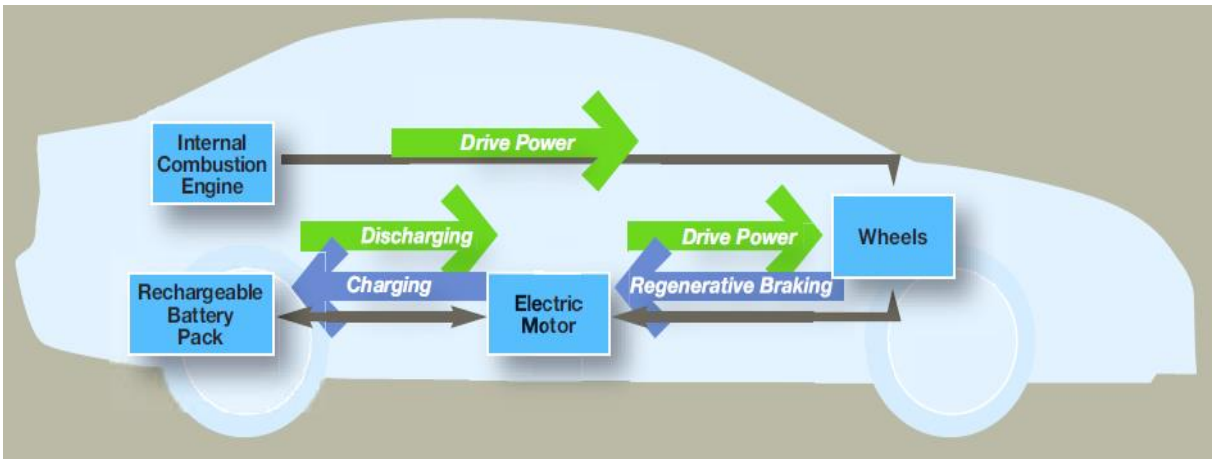


**Figure1-2. Power flow in a parallel HEV powertrain [5]**

Generally, in city driving conditions, series hybrid behavior is preferable; however, during highway driving conditions, a parallel hybrid action is desired [6]. Therefore, the series parallel configuration combines the positive aspects of the series configuration independence of engine operation from the driving conditions with the advantage of the parallel configuration efficient mechanical drivetrain. The complexity of this design remains with the control tasks. Figure1-3 shows the power flow in this architecture.

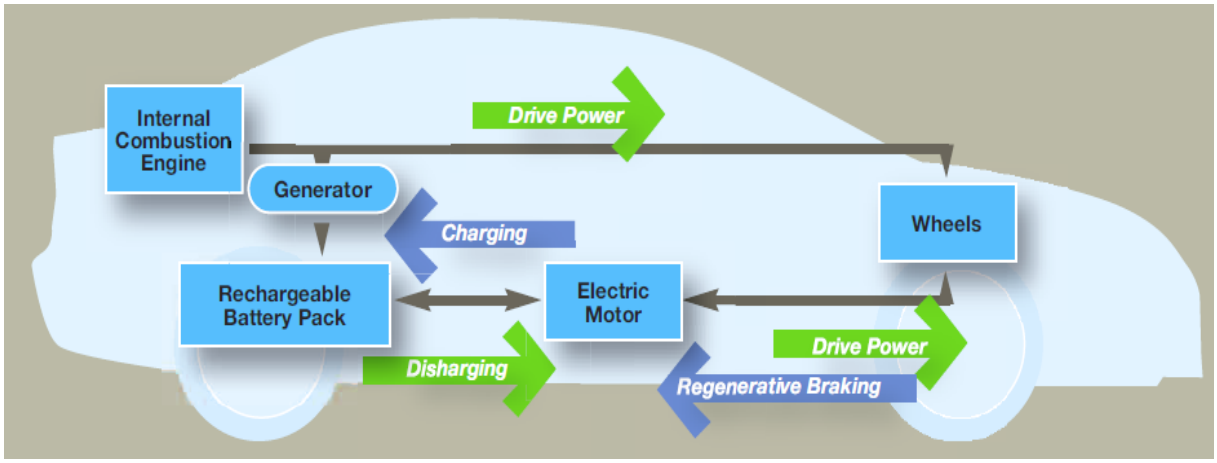


**Figure1-3. Power flow in a series parallel HEV powertrain [5]**

Electrified vehicles, regardless of the powertrain layout, need reliable electric energy storage. Currently, batteries and ultracapacitors are used for this purpose. Important factors in choosing

appropriate energy storage systems are energy and power density, lifetime and cost. Unlike conventional vehicles in which the battery is used only for starting, ignition and lighting, in electrified vehicles, the battery must meet certain design requirements. For example, in HEVs, the battery is designed to operate mostly in a narrow state of charge (SOC) range which is called charge sustaining (CS) mode and it is designed to match the peak power from the engine during acceleration. On the other hand, in PHEVs and pure EVs, the battery is designed to provide the vehicle with a significant all-electric range (AER) while operating in charge depleting (CD) mode. In addition, in these vehicles, the battery experiences deep charge and discharge cycles which adversely affect its lifetime. Therefore, the energy requirement and cycle life of a battery in these vehicles is a crucial consideration [1]. Ultra capacitors, unlike the batteries, store electric energy physically but not chemically; as well, they exhibit much higher power density and cycle life but much lower energy density. Therefore, they have been mostly utilized in mild hybrid vehicles in which the prime energy source is an engine or fuel cell [7, 8]. There is a variety of battery technology and chemistry available today. In earlier generations, nickel cadmium, lead acid, and nickel-metal hydride (Ni-MH) batteries were used as the power source due to their low price and reasonable energy density [9]. In recent years, Li-ion batteries are becoming more common because of their higher energy and power content. Li-ion battery technology is one of the core topics in the development of PHEVs and there is plenty of ongoing research to improve its performance, durability and safety [1, 3].

## 1.1 Problem definition and research objectives

In this thesis, different aspects of Li-ion battery performance and behavior are studied as presented in the following sections.

### 1.1.1 Battery Performance Modeling

Electrical energy storage (battery) continues to be the greatest challenge to the commercialization of both PHEV and EV models. Beside battery price, range anxiety (fear of getting stranded on the road due to lack of charge) is the main concern expressed by consumers

[10]. Range anxiety stems from the fact that the specific energy of the battery packs (~0.25 kWh/kg) compared to fossil fuel (~13 kWh/kg) is very low. Furthermore, refuelling (recharging) stations are not widely available and the charging time is rather high (depending on the method, full recharge times typically range from 30 minutes to almost 12 hours). With a gasoline car, many people are not at all affected by the range they get as refuelling is quick and easily accessible almost everywhere. Several surveys have been conducted on range anxiety. Accenture [11] conducted a survey, in 13 countries, on consumer preference concerning driving an electrified vehicle in which Chinese participants showed the highest tendency to buy and drive an EV as their future choice, while Dutch participants expressed the lowest interest. However, a higher range means a bigger battery size and, consequently, a higher cost vehicle.

A determinant factor on the EV range is the battery management system (BMS). In electrified vehicles, the BMS plays a significant role in the battery and the whole vehicle performance, efficiency and safety. The BMS is actually required to respond to dynamic power demands dependent on driving behavior, road conditions, and electrical accessories [12]. In addition, the BMS is responsible for cell safety. Therefore, accurate prediction of SOC, proper management of current and temperature, and cell potential balance are BMS' crucial tasks [13]. However, the efficiency of a BMS is highly dependent on the fidelity of the battery model built in the BMS. Furthermore, on board processing power is limited. Therefore, it is imperative to have an accurate model that is sufficiently simple to be operated on board the BMS. Model complexity is dependent on application requirements. High fidelity Li-ion electrochemical models, which were first introduced by Doyle et al. [14], are widely used for battery design. Another type of battery model is the equivalent circuit model (ECM). These models are more useful for real-time applications (such as BMSs), in which cost and processing power is strictly limited. An ECM represents the complex electrochemical interactions within a battery as simple circuit components. Components may be added to model observed phenomena and increase accuracy, or may be removed to increase efficiency. ECM circuit elements, such as resistors and capacitors, may also be scaled to account for changes in SOC [15-18], temperature [16, 19-22], aging [23], and C-rate [18], which affect cell performance.

As a contribution to the existing models, this thesis presents a comprehensive ECM developed for two commercially available Li-ion cells used in PHEVs, which, compared to commonly used models, proves to be more efficient (up to 6%) in terms of voltage prediction. Such an improvement in voltage prediction can be interpreted as an additional few kilometers to the vehicle range. Also, the proposed ECM has the capability to be used as an alternative to hybrid pulse power characterization (HPPC) tests within a limited error.

### 1.1.2 Battery Thermal Characterization

Devices with high energy density, such as Li-ion batteries, have the potential for high heat generation and Li-ion batteries are no exception. A single Li-ion polymer cell can undergo a temperature increase of 5 to 20 K at a 1C discharge rate [24], depending on cell geometry and assembly. Thermal management of the cells in a pack is, therefore, an important issue that must be considered to ensure vehicle safety, performance and cycle life.

Depending on ambient conditions, there may be a need to remove or add heat to the battery in order to maintain the optimal temperature range and distribution. Non-uniform temperature distribution results in low charge and discharge performance and cell unbalancing, over time. Existing thermal management techniques include applying liquids, insulations and phase-change-materials [25]. Essential tools in automotive pack design and thermal management are thermal and performance models. Such models require inputs such as system and operational parameters. Not all of these parameters are easy to directly quantify (e.g. heat effect and transport properties) because their effects cannot be isolated; thus, extensive tests are necessary to yield a clear understanding of heat generation and cell performance [26]. Several papers have been published on this topic so far; some proposing a simple one dimensional(1-D) [21, 27] approach and others with further details by three dimensional(3-D) [28]modeling of the heat generation inside the cell. However, for vehicle simulation and BMS applications, a fast and accurate heat generation model based on a limited number of lab tests may serve as an adequate alternative.

In this regard, this thesis contributes to the literature by presenting a simple and accurate modeling approach of Li-ion cell heat generation that can be readily applied for fast simulations

and on-board applications.

### 1.1.3 Battery Degradation

Battery state of health (SOH) has been a hot topic since rechargeable (secondary) batteries were introduced to the industry. To extend the battery lifetime, the focus has been initially on minimizing the power consumption of the devices powered by these batteries. However, such methods would not be adequate, as they ignore important characteristics of the battery source such as the dependency of available capacity on the battery discharge rate and internal temperature, and the cycle aging effect [29]. In recent years, a number of researchers have developed models for battery SOH and degradation rate based on battery detailed electrochemistry coupled with thermal characteristics [30, 31]. In EV applications, battery SOH is known to be very much dependent on the driving and charging habit; therefore, there is a growing desire to evaluate the path dependence of battery degradation. This is due to the fact that a lab environment is far different from what the battery experiences under real operation in EVs. However, real-life testing is expensive and labor intensive and is associated with a very low level of control, which explains why, so far, it has rarely been the subject of research [32-34].

As a contribution to the existing literature, this research presents a field study conducted on the Li-ion battery running in a converted EV to correlate battery degradation with real-life driving and charging profiles.

### 1.1.4 Auxiliary Loads in EVs

In EVs, the on-board battery provides the power not only for driving but also auxiliary loads such as climate control loads. Therefore, the use of a climate control system (air conditioning (AC) & heating) adds more challenges to the EV design. The primary task of AC is to provide passengers' thermal comfort through maintaining the vehicle cabin temperature and humidity at desired levels. AC is believed to be the accessory that requires the largest quantity of power from the traction source. In conventional and hybrid electric vehicles (HEVs), this power is provided by the engine; however, in EVs, the power has to be extracted from the battery [35, 36]. It is

reported that, in an EV, AC may reduce the driving range up to 35%, depending on the AC usage frequency [37]. The loads are more significant when the climate-control systems are used in an initially very hot or very cold cabin at the beginning of a trip. Associated with the range reduction, there would be increased battery degradation for the same distance driven when AC/heating system is operating. Therefore, it is necessary to develop a tool for assessing the climate control system impact on the battery and vehicle performance. A modeling approach will be presented in this thesis that enables quantifying these impacts.

## 1.2 Document Organization

Chapter 2: presents a literature review about the fundamentals and modeling of batteries used in electrified vehicle and plug-in hybrid vehicle general considerations.

Chapter 3: this chapter is based on the papers published and submitted by Ehsan Samadani et al. [38, 39]. In this chapter, first, two commercially available Li-ion batteries are studied through thermal experiments. Profiles of heat generation at different operating conditions are generated and a data driven model for predicting the thermal ramp rate is developed. Afterwards, results of EIS tests conducted on the two cells are presented and, based on the observed phenomena during the EIS tests, an equivalent circuit model to predict the cells performance (voltage) under an arbitrary loading profile is developed.

Chapter 4: is based on the submitted report by Ehsan Samadani et al to the Transport Canada. [40]. In this chapter, results of field tests with a converted EV are presented through four major steps. First, implementation of a system to collect, store, analyze, and report vehicle and grid electricity usage data. Second, development of a powertrain model of the EV that includes battery degradation based on the collected data. Third, a feasibility study of using the EV as a replacement for the conventional fleet vehicles in operation by the owner company. Fourth, study of the battery degradation through collected data over the course vehicle operation. The study focus is to identify the degradation trends in the battery and propose a pathway for degradation modeling.

Chapter 5: presents a vehicle life time modeling considering temperature profiles, powertrain architectures, drive cycles and battery conditioning impacts. For this purpose, a thermal model of the vehicle cabin is developed. This model is able to predict the cabin temperature profile given a certain ambient and initial condition. The model is integrated to the battery model to determine the extra load on the battery and resulting extra capacity loss.

Chapter 6: This chapter summarizes the thesis, and highlights the main contributions of the research. It also contains recommendations for future works.

# Chapter 2

# Background and literature review

In this chapter, related background and literature on the battery modeling is presented.

## 2.1 Battery Elements and Specifications

Battery is an energy storage device consisting of one or more electrochemical cells that produces electrical energy from chemical energy stored in its active materials through electrochemical reactions. Depending on the desired nominal battery voltage and capacity Cells, are connected in series, parallel or both. Main components of a cell are anode, cathode and separator.

### 2.1.1 Anode

Upon the chemical reaction at the anode (oxidation) electrons are released and flow to the cathode through an external circuit. Important parameters in selecting the anode material are efficiency, high specific capacity, conductivity, stability, ease of fabrication and low cost.

### 2.1.2 Cathode

Cathode is the electrode in which reduction (absorbing electrons) takes place. During discharge the positive electrode of the cell is the cathode. During charge the situation reverses and the negative electrode of the cell is the cathode. The cathode is selected based on its voltage and chemical stability over time.

### 2.1.3 Electrolyte

Substances that release ions when dissolved in water are called electrolytes; which could include a wide range of acids, bases, and salts, as they all give ions when dissolved in water. The electrolyte completes the cell circuit by transporting the ions. The electrolyte are desired to be

highly conductive, non-reactive (with the electrode materials), stabile in properties at various temperatures, and economical.

### 2.1.4 Separator

A separator is a porous membrane inserted between electrodes of opposite charge. The key function of the separator is to keep the positive and negative electrodes apart to prevent electrical short circuits and, at the same time allow rapid transport of ionic charge carriers needed to complete the circuit. Care must be taken upon selecting the separator material, as it could adversely affect the battery performance (by increasing electrical resistance). Following considerations should be observed when selecting the separator [41]:

- Electrical insulation
- Minimal electrolyte (ionic) resistance
- Mechanical stability
- Chemical resistance to degradation by electrolyte
- Uniform in property and thickness
- Effective in preventing migration of particles

## 2.2 Battery Gloassary

### 2.2.1 Battery Management System

Battery management unit (BMU) is the central component of the battery system to ensure a healthy and appropriate usage of the sensitive battery cells. The BMU controls the usage of the battery cells by measuring variables such as voltage, current and temperature of each individual cell in the package. It also calculates important state variables such as SOC and power limits for charge and discharge of the battery. This information along with other signals (such as alarm signals) is sent from the BMU to the vehicles main computer which consequently is able to

control the propulsion of the vehicle in a qualitative manner without damaging the battery package [3].

### 2.2.2 State of Charge

The state of charge (SOC) indicates the amount of charge in Amp-hours left in the battery. The SOC can be divided into two types: engineering-SOC (e-SOC) and thermodynamic SOC (t-SOC) [42]. The e-SOC is the SOC apparent to the user of the battery and is rate dependent; it is the state of the capacity at a certain discharge rate, so different discharge rates will result in a different e-SOC at the same amount of charge in the battery. The t-SOC is the SOC of a battery defined by the thermodynamic properties in the cell and can be determined by the open circuit voltage of the battery; it is the state of the useable capacity in the cell.

### 2.2.3 Depth of Discharge-

A measure of how much energy has been withdrawn from a battery, expressed as a percentage of full capacity. For example, a 100 Ah battery from which 30 Ah has been withdrawn has undergone a 30% depth of discharge (DOD). Depth of discharge is the inverse of state of charge.

### 2.2.4 C-rate

The C-rate is a measure for the current of a battery cell and is scaled to the nominal capacity of a cell stated by the manufacturer at reference conditions. The current level that a battery cell can discharge at depends on the capacity of the battery. A current of 1C means that the battery cell is ideally charged or discharged in one hour, C/2 in two hours and 2C in half an hour. So a current of 0.5C for a cell with nominal capacity of 160Ah is equal to 80A.

### 2.2.5 Cell Capacity

The useable capacity is theoretically the possible amount of charge that can be discharged from a fully charged cell with an infinitely small current for a given minimum cell voltage, so that the voltage drop over the internal resistance becomes close to zero. The true capacity is the useable capacity under reference temperature and is used as a measure for the capacity fading

determination. The 1C capacity is determined with a C-rate of 1C under reference conditions and is generally used to measure the capacity fading [43].

### 2.2.6 Cycle

Cycle could be defined as a period of discharge followed by a full recharge. EVs, however, experience regenerative braking during operation, which required a change in cycle definition. Some define a cycle as a period of discharge with regenerative braking followed by a full recharge [44] or an amount of energy discharged with regenerative braking followed by the equal amount recharged [43]. A better alternative to measure the usage of a battery is the charge or energy processed in the battery. The ambiguous definition of a cycle is hereby also avoided.

### 2.2.7 Cell Open Circuit Voltage

By definition, the open-circuit voltage (OCV) is the battery voltage under the equilibrium conditions, i.e. the voltage when no current is flowing in or out of the battery, and, hence no reactions occur inside the battery. OCV is a function of State-of-Charge and is expected to remain the same during the life-time of the battery. Note, however, that other battery characteristics do change with time, e.g. capacity is gradually decreasing as a function of the number of charge-discharge cycles.

Because open circuit voltage shows a strong dependence on SOC for most batteries, it can be used as an estimation method. Because the battery must be at rest (several hours) for an OCV to be determined, it is not practical for real-time or continuous estimation. This poses problems for monitoring devices (e.g. clocks) where rest state is never realized. Additionally, Li-ion batteries (such as those used in vehicle applications) have traditionally shown a “flat” OCV when compared with lead acid batteries which can lead to difficulty in estimation as demonstrated in Figure 2-1and Figure 2-2.

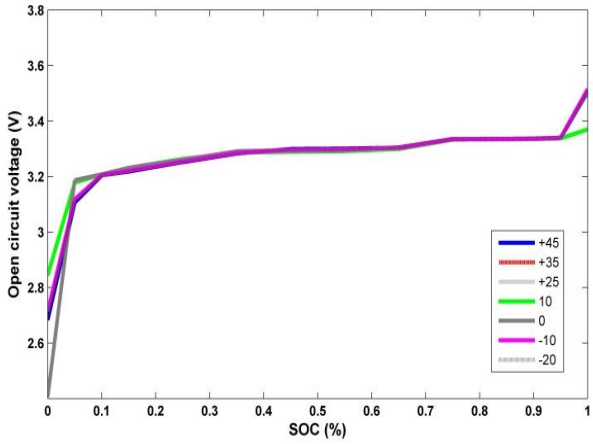


**Figure 2-1 Li-ion battery OCV variation against SOC [45]**

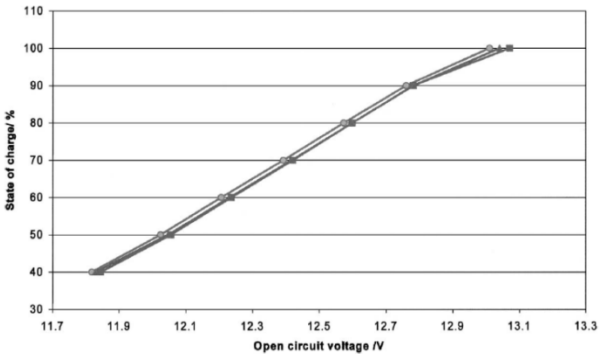


**Figure 2-2 Lead acid battery OCV variation against SOC [46]**

### 2.2.8 Internal Resistance

The internal resistance is sometimes considered as the ohmic resistance of the cell, which is the direct voltage change after application of a current step on a cell in equilibrium [47]. Another definition for the internal resistance is the sum of the ohmic, activation and diffusion polarization resistances [48], which is the largest possible voltage drop in the cell. Nevertheless, the complete voltage drop will result in power dissipation in the form of heat. The voltage drop can be mainly categorized as:

### IR drop

IR drop or ohmic drop is due to the current flowing across the internal resistance of the battery.

### Activation polarization

Activation polarization refers to the various retarding factors inherent to the kinetics of an electrochemical reaction, like the work function that ions must overcome at the junction between the electrodes and the electrolyte.

### Concentration polarization

Concentration polarization takes into account the resistance faced by the mass transfer (e.g. diffusion) process by which ions are transported across the electrolyte from one electrode to another. Figure 2-3 depicts the typical polarization curve of a battery with the contributions of all three of the above factors shown as a function of the current drawn from the cell. Since, these factors are current-dependent, the voltage drop caused by them usually increases with increasing output current. The internal resistance of a battery is dependent on temperature, SOC and C-rate. Depending on the measurement method, different values for the internal resistance can be found [49]. This is caused by the time constants associated with the activation and diffusion polarization resistances; whether the battery electrodes are in equilibrium or not is also important in determining the value of the internal resistance.

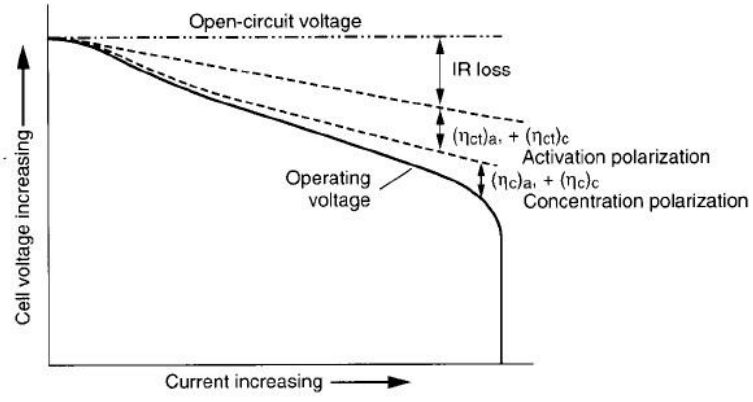

**Figure 2-3. Typical polarization of a battery [50]**

### State of health

The state of health (SOH) indicates the state of the battery between the beginning of life (BOL) and end of life (EOL) in percentages. The EOL of a battery is reached when the battery cannot perform according to the minimum requirements. For EVs this is defined by the battery manufacturers when one of the following conditions is met [51]:

- The capacity of a battery under reference conditions has dropped to 80% compared to the rated capacity under reference conditions. This is known as capacity fading.
- The maximum power delivered by the battery under reference conditions has dropped to 80% compared to the rated power under reference conditions. This is known as power fading.

Batteries in BEVs are normally oversized to have sufficient driving range, so the maximum power drawn from the BEV is much lower than the maximum power rating of the battery, therefore in BEVs generally the capacity fading criteria is taken as the SOH indicator

## 2.3 Electric Vehicles Battery Types

The batteries can either be of high energy density type or high power density type. Energy density is the amount of energy with regards to kg or liters. Power density provides a good measure on how much energy can be released due to discharge at a given time with regards to kg or liters. A high energy density battery is useful in applications where a longer driving distance is desired e.g. in a PHEV, which is intended to be driven on pure electricity for longer distances. A high power density battery is useful in an application where a short but intensive power pulse is required; e.g. in an ordinary HEV as the electric motor often only assists the combustion engine in short periods [50]. The first electric vehicles (EVs) developed in the nineties used lead-acid batteries. The range was around 100 kilometers, but since lead-acid batteries have a low energy density, the weight of the vehicle was high; therefore other chemistries were used in the years

after [52]. Due to the higher power and energy density and improved cycle life, EVs started to use nickel metal hydrate (NiMH).Today NiMH batteries are still used in hybrid electric vehicles (HEV) and plug-in hybrid electric vehicles (PHEV) for their low cost per Watt. But, due to high self-discharge, limited SOC operation range and low energy density, these batteries are unsuitable for EVs. ZEBRA or molten salt batteries are also used in EVs. These batteries have a low cost and high safety, but because of high operating temperature (270-350˚C) and low power density they are not very popular in EV applications [9]. Table 2-1 presents characteristics of different battery types used in EVs. Figure 2-4 also shows the Ragone plot for possible options.

**Table 2-1- Characteristics of battery types used in EVs [9]**

| Characteristic | Lead Acid | NiMH | ZEBRA | Li-ion |
|---|---|---|---|---|
| Nominal voltage | 2 v | 1.2 v | 2.58 v | 2.5 v/ 3.3 v/ 3.6 v |
| Specific energy | 30-45 Wh/kg | 30-80 Wh/kg | 90-100 Wh/kg | 90-220 Wh/kg |
| Energy density | 60-75 Wh/L | 140-300 Wh/L | 160 Wh/L | 280-400 Wh/L |
| Specific power | 180 Wh/kg | 250-1000 Wh/kg | 150 Wh/kg | 600-3400 Wh/kg |
| Cycle life | 500-800 | 500-1000 | 1000 | 1000-8000 |
| Self-discharge | 2-4% /month | 20-30% /month | 0% /month | 2-5% /month |
| Temperature range | -20-60 ℃ | -20-60 ℃ | 270-350 ℃ | -20-60 ℃ |
| Relative costs | Low | Moderate | Low | High |

Today, Li-ion battery is considered as the first choice for EVs, because it is superior in energy density, power density, and low self-discharge and high cycle life. The disadvantages of Li-ion batteries are also the high cost and safety issues. The term ‘Li-ion’ include a number of different chemistries; Table 2-2 shows some of the chemistries under development in EVs. Also, in Figure 2-5 a comparison is given between the best EV suitable Li-ion batteries.

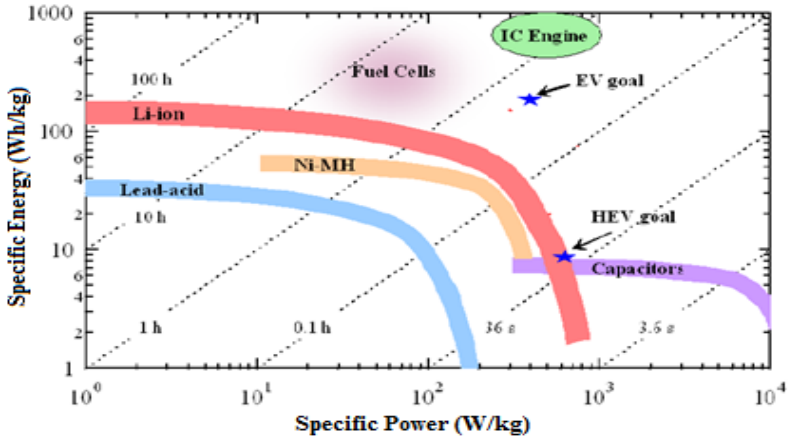


**Figure 2-4. The Ragone plot of various cell types capable of meeting the requirements for EV applications [53] .**

As an example, Lithium-iron-phosphate ($LiFePO_4$/LFP) does not experience thermal runaway and has almost no fire hazards, since no oxygen is released at high temperatures [54]. $LiFePO_4$ cells have the lowest costs per Ah and kW [54, 55], good life span, good power capabilities and are extremely safe, but they have low specific energy and poor performance at low temperatures.

**Table 2-2- Examples of different Li-ion batteries used in EVs [4]**

| Developer | Chemistry | Vehicle | Year |
|---|---|---|---|
| A123 | Doped Lithium nanophosphate | Fisker-Karma<br>Vue-PHEV | 2010<br>2009 |
| Panasonic<br>JCI-Saft | Lithium nickel cobalt<br>Aluminum oxide | Toyota-PHEV<br>S400-HEV | 2010<br>2009 |
| Hitachi | Lithium cobalt oxide | GM-HEV | 2010 |
| Altair Nanotechnologies | Lithium titanate spinel | Phoenix Electric | 2008 |
| EnerDel | Lithium manganese Titanate | Think | 2009 |
| Compact (LG)<br>NEC | Manganese spinel | Volt-EV<br>Nissan-EV | 2010<br>2010 |

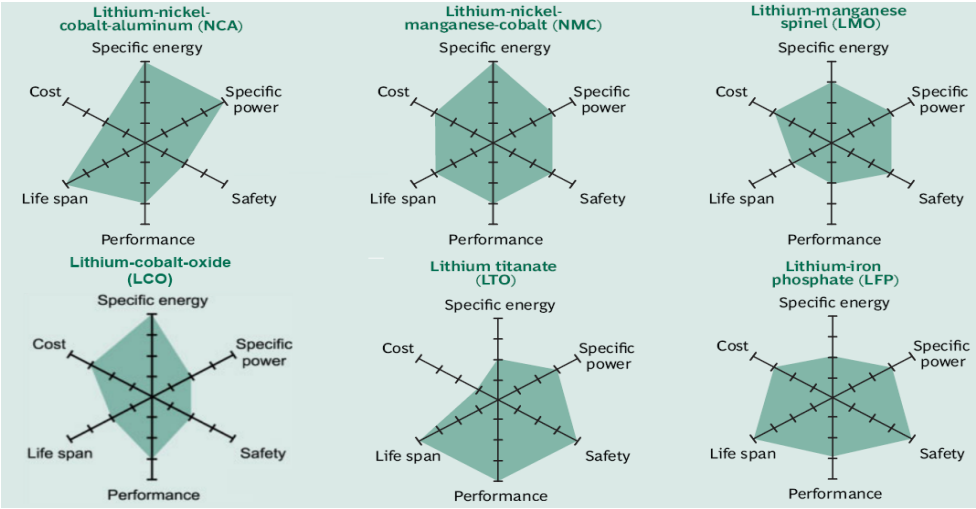


**Figure 2-5. Comparison of suitable Li-ions for EV. The more the colored shape extends along a given axis, the better the performance in that direction [56].**

## 2.4 Li-ion Cell Operation

A battery cell converts chemical energy to electrical energy. This is done by oxidation at one electrode and reduction at the other electrode. Li-ion battery cells utilize lithium ions to store and provide energy. A Li-ion battery cell consists of two electrodes, cathode and anode, with a separator in between, and current collectors on each side of the electrodes. The anode is usually made out of graphite or a metal oxide. The cathode is made of a composite material and defines the name of the Li-ion battery cell. The electrolyte can be liquid, polymer or solid. The separator is porous to enable the transport of lithium ions. It prevents the cell from short-circuiting and thermal runaway [57]. During discharge the lithium ions diffuse from the anode to the cathode through the electrolyte. The lithium ions will intercalate into the cathode, causing the cathode to become more positive. Due to the potential difference between the cathode and anode, an electric current will flow through the external circuit, supplying power to the load. During charging the opposite effect occurs. The current will cause the lithium ions to deintercalate from cathode and diffuse to the anode. At the anode intercalation of the lithium ions occur, charging the battery. These processes are shown in Figure 2-6 for a Li-ion cell.

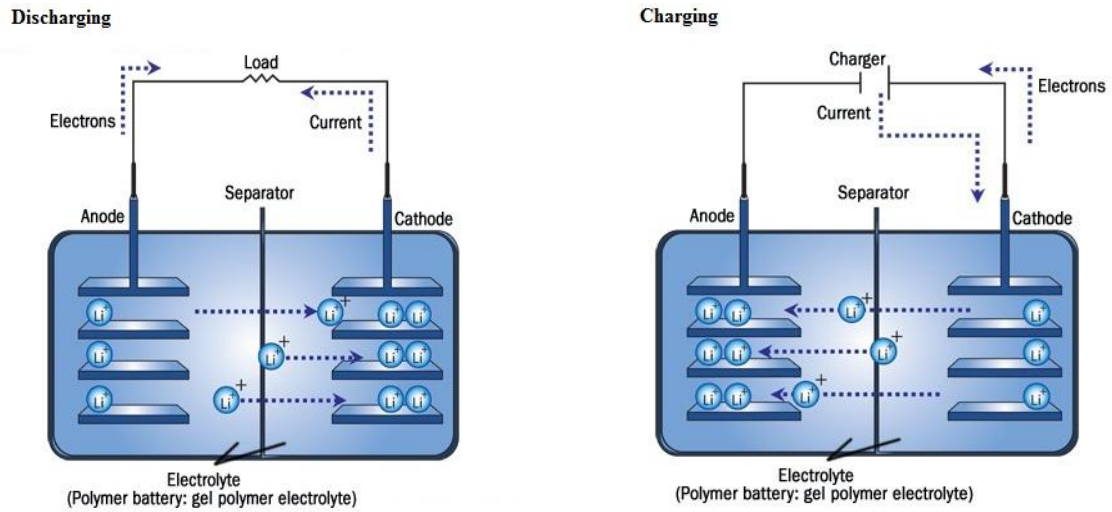


**Figure 2-6.Charge and discharge process in Li-ion battery [58]**

Li-ion cells are manufactured in various types of cell formats and geometries. Some of them are illustrated in Figure 2-7.

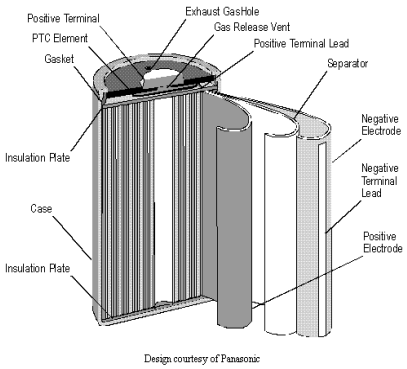


Cylindrical [56]

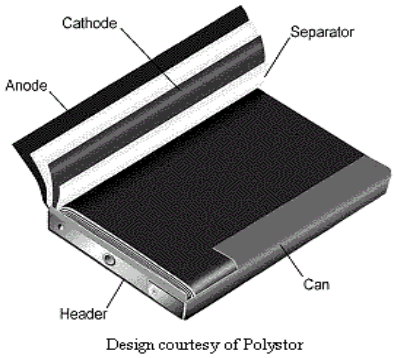


Prismatic [56]

Pouch [56]

**Figure 2-7 Types of Li-ion cell formats: cylindrical, prismatic and pouch cell.**

## 2.5 Battery Models

A major obstacle in PHEV commercialization is the high cost of the battery pack. To address this issue, different solutions such as energy density improvements, reduction of material cost, etc. could be considered. To come up with an optimal solution, one approach is to develop battery models. Battery modeling, in fact, provides information on battery charging/discharging and transient behavior and health status of the battery (battery degradation) as a function of different stress factors (temperature, discharge rate, etc.). EV designer use battery models for sizing the required battery and predict the battery performance. Battery models are also used for on-line self-learning performance and SOC estimation in BMS [59-61]. Common battery models used in the automotive applications are reviewed in the following sections.

### 2.5.1 Electrochemical Models

Battery modeling based on electrochemical equations provides a deep understanding of the physical and chemical process inside the battery and makes it useful when designing a cell, but high computational time makes these models improper for applications with high dynamics. The first electrochemical modeling approach to porous electrodes with battery applications was presented by Newman and Tiedemann in 1975 [62]. In the porous electrode theory, the electrode is treated as a superposition between the electrolytic solution and solid matrix, the matrix itself is modeled as microscopic spherical particles where lithium ions diffuse and react on the sphere surface. This approach was expanded to include two composite models and a separator by Fuller et al. in 1994 [63]. This model was later adapted for Ni-MH batteries [64], and then Li-ion batteries [27].

### 2.5.2 Equivalent Circuit Models

Equivalent circuit-based modeling (ECM) is suitable for automotive real time applications (such as BMS design), since it does not need deep understanding of electrochemistry of the cell

and at the same time it is well capable of simulating the battery dynamics. ECMs simulate the battery as a circuit often composed of resistors, capacitors, and other elements. There is a wide selection of models depending with tradeoffs of accuracy and time required. A large capacitor or ideal voltage source is selected to represent the open-circuit voltage (OCV), with the remainder of the circuit representing battery internal resistance and dynamic effects (e.g. terminal voltage relaxation). Generally, each observed phenomena is modeled with an individual circuit component. For example, the bulk electrolyte resistance is represented with a simple resistor, $R_0$. To keep the model simple, similar phenomena (e.g. concentration and electrochemical polarization effects) could be grouped, although this decreases model accuracy. Resistances of other components such as electrodes and separator are additive, and included in $R_0$. Other phenomena including the polarization effect of the battery are usually represented by capacitors and resistors in parallel. In addition, diffusion effects are represented by a Warburg element. In the following, common ECMs used in PHEV applications are presented.

**Simple Resistance ($R_{int}$) Model-** the Rint model as shown in Figure 2-8 is the simplest equivalent circuit battery model. It includes an ideal voltage source and resistance $R_o$. $R_o$ is usually defined as a function of SOC and temperature and operation modes (charge, discharge) calculated from HPPC tests [65].

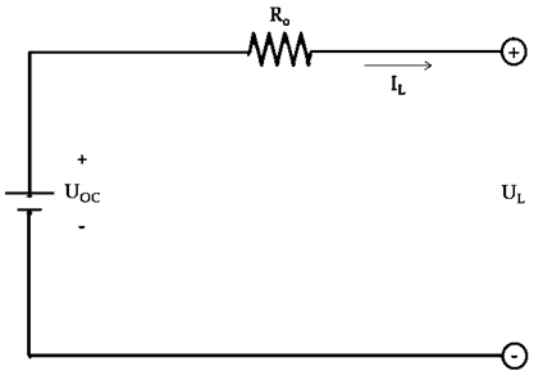


**Figure 2-8 Rint model equivalent circuit diagram**

**RC Model-** The resistor capacitor (RC) model shown in Figure 2-9, consists of three resistors and two capacitors. $R_t$, $R_e$, and $R_c$ represent the resistance across the terminal, bulk

solution, and surface respectively. $C_b$ represents the battery's ability to chemically store charge. $C_c$, which has a small value, represents battery surface effects [65].

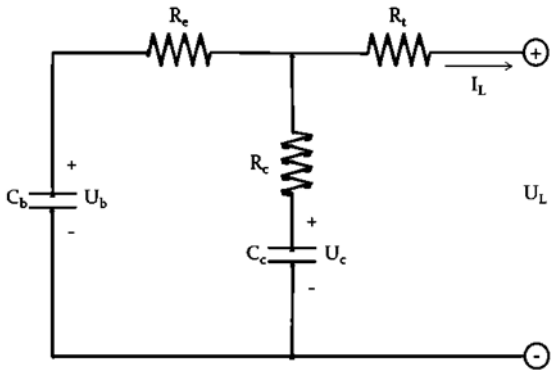


**Figure 2-9 RC model equivalent circuit diagram**

**Thevenin Model-** Thevenin Model circuit structure is shown in Figure 2-10. $E_0$ describes the battery's open circuit voltage. $R_0$ describes battery's internal resistance. I (t) is the battery's charge or discharge current and U (t) is the battery's terminal voltage. The RC circuit describes the battery polarization [66].

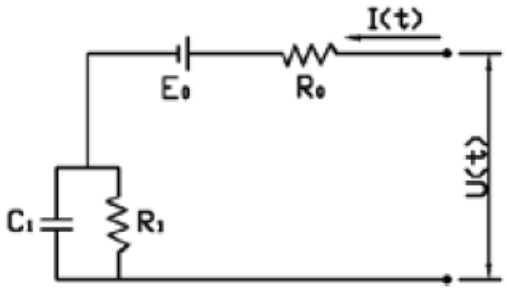


**Figure 2-10 Thevenin model equivalent circuit diagram [66]**

**DP Model-** Although a single RC component is capable of modeling polarization (like Thevenin), but, it becomes less accurate at the end of charge or discharge. The DP model shown in Figure 2-11 improves the polarization characteristics by simulating the concentration and electrochemical polarization effects separately. $R_{pa}$ and $R_{pc}$ represent electrochemical and

concentration polarization respectively. $C_{pa}$ and $C_{pc}$ characterize the transient response during power transfer for electrochemical and concentration polarization respectively [65].

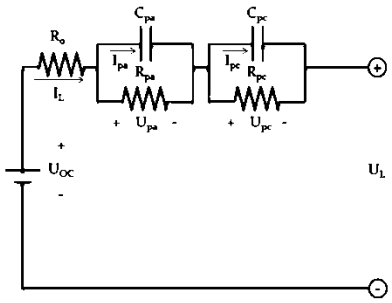


**Figure 2-11 DP model equivalent circuit diagram [65].**

**EDP Model-** The expanded dual polarization (EDP) is shown in Figure 2-12. The model components and their corresponding EIS features are also shown in Figure 2-13. $R_o$ corresponds to the cell bulk resistance (conductivity of the electrolyte, separator, and electrodes). $C_{pa}$ and $R_{pa}$ correspond to the semi-circle at high frequencies representing the SEI layer resistance. Cpc and Rpc correspond to the semi-circle at medium frequencies representing the faradic charge-transfer resistance and double-layer capacitance. Also, the Warburg element corresponds to the low frequencies representing the diffusional effects of lithium ion between the active material and electrolyte, (straight line at the very end in Figure 2-13. ) [19]. The combination of Rct and W are referred to as "faradic impedance," reflecting kinetics of the cell reactions.

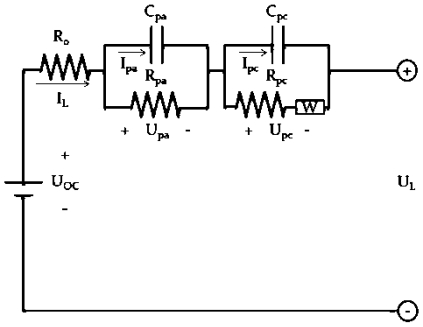


**Figure 2-12 Expanded DP model equivalent circuit diagram**

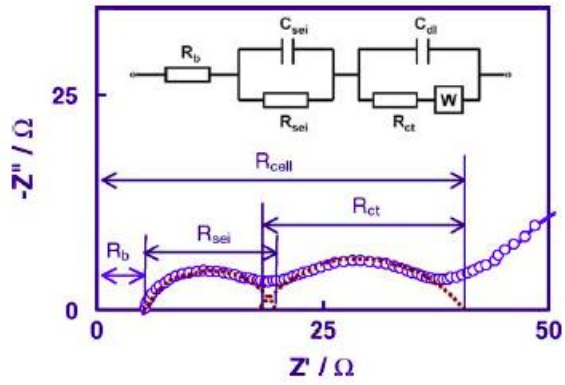


**Figure 2-13 EDP model components correlated with EIS results [19]**

## 2.6 Battery Degradation Modeling

Modeling of degradation is mainly based on the aging experiments and measurements and the complexity of the model depends on the number of stress factors and degradation mechanisms to be incorporated in the modeling. It is worth to mention that each battery type experiences a specific degradation mechanism and not all stress factors have similar impact on different battery chemistries.

To date, assessment and understanding of battery performance in EVs primarily relies on lab testing. Similar to standard driving schedule tests and analyses, these tests and duty cycle analyses have constraints in their validity to real-life operation. A main issue in both cases is that even under specific driving cycles or duty cycles; energy consumption strongly depends on uncontrolled ambient operating conditions. On the other hand, conducting drive cycle analysis using trip data collected from real-life vehicle operation is a challenging task [67]. Although quite helpful in evaluating battery state of health (SOH), very limited effort has been put into field testing with detailed data collection and analysis, mainly because such testing is costly and virtually no control[32].

## 2.7 Degradation Mechanisms of Li-ion Cells

The other aspect of batteries as traction sources is the battery durability and life which is of much concern in PHEVs. As the battery ages, it becomes less able to store and supply energy. The former is known as “capacity fade” and the latter as “power fade”. Knowledge about battery durability is also of much importance from the customer point of view, i.e. knowing how far the battery will operate properly over a reasonable period without needing a replacement and additional costs. Of course, it strongly depends on the operating conditions and the environment that the battery is exposed to.

In PHEV applications, the battery lifetime by convention is defined as the time period that the battery loses 20% of its initial capacity [66]. Batteries are designed for 8-10 years of service. However, battery lifetime is affected by several factors. High power imposed on the battery during acceleration and braking, which could be up to ten times higher than the average power demand, as well as driving behavior, extreme ambient temperature and charging habit all are known to be significant factors on the battery state of health (SOH). To improve the battery performance and lifetime prediction models these effects should be carefully taken into account [67]. Also thermal heating of the cell can significantly reduce the lifetime of a battery.

Li-ion cells undergo degradation in terms of capacity and power capability as result of continuous usage and also during the storage time. The performance degradation during cycling occurs much faster than storage under the same conditions. In the following, normal and accelerated degradation mechanisms for cycling and storage will be described.

### 2.7.1 Degradation under Storage (i.e. Calendar Aging)

Even under storage status, the active anode material is exposed to the electrolyte through the porous SEI layer, and side reactions enhance this SEI layer. High SOCs or high temperatures result in more severe capacity fading and resistance growth (power fading) in the cell as well. Therefore, to slow down the electrochemical processes and improve battery life, Li-ion cells need to be stored under optimal conditions (40% SOC and 15°C [68]).

### 2.7.2 Degradation during Cycling

Capacity fading primarily occurs on the electrode/electrolyte interphase under influence of intercalation and deintercalation of lithium ions. Ideally, loss of lithium ions and active material are the only mechanisms that degrade a Li-ion cell. But, in practice, other degradation mechanisms accelerate the capacity fading. Power fading is also coupled to capacity fading. The growth of the SEI layer results in the internal impedance rise of the battery cell and the deformation of the electrodes in a lower conductivity. As a result the power fading occurs due to the loss of active material. Capacity fading can be divided into four stages as shown in Figure 2-14. During stage "A", on the interphase of the anode with the electrolyte of the separator a Solid Electrolyte Interphase (SEI) film will form as a side reaction; this results in the fast decrease of capacity. This stage does not last for many cycles because as the cell is cycled more, the side reaction rate will gradually decay [69]. A schematic of a Li-ion cell with SEI layer is given in Figure 2-15.

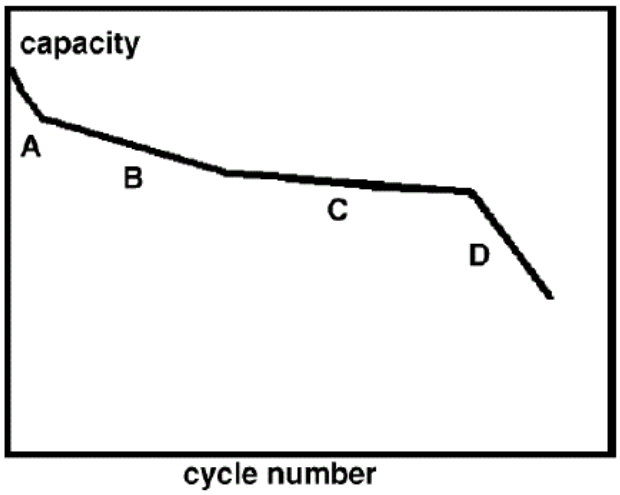


**Figure 2-14. The general shape for capacity versus cycle number [70].**

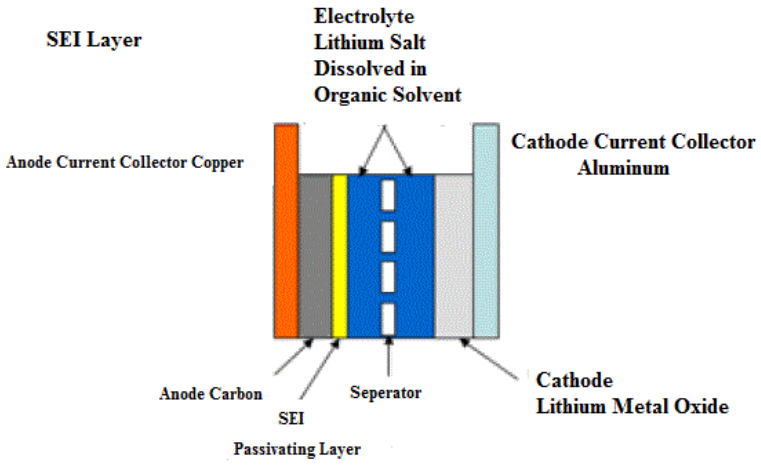


**Figure 2-15.Schematic of SEI film layer in Li-ion battery [71]**

In the stage B, anode is the limiting electrode [69]. Due to the SEI film layer formed on the anode, less active material is available and less lithium ions are intercalated into the anode during charging. As a result the loss rate of lithium ions will be slower, and the SEI layer protects the anode from reduction reactions with the electrolyte. During continuous intercalation and deintercalation the SEI layer cracks and more active material will be exposed. This will cause more side reactions and the SEI layer will continue to grow, leading to a less porous SEI layer and loss of lithium ions.

In stage C, the degradation rate of the active cathode material is higher than the loss of lithium ions. On the cathode/electrolyte interphase layer similar to the SEI layer is formed, which is named the Solid Permeable Interphase (SPI) [72]. This layer will also grow due to cycling and limit the active cathode material. The anode is however still the limiting electrode in this stage, as there is still more active cathode material available than lithium ions.

In stage D, due to the high degradation rate of the cathode, the cathode becomes the limiting electrode. Less active cathode material is available than the amount of 'cycle able' lithium ions [69]. Not all the lithium ions that were intercalated into the anode during charging can be intercalated into the cathode during discharge. Hence, more and more lithium ions are stuck inside the anode. The cathode will be fully intercalated during discharge, which raises the active

cathode material loss rate. These added effects cause an accelerated capacity fading and the capacity will rapidly decrease.

The severity of these stages is not the same for different types of Li-ion cells. For example, for $LiFePO_4$, the main capacity fading mechanism cells is the loss of lithium ions by the lithium ion consuming SEI film later formation, which also results in a loss of active anode material [44]. Loss of cathode material happens at a lower rate for $LiFePO_4$ cells, since neither cycling nor temperature change enhances the formation of the SPI layer [72]. This causes $LiFePO_4$ cells to have a much higher cycling life compared to other chemistries.

## 2.8 Accelerated Degradation during Cycling

Stress factors like extreme temperatures, large C-rates and high SOC have negative impact on the cell capacity and cause accelerated degradation. In the following each of these stress factors will be described.

**Depth of Discharge**- The cycle life of a cell is strongly dependent on the DOD. Figure 2-16 shows typical curve of cycle number against the DOD. The deeper the discharge, the more intercalation and deintercalation takes place in the electrodes. The loss of lithium ions and active electrode material is higher for larger DOD cycles. At high DODs, additional degradation mechanisms can occur resulting in decomposition and dissolution of cathode material and capacity fading [73]. DOD has no influence on the capacity fading of $LiFePO_4$ cells, but the charge or energy processed is the determining factor [74].

**C-rate-** High currents generate more heat and cause the temperature of the cell to rise invoking the high temperature degradation mechanisms. High currents also cause local over potential of the electrodes; it means that the maximum voltage for the cell is reached at an earlier stage at certain areas of the cell. High C-rates will also cause the SEI layer on the anode to crack faster. More active anode material is exposed and the SEI layer will restore itself, reducing lithium ions from the battery cell process. High C-rates will furthermore cause additional strain on the

electrode materials, resulting in increased deformation and loss of active material [73]. These effects will all result in capacity and power fading.

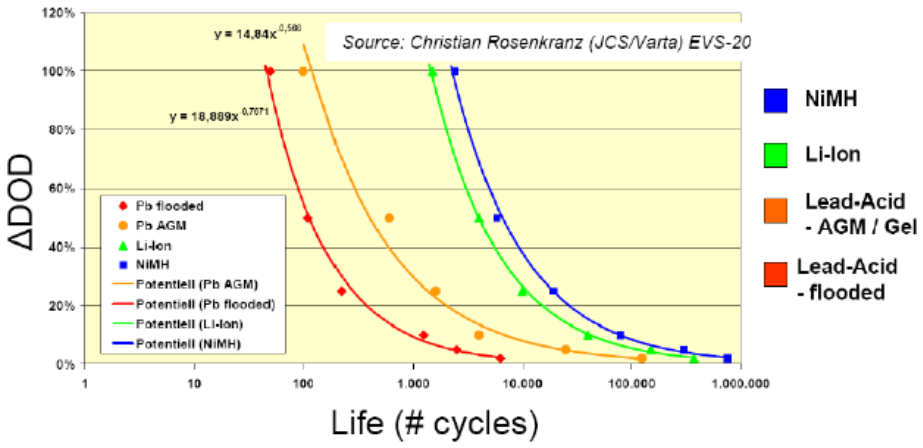


**Figure 2-16. Cycle life vs. ΔDoD curve for different battery cell chemistries[75]**

**Temperature**- Li-ion cells have an optimal temperature operating range (Figure 2-17); outside this range the battery cell undergoes severe loss of capacity. High and low temperatures have different effect on the battery life.

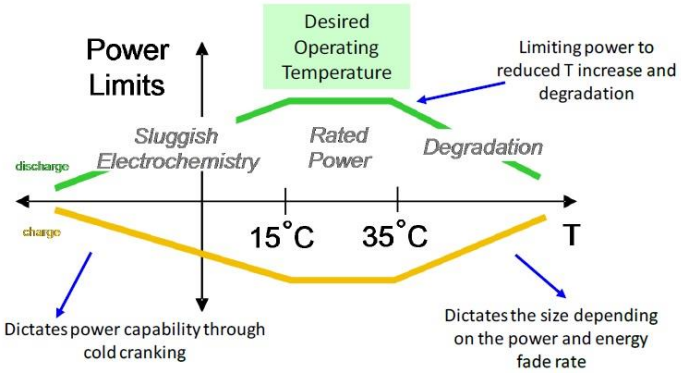


**Figure 2-17. Example-Battery cell's temperature range for optimal cycle life [76]**

**At low temperature**, due to the higher activation energy needed for the chemical reactions and lower ion diffusion; there will be a loss of capacity and deliverable power. However, when the temperature is restored to nominal level, the capacity and power capabilities will be

recovered. Under normal discharge, low temperature on its own does not have any permanent influence on capacity fading, but during charging, lithium plating is likely to happen because the intercalation rate at the anode is inherently slower than the deintercalation rate [77].

**High temperature**, in the long term, may cause severe damages to the cell. As is shown in Figure 2-18 increasing temperatures results in higher capacity fading. Due to high temperatures the SEI layer will slowly break down and dissolve into the electrolyte. The active material of the anode will be partly exposed to the electrolyte again, causing the side reactions. The damaged SEI layer will be restored due to the side reactions or a precipitation of the dissolved SEI particles will take place. Also parts of the cathode can dissolve into the electrolyte and incorporated into the SEI layer. As a result the intercalation at the anode will be more difficult and the ionic conductivity will be lowered. The same degradation mechanism happens at the cathode side with the SPI layer. Another degradation mechanism is the deformation of the anode and cathode. Detailed discussion of high temperature effect is available in [73].

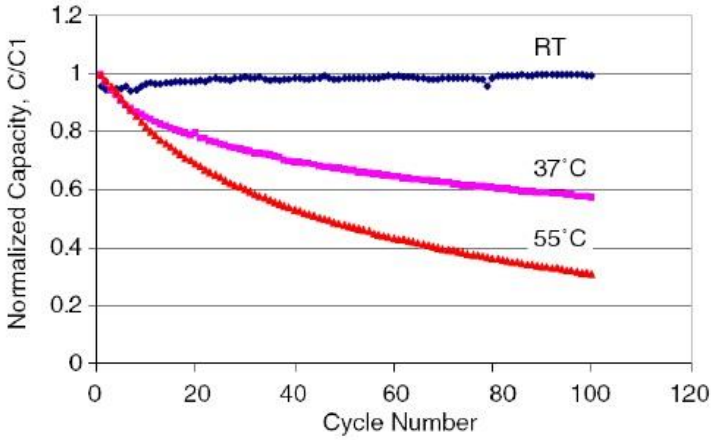


**Figure 2-18. The accelerated capacity fading due to high temperatures [78]**

**State of Charge-** At higher SOC battery cell is more reactive, which will accelerate degradation of the cell. At high SOC the anode will be highly energized and self-discharge will also be higher and the SEI layer will grow faster. Furthermore, electrolyte oxidation occurs at

high SOC, leading to impedance increase [79]. These effects result in capacity and power fading. During storage for a long time, high SOC will have more profound effect. In case of overcharge or over discharge, other degradation mechanisms come into play:

**Overcharge-** When the cell is charged over the specified voltage, a small increase in capacity is initially obtained, but the cycle life is strongly reduced. This effect is stronger as the end of charge voltage increases. During overcharge electrical energy is pumped into the battery, but more intercalation can hardly take place. This will be represented by a sharp increase of internal resistance and the temperature [51]. Decomposition of the binder and electrolyte, forming insoluble products, blocking the pores of the electrodes, and causing gas generation subsequently may take place [80].

**Over discharge-** When the cell is discharged under the specified cut-off voltage, two degradation mechanisms severely damage the cell. 1- Corrosion of the copper current collectors on the anode side of the cell and dissolution into the electrolyte resulting in loss of contact with anode and power fade [81]. 2- Decomposition of the SEI layer on the anode. The high anode potential will cause dissolution of the SEI layer. Upon recharge the exposed active material will cause side reactions to restore the SEI layer and reducing lithium ions, causing capacity fading [82].

## 2.9 Duty cycle & Drive cycle

In the analysis of the driving and charging data, terminologies such as drive cycle, duty cycle, and driving pattern are frequently used. A “drive cycle” refers to a history of driving, typically represented by a speed versus time curve. A “duty cycle” refers to a history of power usage of a device, typically depicted by a power versus time curve. A “driving pattern” is used to describe a driving condition, taking into account both road condition (e.g., road type) and driving behavior. Also, the duration between two successive stop is called driving pulse or micro trip which is represented in Figure 2-19. Among popular standard drive cycles used in vehicle design and development are, urban dynamometer driving schedule (UDDS), US06 and highway fuel

economy test cycle (HWFET), which represent city driving, aggressive driving (high speeds & accelerations) and highway driving respectively [81].

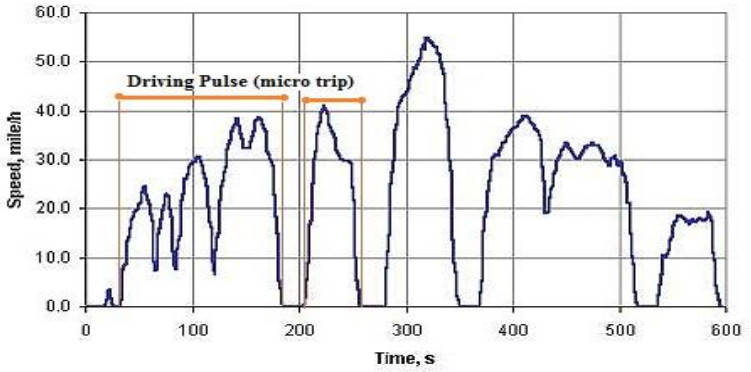


**Figure 2-19- Schematic of a driving cycle broken down into a series of sequential isolated "driving pulses" or "micro trip"**

## 2.10 PHEV and HEV Considerations

Degree of hybridization (DOH)- DOH refers to the hybridization ratio and is defined as the ratio of peak power of electric powertrain to the peak power of the whole powertrain. DOH, in fact, indicates if a PHEV is designed to operate primarily in All-Electric mode or blended mode. High DOH means the PHEV has larger electric motors and is capable of handling high power demands relying mainly on the battery. Although a higher DOH results in fewer amounts of emissions, higher petroleum displacement and efficient usage of the engine (fewer cold starts), it is associated with higher energy storage requirement and higher costs.

**Charge sustaining (CS) and Charge depleting (CD)-** HEVs are designed to operate in the charge sustaining mode (CS); i.e. the vehicle control system keeps the battery run within a narrow SOC range (e.g. 50%). This strategy results in an improved battery life as deep discharge cycles are inhibited. PHEVs have an additional mode called charge depleting (CD) in which the battery is the only energy source for the vehicle motion. Once the battery reaches a minimum SOC (e.g. 30%) the vehicle switches to CS and operate like a hybrid. The SOC range for CD mode is mostly determined by the impact on battery life (usually 95%-30%). From a vehicle

perspective, it is also important to quantify the sensitivity of vehicle fuel economy to CS operation at different SOCs.

**Charge depleting range-** Charge depleting range or all-electric range (AER) refers to the distance a PHEV can travel in CD mode. If the battery and electric motors are big enough, the engine is not used at all (or very sparingly) otherwise the engine is used more frequently (in case of a blended mode PHEV). Clearly, a fleet of PHEVs with higher AER can displace more gasoline and produce fewer emissions; however, a higher initial cost would be expected.

**Fuel Economy-** Fuel economy is described as the miles per gallon (MPG) or liter per 100 kilometers. In case of PHEVs, electrical consumption (kWh/100 mi) should be also reported to the customer. Environmental protection agency (EPA) has defined the term equivalent miles per gallon (MPGe) unit [82] to combine electrical and gasoline consumption numbers. MPGe is defined as:

$$MPGe = \frac{miles\ driven}{\frac{total\ energy\ of\ all\ fuel\ consumed}{energy\ of\ one\ gallon\ of\ gasoline}} \quad (2\text{-}1)$$

One gallon of gasoline is assumed to be equal to 33.7 kWh of electric energy. Using following formula, fuel economy (in MPG) and electrical consumption can be combined to yield the MPGe:

$$MPGe = \frac{100}{\frac{EC}{33.7} + \frac{100}{FE}} \quad \textbf{(2-2)}$$

Due to the dual operating mode, estimating the fuel economy of PHEVs is challenging. In fact, depending on the operation mode, PHEVs deliver very different fuel economy range. Therefore, a test procedure is needed to capture and combine both modes together [83]. Such test relies on the utility factor (UF) curve. UF is defined as the ratio of the distance driven in CD mode to the total distance. Overall PHEV fuel consumption is described in Equation (2-3), where FC represents the PHEV fuel consumption characteristics, and the UF is a function of the

depletion distance, AER [84].

$$FC = UF(AER) \times FC_{CD} + (1 - UF(AER)) \times FC_{CS} \quad \textbf{(2-3)}$$

There are two extremes for the UF; zero, meaning the vehicle totally operates under CS mode and one, when the AER is big enough to fully cover the average daily range driven by the vehicle. In the past, EPA used the city test (UDDS) and highway fuel economy test (HFET) for fuel economy measurement. However, these cycles often tend to overestimate the fuel economy as they do not reflect the real-life operating characteristics; e.g. driving in cold and hot temperatures or with higher aggressiveness. To improve this, in 2008, EPA suggested using a 5-cycle test procedure, including UDDS, HFET and three additional drive cycles and each portion of the test was assigned a different weighting [84]. However, running five cycles for CD and CS multiple times is not economical. Therefore, EPA replaced this test procedure with a modified version of UDDS and HFET test results as described in the Equations (2-4) and (2-5). The city test equation refers to the Federal Test Procedure (FTP) that consists of one cold start and one hot start UDDS.

$$City\ MPG = \frac{1}{0.003259 + \frac{1.1805}{City\ MPG}} \quad \textbf{(2-4)}$$

$$Highway\ MPG = \frac{1}{0.001376 + \frac{1.3466}{Highway\ MPG}} \quad \textbf{(2-5)}$$

Combined fuel economy is calculated by weight averaging of city and highway MPG values (usually 55% for city and the 45% for highway). [84].

# Chapter 3

# Modeling of Battery Thermal Behavior and Performance

The focus of this chapter is on proposing a battery model suitable for vehicle modeling purposes. In the first part, thermal characterization and a thermal ramp model developed for a Li-ion pouch cell is presented. In the second part, a dynamic model of a cell performance based on Electrochemical Impedance Spectroscopy (EIS) tests conducted on a similar cell is proposed and validated.

The following section is based on previously published work of "Thermal Behavior of Two Commercial Li-Ion Batteries for Plug-in Hybrid Electric Vehicles." by "Samadani et.al" [38] and is reproduced by permission from Society of Automotive Research (SAE) editorial office. This thesis author specific contribution to this paper is to: "prepare all the graphics and results, prepare the final manuscript. This paper is co-authored by Dr. Fowler and Dr. Fraser as supervisors. Also, L. Gimenez, W. Scott and S. Farhad contributed in assisting with cell experimental testing and preliminary data analysis.

## 3.1 Thermal Characterization

Depending on ambient conditions, there may be a need to remove or add heat to the battery in order to maintain the optimal temperature range and distribution. Non-uniform temperature distribution results in low charge and discharge performance and cell unbalancing over time. Existing thermal management techniques include applying liquids, insulations and phase-change-materials [25]. Essential tools in automotive pack design and thermal management are thermal and performance models. Such models require inputs such as system and operational parameters. Not all of these parameters are easy to directly quantify (e.g. heat effect and transport properties)

because their effects cannot be isolated; thus extensive tests are necessary to yield a clear understanding of heat generation and cell performance [26]. However, a simple model based on a limited number of lab tests may serve as an adequate alternative. In this section, the heat generation and temperature distribution over the cell surface in two different commercial PHEV pouch cells are evaluated through detailed thermal performance tests. The main objective is to provide a baseline performance model that can be modified to account for ageing in later studies. It should be noted that cycling required for testing will age the cell (affecting subsequent test behavior). Therefore, to minimize these unwanted effects, a fractional factorial design of experiments was employed to determine the minimum number of tests required to characterize thermal performance. Temperature and heat generation trends were identified by statistical analysis of the collected data and an empirical model was developed to predict the temperature and heat generation of the new cells under different loads and ambient temperatures.

### 3.1.1 Experimental setup

The thermodynamics of Li-ion cells is complicated due to the complexity and diversity of materials involved. To obtain a reliable prediction of the temperature profile, the total heat generation must be evaluated. Therefore, the temperature variation and heat dissipation of cells under a variety of loading conditions must be measured to provide a baseline for simple but high fidelity models of batteries at higher scales (module, pack) [26]. In this study, two commercial Li-ion pouch cells utilized in electric vehicles with similar energy densities (mass basis) are characterized. The cells' specifications are described in Table 3-1.

**Table 3-1: Prismatic Pouch Cell Specifications**

| **Parameter** | **Cell 1** | **Cell 2** |
|---|---|---|
| Cathode Material | $LiFePO_4$ | $LiMn_2O_4$ $Li(NMC)O_2$ |
| Anode Material | Graphite | Graphite |
| Electrolyte | Organic Carbonate | Organic Carbonate |
| Rated Capacity range (Ahr) | 18-21 | 14-17 |
| Dimensions (mm) | 7.25 x 160. x 227 | 5.27 x 164 x 250. |

| | | |
|---|---|---|
| Nominal Voltage (V) | 3.3 | 3.7 |
| Mass (g) | 496 | 376 |

The experiments were led by another member of the research group, but, they are represented here for clarity. A MACCOR 4200TM Tester was used to cycle the batteries at various C-rates in accordance with the Nested Face Centered Design of Experiments (see latter NFCD section). The tester has 16 channels that have a current control range of 100 mA – 15 A and a voltage control of 0.0 V to 5.0 V. Eight channels were combined in parallel (to allow a total maximum current of 120 A) for each cell, which was tested using a 4-wire parallel connection (2 low gauge wires deliver current, 2 high gauge wires measure voltage). The accuracy of the eight combined channels for each cell is ±0.1 A and ±1.0 mV. Figure 3-1and Figure 3-2 depict the cell test setup inside thermal chamber. The current-voltage data was logged every second or every change greater than 1 mV. The system directly tracks the charge and discharge capacity based on automatic integration of the current-time data.

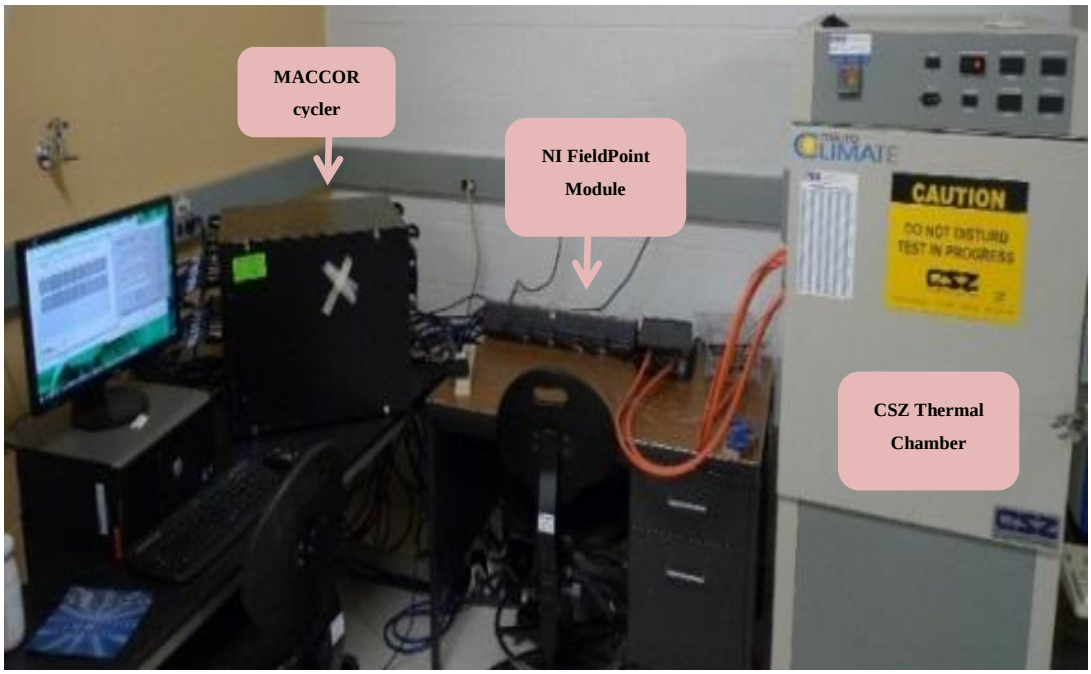


**Figure 3-1: Battery cycling test bench**

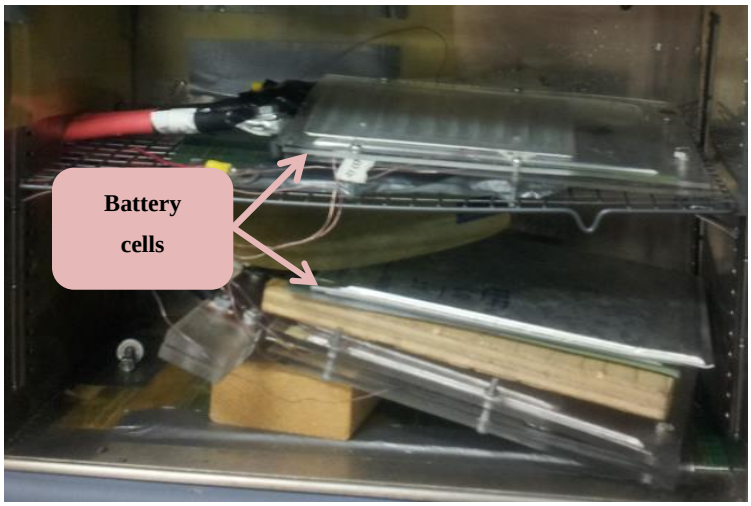


**Figure 3-2: Battery setup in thermal chamber**

The temperature across the surface of the cells was measured by 12 Omega® T-type 30 gauge thermocouples for each cell, 6 on each face (Figure 3-3). These wires are connected to three different National Instruments TC-120 FieldPoint™ modules which record 8 internally calibrated temperature measurements (accuracy ±0.15 K) at 5 second intervals. These measurements are stored through a custom LabVIEW-based data system. The cells are inside a Cincinnati SubZero MicroClimate® 1.2 chamber that can keep the temperature within ±0.5 K of the set point (narrower ranges near room temperature). The cells are enclosed in a jig that applies some compression on the batteries. The jigs consist of two 4 mm thick inner aluminum plates (to simulate pack fins that distribute heat across the surface) and a 5 mm thick acrylic enclosing to prevent heat dissipation through convection.

Ambient temperature and C-rate are taken as the control variables (Table 3-2). To reduce the time, cost, and degradation impacts, a design of experiment (DOE) algorithm called Nested Face Centered Design (NFCD) [85] was applied to determine the minimum number of required tests (Figure 3-4). “A” refers to the ambient temperature (in °C) and “B” to the C-rate (hr-1). To improve accuracy of analysis, the NFCD center-point condition (shaded in Table 3-2) was repeated 7 times.

The cycles follow the same procedure: first the cell is fully discharged at a constant C-rate of

1C and then at the constant cut-off voltage until the C-rate is reduced to C/20. The cells are then rested until thermal and chemical equilibrium is reached; equilibrium here is defined practically as a change in voltage smaller than 5 mV over a period of half an hour or a total rest time exceeding 2 hours. The cell is then fully charged from 0% to 100% SOC via constant current (C-rate specified by the NFCD) and then constant voltage at the upper voltage limit until C/20. The cell is rested again until equilibrium is achieved and then discharged at constant current (specified by the NFCD) and then at the cut-off voltage until a C-rate of C/20. The cell is allowed to rest once more and then the procedure is repeated for a different charge and discharge current.

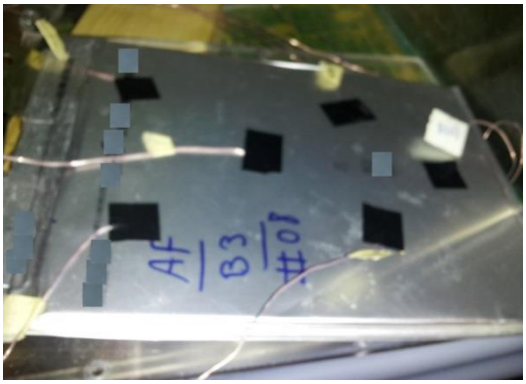

**Figure 3-3: Thermocouple placement on cell surface**

In some instances at low temperatures, the current limits exceeded the manufacturer's operating specifications for one of the batteries. In these cases the cell was cycled at the minimum current, then at the halfway point between the min current and the limit, and finally at the limit. The heat generation was then estimated based on these results and the model developed.

**Table 3-2: Resulting test points from NFCD**

| Factor | Min (-) | | Mid points | | | Max (+) |
|---|---|---|---|---|---|---|
| A (ºC) | -10 | | 1.25 | 12.5 | 23.75 | 35.0 |
| B ($hr^{-1}$) | Dis | 0.50 | 1.50 | 2.50 | 3.50 | 4.50 |
| | Chg | 0.30 | 0.80 | 1.30 | 1.80 | 2.30 |

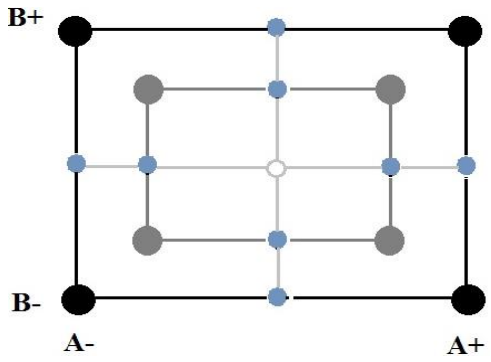


**Figure 3-4: A two factor NFCD used for thermal studies**

### 3.1.2 Analysis of results

The analysis is split into three sub-sections. The temperature distribution is examined first to evaluate the accuracy of using a mean temperature in representing the data. Heat generation is analyzed in the second section. The cell efficiencies are examined in the third section, Greater emphasis is placed in the second section due to its greater relevance to automotive applications.

Temperature Distribution

In order to quantify the heat generated, it is often assumed that the heat generation inside the cell is homogeneous, i.e. the heat is conducted very quickly so that only very small temperature variations exist. However, commercial batteries contain different heterogeneous (diverse in character) materials with different heat transport and generation properties, some of which are known to be anisotropic (direction dependent, such as $LiFePO_4$). Further, the asymmetric arrangement of the different material layers may cause asymmetric heat distributions in at least one dimension.

Statistical analysis of surface temperature variations across thermocouples placements, makes it possible to determine whether the temperature (and, subsequently, heat generation) is uniformly or normally distributed. If this is the case, then a mean heat generation rate for the cell as a whole can be assumed rather than determining localized rates (as would be required for complex heterogeneous systems).

As previously mentioned, 32 cycles were conducted for each cell with 12 thermocouple

readings every 5 seconds throughout the cycle. In order to decrease the computational time and complexity of the analysis, the statistical analysis presented only considers instantaneous measurements at 0%, 50%, and 100% SOC for all cycles. These 'snapshots' must be considered with the error of the thermocouples in mind (±0.15 K accounting for systematic errors) as well as naturally occurring temperature distributions within the chamber (which correspond to the temperature measurements at the initial SOC at the beginning of each charge/discharge step).

Statistics for the 12 thermocouple placements were calculated at each snapshot. The difference between mean and median, the coefficient of skewness and the standard deviation are of particular interest. The former two are indicators of the presence and relevance of a skewed distribution which could point out short-comings in using the mean temperature to represent the entire cell. The latter quantifies the magnitude of spread among the recorded temperature values. The coefficient of skewness was also calculated [86] according to:

$$\gamma_1 = \frac{\sqrt{n(n-1)}}{n-2} \frac{\frac{1}{n}\sum_{i=1}^{n}(T_i - \mu)^3}{\left(\sqrt{\frac{1}{n}\sum_{i=1}^{n}(T_i - \mu)^2}\right)^3} \tag{3-1}$$

Where n is 12 (thermocouple temperatures) and μ is the mean temperature between these 12 readings. The coefficient of skewness should be 0 for any centralized distribution (e.g. normal, Laplace, student t-distribution, uniform) [87]. Any deviation from that value will be the result of a skew, with the sign indicating the direction of the skew. Based on the statistical analysis, it can be stated that the mean is generally an accurate and centered representation of the temperature distribution and that the heat generation is either uniform, normally distributed with a small variance, or that at least the surface materials are conductive enough to keep the surface temperature of the battery even (such that it is unlikely that there would be large temperature variations within a single cell). Therefore the subsequent heat generation analysis will utilize the mean temperature in order to quantify the heat generated by the battery. Details of the statistical analysis can be found in Appendix A.

Heat generation

The main objective of the thermal experiments is to calculate the heat generated during each cycling period. The total heat generated according to the theory can be expressed by:

$$\dot{Q}_{gen} = I(V_{OC} - V) + TI\frac{dV_{OC}}{dT} \quad (3\text{-}2)$$

Where, $V_{OC}$ represents the open circuit voltage; I, is the current applied and V the cell terminal voltage. The first and second terms on the right hand side (RHS) of Equation (3-2) represent the irreversible and reversible heat generation, respectively. However, the term $\frac{dV_{OC}}{dT}$ is difficult to measure and the difference between open circuit potential and applied voltage is not easily determinable. Hence, using the recorded cell surface temperatures, it would be more practical to apply energy balance to calculate the generated heat:

$$\dot{Q}_{gen} = mC_p\frac{dT_{cell}}{dt} + hA(T_{cell} - T_\infty) \quad (3\text{-}3)$$

Where, 'm' is the cell mass(kg). $C_p$, is the specific heat($\frac{kJ}{kgK}$) ; and 'h' is the overall heat transfer coefficient($\frac{W}{m^2K}$). The first term on RHS of Equation (3-3) refers to the portion of heat generated that is translated into the cell temperature change and the second term is the heat rejected to ambient (simplified) where heat loss through radiation is assumed to be small and is incorporated within the overall heat transfer coefficient. It is necessary to first estimate the overall heat transfer coefficient of the cells. Examining the cell temperature curves during the rest periods (i.e. after charging or discharging, when the current is zero) it can be noted that the cell temperature approaches the ambient temperature at the end of rest. The temperature (cooling) curves during these periods can be used for estimating the heat transfer coefficient. During the rest period no heat is generated as the current is zero, hence Equation (3-3) is simplified to:

$$\int mC_p\frac{dT_{cell}}{dt} = \int hA(T_{cell} - T_\infty) \quad (3\text{-}4)$$

Integrating over the rest period time results in:

$$\int_{T_0}^{T_{\text{end of rest}}} \frac{dT_{cell}}{T_{cell} - T_\infty} = \frac{hA}{mC_p} t_{rest} \quad (3\text{-}5)$$

Considering the initial conditions: $t = 0$ and $T = T_0$, and allowing $\frac{hA}{mC_p} = \propto$ the cell temperature at any point of the rest period ($t_{rest}$) can be expressed as:

$$T_{cell} = T_\infty + (T_0 - T_\infty) \exp(-\propto t_{rest}) \quad (3\text{-}6)$$

Cell temperature at the end of each rest period was compared against the measured values in the tests and using least square linear regression in MATLAB, α was estimated as $8.5 \times 10^{-4}$ (s-1) for Cell 1 and $11 \times 10^{-4}$ (s-1) for Cell 2. As an example, modeled cooling curves are plotted against the measurements for the 23.75 ℃ ambient temperatures for Cell 1 in Figure 3-5. Given that the mass ratio $\left(\frac{m_{Batt1}}{m_{Batt2}} = 1.32\right)$ and the respective α coefficient ratio $\left(\frac{\propto_{Batt2}}{\propto_{Batt1}} = 1.29\right)$ are almost equivalent we can determine that both cells have similar overall heat transfer coefficients and therefore dissipate heat at similar rates. This is not surprising since the cells have similar geometry and contain materials with similar properties (e.g. both have copper and aluminum current collectors and thin plastic enclosing). It must also be noted that α coefficients are time-averaged over the duration of the rest period and may vary along with fluctuations of air circulation patterns in the thermal chamber.

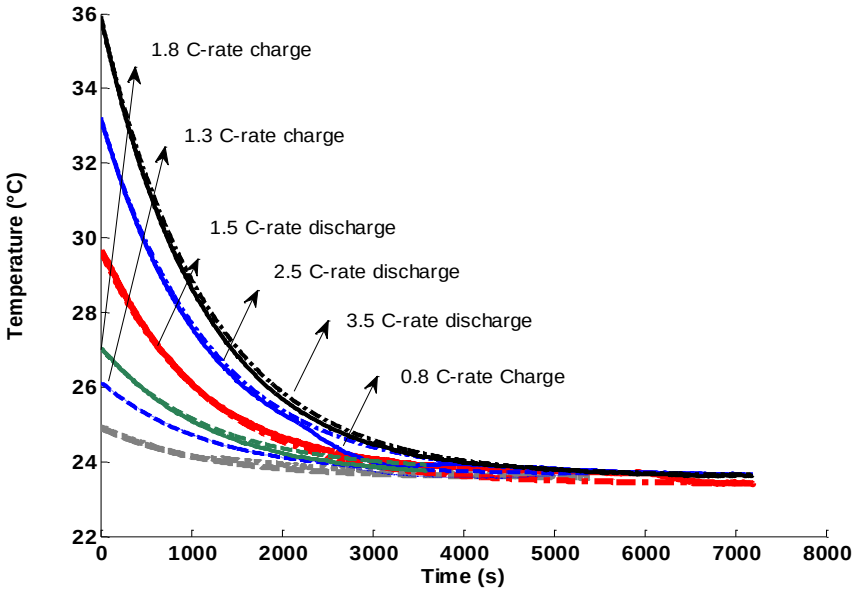


**Figure 3-5: $LiFePO_4$ Cell temperature changes during rest period at 23.75 °C- measured against fitted values**

Having estimated suitable values for the heat loss coefficient, the charge and discharge periods where heat is generated can now be analyzed. Figure 3-6 through Figure 3-9 show the cell temperature profile at high-mid-low chamber temperatures and lowest and highest C-rates for charge and discharge tested. At lower temperatures the cells experience higher temperature rise due to increased cell resistance and therefore decreased efficiency can be expected. Increasing the C-rate also results in higher temperature increase over the test cycle as dictated by Equation (3-2) (as well as a decrease in the charge and discharge capacity). The next step in the analysis is to calculate the heat generation rate and also the accumulated generated heat which is simply calculated based on Equation (3-2).

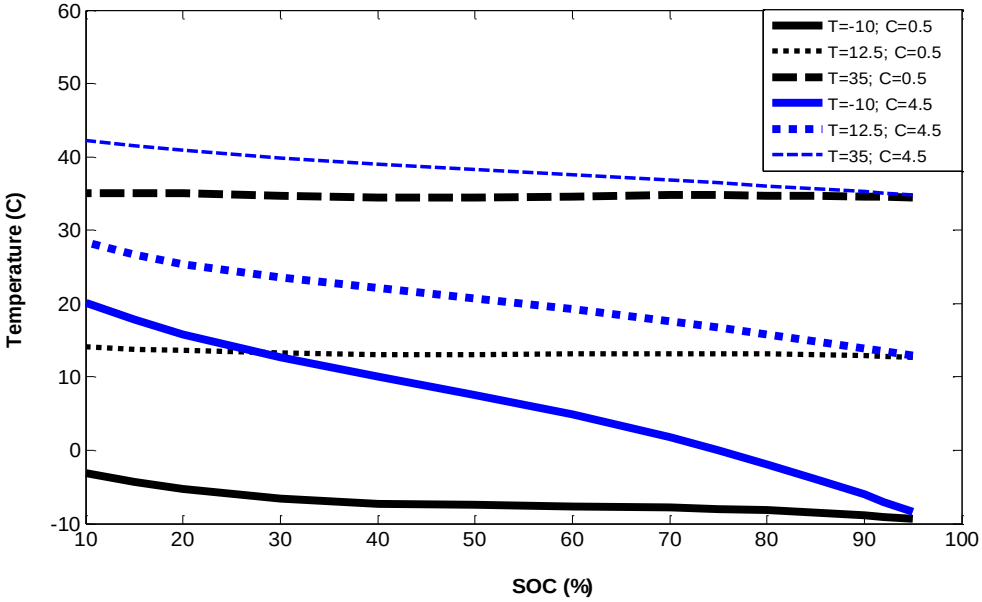


**Figure 3-6: $LiFePO_4$ cell temperature changes during discharge cycles**

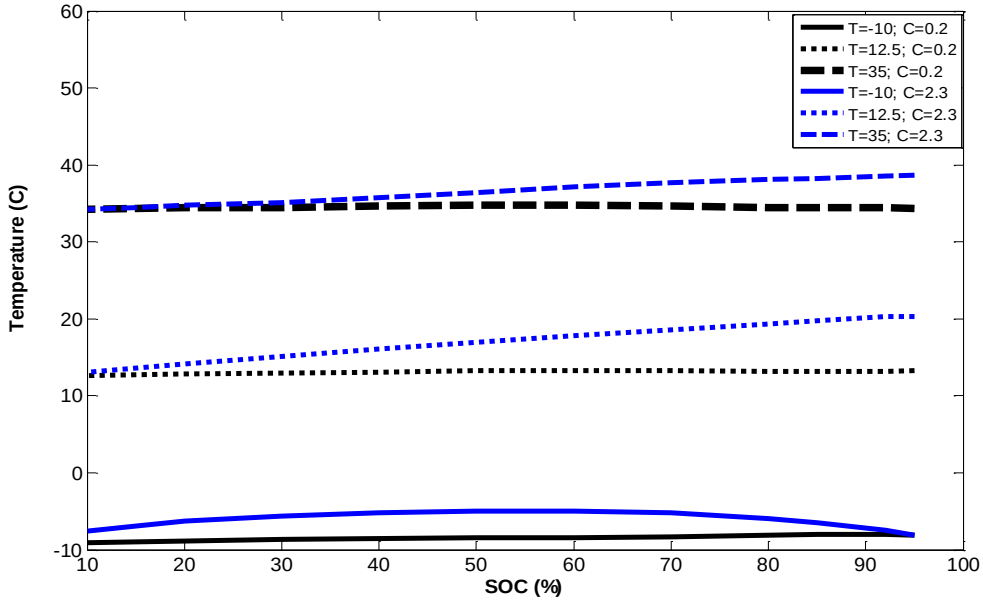


**Figure 3-7: $LiFePO_4$ cell temperature changes during charge cycles**

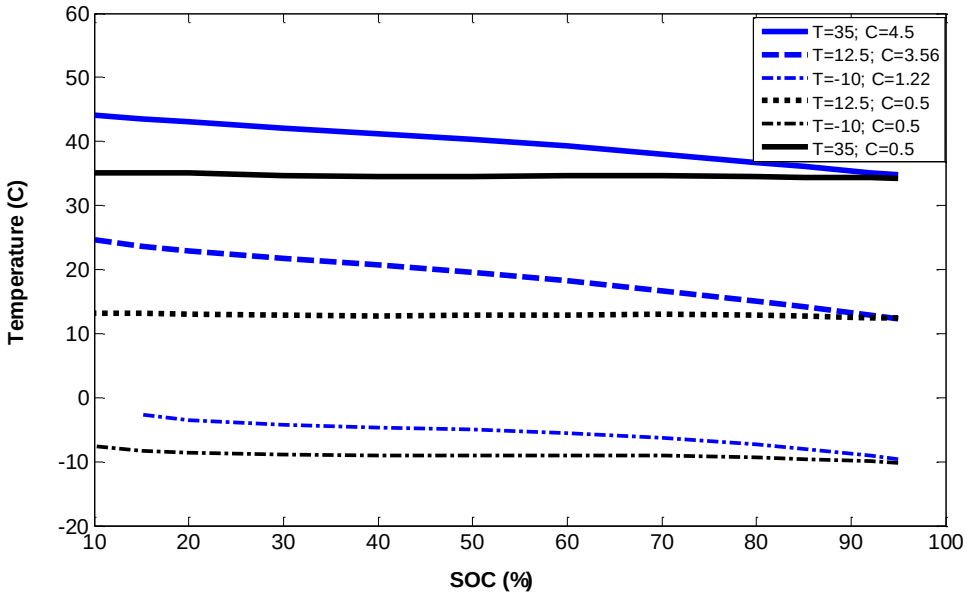


**Figure 3-8: $LiMn_2O_4$ cell temperature changes during discharge cycles**

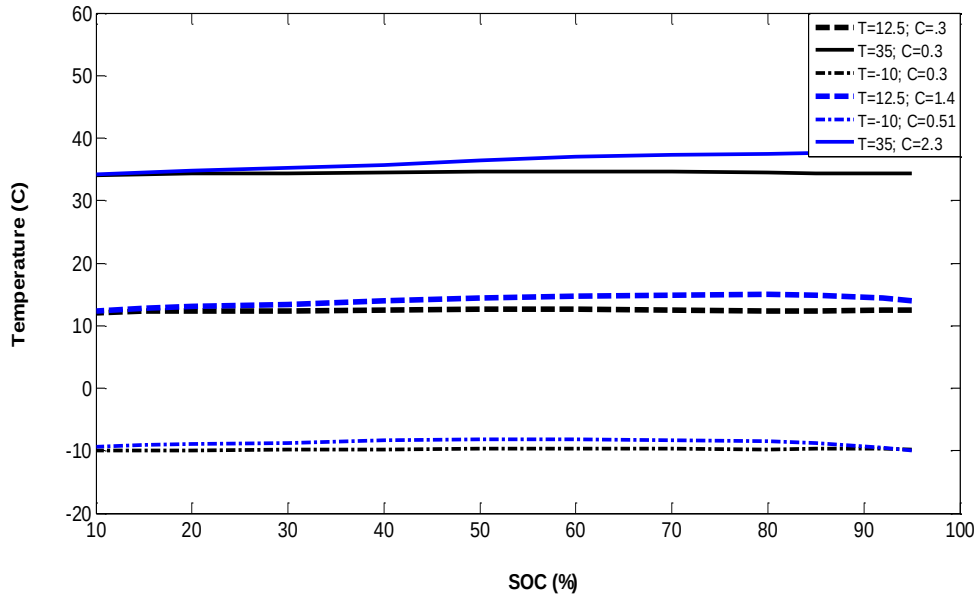


**Figure 3-9: $LiMn_2O_4$ cell temperature changes during charge cycles**

At each SOC, the accumulated heat is calculated with reference to either 100% SOC (for discharge) or 0% SOC (for charge) as:

$$Q_{acc} = \int_{soc\ 0\%\ or\ 100\%}^{desired\ soc} \dot{Q_{gen}}\, dt \qquad (3\text{-}7)$$

Figure 3-10 through Figure 3-13 show the accumulated heat of the cell at different ambient temperatures and C-rates. Both cells generated more heat in lower temperatures which results in a less efficient operation. Also, it is observed that the heat generation is linear between 95% - 20% SOC, the operating range of PHEVs. However the end regions exhibit increased heat generation rates (0-10% for discharge and 95-100% for charge). This jump in the heat generation is related to increased resistance, possibly from mass transport or side reactions occurring in the cells at very high and very low SOCs. This region is increased at lower temperatures and higher SOCs, suggesting mass transport limitations are the cause of the increased resistance.

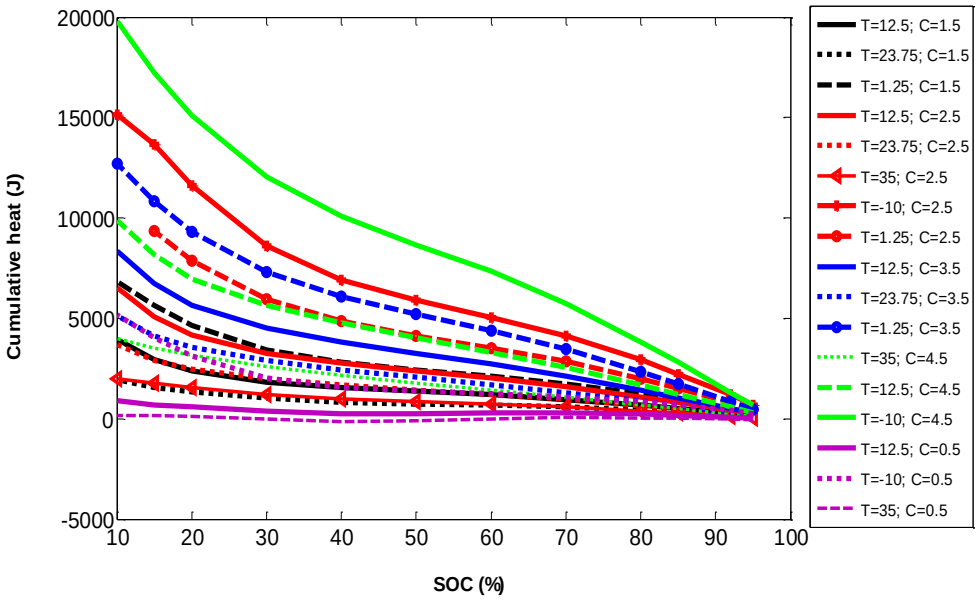


**Figure 3-10: $LiFePO_4$ cell cumulative heat during discharge cycles**

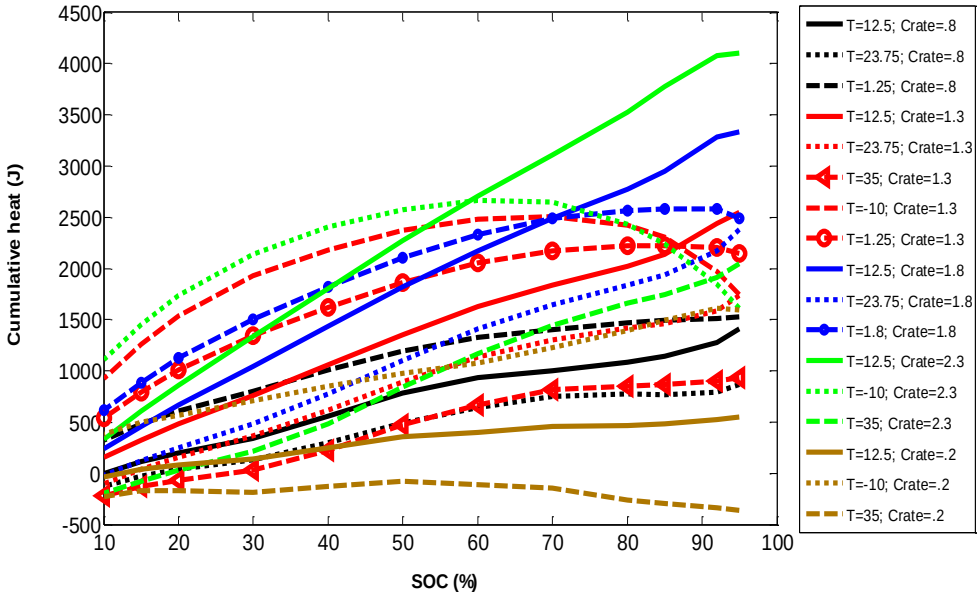


**Figure 3-11: $LiFePO_4$ cell cumulative heat during charge cycles**

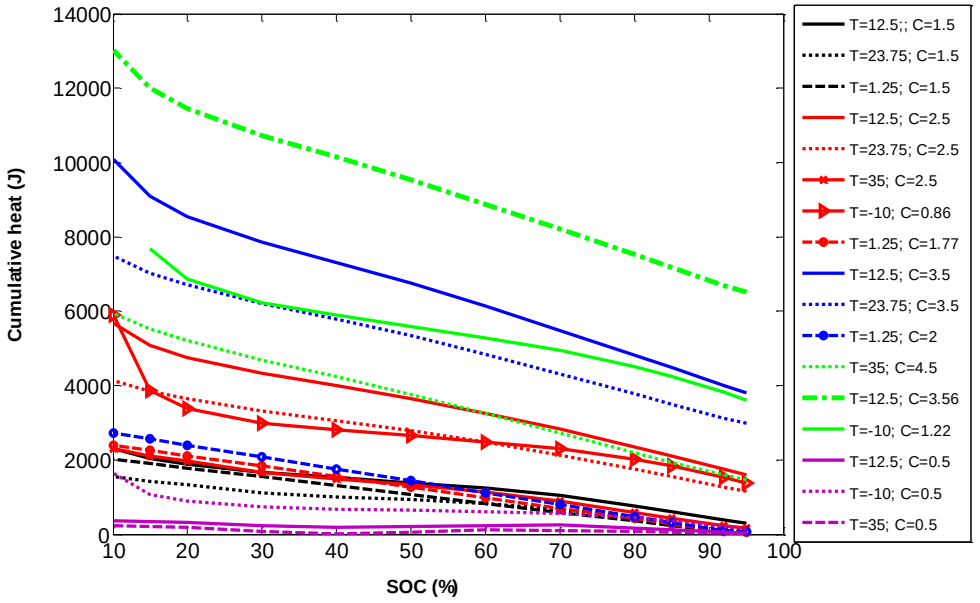


**Figure 3-12: $LIMn_2O_4$ cell cumulative heat during discharge cycles**

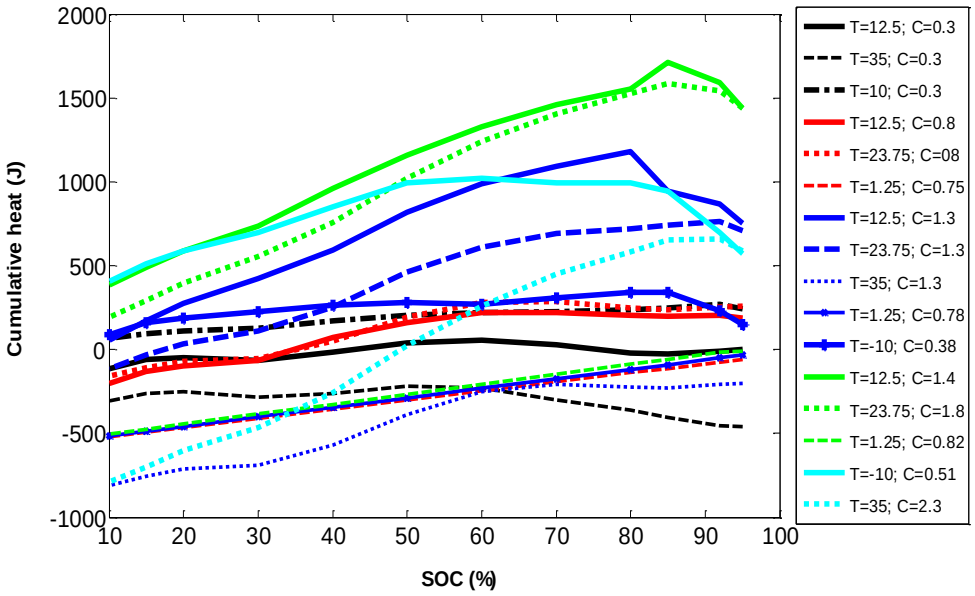


**Figure 3-13: $LiMn_2O_4$ cell cumulative heat during charge cycles**

Battery efficiencies

A significant factor in reducing the operating cost and increasing the service life of all hybrid and electric vehicles is to maximize utilization of the energy stored in the battery. In this regard, ensuring its efficiency remains at a specified performance level is important, not only for calculations of true cost of 'fuel' (electrical energy) and range prediction, but also for end of life determination and repurposing applications. There are several efficiencies defined for batteries [88] which will be employed in this section. It is believed that some, if not all, efficiencies decrease through the lifetime of the battery (with ageing). It is therefore possible that these efficiencies could be measured on-board as a diagnostic tool for determining the SOH of the battery. In order to establish a baseline for the batteries, the effects of temperature and C-rate must be established. In this section, such a baseline for three efficiencies will be established and discussed.

**Electrical Efficiency**: sometimes referred to as energy efficiency, it is defined as the ratio of electrical energy that can be removed from the battery to the electrical energy supplied:

$$\eta_{electrical} = \frac{\int (VI)_{dis} dt}{\int (VI)_{chg} dt} \quad (3\text{-}8)$$

This efficiency is not observed carefully by vehicle manufacturers but it has important implications to the vehicle driver. Essentially, it tells the driver how much usable electrical energy is available based on the previous charge, allowing for an accurate calculation of energy (fuel) costs. This efficiency was determined over the entire range of SOC, including the constant voltage portions of the charge and discharge. In practice, the actual electrical efficiency observed will vary according the usable SOC window within each vehicle application as well as the drive cycle intensity.

Electrical efficiency of the two cells is reported in Table 3-3 and Table 3-4. In moderate and high temperatures both cells show to have high electrical efficiency. At low temperatures, both cells experience decreased electrical efficiency though the impact on the $LiFePO_4$ cell is significantly greater. In vehicular applications, this effectively translates into a reduced range in cold weather (as well as higher electricity cost per mile). Increasing the C-rate also decreases the electrical efficiency suggesting more intense drive cycles will also provide reduced range, though the impact may not as significant as observed with temperature.

**Table 3-3 Electrical efficiency of the $LiFePO_4$ cell**

| Chamber Temperature (°C) | Discharge C-rate (Charge C-rate is ½ of the discharge) | | | | |
|---|---|---|---|---|---|
| | 0.5 | 1.5 | 2.5 | 3.5 | 4.5 |
| -10.00 | 78.61 | | 73.40 | | 68.79 |
| 1.25 | | 81.36 | 78.21 | 75.88 | |
| 12.50 | 93.46 | 88.50 | 85.36 | 82.84 | 80.87 |
| 23.75 | | 91.85 | 89.72 | 87.67 | |
| 35.00 | 97.33 | | 93.23 | | 89.67 |

**Table 3-4 Electrical efficiency of the $LiMn_2O_4$ cell**

| Chamber Temperature (°C) | Discharge C-rate (Charge C-rate is ½ of the discharge) | | | | |
|---|---|---|---|---|---|
| | 0.5 | 1.5 | 2.5 | 3.5 | 4.5 |
| -10.00 | 89.60 | | 87.80* | | 85.89* |
| 1.25 | | 89.91 | 88.91* | 88.16* | |
| 12.50 | 96.67 | 93.63 | 91.14 | 89.31 | 89.13* |
| 23.75 | | 94.97 | 93.44 | 91.68 | |
| 35.00 | 97.91 | | 95.00 | | 92.17 |

* The cell was not cycled at the labeled C-rates because these lie beyond manufacturer's allowable cycling specifications for that temperature. Instead, it was cycled at the limiting C-rate (where the column states 3.5 or 4.5), or half-way between the limit and the 0.5 C-rate (where the column states 2.5).

**Coulombic efficiency:** defined as the ratio of the discharged capacity to the Ah needed to in order to bring the battery to the discharge initial state (SOC), expressed as follows:

$$\eta_{coulombic} = \frac{\int I_{dis} dt}{\int I_{chg} dt} \quad (3\text{-}9)$$

Where, $I_{dis}$ and $I_{chg}$ refer to the discharge and charge current respectively and the SOC is the same at the beginning of discharge and at the end of charge.

Several factors affect the coulombic efficiency, such as charge and discharge current and charging method (constant voltage/power/current). The occurrence of secondary chemical reactions (especially at high SOCs) also significantly reduces the coulombic efficiency; i.e. charging at high SOCs is less efficient [89]. It is therefore possible to examine coulombic efficiency in order to estimate the extent of electrochemical side reactions occurring in the cells.

Coulombic and electrical efficiency are related to each other through the voltage efficiency which is defined as the ratio of the average voltage during discharge to the average voltage during charge[88]:

$$\eta_{electrical} = \eta_{coulombic} \times \eta_{voltage} \quad (3\text{-}10)$$

The coulombic efficiency of the cells over the range of 0% to 100% SOC was found to be 99% or higher for all instances except for cell 1 at 0.5C and -10°C where it was 97.58%. The cells show a high coulombic efficiency which is reasonable as both cells were fresh at the time of

testing. No effect of C-rate or temperature was observed suggesting that the electrical inefficiency is entirely caused by decreased voltage efficiency.

**Thermal loss:** Knowing the electrical energy input/output and heat generated, the thermal losses of the module under cycling can be measured. Thermal loss is a metric that reflects the ability of a cell is able to produce useful work and is determined by

$$Thermal\ loss\ (\%) = \left(1 - \frac{Energy_{\frac{in}{out}}}{Energy_{\frac{in}{out}} + Heat_{gen}}\right) \times 100 \quad (3\text{-}11)$$

$Energy_{in/out}$ refers to the energy measured at the battery terminals ($= \sum V \times I \times t$) during a charge or discharge cycle. A part of the energy fed into the battery by the charger converts to the thermal loss and is denoted by '$Heat_{gen}$' in Equation (3-11). This energy is equivalent to $Q_{acc}$ as defined in Equation (3-7).

Table 3-5and Table 3-6 show the thermal loss calculated for the $LiFePO_4$ cell in discharge and charge modes. The thermal loss is inversely correlated with the temperature. The cell shows the best performance at 35°C but it is known that higher temperature cycling corresponds to rapid ageing, so this may not be the best cycling temperature. The thermal loss correlation with C-rate is positive. However, some values during the charge indicate negative (decreasing) correlation because the constant voltage portion of the charge took a long time at low current, so the cell was allowed to cool and thus a lower than expected heat was generated at the end of the step. These points are marked on the LFP tables by an asterisk. The thermal loss is also greater during discharge than during charge (comparing amongst the same C-rates). This supports the idea that vehicles should have adequate heat management systems on the road, and not necessarily during charge.

**Table 3-5: Thermal loss (%) of $LiFePO_4$ cell during discharge**

| C-rate / Temp | 0.5 | 1.5 | 2.5 | 3.5 | 4.5 |
|---|---|---|---|---|---|
| -10.00 | 12.96 | | 12.94 | | 11.45 |
| 1.25 | | 8.79 | 8.82 | 8.76 | |
| 12.50 | 5.52 | 6.83 | 6.89 | 6.46 | 6.42 |
| 23.75 | | 4.43 | 4.66 | 4.58 | |
| 35.00 | 1.05 | | 2.98 | | 3.35 |

**Table 3-6: Thermal loss (%) of $LiFePO_4$ cell during charge**

| C-rate / Temp | 0.3 | 0.8 | 1.3 | 1.8 | 2.3 |
|---|---|---|---|---|---|
| -10.00 | 4.81* | | 1.69* | | 0.91* |
| 1.25 | | 4.45* | 3.77* | 3.72* | |
| 12.50 | 8.58 | 7.07 | 4.47* | 3.3* | 2.58* |
| 23.75 | | 1.45 | 2.29 | 2.23 | |
| 35.00 | 0.39 | | 1.5 | | 2.04 |

Table 3-7 and Table 3-8 show the thermal loss calculated for the $LiMn_2O_4$ cell in charge and discharge modes. The values in red show the modified C-rates applied on the cell according to the test limits recommended by the manufacturer. $LiMn_2O_4$ cells have an overall lower thermal loss than the $LiFePO_4$ cell, but, in terms of dependence on the temperature, similar trends can be observed.

**Table 3-7 Thermal loss (%) of $LiMn_2O_4$ cell during discharge**

| C-rate / Temp | 0.5 | 1.5 | 2.5 | 3.5 | 4.5 |
|---|---|---|---|---|---|
| -10.00 | 5.69 | | 0.86* | | 1.22* |
| | | | 5.91 | | 5.89 |
| 1.25 | | 1.5* | 1.77* | 2.0* | |
| | | 2.76 | 3.18 | 2.9 | |
| 12.50 | | | | | 3.56* |
| | 2.11 | 2.66 | 2.61 | 2.51 | 1.77 |
| 23.75 | | 2.61 | 2.13 | 1.92 | |
| 35.00 | 1.35 | | 1.95 | | 1.7 |

**Table 3-8 Thermal loss (%) of $LiMn_2O_4$ cell during charge**

| Temp \ C-rate | 0.3 | 0.8 | 1.3 | 1.8 | 2.3 |
|---|---|---|---|---|---|
| -10.00 | | | 0.38* | | 0.51* |
| | 1.13 | | 0.62 | | 3.85 |
| 1.25 | | 0.75* | 0.78* | 0.82* | |
| | | 0.64 | 1.83 | 1.47 | |
| 12.50 | | | | 1.43* | |
| | 0.01 | 0.46 | 0.38 | 0.31 | |
| 23.75 | | 0.47 | 0.86 | 0.18 | |
| 35.00 | 0.02 | | 0.36 | | 0.89 |

Model development

Efficient and safe operation of the battery relies on the efficiency of the vehicle battery thermal management system (BTMS). The BTMS designer must be able to predict the amount of heat generation and temperature fluctuation of the battery during a driving or charging cycle. For this purpose, a thermal model is required to enable prediction of battery temperature changes according to the battery thermodynamic and chemical status. Based on the observed trends in the cell surface temperature and the heat generation profiles, it is possible to develop a model to predict the temperature changes and generated heat in the cell as a function of SOC, cell temperature, ambient temperature and C-rate. A multiple linear regression analysis was performed on the data of heat generation for charge and discharge separately. Results of regressions on the cell #1 (LiFePO4) are presented here. A quadratic fit presented in Equation (3-12) including the interaction terms between the SOC, C-rate, cell temperature and the ambient temperature, was applied to the data of heat generation rate.

$$\dot{Q}_{gen} = b_1 + b_2 C_{rate} + b_3 T_{cell} + b_4 SOC + b_5 C_{rate}^2 + b_6 SOC^2 + b_7 T_{cell}^2 + b_8 C_{rate} \times SOC + b_9 C_{rate} \times T_{cell} + b_{10} SOC \times T_{cell} + T_{amb} \quad (3\text{-}12)$$

The temperature change will be calculated as:

$$\frac{dT}{dt} = [\dot{Q}_{gen} - hA(T_{cell} - T_{amb})]/mC_p \quad (3\text{-}13)$$

The term $hA(T_{cell} - T_{amb})$ is the heat rejection to the ambient. Table 3-9 and Table 3-10 show the values of regression parameters. The $R^2$ value from this analysis was determined to be 0.98 for discharge (0.94 for charge) which implies that the model is well able to explain the variability in the data. Significant parameters are identified as those having a P-value of less than 0.05. In discharge, SOC and interaction of SOC with C-rate and temperature are found to be insignificant; hence, could be dropped to further simplify the model. In charge, a linear equation with no interaction terms fits the data pretty well.

**Table 3-9 Results of regression analysis on the heat generation rate during discharge of $LiFePO_4$ cell**

| Parameter | Coefficient | Standard Error | P-Value |
|---|---|---|---|
| $C_{rate}$ | 17.76155376 | 2.002466417 | 4.80179E-16 |
| $T_{cell}$ | 0.673897479 | 0.090246009 | 2.70729E-12 |
| SOC | 1.15132144 | 9.495374757 | 0.903617912 |
| $C_{rate}^2$ | 0.507951653 | 0.038145608 | 3.68856E-29 |
| $SOC^2$ | 11.09065208 | 1.163086743 | 6.43565E-18 |
| $T_{cell}^2$ | 0.000228554 | 8.33169E-05 | 0.006654842 |
| $C_{rate}$ x SOC | -0.108429712 | 0.488451157 | 0.824557664 |
| $C_{rate}$ x $T_{cell}$ | -0.061778332 | 0.005791103 | 3.34412E-21 |
| SOC x $T_{cell}$ | -0.044569604 | 0.031712953 | 0.161499694 |
| $T_{amb}$ | -0.732070097 | 0.10786538 | 1.3568E-10 |
| **R2: 0.98 Adjusted R2: 0.97** | | | |

**Table 3-10 Results of regression analysis on the heat generation rate during charge of $LiFePO_4$ cell**

| Parameter | Coefficient | Standard Error | P-Value |
|---|---|---|---|
| $C_{rate}$ | 0.750183 | 0.048531 | 1.42E-37 |
| $T_{cell}$ | 0.376412 | 0.018508 | 1.47E-53 |
| SOC | -0.54216 | 0.135544 | 8.51E-05 |
| $T_{amb}$ | -0.37593 | 0.018423 | 8.98E-54 |
| **R2: 0.94 Adjusted R2: 0.93** | | | |

It should be noted that in the regression analysis, adding more terms will always result in a higher value of $R^2$. However, a high value of $R^2$ does not necessarily imply a more accurate model. To avoid such a misinterpretation, another metric, called adjusted $R^2$ should be taken into

account. If adjusted R square is significantly lower than R square, this normally means that some explanatory variable(s) are missing. Also, if adding a new term results in a decreased adjusted $R^2$, it implies that that term is not significant [90]. Two other diagnostic tools were also used in this regression analysis: residual plots and normal probability plot. In general, the scatter plot of the residuals will be disordered if the regression is good. A trend means that the residuals are not independent (see Figure 3-14). An increasing trend suggests that the error variance increases with the independent variable; while a distribution with a decreasing trend indicates that the error variance decreases with the independent variable. Such trends indicate that the assumption of constant variance (which is assumed in a regression analysis) is not true and the regression is not reliable [88]. Finally, in a reliable regression model, the normal probability plot should be close to a line of 45° slope.

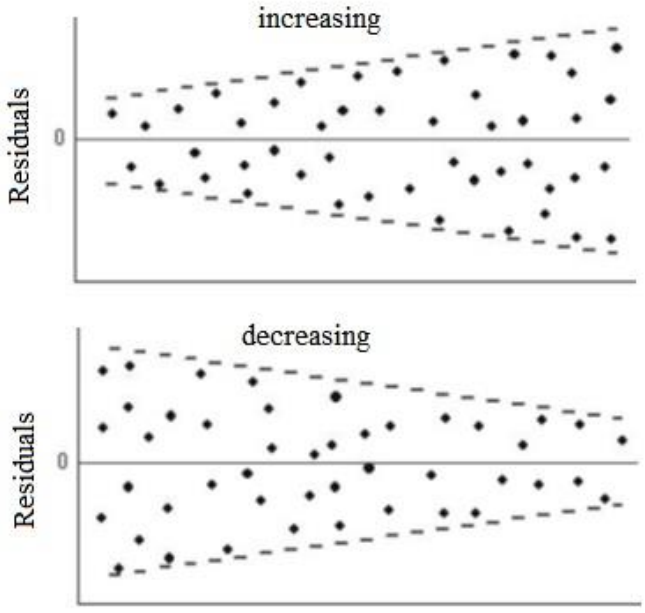


**Figure 3-14 Residuals showing a trend (variable variance) [88]**

To illustrate the model performance, a comparison is made between the experimental and the simulated temperature profile of cell #1 at 2.5 C-rate and 23.75°C ambient and shown in

Figure 3-15. Also, in Figure 3-16, simulated temperature profile of the cell #1 during charging at 12.5°C and 1.75 C-rate is compared against the measurements. The average error in both cases is less than 3%.

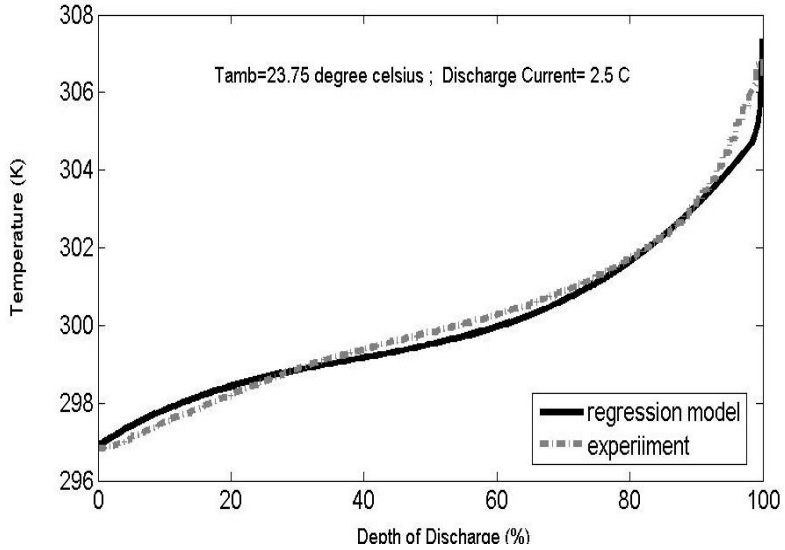


**Figure 3-15 Temperature profile of cell #1 ($LiFePO_4$) during discharge at 2.5 C-rate and 23.75 °C ambient**

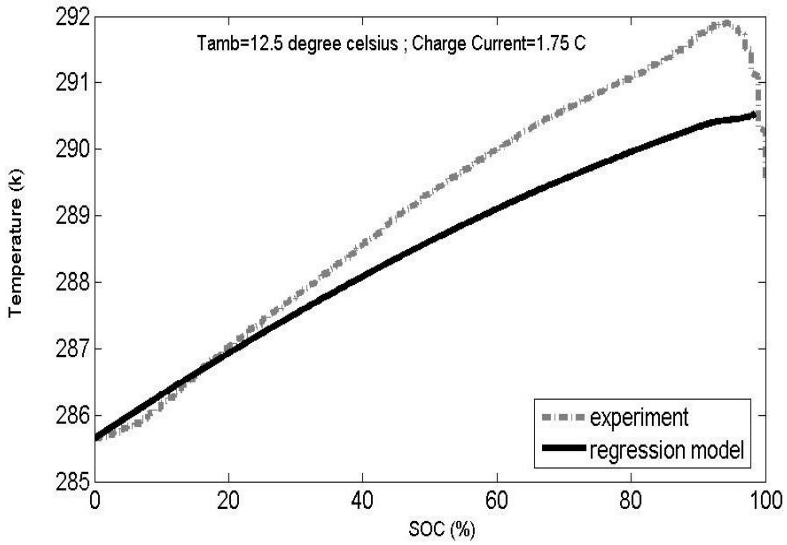


**Figure 3-16 Temperature profile of cell #1 ($LiFePO_4$) during discharge at 1.75 C-rate and 12.5 °C ambient**

For drive cycle simulations, Equation (3-12) and (3-13) were implemented in Matlab/Simulink as the battery thermal sub model and integrated to the whole battery model. Figure 3-17 and Figure 3-18 show the model validation against experiment with US06 drive cycle at 35°C and 12.5°C. maximum error of 6% and root meat square error (RMSE) of 3% was observed.

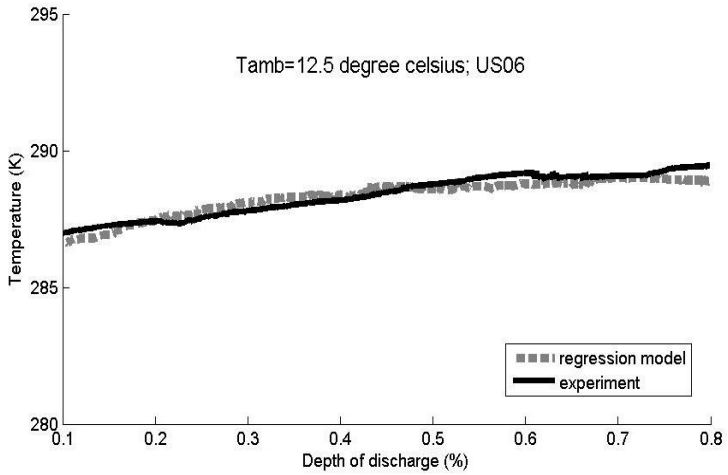


**Figure 3-17 Temperature profile of cell #1 (LiFePO4) under US06 profile and 12.5 °C ambient**

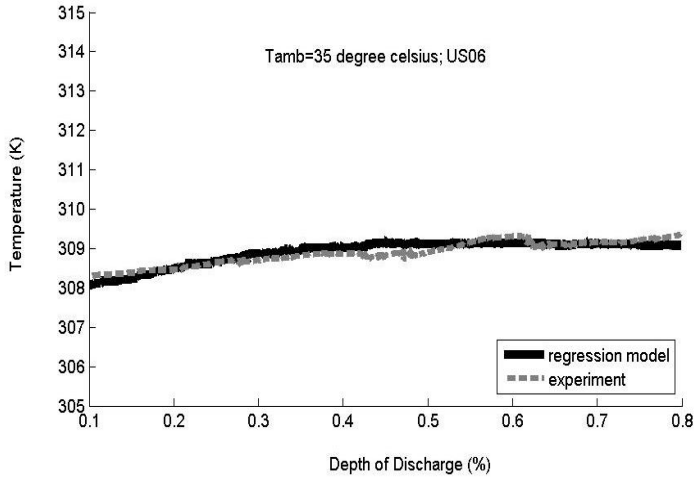


r

**Figure 3-18 Temperature profile of cell #1 (LiFePO4) under US06 profile and 35 °C ambient**

## 3.2 Modeling of Battery Performnce Based on EIS Tests

The following section is based on the paper titled “Empirical Modeling of Li-ion Batteries Based on Electrochemical Impedance Spectroscopy Tests” by “Samadani et.al” published in the Journal of Electrochimica ACTA [39]. This thesis author specific contribution to this paper is to analyze the data, prepare the graphics and results and write the final manuscript. This paper is co-authored by Dr. Fowler and Dr. Fraser as supervisors. Also, L. Gimenez, W. Scott and S. Farhad contributed in collection of some of the experimental data and preliminary data analysis.

As pointed out in section 2.5.2, equivalent circuit models (ECMs) are used in the real-time applications such as BMS. ECMs utilize equivalent circuit components to predict the terminal characteristics of the batteries (current and voltage). There exist several approaches in the literature for modeling batteries in the electrical domain. In [91], a Li-ion battery model capable of predicting runtime and I-V performances of the battery is proposed. However, temperature variation is not taken into account in their calculation; something which is critical for the battery models to consider for lifetime and safety considerations [59, 92]. In [59, 93], dynamic models are proposed for Li-Ion batteries which consider the cell temperature. However, these models do not dynamically update the model parameters based on cell temperature variations due to self-heating.

In this chapter, an approach is proposed to design a dynamic electrical battery model for use in real-time BMS. The novelty of this approach is that the model parameters are dynamically updated based on SOC and cell temperature. The proposed empirical model is based on observed phenomena during electrochemical impedance spectroscopy (EIS) tests on two commercially available Li-Ion batteries at various battery SOCs and temperatures. This model can precisely predict the battery operating voltage in electrified vehicles at various operating conditions. Results also show, depending on the designer expected accuracy, this model can be used to predict the battery internal resistance obtained from hybrid pulse power characterization (HPPC) tests. In total, this simple battery model can be employed as a real-time model in electrified vehicle battery management system design.

### 3.2.1 Experiment Setup and Tests Procedure

To be clear for the reader, the experiments are explained in this section. Two commercial Li-ion pouch cells already described in Table 3-1 were characterized by HPPC and EIS tests over a range of temperatures and SOCs.

A *MACCOR 4200*$^{TM}$ battery cycler was employed for this test and to discharge the cells to the desired SOC. This cycler has 16 channels with a current control range of 0.1 – 15 A and a voltage control of 0.0 – 5.0 V for each channel. Eight channels were combined in parallel to achieve the maximum current of 120 A using a 4-wire parallel connection, where two low gauge wires deliver current and two high gauge wires measure voltage. The accuracy of the eight combined channels for each battery was ±0.1 A and ±1.0 mV. The current-voltage data was logged every second or every change in 1 mV. The HPPC tests were preceded by a full charging at 1C constant current, followed by constant voltage charging until the current decreased to C/20. The batteries were then rested until equilibrium was reached. Equilibrium was defined as a change in voltage smaller than 5 mV over a period of half an hour or a total rest time longer than 2 hours. Afterwards, the batteries were discharged to each test SOC at a rate of 1C, and the HPPC current profile including a 10 s 5C discharge pulse, a 40 s rest and a 10 s 3.75C regenerative (charge) pulse was applied and the battery voltage response was measured. The equipment located at the right in is *SubZero MicroClimate® 1.2* temperature control chamber that maintains the battery temperature within ±0.5 K of the set point. The battery was enclosed in a vice that simulates a battery pack enclosure (two 4 mm thick inner aluminum plates, which simulate pack fins that distribute heat across the battery surface, inserted between two 5 mm thick acrylic plates, which simulate battery casing).

Figure 3-19 illustrates the experimental setup for the EIS test. This test was performed using a *METROHM AutoLAB PGSTAT 302* galvanostat/potentiostat with a current range of ±2 A and a voltage range of ±10 V. The measurement range for the frequency response analysis is 10 µHz to 1 MHz. The current and voltage accuracy ranges were set to ±10 µA and ±1.0 mV respectively. To achieve the desired SOC, the battery is fully discharged at a 1C constant current to reach the

cut-off voltage and then at the constant cut-off voltage until the current rate is reduced to C/20. The batteries are then rested until equilibrium is reached; then, the battery is charged to the desired SOC by coulomb counting at 1.25C current.

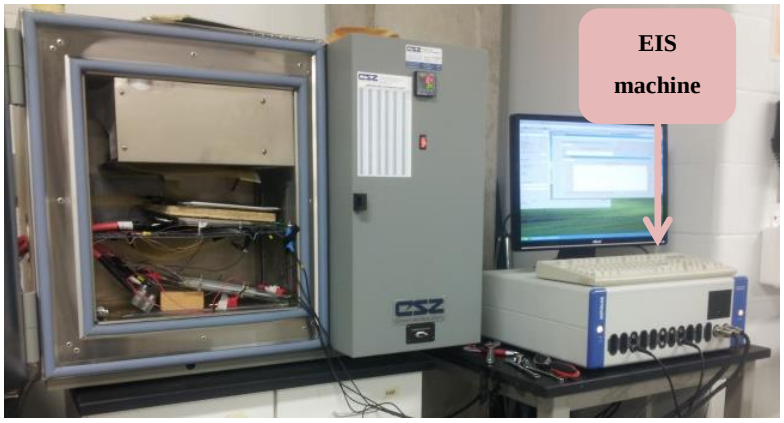


**Figure 3-19: Experimental setup for the EIS test.**

The EIS tests were obtained by scanning 51 points logarithmically spaced between 5 kHz and 5 mHz using a two electrode configuration with the reference and counter electrodes being the same. The two, rather than three, electrode configuration was chosen due to the difficulty of placing the third electrode within a sealed commercial pouch cell. The frequency range was chosen based on analysis of the pertinent parts of the Nyquist plots, and extended to 100 µHz for some scans at lower temperatures to confirm the presence of the Warburg tail. For the galvanostatic scans, the baseline current is set to 0 A and the pulse amplitude set to 300 mA. The batteries were then reconnected to the MACCOR cycler and discharged to the next desired SOC. Both EIS and HPPC tests were performed at the states of charge of 10%, 30%, 60%, and 90% for temperatures of 12.5°C, 23.75°C and 35°C. It should be noted that even though the battery might be exposed to very low or high ambient temperatures in vehicle operation (e.g. aggressive driving), the BTMS regulates the battery temperature to the optimum range (25-40°C [94]) very quickly to prevent adverse effects on the cell performance (charge acceptance, power and energy capability), cycle life, and safety [95]. Therefore this study does not consider extreme temperatures. The third phase of experiments was measuring the cell response voltage to the current profile of standard drive cycles (US06, UDDS, and HWFET). For this purpose, a model

of an extended range electric vehicle (EREV), initially developed by UWAFT [96] in Autonomie software, was used to determine the battery current profile under each of the targeted drive cycles. The main components of the powertrain of this vehicle are listed in Table 3-11. The battery pack consists of three parallel strings each including 105 batteries in series (315 batteries in total). Each drive cycle was applied on the vehicle model and the resulting battery pack current profile was scaled to a cell level. Afterwards, the cell was cycled under the obtained current profile for a full discharge by the MACCOR cycler and the voltage response was recorded.

**Table 3-11 Powertrain components specifications of the EREV modified Chevrolet Malibu used in the Autonomie model [45, 96]**

| Component | Option |
|---|---|
| Engine | GM LE9 Engine (E85)<br>2.4 L E85 engine provided by GM |
| Generator | TM4 Motive (105 kW) |
| ESS (Battery) | Battery Pack (19.7 kWh @ 346 V) |
| Motor | TM4 Motive (206 kW) |
| Final drive | Borg Warner eGearDrive |
| Chassis | 2013 Malibu |
| Power convertor | New Eagle DCDC Converter |
| Electrical accessory | The average power draw from accessories was assumed to be 1500 W |

### 3.2.2 Establishment of the Equivalent Circuit

The observed trends in the Nyquist plots are presented in Figure 3-20 through Figure 3-25. The number of RC pairs required to describe a cell response is determined from impedance analysis. For instant, charge transfer reaction is usually modeled by a single RC pair [97]. The circuit structure is also dependent on cell age and operating conditions. For example, at very low temperatures additional elements may be required to account for increased resistance as a result of frozen electrolyte or slow solid diffusion.[98].

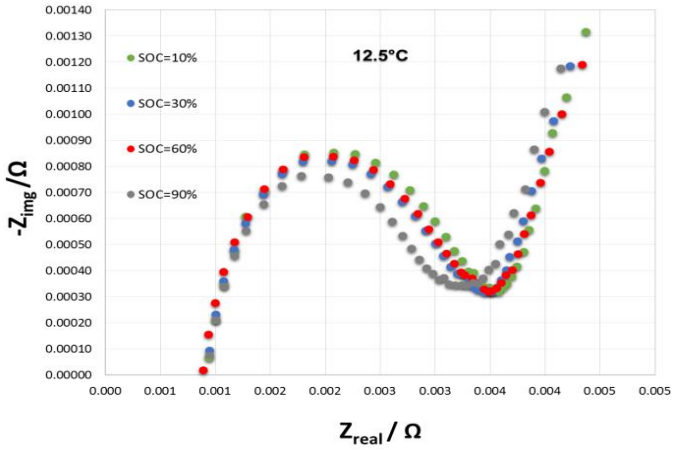


**Figure 3-20 EIS test results of battery #1 with $LiFePO_4$ cathode 12.5 °C**

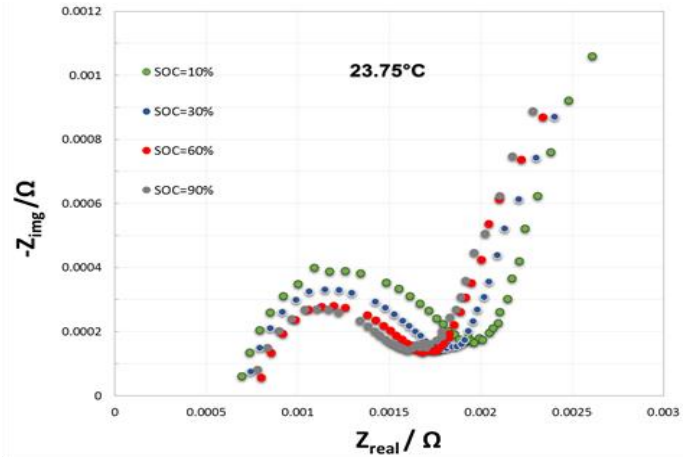


**Figure 3-21 EIS test results of battery #1 with $LiFePO_4$ cathode 23.75 °C**

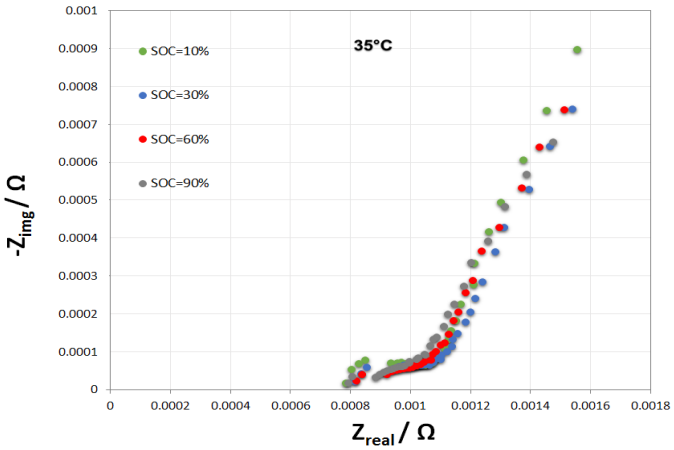


**Figure 3-22 EIS test results of battery #1 with $LiFePO_4$ cathode 35 °C**

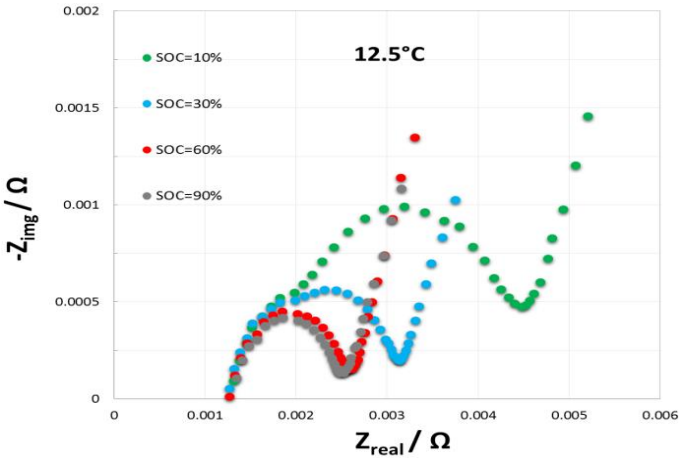


**Figure 3-23 EIS test results of battery #1 with $LiMn_2O_4$**

**& $Li(NMC)O_2$cathode cathode 12.5 °C**

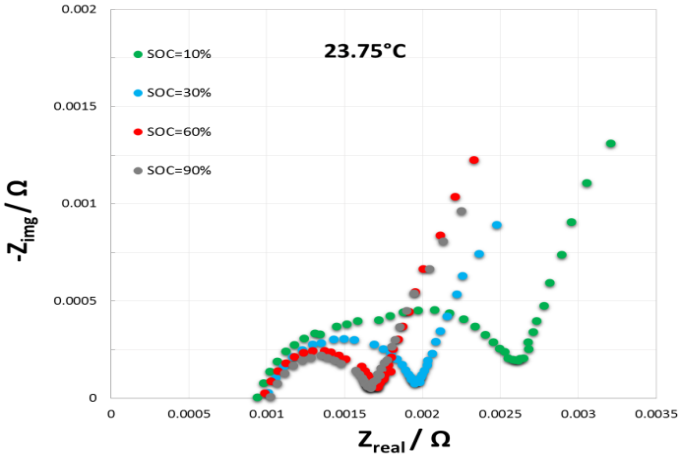


**Figure 3-24 EIS test results of battery #1 with $LiMn_2O_4$ & Li(NMC)$O_2$cathode cathode 23.75 ºC**

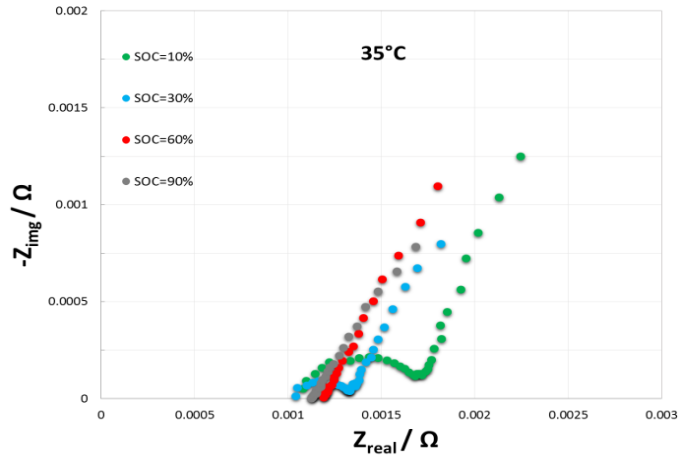


**Figure 3-25 EIS test results of battery #1 with $LiMn_2O_4$ & Li(NMC)$O_2$cathode cathode 35 ºC**

Careful investigation of these plots reveals that at most two semicircles with center-points off the x-axis and a straight line exist in the impedance spectrums. Figure 3-26 shows, two examples where the response curve includes two semicircles.

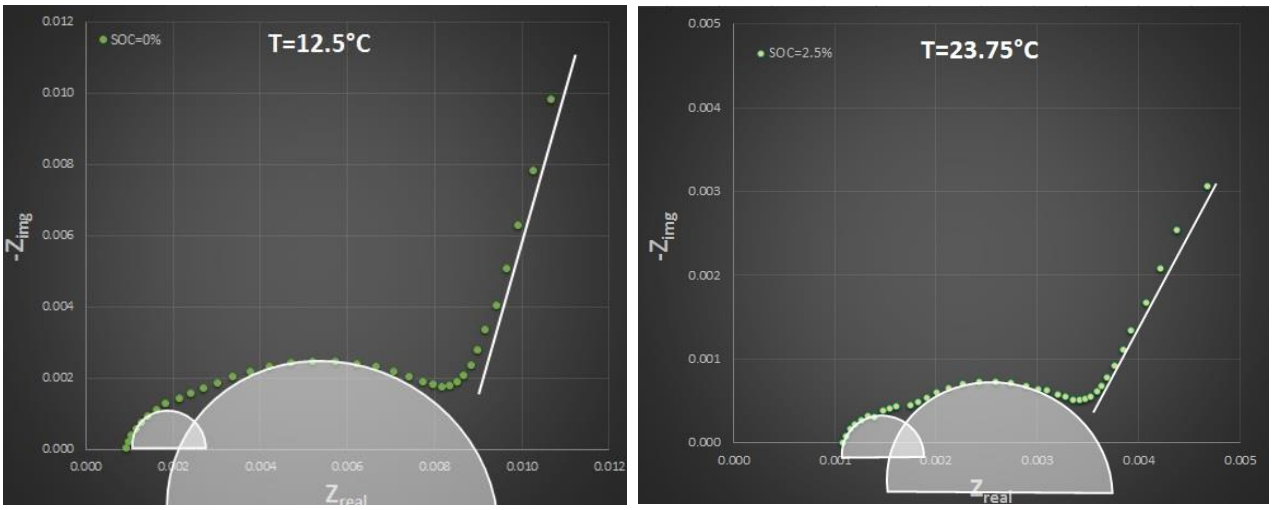


**battery #1 with $LiFePO_4$ cathode** **battery #2 with $LiMn_2O_4$ & $Li(NMC)O_2$cathode**

**Figure 3-26 Examples of the EIS plots showing two semicircles justifying the need for CPE element in the circuit structure**

The second semicircle appears at lower temperatures and states of charge for both batteries studied. These semi-circles represent polarization due to a slow charge transfer reaction in electrodes and the straight line accounts for the polarization due to slow mass diffusion in the electrolyte and active electrode materials [99]. The semicircles may originate from: distributed electrode reactivity, electrode inhomogeneity, roughness or fractal geometry, or current and potential distributions across the electrode [99]. A semicircle with the center-point not on the x-axis can be modeled by a parallel resistor and imperfect capacitor, or constant phase element (CPE). The straight line can be modeled by a Warburg impedance element [96]. The proposed circuit is shown in Figure 3-27.

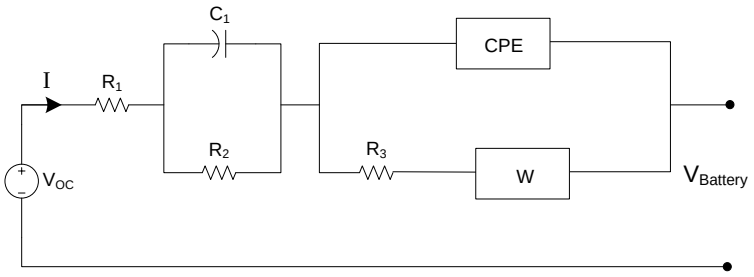


**Figure 3-27. Proposed equivalent circuit in frequency domain**

Because the CPE is a non-intuitive electrical circuit component and cannot be easily transformed from the frequency to time domain, the CPE was approximated by a perfect capacitor. Also, it has been shown that the Warburg impedance can be simplified to multiple parallel RC pairs (as a limiting case, a single RC pair) [100]. In this study, the Warburg element is replaced by two RC pairs as shown in Figure 3-28. In this fashion, the circuit is simplified to the one shown in Figure 3-28. The model parameters were determined by an EIS equivalent circuit solver (Z-man), which uses a genetic mutation algorithm to change model parameters until the model estimate best approximates measured values. Each circuit component is a function of SOC and temperature. For each circuit component, this function was determined through a curve fitting process including all EIS tests points (at various temperatures and SOCs).

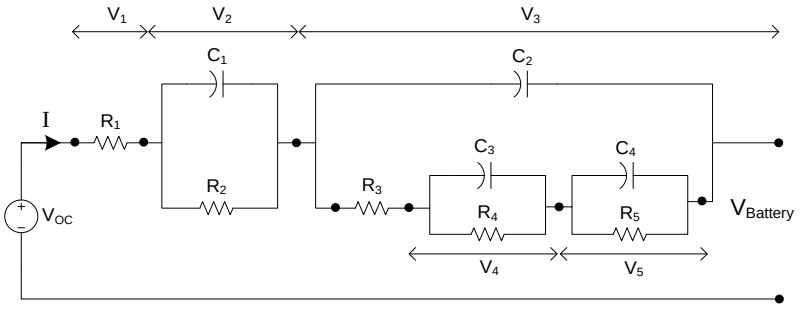


**Figure 3-28. Simplification of the proposed circuit for time domain solution.**

### 3.2.3 Parameters Fitting

The equivalent circuit parameter values were determined using Z-man software. Z-man uses

the Levenberg-Marquardt algorithm (LMA), or damped least squares method, to minimize the error between the parameter assigned and empirical values. The parameters of an ECM are generally a function of temperature and SOC. In case of high degrees of freedom in the model, due to highly fluctuating trends in the parameters, the designer should try different fittings by changing initial values using his interpretation and judgment to choose a proper fitting. Also, imposing restrictions on the parameters would help reduce the degrees of freedom and obtain a smooth trend for each parameter.

After parameters were determined, they were exported to Microsoft Excel for cross-comparison. Select data series were then re-evaluated using Z-man software in the event that a parameter was an outlier. Like most numerical minimization methods, the LMA is an iterative process and requires an initial guess[101]. When possible, the value of the initial guess was determined from the previous fitted parameter value. For the initial guess for the first parameter of a series (e.g. guess $SOC_0$), the Z-man software's search heuristic method was used. This heuristic is an evolutionary approach of the particle swarm optimization algorithm. After all parameters have been fit, they were exposed to cross analysis. When a parameter fit exceeded an order of magnitude of a previous value, all parameters for that temperature and state of charge were re-evaluated using the heuristic evolutionary approach until complying with the parameter series. In the event that the parameter series did not have aligning fits, the entire series was re-evaluated. As an example, Figure 3-29 and Figure 3-30 show fitted values of $R_1$ (Ohmic resistance) for both batteries at three temperatures.

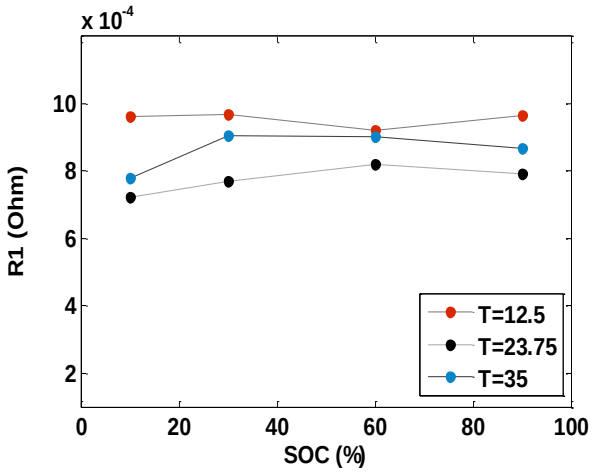


Figure 3-29. Fitted values of R1 for battery #1

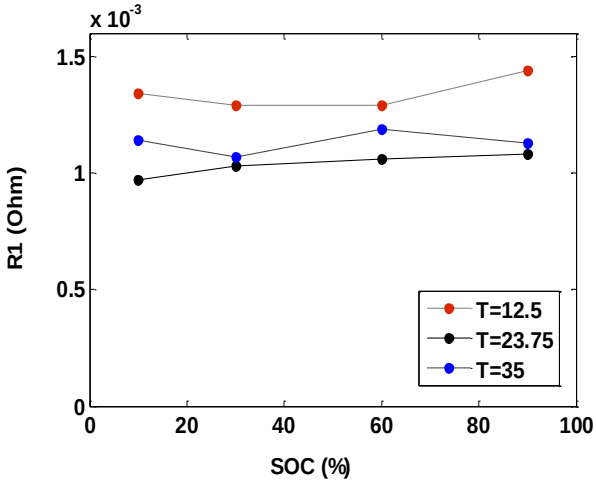


Figure 3-30 Fitted values of R1 for battery #2

### 3.2.4 Determination of the Voltage Response in Time Domain

The terminal voltage of the battery can be determined from the simplified equivalent circuit shown in Figure 3-28 as Equation (3-14).

$$V_{Battery} = V_{OC} - V_1 - V_2 - V_3 \quad \textbf{(3-14)}$$

$V_1$ is the instantaneous change of the battery voltage determined from the Ohm's law in Equation (3-15).

$$V_1 = R_1 i \quad \textbf{(3-15)}$$

$V_2$ and $V_3$ are the time dependent voltage of the battery. $V_2$ and its corresponding time constant are determined from Equations (3-16) and (3-17) respectively.

$$V_2 = R_2 i\left(1 - e^{-t/\tau_1}\right) \quad \textbf{(3-16)}$$

$$\tau_1 = R_2 C_1 \quad \textbf{(3-17)}$$

$V_3$ is complex and can be determined from the system of ordinary differential equations in Equation (3-18).

$$\begin{cases} \tau_2 \dfrac{dV_3}{dt} = -V_3 + V_4 + V_5 + R_3 i \\ \tau_3 \dfrac{dV_4}{dt} = \left(\dfrac{R_4}{R_3}\right) V_3 - \left(\dfrac{R_4}{R_3} + 1\right) V_4 - \left(\dfrac{R_4}{R_3}\right) V_5 \\ \tau_4 \dfrac{dV_5}{dt} = \left(\dfrac{R_5}{R_3}\right) V_3 - \left(\dfrac{R_5}{R_3}\right) V_4 - \left(\dfrac{R_5}{R_3} + 1\right) V_5 \end{cases} \quad \textbf{(3-18)}$$

$\tau_2$, $\tau_3$, and $\tau_4$ are defined as follows:

$$\tau_2 = R_3 C_2 \quad \textbf{(3-19)}$$

$$\tau_3 = R_4 C_3 \quad \textbf{(3-20)}$$

$$\tau_4 = R_5 C_4 \quad \textbf{(3-21)}$$

The solution of Equation (3-18) employs transformation into the Laplace domain:.

$$\begin{cases} \mathcal{L}[V_3] = \dfrac{1}{(\tau_2 s + 1)} \mathcal{L}[V_4] + \dfrac{1}{(\tau_2 s + 1)} \mathcal{L}[V_5] + \dfrac{(R_3 i)}{(\tau_2 S + 1)} \dfrac{1}{s} \\ \mathcal{L}[V_4] = \dfrac{\left(\dfrac{R_4}{R_3}\right)}{\left(\tau_3 s + \left(\dfrac{R_4}{R_3} + 1\right)\right)} \mathcal{L}[V_3] - \dfrac{\left(\dfrac{R_4}{R_3}\right)}{\left(\tau_3 s + \left(\dfrac{R_4}{R_3} + 1\right)\right)} \mathcal{L}[V_5] \\ \mathcal{L}[V_5] = \dfrac{\left(\dfrac{R_5}{R_3}\right)}{\left(\tau_4 s + \left(\dfrac{R_5}{R_3} + 1\right)\right)} \mathcal{L}[V_3] - \dfrac{\left(\dfrac{R_5}{R_3}\right)}{\left(\tau_4 s + \left(\dfrac{R_5}{R_3} + 1\right)\right)} \mathcal{L}[V_4] \end{cases} \quad \textbf{(3-22)}$$

After simplification of Equation (3-22), $V_3$ is obtained as Equation (3-23). To take Laplace inverse from the right side of Equation (3-23), this equation should be written as Equation (3-24).

$$V_3 = (i)\mathcal{L}^{-1}\left[\frac{\left(\dfrac{R_3}{\tau_2}\right)s^2 + \left(\dfrac{R_3 + R_5}{\tau_2\tau_4} + \dfrac{R_3 + R_4}{\tau_2\tau_3}\right)s + \left(\dfrac{R_3 + R_4 + R_5}{\tau_2\tau_3\tau_4}\right)}{s\left(s^3 + \left(\dfrac{1}{\tau_2} + \dfrac{1 + \dfrac{R_4}{R_3}}{\tau_3} + \dfrac{1 + \dfrac{R_5}{R_3}}{\tau_4}\right)s^2 + \left(\dfrac{1}{\tau_2\tau_3} + \dfrac{1}{\tau_2\tau_4} + \dfrac{1 + \dfrac{R_4}{R_3} + \dfrac{R_5}{R_3}}{\tau_3\tau_4}\right)s + \dfrac{1}{\tau_2\tau_3\tau_4}\right)}\right] \quad \textbf{(3-23)}$$

$$V_3 = (R_3 + R_4 + R_5) i \mathcal{L}^{-1}\left[\frac{1}{s} - \frac{A}{(s + r_1)} - \frac{B}{(s + r_2)} - \frac{C}{(s + r_3)}\right] \quad \textbf{(3-24)}$$

Where, r1, r2 and r3 in Equation (3-24) are the three real roots of Equation (3-25) as it appeared in the denominator of Equation (3-23). These three real roots are obtained from Equations (3-26) to (3-28).

$$s^3+\left(\frac{1}{\tau_2}+\frac{1+\frac{R_4}{R_3}}{\tau_3}+\frac{1+\frac{R_5}{R_3}}{\tau_4}\right)s^2+\left(\frac{1}{\tau_2\tau_3}+\frac{1}{\tau_2\tau_4}+\frac{1+\frac{R_4}{R_3}+\frac{R_5}{R_3}}{\tau_3\tau_4}\right)s+\frac{1}{\tau_2\tau_3\tau_4} \quad \textbf{(3-25)}$$

$$r_1=\frac{a}{3}+\left(\frac{2}{3}(a^2-3b)^{0.5}cos\left(\frac{arccos\left(\frac{2a^3-9ab+27c}{2(a^2-3b)^{1.5}}\right)}{3}\right)\right) \quad \textbf{(3-26)}$$

$$r_2=\frac{a}{3}+\left(\frac{2}{3}(a^2-3b)^{0.5}cos\left(\frac{arccos\left(\frac{2a^3-9ab+27c}{2(a^2-3b)^{1.5}}\right)+2\pi}{3}\right)\right) \quad \textbf{(3-27)}$$

$$r_3=\frac{a}{3}+\left(\frac{2}{3}(a^2-3b)^{0.5}cos\left(\frac{arccos\left(\frac{2a^3-9ab+27c}{2(a^2-3b)^{1.5}}\right)-2\pi}{3}\right)\right) \quad \textbf{(3-28)}$$

Where, a, b, and c are obtained from the following equations:

$$a=\frac{1}{\tau_2}+\left(1+\frac{R_4}{R_3}\right)\frac{1}{\tau_3}+\left(1+\frac{R_5}{R_3}\right)\frac{1}{\tau_4} \quad \textbf{(3-29)}$$

$$b=\frac{1}{\tau_2\tau_3}+\frac{1}{\tau_2\tau_4}+\left(1+\frac{R_4}{R_3}+\frac{R_5}{R_3}\right)\frac{1}{\tau_3\tau_4} \quad \textbf{(3-30)}$$

$$c=\frac{1}{\tau_2\tau_3\tau_4} \quad \textbf{(3-31)}$$

A, B, and C in Equation (3-24) are determined from Equation (3-32) and (3-33).

$$A=\frac{\tau_3\tau_4R_3r_1+\frac{1}{r_1}(R_3+R_4+R_5)-(R_3+R_5)\tau_3-(R_3+R_4)\tau_4}{(R_3+R_4+R_5)(\tau_2\tau_3\tau_4)(r_1-r_2)(r_1-r_3)} \quad \textbf{(3-32)}$$

$$B=\frac{\tau_3\tau_4R_3r_2+\frac{1}{r_2}(R_3+R_4+R_5)-(R_3+R_5)\tau_3-(R_3+R_4)\tau_4}{(R_3+R_4+R_5)(\tau_2\tau_3\tau_4)(r_2-r_1)(r_2-r_3)} \quad \textbf{(3-33)}$$

$$C = \frac{\tau_3\tau_4 R_3 r_3 + \frac{1}{r_3}(R_3+R_4+R_5) - (R_3+R_5)\tau_3 - (R_3+R_4)\tau_4}{(R_3+R_4+R_5)(\tau_2\tau_3\tau_4)(r_3-r_1)(r_3-r_2)} \quad \textbf{(3-34)}$$

After determination of $r_1$, $r_2$, $r_3$, A, B, and C and taking Laplace inverse from Equation (3-24) , $V_3$ is determined as:

$$V_3 = (R_3+R_4+R_5)i[1 - Ae^{-r_1 t} - Be^{-r_2 t} - Ce^{-r_3 t}] \quad \textbf{(3-35)}$$

Substituting Equations (3-15), (3-16) and (3-35) into Equation (3-14), the battery voltage is determined as Equation (3-36)

$$V_{Battery}(t) = V_{OC} - R_1 i - R_2 i\left(1 - e^{-t/\tau_1}\right) - (R_3+R_4+R_5)i[1 - Ae^{-r_1 t} - Be^{-r_2 t} - Ce^{-r_3 t}] \quad \textbf{(3-36)}$$

In Equation (3-36), the battery current is positive on discharge and negative in change. This equation is suitable to determine the voltage response when a constant current is drawn from the battery. However, under a drive cycle operation, the battery current profile shows high fluctuations due to instantaneous changes in the power demand. Therefore, Equation (3-36) should be modified to account for the effect of a time varying current profile on the battery voltage. For this purpose, the current profile is binned into constant current segments. The voltage response for the first bin is calculated form Equation (3-37) where the battery starts from equilibrium state.

$$V_{Battery,1}(t) = V_{OC} - R_1 i_1 - R_2 i_1\left(1 - e^{-\frac{t}{\tau_1}}\right) - (R_3+R_4+R_5)i_1[1 - Ae^{-r_1 t} - Be^{-r_2 t} - Ce^{-r_3 t}] \qquad (0 \le t < t_1) \quad \textbf{(3-37)}$$

For other segments, the voltage response is considered to be a function of the current applied in that segment as well as the current applied in previous segments; therefore, Equation (3-37) is modified to Equation (3-38), where, the term $V_{Battery,j}(t)$ refers to the battery voltage at time "t" in the segment "j" and $V_{Battery,j-1}(t)$, refers to the battery voltage at the time "t" due to the current applied in the previous segment 'j-1'. "$i_j - i_{j-1}$" is the difference between the applied current in the two adjacent segments.

$$V_{Battery,j}(t) = V_{Battery,j-1}(t) - R_1(i_j - i_{j-1}) - R_2(i_j - i_{j-1})\left(1 - e^{-\frac{(t-t_{j-1})}{\tau_1}}\right) - (R_3 + R_4 + R_5)(i_j - i_{j-1})\left[1 - Ae^{-r_1(t-t_{j-1})} - Be^{-r_2(t-t_{j-1})} - Ce^{-r_3(t-t_{j-1})}\right] \quad (t_{j-1} \le t < t_j)\ \&\ (j \ge 2) \tag{3-38}$$

Where the values of $V_{OC}$, $R_1$, $R_2$, $R_3$, $R_4$, $R_5$, A, B, C, $\tau_1$, $r_1$, $r_2$, $r_3$ were updated with the current state of charge of the battery obtained from Equation (3-39).

$$\Delta(SOC) = -\frac{i_j \Delta t}{Q_{Battery}} \tag{3-39}$$

The model parameters are a function of temperature and SOC. Therefore, a 2-D look up table was created which updates the parameters according to the instantaneous SOC and temperature. The temperature is updated by a thermal sub model which predicts the cell temperature changes according to its losses and convection to the ambient already presented in the section 3.1.

### 3.2.5 Results and Discussion

Verification of the proposed model is accomplished in two stages. First, the ability of the model is evaluated for prediction of the battery internal resistances obtained from HPPC tests. Second, the model is studied under standard drive cycles for output potential difference predictions in a hypothetical EREV. The focus of this section will be the battery with a LFP cathode, and the model validation is performed mainly for the LFP battery. It should be noted that the SOC window considered for the simulations is 10 to 90 % due to two observations: first, the HPPC test does not provide reliable results at extreme SOCs, and second, the BMS is designed to limit the battery from being over charged or discharged.

#### Cell 1 (LFP Cathode)

To verify the accuracy of the proposed empirical model, the model was run under HPPC current profile (as shown in ) and the resultant battery internal resistances were compared with those obtained from a Thevenin model [65] as well as HPPC tests. The Hybrid Pulse Power Characterization (HPPC) test, recommended by the U.S. Department of Energy FreedomCAR

battery test manual [102], is used for cell characterization in terms of internal resistance and power capability at different SOCs and temperatures.

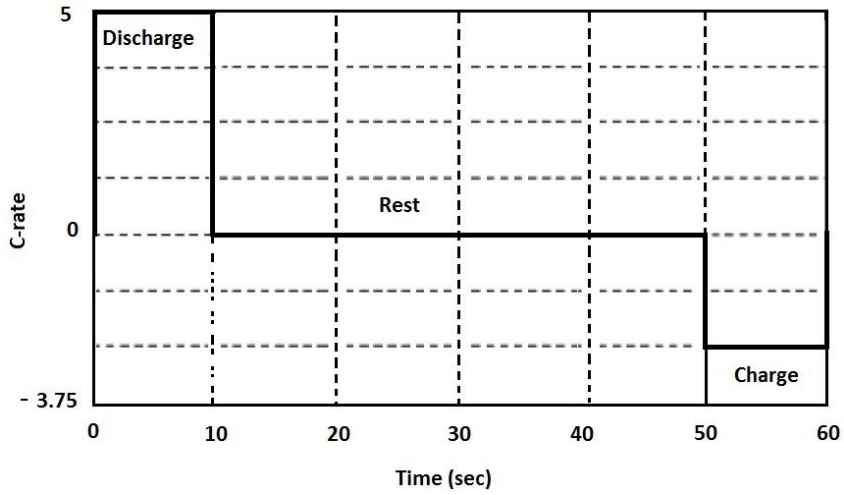


**Figure 3-31 : HPPC test- pulse power characterization profile**

Several studies have utilized the HPPC method to fit a simple RC circuit or internal resistance (Rint) model for simplicity and ease of implementation [12, 103, 104]. Another study employs a simple RC model to predict the mean pack behavior and a Rint model to simulate differences between the individual cells [105]. EIS provides an alternative approach to defining the circuit parameters[22, 106]. Unlike the HPPC test, EIS does not assume that battery response is unaffected by pulse duration or that there is no significant time delay between input and response. These assumptions have been shown to be false through examination of Nyquist plots used in EIS studies [22, 107]. In addition, the HPPC test, when compared to EIS, has been shown to impose more stress on the battery [108]. Lastly, compared to HPPC, EIS test facility is much more economical; therefore, it would be desirable to verify the possibility of replacing HPPC test with EIS.

Results of comparison for the battery with LFP cathode at temperatures of 12.5°C, 23.75°C and 35°C are shown in Figure 3-32. It is observed that the proposed model better matches the experimental results than the Thevenin model. An average error of 20 % is observed in values

predicted by the proposed empirical model. Further investigations also revealed that the empirical model can predict the charge resistances of both batteries with an average error of about 13%. Charge and discharge error may be reduced by increasing the number of EIS tests (e.g. from four SOCs to eight). Additionally, replacing the perfect capacitors $C_1$ and $C_2$ with CPEs would incorporate the effects of: distributed electrode reactivity, electrode inhomogeneity, roughness or fractal geometry, and the current and potential distributions across the electrode, which could further reduce model error.

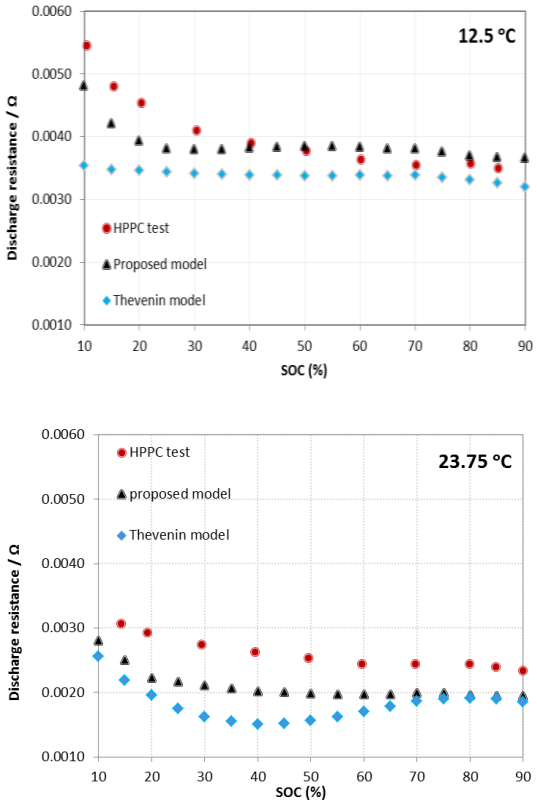

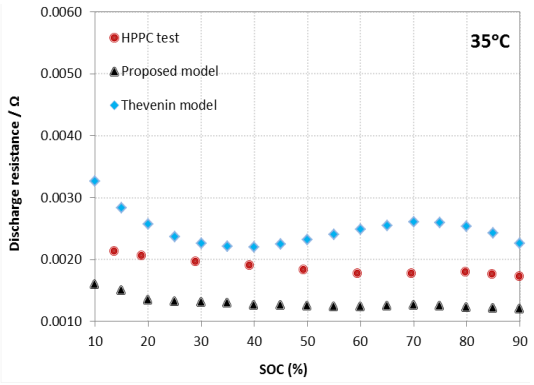


**Figure 3-32. Comparison of discharge resistances obtained from HPPC tests and modeling for the battery with LFP cathode at different temperatures.**

The model was further evaluated by simulating the cell voltage profile over three standard drive cycles (US06, UDDS, and HWFET). The cycle current profiles were separately aggregated and applied to the proposed, Thevenin, and simple resistance ($R_{int}$) models. Resulting battery voltages were compared with the experimental data over a 90% to 10% SOC range. The voltage obtained from the model and experiment for this battery at operating temperature of 35°C is shown in Figure 3-33. As seen in this figure, there is an excellent agreement between the model and experiment. At this temperature, the highest error was observed during the US06 drive cycle with an average error of 1.2% and the maximum instantaneous error of 5.3%.

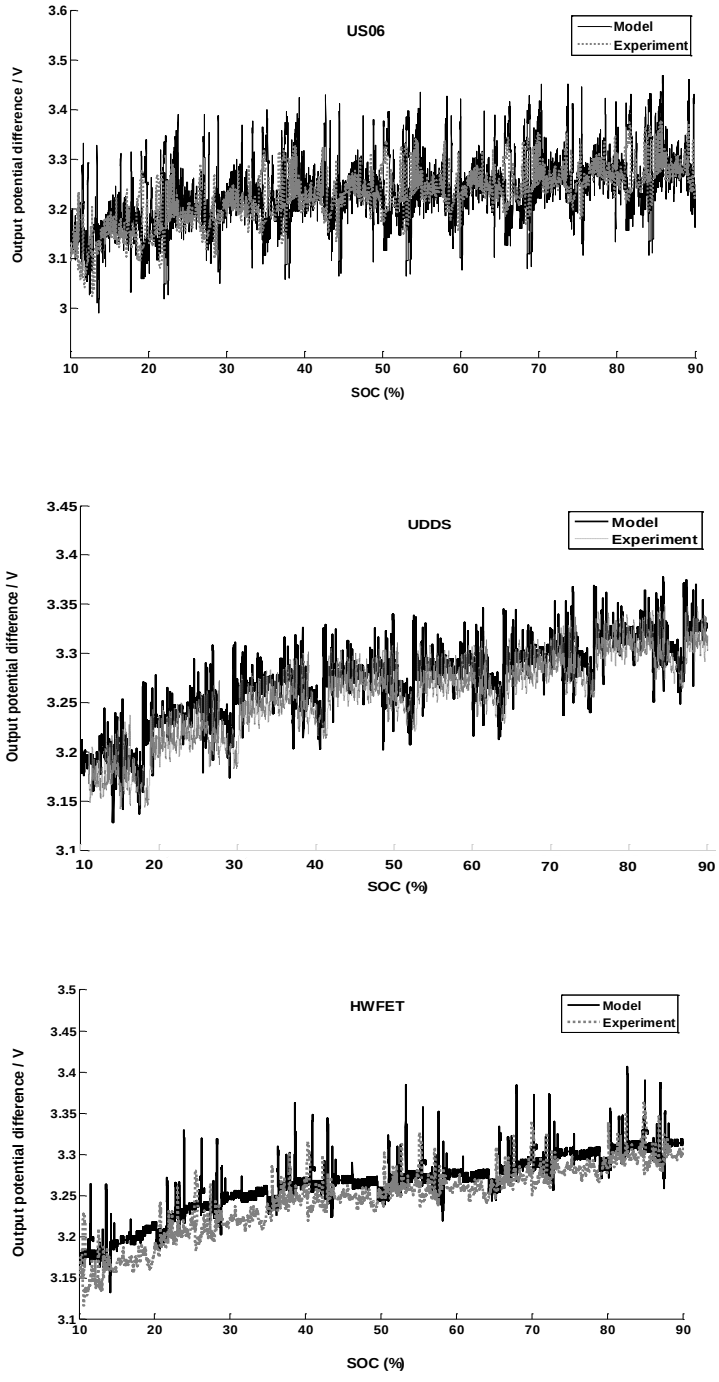


**HWFET**

**Figure 3-33. Comparison of the battery voltage obtained from the empirical model and experiment for the battery with LFP cathode at 35°C standard EPA drive cycles.**

This battery was also studied at operating temperatures of 23.75°C and 12.5°C. The average and maximum instantaneous errors of the model for voltage predication under US06, UDDS, and HWFET drive cycles are listed in Table 3-12. At all temperatures studied, the highest errors belong to the US06 drive cycle. For this drive cycle, at temperatures of 23.75°C and 12.5°C, the average error was about 2.1% and 5.4% and the maximum instantaneous error was about 6.8% and 22.1%, respectively. Model error increases at lower operating temperatures. This could be due to the assumption of replacing the CPE element to the perfect capacitor in the equivalent circuit. Table 3-12 further presents a comparison between the proposed model and two simpler models; Thevenin and simple resistance ($R_{int}$) model. All three models show best performance in higher temperatures and city driving conditions. It can be observed that the $R_{int}$ model has the biggest error since the polarization characteristic has been ignored. The Thevenin model shows a better dynamic performance in following the experimental data, and its maximum error rate is less than 6% at high temperatures following a city drive cycle. The proposed model offers an improvement of up to 6% in terms of average and maximum error in voltage predictions; which is still significant for EV applications in terms of extending the allowable battery discharge window and the vehicle range.

**Table 3-12. Average and maximum errors of the proposed empirical model for voltage prediction of the battery with LFP cathode in various drive cycles over 90% to 10% SOC.**

| Drive cycle | Average error (%) | | | Maximum error (%) | | |
|---|---|---|---|---|---|---|
| | Proposed model | Thevenin | $R_{int}$ | Proposed model | Thevenin | $R_{int}$ |
| | **@ 35 (°C)** | | | | | |
| US06 | 1.2 | 1.4 | 3.8 | 5.3 | 5.9 | 12.9 |
| UDDS | 0.6 | 0.8 | 0.8 | 2.5 | 3.7 | 3.9 |
| HWFET | 1.1 | 1.3 | 1.4 | 3.6 | 4.1 | 7.5 |
| | **@ 23.75 (°C)** | | | | | |
| US06 | 2.1 | 2.2 | 3.2 | 6.8 | 8.2 | 12.9 |
| UDDS | 1.2 | 1.5 | 1.6 | 4.2 | 5.3 | 5.6 |
| HWFET | 1.8 | 1.9 | 1.9 | 4.5 | 4.6 | 7.7 |
| | **@ 12.5 (°C)** | | | | | |
| US06 | 5.4 | 5.7 | 6.1 | 22.1 | 22.8 | 23.8 |
| UDDS | 2.3 | 3.1 | 3.8 | 10.4 | 11.5 | 13.1 |
| HWFET | 4.6 | 4.7 | 5.1 | 13.7 | 14.3 | 15.2 |

Cell 2 (Composite LMO & NMC Cathode)

Figure 3-34 illustrates the results of the discharge resistances obtained from HPPC tests through modeling and experiment for the battery with composite LMO & NMC cathode. As before, the results corresponding to the empirical model, as compared to the Thevenin model, better follow the experimental with the empirical model resistances averaging 12 % error. An average error of 10 % is observed in the predicted charge resistances for this battery. The proposed model can be further evaluated if drive cycle test data is made available for the LMO & NMC battery.

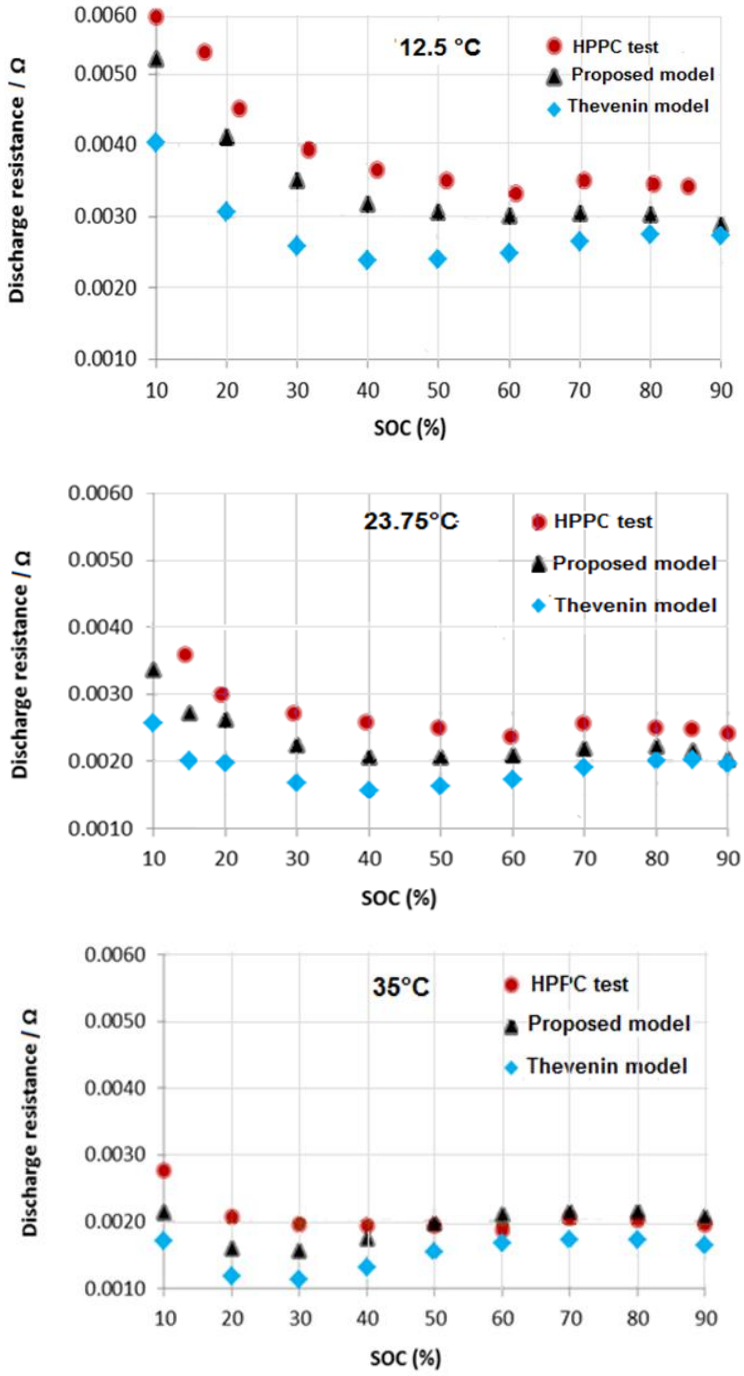


**Figure 3-34. Comparison of discharge resistances obtained from HPPC tests and modeling for the battery with composite LMO & NMC cathode at different temperatures.**

### 3.2.6 Impact of convection coefficient on the temperature profile

One important design criteria of battery operation is that the battery temperature stays smooth and within a controllable range to maintain optimal performance. In this section, the sensitivity of the battery temperature rise to the convection coefficient is investigated. For this purpose, the battery model (DPW) is run under different convection coefficient ranging from 1h (2 $W/m^2K$), corresponding to the natural convection, to 10h (~20 $W/m^2K$) resembling a mild forced convection condition. As the plots in Figure 3-35 suggest, a convection coefficient value of 7.5h (15 $W/m^2K$) would result in a saturated temperature profile with minimum fluctuation over different drive cycles; which is an affordable value and could be fulfilled by using a fan. Also, in Figure 3-35 (4) effect of the convection coefficient on the battery maximum temperature rise under different drive cycles is illustrated. This plot reassures the feasibility of designing a thermal management unit for the cells with minimal temperature fluctuations.

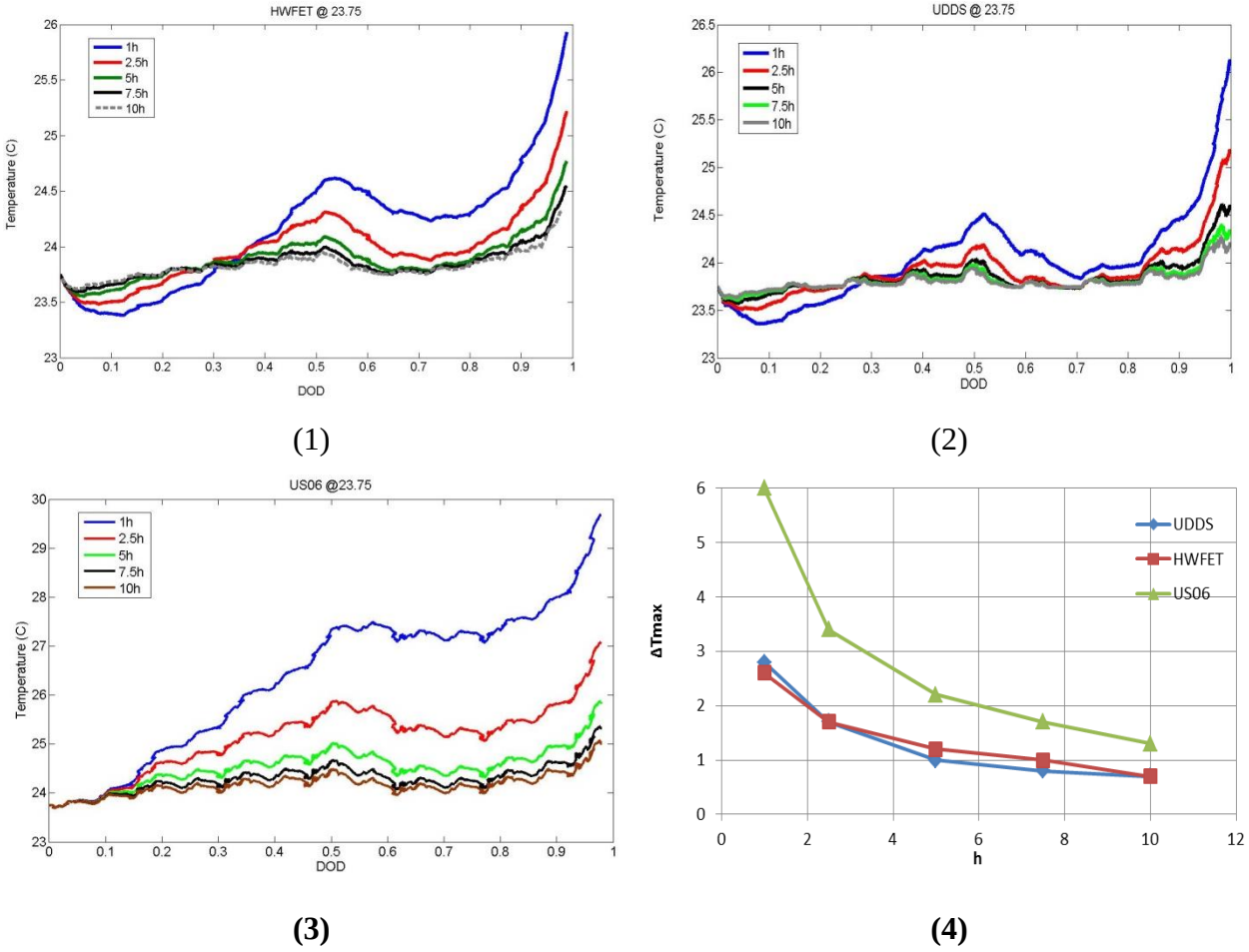


**Figure 3-35 Simulation of temperature profile under EPA drive cycles; (1)-(3): Impact of convection coefficient on the temperature, (4) maximum temperature change as a function of convection coefficient**

## 3.3 Conclusions

In this chapter two experimental studies on Li-ion battery were presented. First, thermal behavior of two commercial Li-ion cells ($LiMn_2O_4$ and $LiFePO_4$) was studied through a comprehensive set of charge and discharge cycling tests at different ambient temperatures. A design of experiment algorithm (called NFCD) was utilized to determine the minimum required test points (ambient temperatures and C-rates). Energy efficiency and columbic efficiency of the cells were determined for each testing condition. Results agree with the belief that the Li-ion

cells have a better performance at higher temperatures. The temperature distribution of the cells was found to be approximately uniform within the confines of the experimental error. Also, heat generation of the cells was calculated assuming natural convection mechanism for heat rejection to the ambient. It is planned to validate the calculated heat generation against the theoretical heat generation inside the cell. Finally, a statistical model of the temperature and also cumulative generated heat was developed for each cell (charge and discharge).

In the second section, a simple real-time empirical model for voltage prediction of Li-ion batteries was developed based on the observed phenomena at various battery states of charge and temperatures under EIS test. It was shown that this model can precisely predict the battery voltage during various drive cycles of electrified vehicles. The model was compared with both the simple resistance and Thevenin models and up to 6% improvement in the battery voltage prediction was observed. The model was also evaluated in terms of predicting the HPPC test results. The investigations confirmed the model capability in following the HPPC test trends within about 20% error. This error can be significantly reduced by using CPEs instead of perfect capacitors in the equivalent circuit model. In this condition, the effects of distributed electrode reactivity, electrode inhomogeneity, and distributed current and potential across the electrode could be considered. This model is desirable to designers as an alternative method for the HPPC test, as this test imposes stress to the battery and its setup is expensive for high capacity batteries and battery packs. Although the model developed was based on data of two commercial Li-ion batteries, this modeling approach is applicable to model Li-ion batteries of different chemistries.

# Chapter 4

# Battery Characterization through Field Tests

The following section is mainly based on the paper titled "Modeling and Evaluation of Li-Ion Battery Performance Based on the Electric Vehicle Field Tests" by "Samadani et.al" published by the Society of automotive Engineer (SAE). This thesis author specific contribution to this paper is conducting the experiment, analyzing the data, preparing the graphics and results and the final manuscript. This paper is co-authored by Dr. Fowler and Dr. Fraser as supervisors. Also, L. S. Farhad assisted with advice in the data analysis.

Although Li-ion battery offers many advantages such as high specific power and capacity, their performance and reliability in actual EV application need to be further verified. In this context, a systematic approach is required to enable assessment of the operational requirements specific to EV applications. This chapter describes the results of a research conducted for the Burlington Hydro as a part of its GridSmartCity$^{TM}$ project [109]. The results are based on the field test conducted on an electrified Ford Escape 2009 which is a part of Burlington Hydro's fleet and is equipped with three packs of cylindrical Li-ion battery ($LiFePO_4$) including an overall 20 modules in series. Through monitoring various performance and utilization parameters of an EV, this study provides practical in-situ data on EV operation and grid electricity requirements and helps addressing the following key technical issues of EVs and their connection to the grid:

- Charging and charge management;
- Applicability as a fleet vehicle;
- Vehicle performance modeling; and;
- Li-ion battery degradation modeling.

As the ultimate objective of this study, an attempt has been made to bridge the gap between laboratory studies and real life environment and to study the battery degradation in real-life

conditions. There are many factors that affect the Li-ion battery performance and health. Also, in EV applications, battery health is known to be very much dependent on the driving and charging habit. Therefore, there is a growing desire to evaluate the path dependence of battery degradation. This is due to the fact that lab environment is far different from what the battery experiences under real operation in EVs and relying solely on the results of lab testing may cause a great mislead in estimating the battery state of health (SOH) and remaining life. However, real-life testing is expensive and labor intensive and is associated with a very low level of control ; therefore it has not been the subject of researches very much so far [32]. In the following sections, the data management system installed on the vehicle, and the powertrain and battery characterization and modeling are presented.

## 4.1 Data Management System and Battery Packs

Figure 4-1 shows the converted EV under study. There are three packs of Li-ion battery installed on the vehicle; including a total of 20 battery modules in series. Figure 4-2 shows a schematic of the battery packs locations in the vehicle. Each module contains 6serisesx49parallel IFR18650e cylindrical Valence cells. The data management system consists of a data logger installed in the vehicle, a cellular network data connection for data collection, and processing scripts that convert the logged data into monthly usage reports. The data logger unit records data from the battery, powertrain, and GPS. A list of recorded signals that are necessary for modeling of vehicle performance and battery degradation is presented in Table 4-1. The data logger is installed beneath the front passenger seat and connects to the vehicle controller area network bus (CANBus). The global positioning system (GPS) unit is mounted on the ceiling of the passage cabin near the central mirror to reduce the possibility of poor satellite acquisition. The data recording unit (DRU) and modem are located beneath the front passenger seat. The data logger is powered by the existing 12V battery in the vehicle.Figure 4-3 shows the data recorder unit seat and Figure 4-4 shows the data logger connection and shut down wire in vehicle. The ‘shut down’ wire is used to automatically power-off the recorder and its peripherals after 4 hours of inactivity. The cellular antenna that enables wireless data transmission is located on top of the

car.


**Figure 4-1 Converted Ford Escape (EV-ACX2.5)**

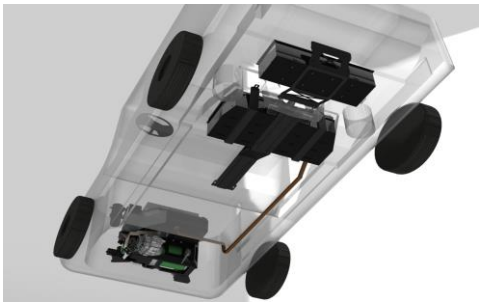

**Figure 4-2. integration of multiple batteries packs [110]**

**Table 4-1 Data logging signals**

| Component | Recorded Signal | significance |
|---|---|---|
| Battery | • Voltage & current<br>• SOC<br>• Temperature | • Verify vehicle energy use and regenerative braking<br>• Verify battery health status as both extreme temperature and SOCs are known to escalate degradation |
| Electric motor | • Voltage & current<br>• Speed<br>• Torque | • Monitor powertrain energy use |
| Vehicle | • Speed & Acceleration | • Monitor vehicle performance |

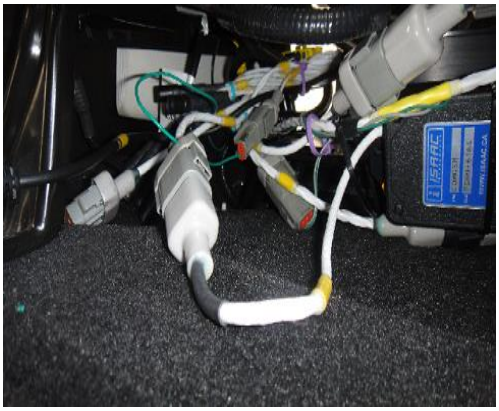

**Figure 4-3: Data recorder unit**

**Figure 4-4: Data logger connection and shut down wire**

## 4.2 Results and Analysis

### 4.2.1 Individual Event Analysis

In this section, an individual trip analysis for the EV-ACX2.5 is presented. The relevant drive cycle of this trip is illustrated in Figure 4-5. This trip, occurring on November 25, 2011, is actually the longest recorded trip of 106 kilometers and is summarized in Table 4-2. This specific trip is chosen to be displayed here because it shows the quality and quantity of the data collected from the vehicle, and because it contains a large set of driving conditions that demonstrate some of the performance characteristics of the vehicle (range, acceleration, etc.). According to Table 4-2, EV-ACX 2.5 is driven for 2 hours and 16 minutes with a battery SOC initially at 100% and decreasing to 2%. The peak speed is 125 kph, during highway driving. The average speed is 46.9 kph. During the trip the outside temperature was $5^0$C. The total energy used by EV-ACX 2.5 is 23.68 kWh and the cost of the trip at a rate of 11 cents per kWh was $2.60, which is the price that Burlington Hydro is currently paying for the EV-ACX2.5. This trip includes both highway and city driving. Figure 4-5 shows the drive cycle and Figure 4-6 shows the acceleration profile for this trip. As Table 4-3 suggests, this drive cycle is close to US06 drive cycle in terms of aggressiveness.

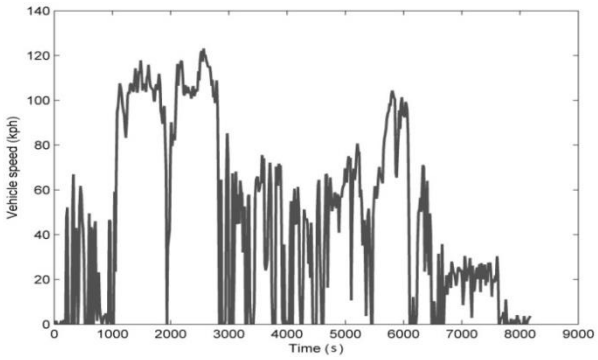


**Figure 4-5: Drive cycle for longest recorded trip with EV-ACX2.5**

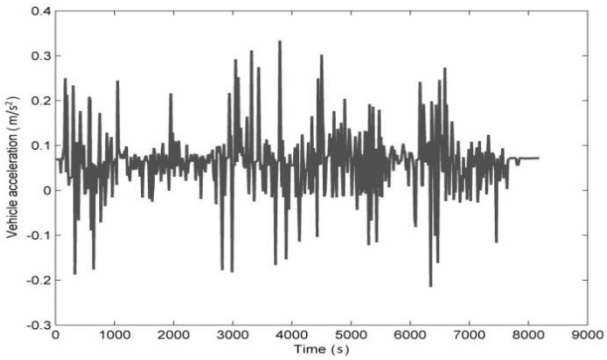


**Figure 4-6: Acceleration profile for longest recorded trip with EV-ACX2.5**

**Table 4-2 Cycle details, November 25, 2011**

| | | |
|---|---|---|
| Trip Time | 2 hour,16 min | |
| Trip Distance | 106 | km |
| Starting SOC | 100 | % |
| Ending SOC | 2 | % |
| Total Energy | -23.68 | kWh |
| Cycle Average Speed | 46.92 | kph |
| Cycle Peak Speed | 125 | kph |
| Average Positive Acceleration | 0.59 | m/s2 |
| Peak Positive Acceleration | 3.43 | m/s2 |
| Trip Cost (at $ 0.11/kWh) | 2.60 | CAD |
| Cost per km (at $0.11/kWh) | 0.024 | CAD/km |
| Outside Temperature | +5 | 0C |

**Table 4-3: Acceleration comparison between Nov25 drive cycle and standard drive cycles**

| Cycle | Maximum acceleration (m/s2) | Average acceleration (m/s2) |
|---|---|---|
| UDDS | 1.47 | 0.55 |
| HWFET | 1.43 | 0.19 |
| US06 | 3.75 | 0.67 |
| Nov25-EV-ACX2.5 | 3.43 | 0.59 |

Figure 4-7 and Figure 4-8 show the battery voltage and current profiles for the trip. The minimum battery voltage is 350 V and the maximum battery voltage is 414 V. It can be observed that there is a decreasing trend in the battery terminal voltage which is a result of continuous loading on the battery packs during driving. The peak battery discharge current is -195 A and the peak battery regenerative braking current is 100 A. Thus, the peak battery discharge power is -68.25 kW and peak regenerative braking charge power is 43.88 kW. Figure 4-9 also shows the SOC profile of the battery for this trip. There is a drastic reduction in SOC between 1000 sec to 3000 sec because during this time span, the vehicle was highway driven with very high speed of 120 kph. After 3000 sec, a fluctuating trend in the SOC curve is observed which is due to the in-city driving condition where regenerative braking frequently occurs.

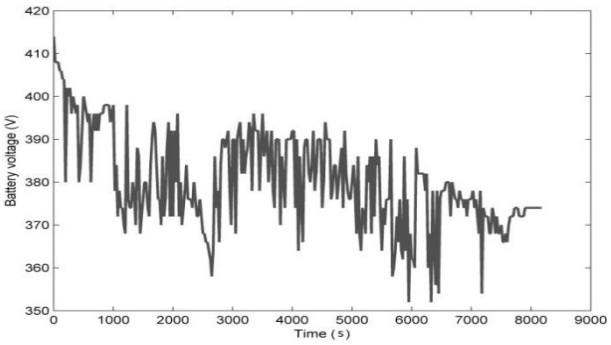


**Figure 4-7: Battery voltage profile for longest recorded trip with EV-ACX2.5**

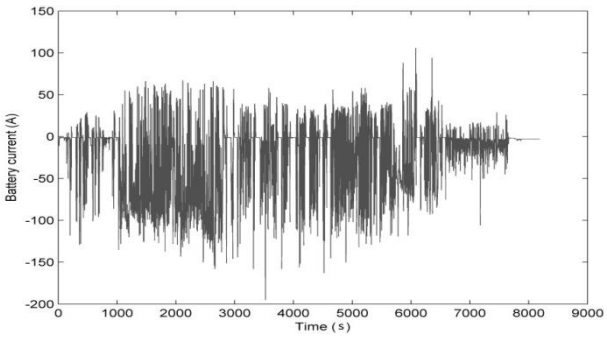


**Figure 4-8: Battery current profile for longest recorded trip with EV-ACX2.5**

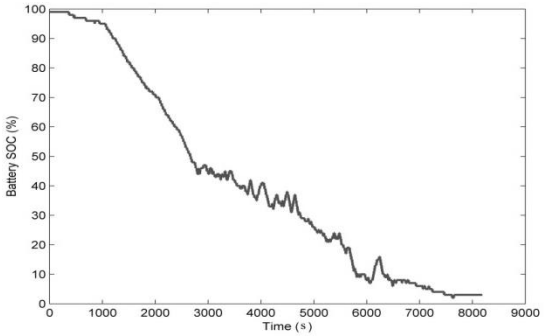


**Figure 4-9: Battery SOC profile for longest recorded trip with EV-ACX2.5**

Figure 4-10 depicts the battery maximum and minimum temperature profiles (as measured over all of the battery modules) as a function of time for this trip. It is very well known that the heat generation from a battery is due to resistive ($I^2R$) losses and the enthalpy changes due to electrochemical reactions during discharge or charge. Heat generation rate from a battery module depends on several parameters like battery temperature, initial and final state of charge, charge and discharge rate and profile and also on chemistry and construction. The EV-ACX2.5 uses 20 passively cooled battery modules located in three packaged locations on the vehicle. It is evident that these different locations are causing significant differences in cell temperature over the drive cycle. These differences may cause differential cell ageing, which can be monitored. Since the data loggers collect battery voltage, current, and temperature at the module level, degradation

models can be validated at that level to identify the extent of the differential ageing as data continues to be collected. It can be seen from Figure 4-10 that the battery minimum temperature has a minimum value of $15^0$C and a maximum value of $30^0$C, while the battery maximum temperature has a range of $25^0$C to $39^0$C. It can be also observed that there is a drastic change in temperature between 1000 sec to 3000 sec; this is due to the fact that the vehicle was in continuous operation and all three battery packs continuously generated heat.

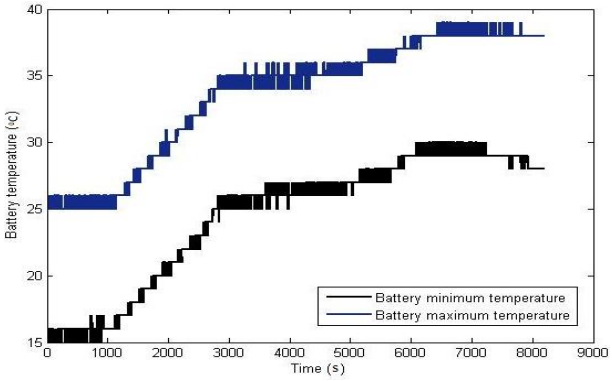


**Figure 4-10: Battery temperature profile for longest recorded trip with EV-ACX2.5**

### 4.2.2 Energy and Cost Analysis of EV-ACX 2.5

Table 4-4 shows the energy and cost analysis of EV-ACX2.5 for the monthly data collected between October 2011 and February 2012. It gives a monthly record of the total distance travelled by EV-ACX2.5, the energy used during driving, the cost of driving, the energy required for charging, and the charging cost.

**Table 4-4: Energy and cost analysis of EV-ACX2.5 (October 2011-February 2012)**

| Month | Distance travelled (km) | Driving Energy (kWh) | Cost of driving (@ 0.11 $/kWh) | Charging Energy (kWh) | Charging Cost (Charging on 220 V) (@ 0.11 $/kWh) |
|---|---|---|---|---|---|
| Oct-2011 | 100.8 | 19.6 | $2.156 | 24.4 | $2.684 |
| Nov-2011 | 308.2 | 65.5 | $7.205 | 80.6 | $8.866 |
| Dec-2011 | 149.3 | 37.4 | $4.114 | 47.6 | $5.236 |
| Jan-2012 | 121.0 | 28.6 | $3.146 | 35.1 | $3.861 |
| Feb-2012 | 113.3 | 27.9 | $3.069 | 34.9 | $3.839 |
| Total | 792.6 | 179 | $19.69 | 222.6 | $24.48 |

During its time in Burlington, the EV-ACX2.5 is driven for 792.6 kilometers over five months. The project team needs to have Burlington Hydro dramatically increase EV-ACX2.5 driving to get the battery data for degradation analysis. The total vehicle energy consumption (charging energy) in the last five months is 222.6 kWh and the cost of charging is $24.48.

### Detailed Monthly Report for EV-ACX 2.5

In Figure 4-11 a detailed monthly vehicle report for November 2011 is presented. The key metrics contained in this report are distance travelled, hours in operation, hours spent charging, total driving and charging energy, time-of-use for vehicle charging, an energy usage path breakdown (from the grid to the powertrain), vehicle energy efficiency plotted against ambient temperature, and a histogram of battery SOC for the start and end of each recorded trip. The "Distance" section shows how many kilometers the vehicle was driven in gasoline mode and electric mode. This is a general report format that can accommodate hybrids, but since the EV-ACX 2.5 is a pure EV, all 308 kilometers are in electric mode.

The "Time" section contains a breakdown of the time the vehicle spent ON and OFF. ON is further broken down into driving hours (vehicle is in motion) and idling hours (vehicle is ON but is not in motion). OFF hours are further broken down into charging hours (vehicle is plugged in and battery is charging) and resting hours (vehicle is either plugged in and battery is full, or vehicle is not plugged in). The "Driving Energy" section shows how much energy is being consumed by the vehicle during ON hours. Again, because this is a pure EV there is no gasoline energy consumption. Both gasoline and electric energy consumption are expressed in Wh/km and $L_{equivalent}$/100km ($L_e$) for easy comparison. Total driving energy for the month, in kWh, is

also shown.

The “Charging Energy” section provides both the total charging energy used in the month, and a percentage breakdown of how those kWh were obtained. In Ontario’s time-of-use (TOU) pricing system electricity charges per kWh vary depending on the time of day and time of year. Prices increase as the time moves from off-peak to mid-peak to on-peak, so it is desirable to plan activities such that the vehicle can be charged off-peak as much as possible. This section also shows the percentage of charging energy obtained from 110V, 220V, and DC quick charge stations. It is important to note that the breakdowns in this section are in kWh (energy), not hours (time). The “Energy Path” section shows where energy is consumed in the vehicle. The charger energy is that energy consumed by the vehicle’s on-board charger in converting grid electricity from AC to DC energy that is compatible with the vehicle battery. The powertrain energy is the battery energy consumed by the vehicle to operate. The regenerative energy is the energy recovered by the regenerative braking system, resulting in reduced powertrain energy. All values are given per kilometer travelled for that month.

The “Temperature” section plots the vehicle energy consumption in $Whkm^{-1}$ against ambient temperature for each recorded trip. This plot is useful for demonstrating the effects of ambient temperature (and the resulting vehicle climate control energy consumption) on energy efficiency.

The “Battery Charge” section is a histogram of battery SOC at the start and end of each trip. It provides an at-a-glance view of the typical battery SOC utilization. The monthly reports for October 2011, December 2011, January 2012, and February 2012 are provided in Appendix D.

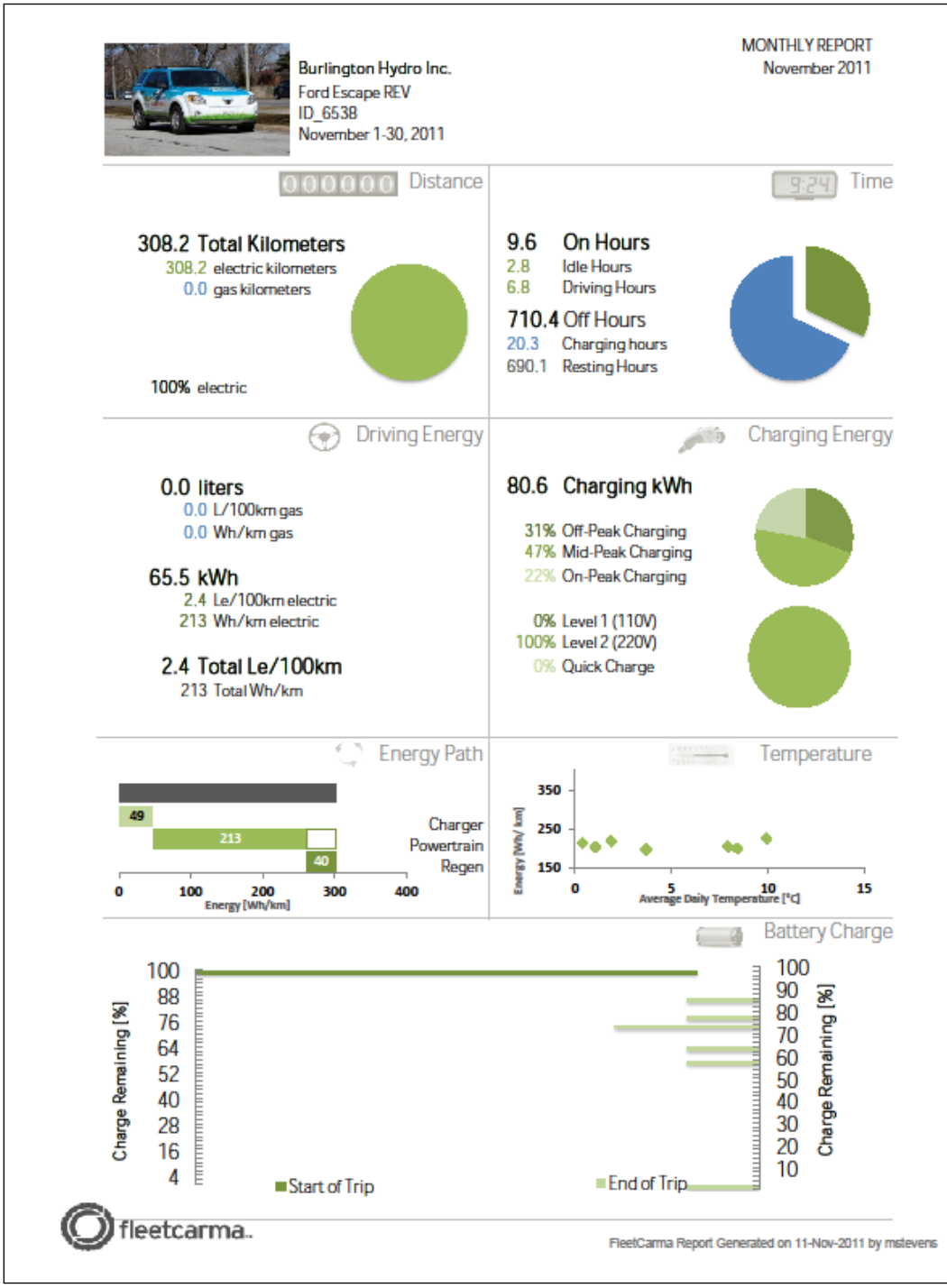


**Figure 4-11: ACX 2.5 November 2011 monthly report [111]**

Comparison between EV-ACX 2.5 and HEVs

In order to compare the energy consumption and energy cost of the EV-ACX 2.5 with that of Burlington Hydro's other fleet vehicles, drive cycles from two of Burlington Hydro's Ford Escape Hybrid (2008 and 2009 model years) fleet vehicles were recorded over four months, between November 2011 and February 2012. Table 4-5 summarizes the monthly distance travel, fuel consumption, and the equivalent energy use in kWh for the HEVs. The equivalence ratio of 9.7 kWh per litre is used for gasoline [104] It is seen that HEV #4 has the most utilization of the two HEVs and yields the richest data set. Therefore further analysis was performed based on the HEV #4 recorded data to compare the energy usage and cost with EV-ACX2.5. The results are reported in Table 4-6.

**Table 4-5: Distance travelled and energy consumption by fleet vehicles**

| Month | HEV #3 | | | HEV#4 | | |
|---|---|---|---|---|---|---|
| | Distance travelled (km) | Fuel (L) | Equivalent Energy (kWh) | Distance (km) | Fuel (L) | Equivalent Energy (kWh) |
| Nov.2011 | 252.8 | 21.9 | 212.43 | 742.9 | 51.09 | 495.57 |
| Dec.2011 | - | - | - | 793.48 | 53.15 | 515.57 |
| Jan. 2012 | 150 | 10.2 | 98.94 | 1214 | 80 | 776 |
| Feb.2012 | 104.5682 | 8.8618 | 85.95 | 769.16 | 50.61 | 490.917 |

**Table 4-6: Energy and cost comparison between EV-ACX2.5 and HEV#4**

| Month | HEV#4 | | | | ACX 2.5 | | |
|---|---|---|---|---|---|---|---|
| | Distance travelled (km) | Fuel (L) | Equivalent Energy (Kwh) (kWh=Lx9.7) | Cost (@11cent /kWh) | Distance (km) | Energy (kWh) (kWh=Lx9.7) | Cost (@11cent /kWh) |
| Nov-2011 | 742.9 | 51.09 | 495.57 | $54.51 | 308.2 | 65.5 | $7.205 |
| Dec-2011 | 793.48 | 53.15 | 515.57 | $56.71 | 149.3 | 37.4 | $4.114 |
| Jan-2012 | 253.53 | 80 | 160.923 | $17.70 | 121 | 28.6 | $3.146 |
| Feb-2012 | 769.16 | 50.61 | 490.917 | $54 | 113.3 | 27.9 | $3.069 |
| Total | 3519.54 | 234.85 | 2278 | $182.92 | 691.8 | 159.4 | $17.53 |
| Economy | 0.0512 ($/km) | | | | 0.025 ($/km) | | |

From Table 4-6, it is observed that the EV-ACX2.5 has travelled a much shorter distance over the last four months as compared to the HEV#4. Over four months, the HEV #4 is driven for

3519.54 km while the EV-ACX2.5 is driven for only 691.8 km. It is clearly seen that there is a huge difference in energy consumption, distance travelled, and cost of driving. The total fuel consumption over four months of the HEV #4 is 234.85 liters and the equivalent energy consumption is 2278 kWh, while for EV-ACX2.5 the energy consumption is 159.4 kWh. The cost of driving for HEV for four months is $182.92 while for EV-ACX2.5 it is $17.53. So the cost per km for HEV#4 is $0.0512 while for EV-ACX2.5 it is only $0.025. Hence, if EV-ACX2.5 is driven for same km as HEV#4 (3519.54km), the cost of driving is only $87.98, which is much lower than HEV#4 driving cost ($182.92) and there is a saving of $94.94.So it is clear that EV-ACX2.5 is cheaper in operation as compared to HEV.

## 4.3 Vehicle Powertrain Modeling

The converted EV was modeled in PSAT [112] based on the available specifications of the vehicle (see Table 4-7). The powertrain configuration used in the model is shown in Figure 4-12. As the high voltage battery and traction motor have the most influence on the model's accuracy, the reliability of the model developed for these components should be evaluated. To do this, some trip data collected from the vehicle were used for calibrating the battery and electric motor performance maps. In PSAT, the Li-ion battery is modeled as a charge reservoir and an equivalent circuit. The battery is represented by an open circuit voltage source and an internal resistance which accounts for the charging and discharging modes. The amount of charge that the battery is able to hold is assumed to be constant (no degradation). In Figure 4-13, the battery model structure is shown. The model takes the current as an input and calculates the output voltage. Once the model is calibrated, it will be validated against other sample road tests to verify its capability.

**Table 4-7 Key specifications for the electrified Ford Escape**

| Specification | Value |
|---|---|
| Mass (Empty) | 1814 kg |
| Motor Peak Power | 90 kW |
| Motor Peak Efficiency | 98% at 4000 RPM |
| Motor Peak Torque | 239 Nm |
| Battery Module Nominal Voltage | 19.2 V |
| Battery Module Energy Density | 89 Wh/kg |
| Battery Module Nominal Capacity | 69 Ah |
| Total Battery Pack Energy Capacity | 25 kWh |
| Typical Range for a full discharge | 100 km |

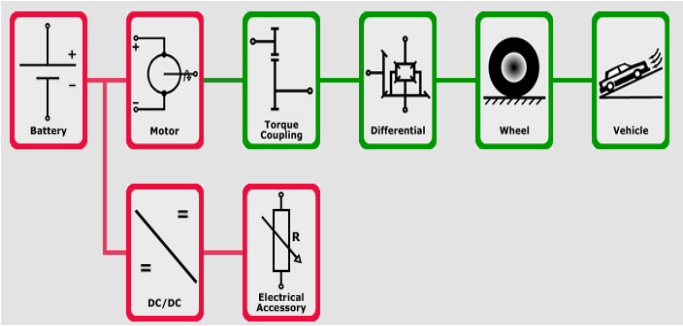


**Figure 4-12 Drivetrain configuration of the converted EV in PSAT [111]**

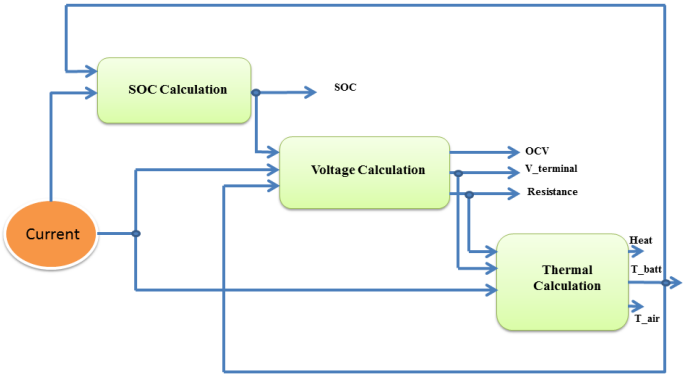


**Figure 4-13 Top level of the battery model in PSAT**

In the first step, a drive cycle that is representative of the expected driving conditions is needed to be developed. To achieve a comprehensive set of data, this cycle should cover a wide

range of driving conditions such as various driving behaviors (aggressive, gentle), driving environment (highway, city), battery SOC (full to near zero) and motor torque/speed. For this purpose, the data of two trips were aggregated. These trips were made in a winter day and encompass both city and highway driving. The resulting drive cycle is called drive cycle #1 and shown in Figure 4-14.

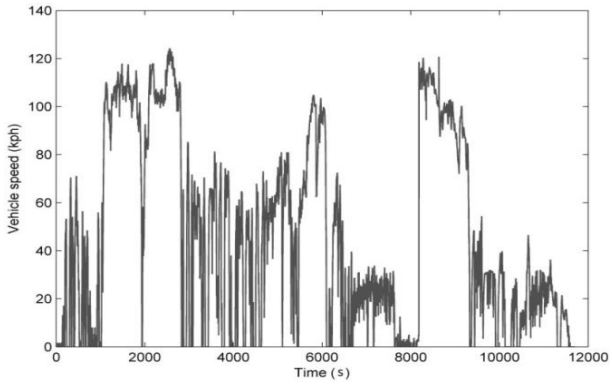


**Figure 4-14. Drive cycle #1 Synthesized for calibrating the battery model**

Relevant statistics of drive cycle #1 are given in Table 4-8. The battery and electric motor data corresponding to drive cycle #1 was analyzed to derive battery open circuit voltage (OCV) map, battery internal resistance map and electric motor efficiency.

**Table 4-8 drive cycle #1 statistics**

| | |
|---|---|
| Cycle Duration (sec) | 11693 |
| Cycle Distance (km) | 149 |
| Speed (kph) | Max:124.3 |
| | Average: 46 |
| Acceleration ($\frac{m}{s^2}$) | Max: 5.3 |
| | Average: 0.38 |
| Deceleration ($\frac{m}{s^2}$) | Max: -4.97 |
| | Average: -0.45 |

### 4.3.1 Estimation of the Battery OCV and Internal Resistance

If lab testing is not available, the battery OCV can be estimated from the road test data. For

this purpose, a scatter plot of battery voltage should be employed. As an example, the battery voltage profile during a sample driving and corresponding charging profile is illustrated in Figure 4-15.

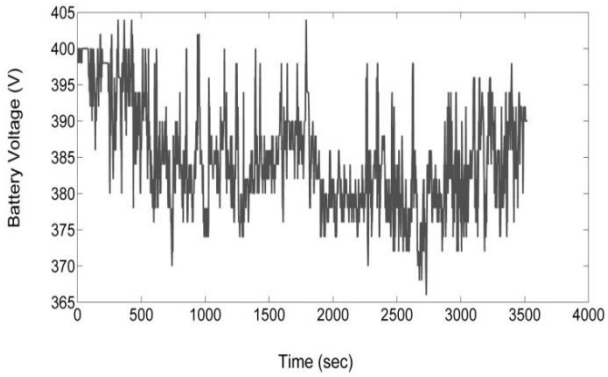


Driving; SOC 91-35 %

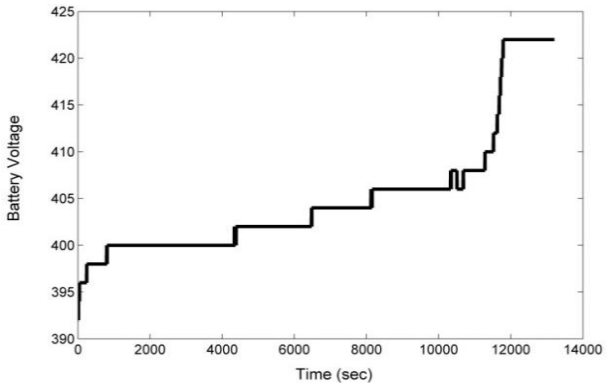


Charging; SOC 35-99 %

**Figure 4-15: Sample battery pack voltage profile**

By selecting the minimum load points in the voltage-SOC scatter plot, (where the battery current < C/20), and fitting a polynomial curve, the approximated value of the battery OCV at various SOC can be estimated. This method was applied on the drive cycle #1 battery data. To verify the accuracy of this estimation method, a test was conducted to measure the OCV in a more realistic way. In this test, through in-city driving, the battery was drained from fully charged state to almost 0% SOC in intervals of 10% SOC followed by 2 hours rest at each SOC.

The initial battery voltage once the vehicle is on after each resting time represents approximately the real OCV. Figure 4-16, illustrates a comparison between the measured values of the OCV and the estimated ones from drive cycle #1. Overall, less than 5% discrepancy was observed between the two curves.

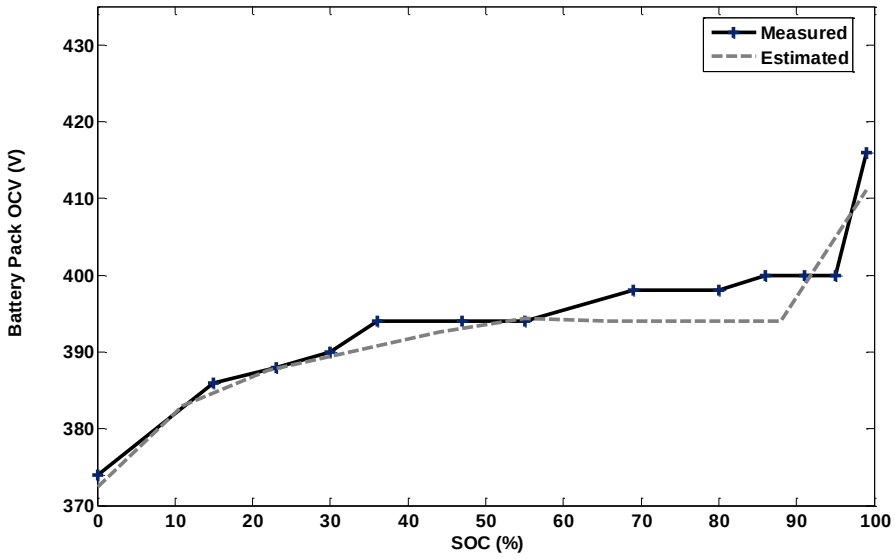


**Figure 4-16: Comparison of OCVs estimated from the road test and measured after 2hr resting time.**

Once the OCV is determined, the internal resistance of the battery pack can be estimated from Eq. 1:

$$r_{int} = \frac{|V - OCV|}{I} \quad (4\text{-}1)$$

Where, V and I are the recorded voltage and current applied/drawn from the battery pack, respectively. To estimate the internal resistances from the road test, a scatter plot of resistances vs. SOC is to be obtained using Eq. 1 and then the redundant data (outliers) filtered out. To improve the battery resistance estimation, different trips data were combined and a rich pool of data was created. Figure 4-17 illustrates the derived internal resistances for each battery string. It should be noted that each battery module includes six strings of battery cells in series and each string contains 49 cells in parallel resulting in a total of 240 cells in each battery module.

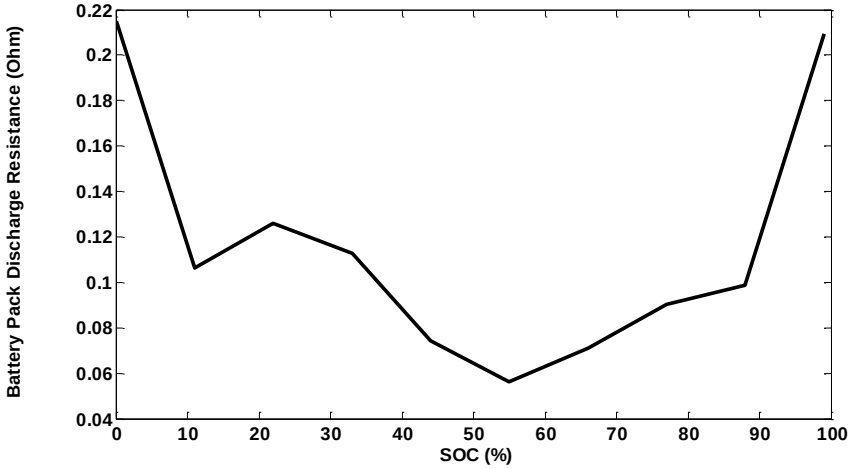


**Figure 4-17: Internal resistance of the battery module derived from data of drive cycle #1**

It should be noted that the procedure presented here is solely based on the road test data; while for measuring the battery resistance in the lab, standard tests are available and all the parameters are controlled. In a real-life situation, there is almost no control over the circumstantial factors. Also, the estimation presented here is limited to the specific environment in which the vehicle is tested. Therefore, to obtain the battery internal resistance from the road test data under different ambient temperatures, the vehicle road test data in different seasons is required. Considering the battery aging, namely, the calendar life and cycling life, associated with this waiting time that may increase the battery internal resistance, one may not be able to fully differentiate the effect of aging and the ambient temperature.

### 4.3.2 Model Testing and Validation

The estimated battery OCV and internal resistance are employed to model the battery pack in PSAT software. To simplify the modeling, a cell level model is up scaled linearly to represent a pack (unbalancing and cell-to-cell variations are ignored). Figure 4-18 shows the SOC curves obtained from the model and the road test data (drive cycle #1). As seen in this figure, the model is able to track the experimental SOC curve with an error of about 3.8%. There are some discrepancies in the in-city portion of the SOC curve, which is related to the regenerative control strategies. However, as long as the model is able to track the SOC changes and the battery

energy consumption, these discrepancies do not significantly affect the modeling accuracy. The total energy processed in the battery was also examined using the following formula:

$$Total\ energy = \sum (Current \times Volt) \times time \tag{4-2}$$

Our studies also indicated that the battery model is able to track the total energy drawn from the battery pack with an error of less than 2.3%.

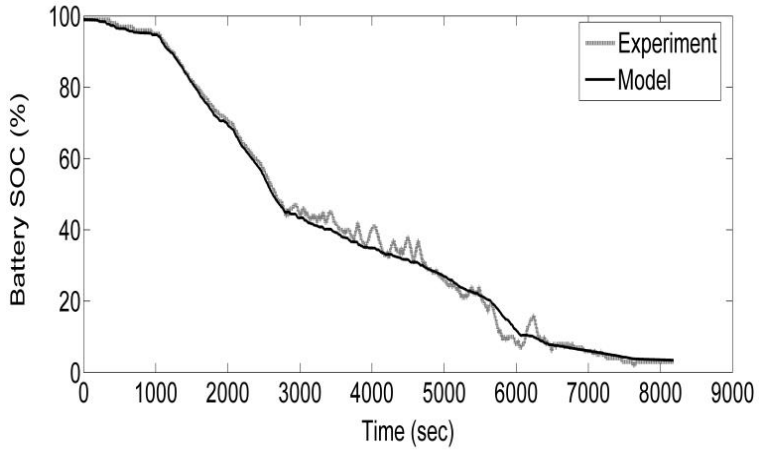


**Figure 4-18: SOC versus time; obtained from the model and drive cycle #1**

In addition, based on the scatter plot of torque-speed of the electric motor, the braking control strategy is modified in order to match the maximum regenerative energy produced by the motor at different speeds with the test data. Figure 4-19 shows the power flow of the motor calculated from the model and experiment. An average error 4% was observed in the results.

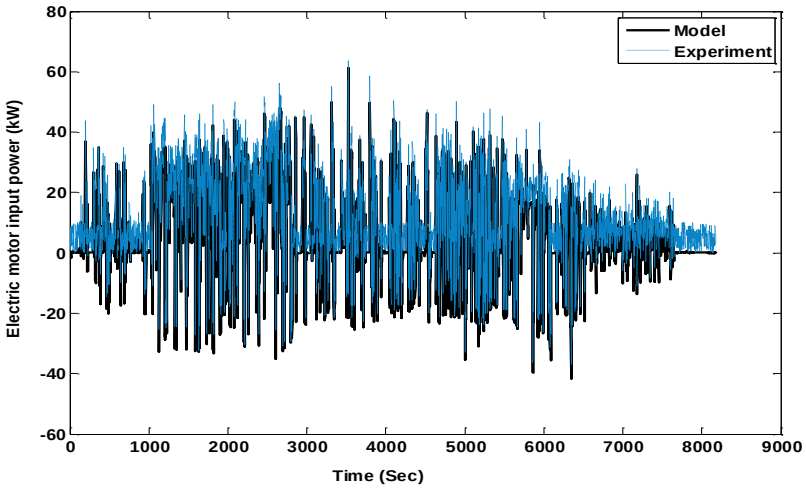


**Figure 4-19: Power Flow into the Electric Motor, model and drive cycle #1 (first 8000 sec)**

As shown in Figure 4-20, inputs to the motor are the voltage and current coming from the battery and the outputs are in terms of torque and speed; therefore the overall efficiency of the motor is calculated as follows:

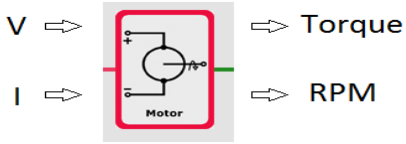


**Figure 4-20. Inputs and Outputs to the Electric Motor**

$$\eta = \frac{\sum(Torque \times Speed)}{\sum(Current \times Voltage)} = \begin{cases} 91.7\ \% & (model) \\ 90\ \% & (expriment) \end{cases}$$

The model slightly overestimated the efficiency of the electric motor.

Figure 4-21 compares the vehicle acceleration from the model and test data under Nov25 drive cycle. The model is able to predict the vehicle acceleration with an average 6% error. The model was then tested with another drive cycle called drive cycle #2. Drive cycle #2 which is mostly representative of highway driving in a winter day is shown in Figure 4-22 and relevant statistics are presented in

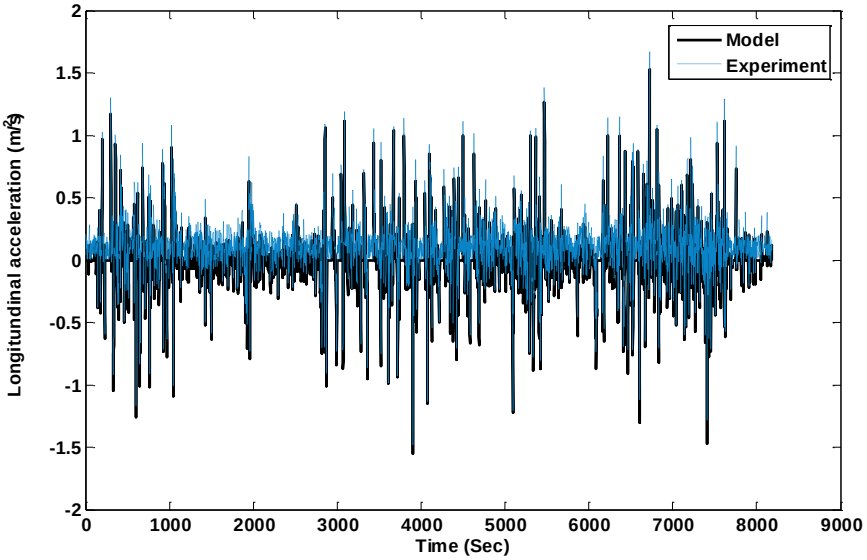


**Figure 4-21. Vehicle Longitudinal Acceleration; drive cycle #1 (first 8000 sec)**

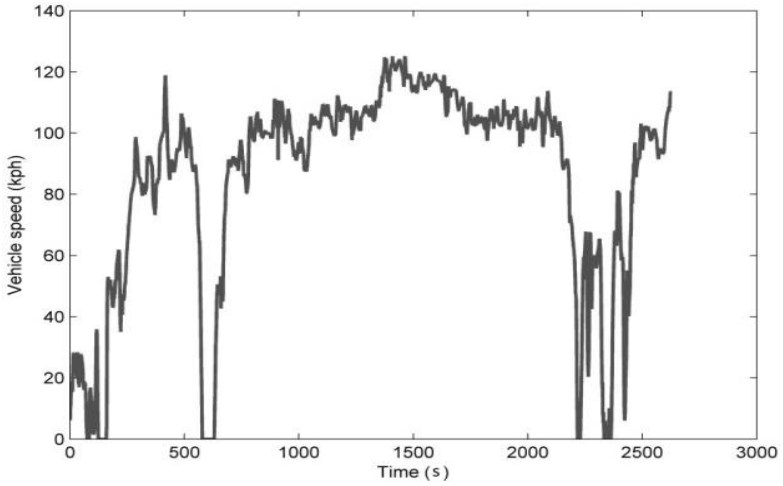


**Figure 4-22: Drive cycle #2 used for testing the model**

Figure 4-23 shows the SOC curve obtained from the model and test data of drive cycle #2. The model is able to simulate the SOC experimental curve for the drive cycle #2 with an error of less than 5%. The battery model is also able to track the total energy drawn from the battery pack with an error of less than 4.6%. Figure 4-24 show the power flowing flow of the motor calculated from the model and experiment. An average 8% error was observed in the results.

Figure 4-25 compares the vehicle acceleration from the test data and the model under the test drive cycle. The model is able to predict the vehicle acceleration with an average 7% error

**Table 4-9: Statistics of test drive cycle #2**

| | | |
|---|---|---|
| Cycle duration (sec) | 2623 | |
| Cycle distance (km) | 98.7 | |
| Speed (kph) | max | average |
| | 124 | 84.6 |
| Acceleration ($\frac{m}{s^2}$) | 6.44 | 0.34 |
| Deceleration ($\frac{m}{s^2}$) | -5.41 | -0.33 |
| Ambient Temperature | 2 ℃ | |

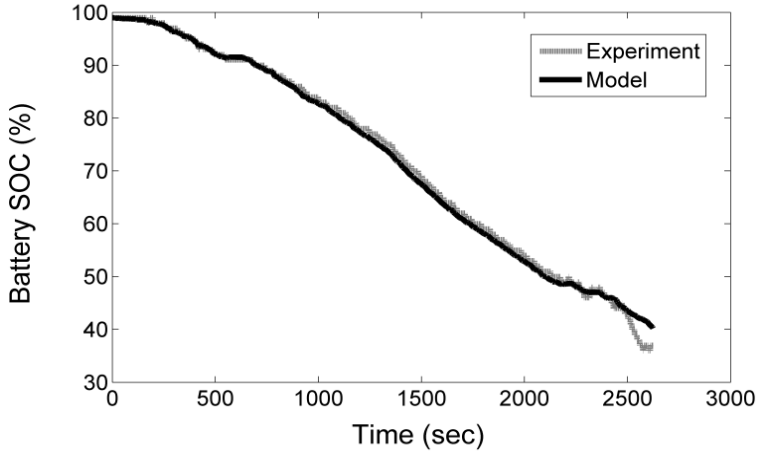


**Figure 4-23: SOC versus time; obtained from the model and field test related to drive cycle #2.**

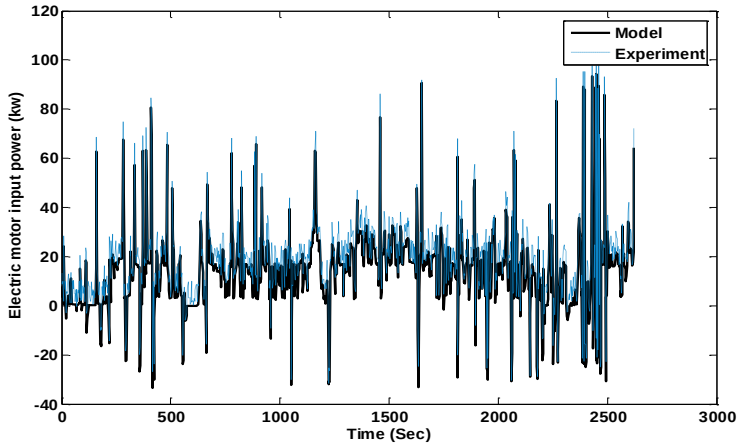


**Figure 4-24. Input Power from Electric Motor; Test Drive Cycle(Dec7-Part1)**

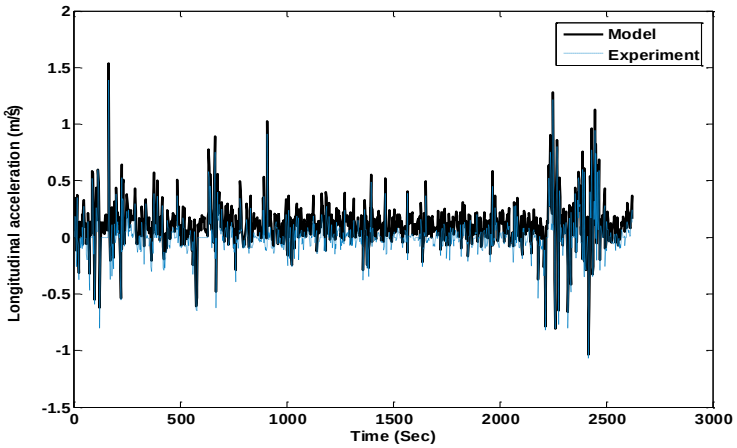


**Figure 4-25. Vehicle Longitudinal Acceleration; Test Drive Cycle(Dec7-Part1)**

To further examine the battery model fidelity, a drive cycle with different environmental and driving conditions was used for validation. A trip made in a summer day in Waterloo (Ontario, Canada) was used for this purpose. The characteristics of this drive cycle (called drive cycle #3) are listed in Table 4-10. The data is representative of a round trip consisting of the city and highway driving. The corresponding drive cycle is also illustrated in Figure 4-26. The battery C-rate histogram during the trip is also depicted in Figure 4-27. The maximum C-rate that the battery experiences, is equal to two, which is normal for an electric vehicle. The low value of C-

rate in EVs ensures the battery will not undergo accelerated degradation due to high C-rates.

**Table 4-10: Drive Cycle #3 Specification**

| | |
|---|---|
| Trip Duration (sec) | 3600 |
| Trip Distance (km) | 75.8 |
| Average Speed (kph) | 75.1 |
| Maximum Speed (kph) | 118.5 |
| Average Acceleration (m/s2) | Positivie:0.11<br>Negative: 0.13 |
| SOC Changes (%) | 91-36 |
| Battery Energy Economy (kWh/km) | 0.19 |
| Total Battery Capacity (Ahr) | 36.35 |
| Battery Average Temperature (0C) | 28-35.8 |
| Ambient Temperature (0C) | +29.4 |

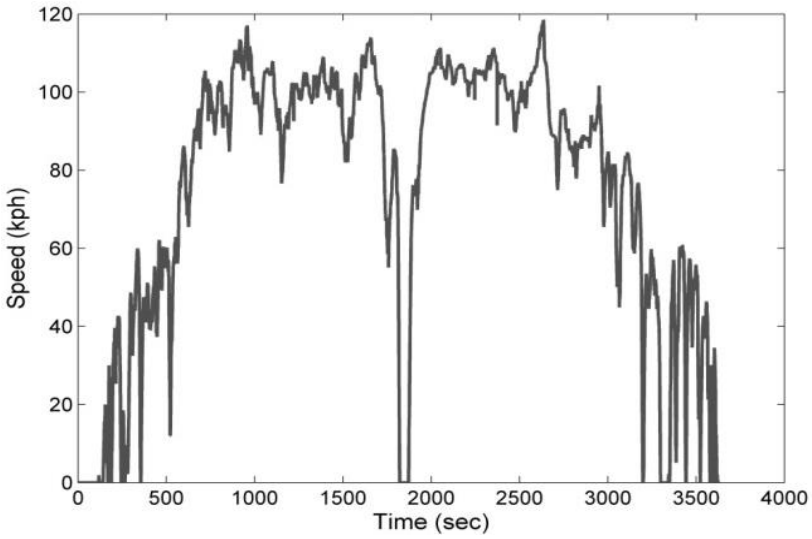


**Figure 4-26: Drive cycle #3**

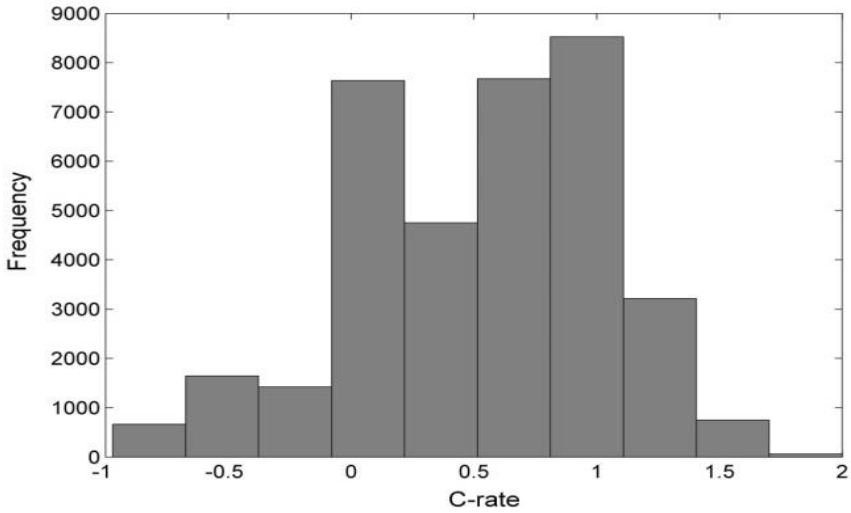


**Figure 4-27: Frequency of the Battery pack C-rates for the drive cycle #3**

The modeled battery SOC is compared against the test data in Figure 4-28. The model shows up to 10% overestimation in tracking the SOC. One reason could be related to the coulomb counting algorithm that the current model is based on. In fact, SOC depends not only on the accumulative charge processed in the battery but also on the rate of change of the current. This is due to the fact that the available capacity of the battery is a function of the discharge rate and a robust SOC estimation algorithm should be able to take this into account to give the driver in time warning of the available capacity. Also, temperature is an important parameter that affects the available capacity of the battery. To improve the SOC algorithm, one might need to incorporate the effect of temperature by measuring the battery capacity at different ambient temperature. Finally, for this study, road grade impact is ignored. Taking the road grade effect on the required power from the battery into account, might improve the SOC calculations. However, the current model is quite powerful in estimating the total and accumulated discharged and regenerated energy in the battery back over the drive cycle as demonstrated in Figure 4-29.

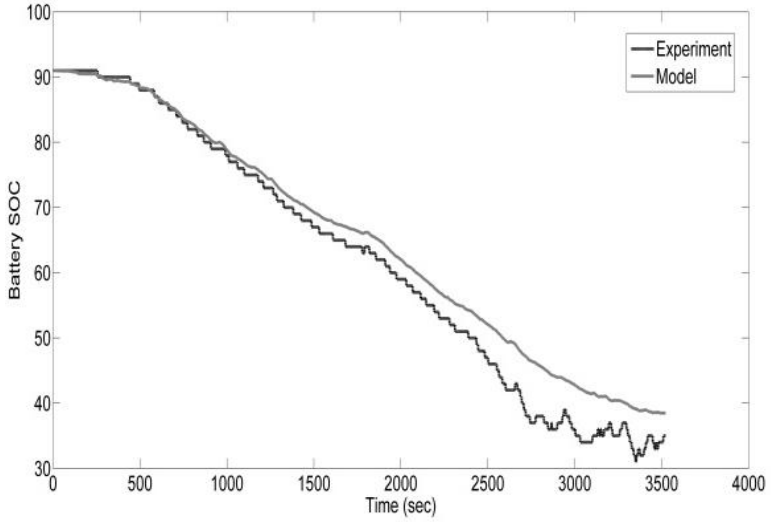


**Figure 4-28: Battery SOC Validation Against drive cycle #3**

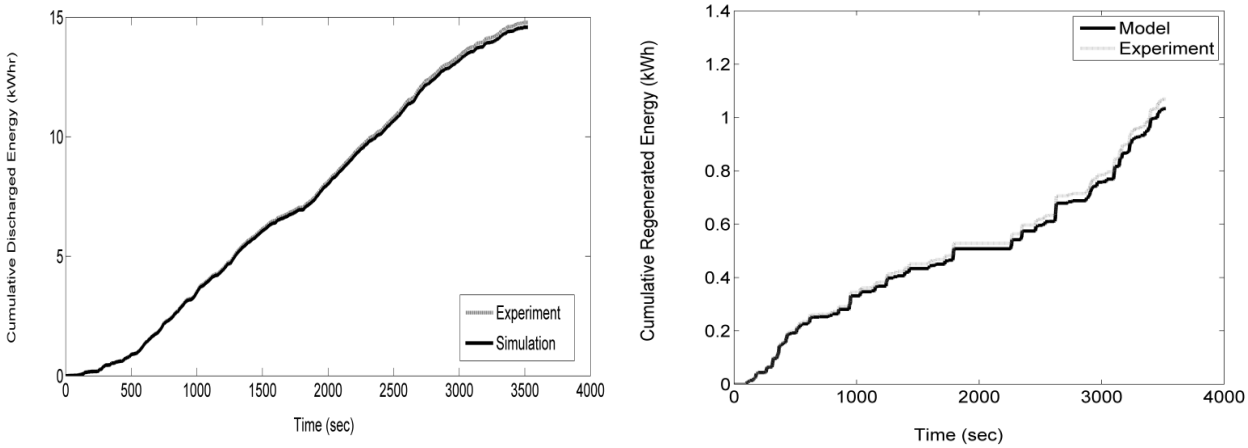


Discharged energy

Regenerated Energy

**Figure 4-29: Battery Model Validation against Test Data over Drive cycle #3**

## Battery Thermal Behavior

The performance, life, and safety of Li-ion batteries are affected by their operation temperature. Therefore, for designing the battery pack for EVs, it is important to take into account the thermal behavior of these batteries. In this section, the thermal behavior of the

battery pack based on the field test data and the thermal model developed with consideration of the effect of the battery reversible and irreversible heat generations is studied. The pack is cooled by a fan with a flow of air which is assumed to be divided in parallel so that the same amount of air passes through each module of the pack. Therefore, it is enough to model one single module to obtain the temperature profile of the whole pack. The cell temperature at each time step is a function of the generated heat and the rejected heat by forced convection. However the BMS on this vehicle turns the fan on once the module temperature exceeds 40℃ . Considering the weather conditions in Waterloo, such a situation rarely happens and therefore it is reasonable to ignore the forced convection in the battery pack thermal modeling. The heat generation rate inside the Li-ion cell can be determined from Eq. 2 [26].

$$\dot{Q}_{gen} = \dot{Q}_{gen,\text{reversible}} + \dot{Q}_{gen,irreversible} = R_{int}I^2 + IT\frac{d(OCV)}{dT} \quad (4\text{-}3)$$

Where, $\dot{Q}_{gen}$, is the rate of heat generation in the battery pack, I, is the current drawn from the battery pack, and $R_{int}$, is the internal resistant of the battery pack obtained from Eq. 1. In Eq. 2, the rate of heat generation is expressed as the summation of two terms. The first term represents the irreversible heat generation, which is always exothermic and the second term is the reversible heat generation, which can be exothermic or endothermic. In this term, the coefficient of d(OCV)/dT for a single cell at various SOC are adopted from [48] and plotted in the Figure 4-30.

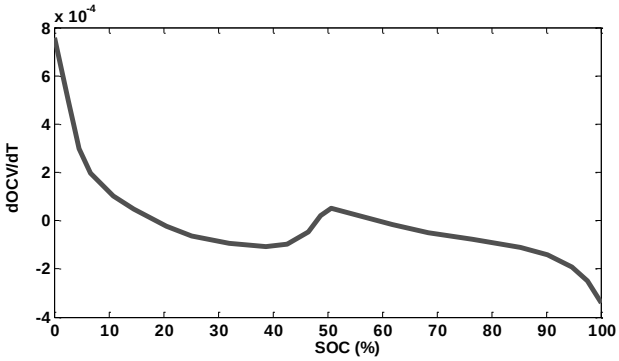


**Figure 4-30: The coefficient of d(OCV)/dT versus SOC for the single cell of the battery back under study [48].**

It is noted that this coefficient should be multiplied by the number of series cells in the battery

pack before using in Equation (4-3). The reversible heat calculated based on this coefficient is plotted versus SOC in Figure 4-31. It is observed that at high SOCs the reversible heat has a cooling effect. Once the heat generation is determined from Eq. 2, the temperature of the battery pack is determined from the energy balance equation neglecting any losses:

$$mC_p \frac{dT}{dt} = \dot{Q}_{gen} \tag{4-4}$$

where, $C_p$, is the specific heat capacity (~ 800 kJ/kg [113]) and m, is the total weight of the battery pack.

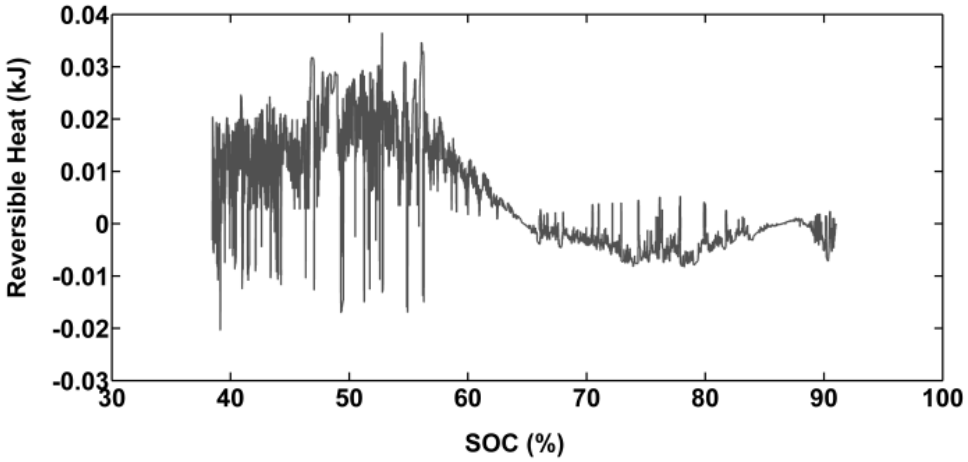


**Figure 4-31: Reversible heat generated during drive cycle #3**

Figure 4-32 represents the battery pack temperature during the drive cycle #3 based on the model and field test data. Figure 20 also shows the error in the battery pack temperature prediction based on the thermal model developed. As seen in Figures. 19 and 20, the model is well able to track the measured battery pack temperature with the maximum error of 3%. It is noted that the battery faces ~8 $^{\circ}$C temperature increase during the entire drive cycle #3. During this driving event a total heat of $Q_{gen} = Q_{irr} + Q_{rev} = 1200\ kJ$ is generated (~2.5% of the total discharged energy) and the reversible and irreversible heats have a share of ~10% (112 kJ) and 90% (1088 kJ) accordingly.

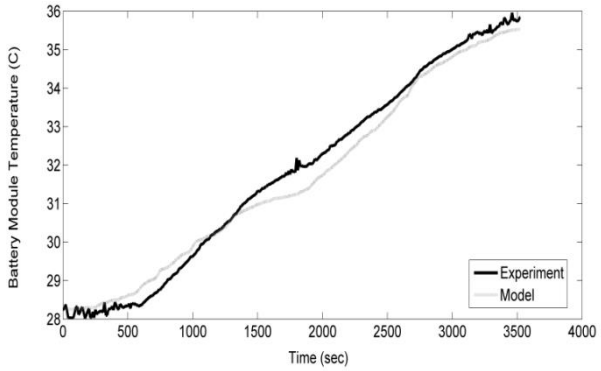


**Figure 4-32: Validation of the battery pack thermal model for drive cycle #3.**

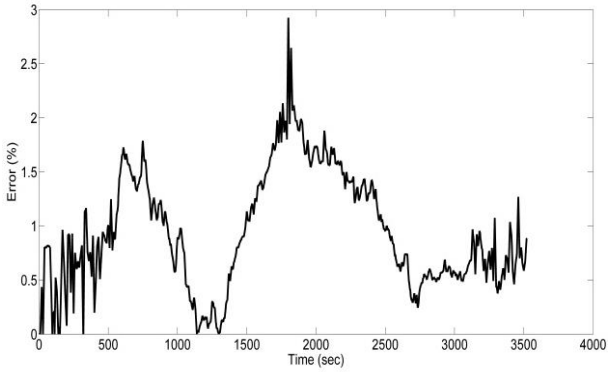


**Figure 4-33: Modeling error in predicting the battery pack temperature over drive cycle #3**

### 4.3.3 Case study- Testing the proposed ECM with a Real-life drive cycle

In this section, performance of the proposed ECM in Chapter 3 is evaluated with a real-life drive cycle (drive cycle #3-Figure 4-26). For this purpose, it is assumed that the battery pack on the research EV is comprised of the battery cells for which the ECM was developed. As these cells are different from the original battery cells on the research EV (cylindrical Valence batteries, $LiFeMgPO_4$) in terms of geometry and chemistry, a different thermo-electrical performance would be expected from the new battery pack. Therefore, the first step in this analysis would be scaling the battery current profile according to the specifications of the new battery cells.

The cells arrangement in the new pack is assumed to be $3p \times 105s$. As the vehicle dynamics and power demand over the test drive cycle remains the same, the new battery pack would have to provide the same power requirement (but a different current and voltage profile). Afterwards, the Autonomie model of the vehicle has to be modified to take the power profile as the input. It is worth to mention that in Autonomie, the input is the drive cycle and based on the instantaneous difference between the actual speed and the desired speed, a PI controller determines the adjustments to the torque demand signal in the driver sub-model. Therefore, for the current analysis, the controller (in the driver sub-model) was modified to take the battery

power difference as its decision criteria. Also, the PI controller was upgraded to a PID controller to increase the accuracy of the model in following the power profile fluctuation as shown in Appendix C. the simulated battery power is plotted against the experimental data in Figure 4-34. An average error of 5% was observed in the simulated power profiles.

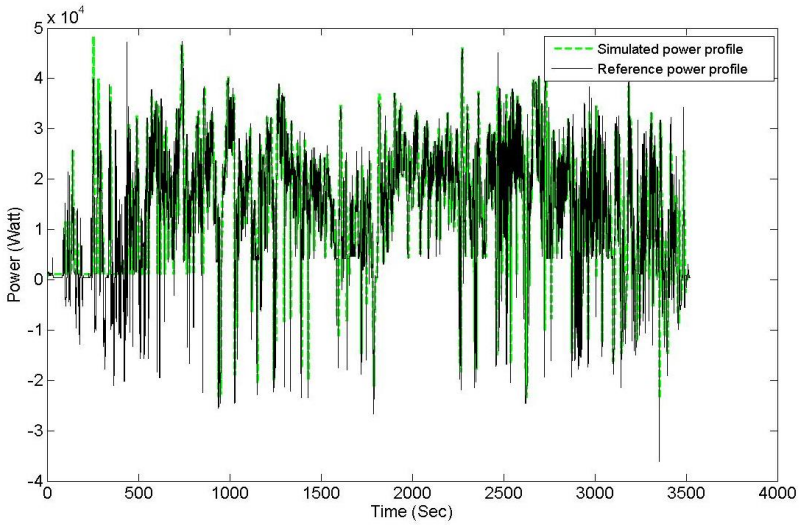


**Figure 4-34 Battery power profiles under test drive cycle operation**

The resulting current profile is shown in Figure 4-35

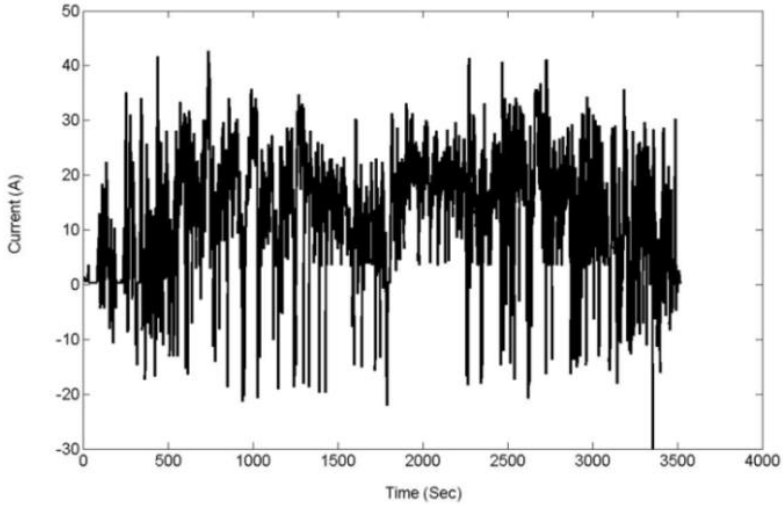


**Figure 4-35 Profile of battery current of the drive cycle #3**

The DPW was then run with this current profile. Figure 4-36 illustrates the simulated SOC profile against the measured values. The temperature profile is also compared against the original battery temperature profile in Figure 4-37. It is observed that the battery cells in the assumed pack experience much lower temperature (< 2℃) increase during the driving cycle, which is due to the different heat transfer boundary conditions and chemistry. Also, the effect of convection coefficient on the temperature profile is shown in Figure 4-38. As can be seen a 10h heat transfer coefficient would be able to keep the battery temperature profile uniform.

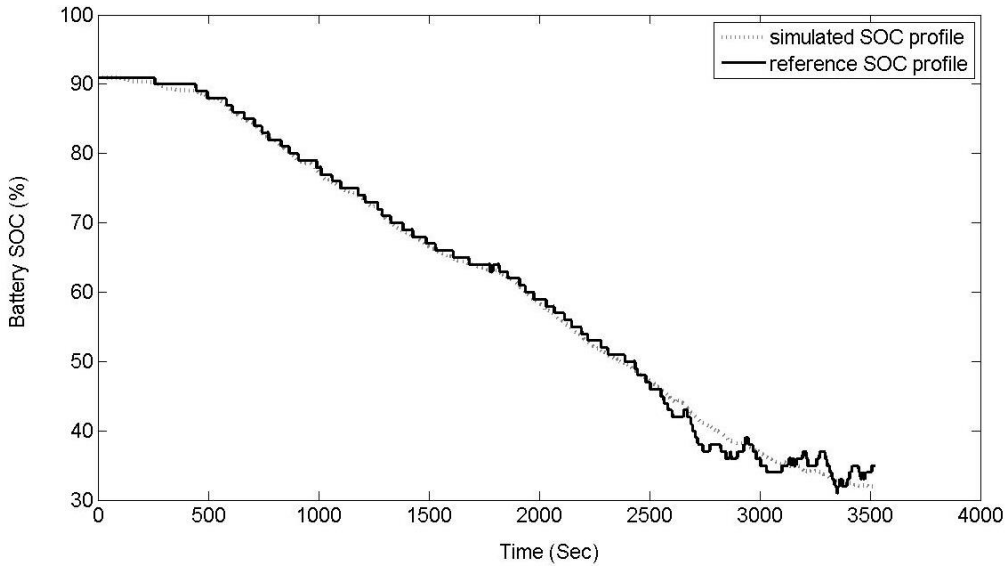


**Figure 4-36 Battery SOC power profiles under test drive cycle operation**

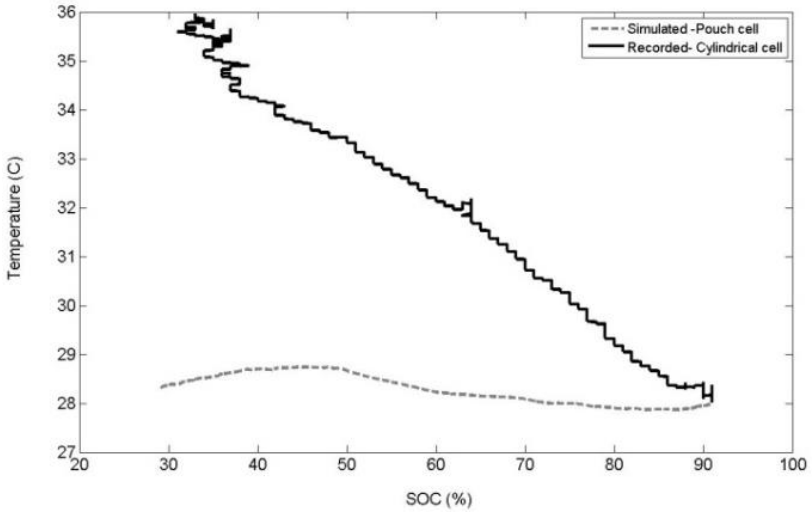


**Figure 4-37 Profile of battery temperature during the tests drive cycle**

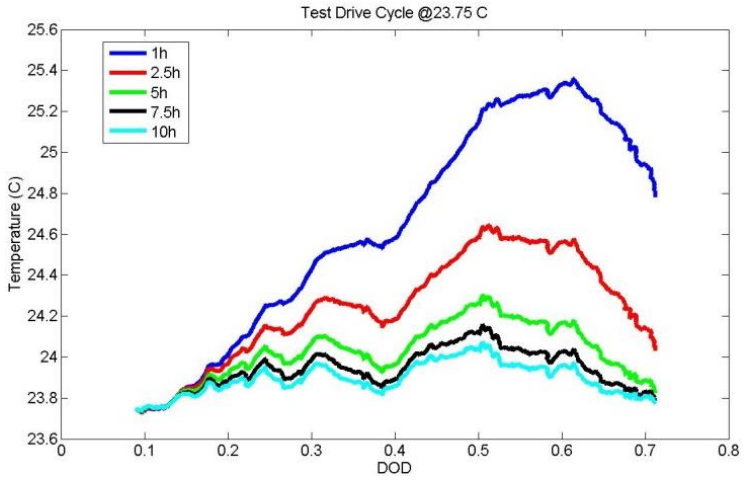


**Figure 4-38 Tests drive cycle and relevant battery performance profiles**

### 4.3.4 Overall Powertrain Efficiency of EV-ACX2.5

To evaluate the overall powertrain efficiency of the EV-ACX2.5 vehicle, the efficiency of each component must be first calculated. The main components involved in vehicle energy conversion, from the wall to the wheel, are the charging station, AC/DC convertor (on-board vehicle charger), the vehicle battery, and the electric traction motor. The efficiency of each

component is simply defined as the ratio of the output energy to the input energy and the overall efficiency is equal to the product of all component efficiencies. Table 4-11 shows the input and output energy measurement points for each component in the EV powertrain. As the amount of energy being fed from the charging station was not available at the time of writing this report, although, assuming the loss through the wall charger to be near zero is a reasonable assumption.

calculations were performed considering the AC/DC convertor input current and voltage as the input to the powertrain. Data for charging and driving from October 2011 to February 2011 has been aggregated to calculate the average powertrain efficiency.

Table 4-12 summarizes results of the efficiency calculations. The powertrain efficiency on average is found to be 77%, which is the fraction of the input energy resulting in useful work at the wheels. This is notable when compared to an internal combustion engine vehicle, where the engine efficiency itself is less than 40% not to mention drivetrain losses in the transmission, torque converter, and final drive. However, it should be noted that calculations on powertrain efficiency suffer from limitations. This is due to the fact that the electric motor torque reported by CAN signals is not based on a sensor measurement, as the electric motors are not equipped with torque sensors, but derived from lookup tables programmed by the manufacturer.

The motor efficiency is obtained through dynamometer tests for a given voltage, current, and speed and the manufacturer uses this efficiency to calculate and transmit the "estimated" torque over CAN.

**Table 4-11: Input and output of each component in the EV powertrain**

| Component | Input | Output |
|---|---|---|
| AC/DC Convertor | Alternative current and voltage (during charge event) | DC and voltage (during charge event) |
| Battery | Current and voltage coming from the AC/DC convertor (during charge event) | Current and voltage during discharging event (during driving) |
| Electric Motor | Current and voltage provided by the battery (during driving) | Angular velocity and torque (during driving) |

**Table 4-12: Monthly efficiency of the EV-ACX2.5 powertrain**

| Month | AC/DC convertor | Battery | Electric Motor | Overall efficiency |
|---|---|---|---|---|
| October, 2011 | 91.36 | 98 | 87 | 78 |
| November, 2011 | 91.37 | 97 | 85 | 75.3 |
| December, 2011 | 91.39 | 99 | 85.4 | 77 |
| January, 2012 | 91.36 | 99 | 87 | 78 |
| February, 2012 | 91.37 | 98 | 86.2 | 77.1 |

### 4.3.5 Energy Requirement of EV-ACX2.5 as a Fleet Vehicle

To perform a more in-depth comparison between EV-ACX2.5 and fleet performance, the EV PSAT model was run through all of the collected 'HEV' drive cycles from HEV vehicles over three months (November, December, January) to yield the amount of energy required as if the EV was used as a fleet vehicle by Burlington Hydro. For this purpose, first the HEV drive cycles were defined and saved as velocity-time data sheets; afterwards a script written in Matlab called and ran the PSAT model for each of the drive cycles and updated the consumed energy value accordingly. Results are shown in Table 4-13. The results are based on the assumption that the battery was fully charged at the beginning of each trip. The consumed energy reported in Table 4-13 is calculated by integrating instantaneous power drawn from the battery (as was simulated by PSAT) over each trip. On average, the EV-ACX2.5 is able to complete all of the HEV cycles using only 60% of the energy used by the HEV. This is equal to a 64% cost saving as is represented in Table 4-14. The cost of HEV fuelling is calculated based on average monthly price of gas in Burlington-Hamilton area [106]. It is also of interest to perform a well-to-wheel life cycle analysis and compare the emissions of the EV with the HEV. For this purpose a validated model of the HEV needs to be developed. This task can be considered for future analysis.

**Table 4-13: Energy saving of EV-ACX2.5 as a fleet vehicle based on the HEV drive cycles**

| Month | Distance driven by HEVs (km) | Consumed Energy by HEVs (KWh) | Consumed energy by EV-ACX2.5 as a fleet (KWh) | Energy Saving (%) |
|---|---|---|---|---|
| Novemebr,2011 | 995.7 | 708 | 259 | 63.4 |
| Decemebr,2011 | 793.48 | 514.1 | 206 | 60 |
| January,2012 | 1364 | 873 | 374.7 | 57 |
| | | | | Average: 60% |

**Table 4-14 Cost saving of EV-ACX2.5 as a fleet vehicle based on the HEV drive cycles**

| Month | Fuel consumed by HEVs | Average gasoline price ($) [106] | Cost of HEVs fueling ($) | Cost of EV-ACX2.5 as a fleet ($) | Cost saving (%) |
|---|---|---|---|---|---|
| November,2011 | 73 | 1.186 | 86.6 | 28.5 | 67 |
| December,2011 | 53 | 1.165 | 61.7 | 22.6 | 63 |
| January,2012 | 90 | 1.21 | 109 | 41.2 | 62 |
| | | | | | Average: 64% |

### 4.3.6 Studies on Battery Degradation

A major objective of field testing and data collection from the EV-ACX2.5 was to analyze and model the battery degradation as a function of operation parameters. As pointed out earlier, different parameters affect the battery degradation; among them, driving and charging behavior and battery temperature profile are of high significance. Trends of capacity fade and power fade as indicators of degradation can be identified from the test data provided that the data are collected over a reasonably wide range of time (that visualize a degradation trend) and under regular daily vehicle operation. Note that by regular driving it is assumed that a vehicle travels 20-25 thousand kilometer annually on average. The other metric is the charge/discharge efficiency, which, is an indicator of the amount of energy required/delivered to fulfil a similar power demand profile. As battery ages, with reference to a similar charge input, it would deliver less energy (resulting in a reduced electric range) or consumes more energy to reach to a target SOC. In EVs, battery capacity is the determinant factor of vehicle performance and usability. Therefore, capacity fade is taken as the main criteria for battery life studies.

Driving experience with the EV-ACX2.5

The collected driving and charging data of the vehicle revealed that this vehicle had not been utilized to the maximum capacity but mostly experienced partial charges and discharges. For the purpose of demonstration, a summary of the vehicle usage over January, 2012 till October, 2012 is represented in Table 4-15.

**Table 4-15 EV-ACX2.5 usage over January 2012- October 19, 2012**

| Distance driven (km) | number of trips (>5 km) | number of charging events (>5 min) | Total charge in (kWhr) |
|---|---|---|---|
| 1208 | 80 | 58 | 263 |

Considering the 25 kWhr Li-ion battery pack installed on the vehicle, it is observed that the battery has gone through less than 11 equivalent full discharges over ten months which is not a significant value. The total distance driven is only 1208 (km) which confirms very light usage of the vehicle. Figure 4-39 and Figure 4-40 show the distribution of charging and driving events over 10 months.

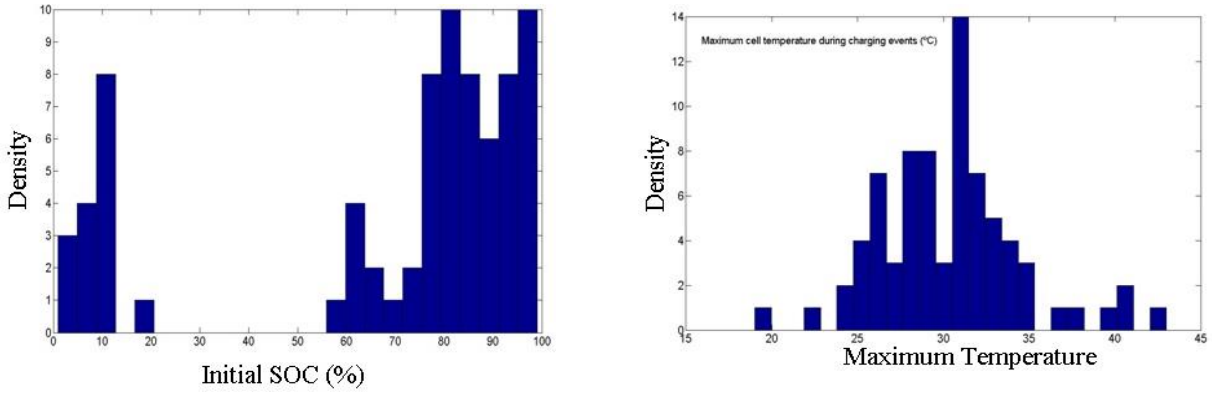


**Figure 4-39 Histogram of charge data (over Jan-Oct, 2012)**

According to the figures, most of the driving events cover in city routes with less than 10 km length and more than 70% of the charging events started at an initial SOC greater than 60%. There are also gaps observed in the driving events history, meaning that the vehicle has been out of operation for days (even more than a week). Such a halt in operating the vehicle slows down the process of degrading the battery. Although not adequate, the collected data can be yet used to

propose methods for identifying the battery degradation.

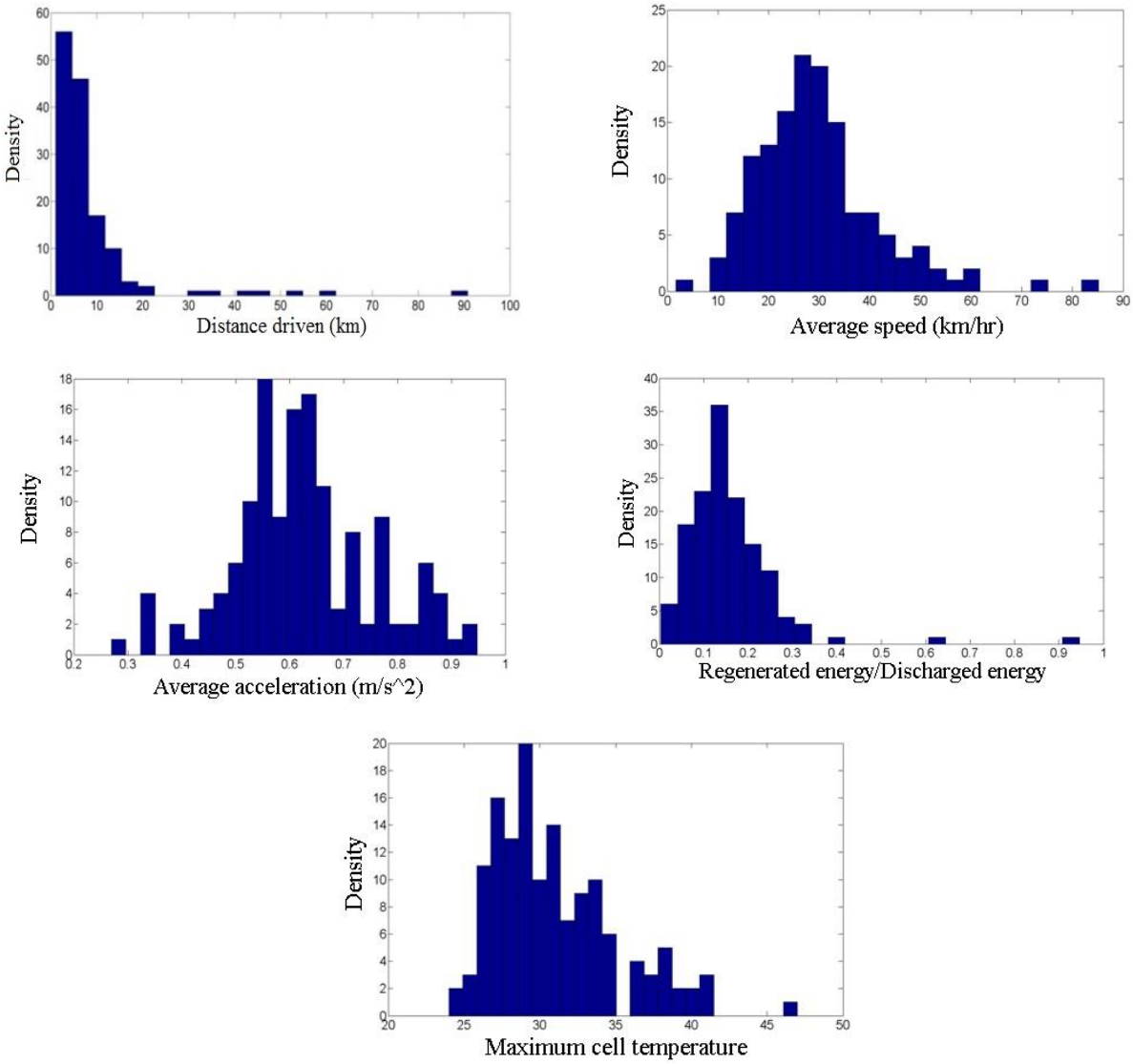


**Figure 4-40: Trips distance driven by EV-ACX2.5**

## Power fade

The battery polarization curve provides useful information to identify the power fade trend. The polarization curve shows how the battery voltage and current change during charge and discharge events. From this curve an estimate of the internal resistance of the battery can be

obtained; internal resistance is the parameter that directly represents the power-fade inside the battery. It is expected that after a sufficiently large time period, the polarization curve slope will change and show a growth in internal resistance. In order to investigate how the battery internal resistance has changed over one year of operation, data from three drive cycles driven on November 25, 2011, December 7, 2011 and October 05, 2012 have been used to generate the polarization curve by making scatter plots of voltage versus charge processed (Figure 4-41) and fitting a polynomial curve. The average battery temperature range was 20-35 $^{\circ}$C for the November 25 drive cycle, 20-47 ºC for October 5 and 15-38 ºC for December 7. The high temperature changes in the December 7 and November 25 drive cycles are due to the aggressive driving, which results in higher discharge currents and heat generation as well. As shown in Figure 4-42 as the battery ages, its polarization curve will have a greater slope, i.e. for the same amount of charge processed, the battery will experience a higher voltage decrease. Also, the highest discrepancy in the fitted voltage profile was observed to be at 63 Ahr (~ 90% DOD) showing 6% increase in the bulk internal resistance.

However, care should be taken when interpreting such polarization curves; because the polarization not only depends on the battery SOH, but also on the battery operating temperature. Therefore, unless one could differentiate the temperature and SOH impacts on the polarization curve, the observed decrease in the voltage could not be solely translated as resistance increase in the battery. Therefore, to enable a comparison of battery polarization curves that yields an indication of power fade, the test data should be collected from trips with identical battery operating temperatures. Again, dynamometer testing in a controlled environment is much preferred for this purpose. Other option is implementing an active thermal management for the battery pack which is able to keep the battery temperature in a narrow operating range. In addition, driving behavior which directly affects the current demand from the battery is the other significant parameter on the polarization curve. For a reasonable comparison, polarization curves over similar driving events (in terms of average and maximum speed and acceleration) should be compared against each other.

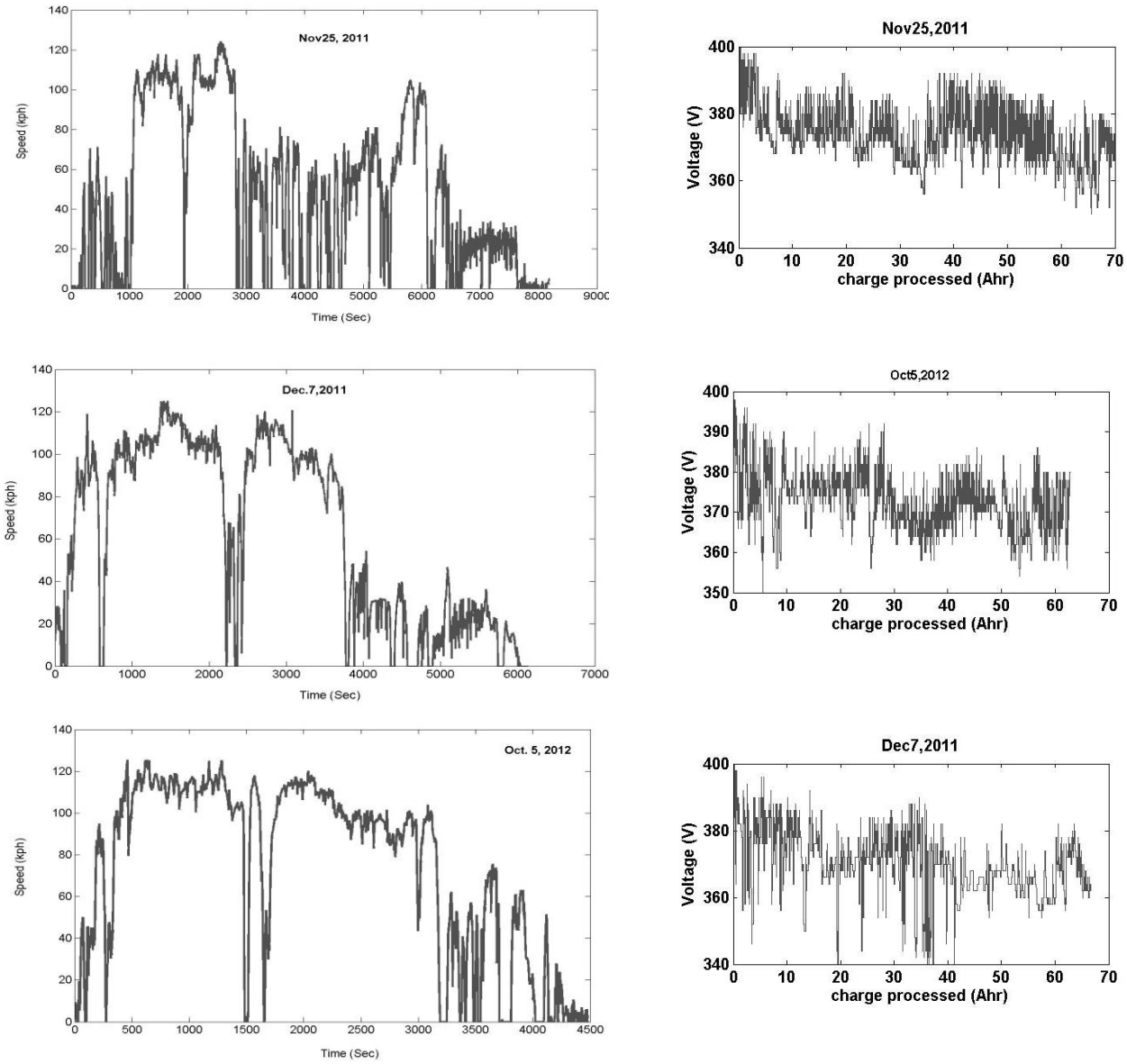


**Figure 4-41 selected drive cycles for comparing the polarization curves**

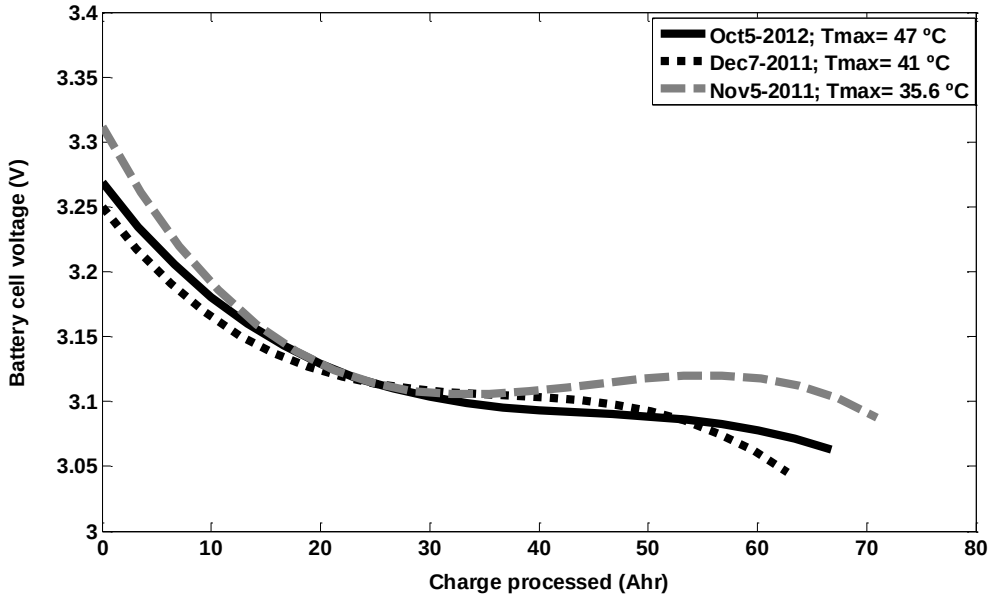


**Figure 4-42 Battery polarization curve for three selected trips with EV-ACX2.5**

Charge efficiency

To calculate the charge efficiency, the first step is to classify drive cycles and charge cycles according to some predefined characterising parameters. For example, a drive cycle can be identified by the average velocity and acceleration, maximum velocity and acceleration, the ratio of battery regenerative to propelling power and temperature profile. A charge cycle also, can be identified by the initial SOC, charging power, and battery temperature profile. Once the events are classified, loss metrics could be defined as suggested in the following:

For charge data: variation of battery charging capability over time:

$$\Delta\left(\frac{\text{Energy stored}}{\text{charging time}}\right) = f(\text{net energy processed}) \tag{4-5}$$

For driving data: variation of discharged energy per km driven under similar drive cycles:

$$\Delta\left(\frac{\text{Battery discharged energy}}{\text{Distance driven}}\right) = f(\text{net energy processed}) \tag{4-6}$$

The data collected over a ten month period is used here for charge/discharge efficiency

analysis. Constraints for extracting similar charge and driving data are presented in Table 4-14. Similar charge and driving events extracted accordingly are illustrated in Figure 4-43 and Figure 4-44. It is expected to see a decreasing trend in both figures (as discussed earlier). Figure 4-44 shows an overall decrease, however, due to the limited data points used for classification and measurement error this trend is not very obvious in these plots. A large data pool (over a time span of 2-3 years) should result in the expected trend.

**Table 4-16 Extraction of similar charge and driving events**

| | charge | driving |
|---|---|---|
| **Range observed** | Maximum cell temperature: 19°C-43°C<br>Initial SOC: 1%-99% | maximum cell temperature: 24°C-47°C<br>Average speed: 5-85 (kph<br>Average positive acceleration: $0.95 - 0.27\ (\frac{m}{s^2})$<br>Regenerative to discharged energy ratio: 0.0037-0.95 |
| **Selected range** | Maximum temperature: 28°C -35 °C<br>Initial SOC: 80%-90% | Maximum temperature: 26°C -32 °C<br>Average speed: 25-30 (kph)<br>Average acceleration: 0.5-0.7 $\left(\frac{m}{s^2}\right)$<br>Regenerative energy to discharged energy: 0.08-0.13 |

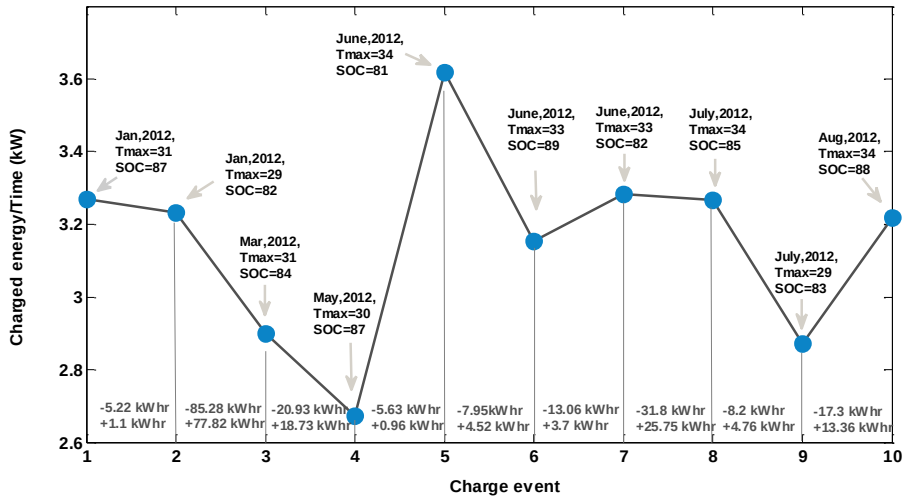


**Figure 4-43 Charge input over time for 10 similar charging events**

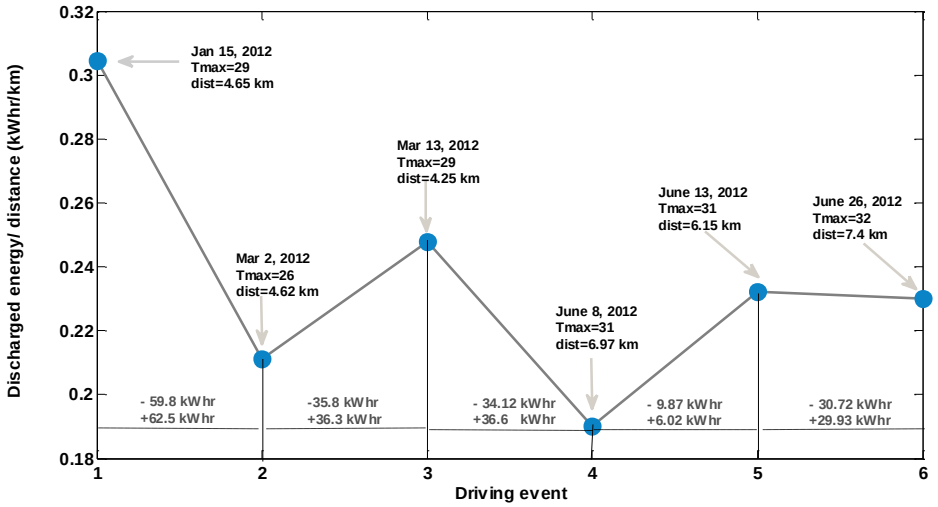


**Figure 4-44** Energy discharged per km driven for 6 similar driving events

**Considerations-** With this suggestion it is assumed that the SOC reported on the CAN is calculated based on an adaptive algorithm which is able to incorporate the effect of different parameters on capacity (such as discharging rate and temperature). However, there are always uncertainties with the road test data as there is no control on the weather conditions and traffic (such as stops at red lights), it is not possible to drive exactly the same trips and evaluate the capacity trends. To get the most accurate determination of capacity fade, it is necessary to run capacity measurement experiments in a controlled environment. A test station could be developed to enable cycling the battery under a set of pre-defined duty cycles allowing better observation of the capacity degradation.

### Capacity Fade

In order to calculate the capacity fade it is required that a baseline capacity value be established when the battery is new, and that a standard procedure be developed for measuring the capacity of the battery as time progresses. The suggested method for measuring the battery capacity on vehicle is as following:

1- Fully charge the battery; Burlington was asked to leave the charger plugged in from the night before the testing day.

2- Drive the car; starting from the parking lot including a city and a highway range, should not cover more than 90-95 km (3-4 % SOC) otherwise the battery dies on the road

3-bring the car back to the parking and drive it down to 1% SOC.

4- Leave the car in the parking spot with lights, AC, and radio on. When the car shuts off the battery is dead.

6- Plug in the charger at least for 7-8 hr., when the battery is fully charged data logger stops recording, afterwards the available capacity can be measured by measuring the charging time and current into the battery from the recorded data.

Depending on the availability of the vehicle and collected data two approaches c considered for modeling the battery capacity degradation.

**Approach 1-** If the vehicle is available over a period of at least one year, an empirical life model of the battery could be developed. Such a model would be based on observed correlations between the SOH measured points and operating parameters (energy processed C-rate, etc.). However, considering the typical 10-year life time of the EV batteries, a minimum two-year testing without interruption seems unavoidable. It is also necessary to operate the EV under a systematic fashion and keep the battery running under similar conditions. Following table shows the important parameters in the model development:

**Table 4-17 Important parameters in the battery degradation field test**

| Variables | How is going to be treated |
|---|---|
| Driving profile | Drive daily on a similar route with similar traffic and driving style |
| Charging profile | Start at the same time of the day , without interruption |
| Initial State of charge | Start all the trips from fully charge state |
| Ambient Temperature | Record as an independent variable |
| Capacity | Measure 2-3 times in a month to observe changes |
| Energy processed (in and out) | Measure over the entire time period |

Any interruption will change the battery usage profile and impacts the model accuracy. Figure 4-29 illustrates the proposed structure for modeling capacity fade as a function of processed energy, assuming two capacity measurements per month.

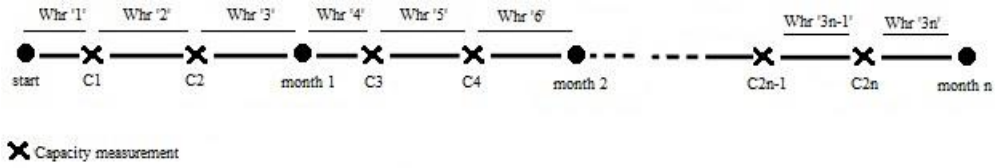


**Figure 4-45 Test plan provided that the vehicle is available for systematic usage**

Based on this plan, the model will be of the following structure:

$$C_n = C_{n-1} - f(Whr, \overline{T}) \quad (4\text{-}7)$$

Where, $C_n$ is the battery capacity at stage "n". $\overline{T}$ is the average battery operating temperature over two successive capacity measurement stage. "Whr" is the total energy processed in and out of the battery over two successive capacity measurement stage. According to this model, the battery capacity in each measurement stage shows a decrease compared to the previous measurement, which is a function of the processed energy in the battery and the average ambient temperature.

**Approach 2-** If the vehicle is not available for a systematic driving/charging, the data of random operation of the vehicle still could be used for validation and identification of a battery life model. For this purpose, the battery capacity should be measured and recorded from time to time over the course of vehicle operation. To simulate the corresponding capacity fade, the battery operation profiles (including current, temperature and SOC) over this period are collected and fed to the battery life model chronologically. Comparing the simulated capacity fade curve with the measured curve, the model parameters can be calibrated and validated.

**Considerations**

We should be aware that the only parameter that can be fairly kept constant during the driving

is the drive cycle (v-t) profile but not the C-rate profiles. The reason is that as the battery ages, more energy will be wasted as heat (due to resistance growth) and therefore to cover a similar driving distance more energy would be discharged from the battery in total, and, the c-rate profile would also change over time.

Also, SOH measurement itself impacts the battery health. When running life tests in the lab, the degradation effects associated with SOH (capacity) test is minimized by using a very low C-rate profile to the battery. In case of field testing, two solutions can be considered: 1) running the vehicle with very low c-rates (e.g. 10-15 kph) and cycle the battery down to zero percent SOC, which is a time consuming procedure. 2) Minimize the frequency of SOH measurement tests; to limit the number of full discharge & charge cycles minimize the SOH test impacts. But, from the modeling aspect, decreasing the number of SOH tests results in a less reliable model development as fewer response points will be available.

It should be noted that a model described in the approach 1 would be valid for only one specific duty cycle. As there are infinite combinations of driving and charging profiles possible in reality, it would be best to employ multiple test vehicles, each with a different duty cycle.

Due to the technical issues, the vehicle operation was interrupted several times during the course of the project. Also, as the operation data histogram showed, the vehicle was not used very much by the company staff. Therefore, it was decided to bring the vehicle to Waterloo and drive it in a daily fashion. A route containing in-city and highway driving as presented earlier in Figure 4-26 was chosen for this purpose and two graduate students involved in the project drove the vehicle every day. After each driving, the vehicle was taken to the charge station for a full recharge and finally back to the parking lot for the next day driving. The tests were repeated every day for four months until again the vehicle went inoperable and tests were halted. During the test period, the battery capacity was measured and recorded twice a month (~ every 15 days). Results of capacity tests over four months of continuous test are presented in Table 4-18 and plotted in Figure 4-46. As in real life vehicle operation, the current profile is continuously changing; it makes more sense to express the battery capacity in terms of the capability in

delivering or storing electric energy (Wh) rather than electric charge (Ahr). Therefore, both capacities are plotted in Figure 4-46. Over the four months the battery pack has gone through 91 equivalent cycles (full discharge followed by a full charge) and lost 6% of its capacity. This is a fairly high amount of degradation which could be due to the inefficiency of the custom-designed BMS resulting in cell balancing or thermal management issues.

**Table 4-18 Capacity measurement, Dec.7, 2011**

| test # | Energy capacity (kwh) | Charge capacity (Ah) | Net processed energy (kwh) | Capacity fade (%) | Equivalent cycle number |
|---|---|---|---|---|---|
| 1 (reference) | 24.31 | 60.19 | 0 | 0 | 0 |
| 2 | 23.98 | 59.69 | 210.62 | 0.83 | 8 |
| 3 | 23.83 | 59.34 | 440.55 | 1.44 | 18 |
| 4 | 23.50 | 58.61 | 640.93 | 2.69 | 26 |
| 5 | 23.26 | 57.83 | 935.89 | 4.04 | 37 |
| 6 | 23.14 | 57.75 | 1275.36 | 4.23 | 51 |
| 7 | 23.05 | 57.54 | 1616.48 | 4.60 | 65 |
| 8 | 23 | 57.03 | 1991.23 | 5.50 | 80 |
| 9 | 22.86 | 56.66 | 2283.54 | 6.20 | 91 |

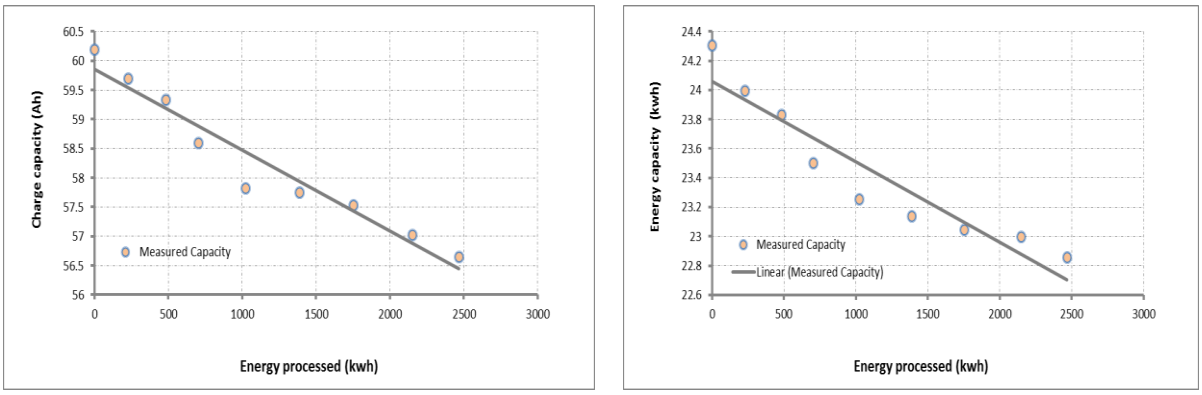


**Figure 4-46 ACX2.5 battery capacity profile during four months test**

As discussed earlier, temperature plays an important role on the battery degradation. It is quite important to verify whether the observed degradation has been due to the extreme temperature conditions. As Figure 4-47 shows, the maximum and minimum temperature of the battery pack

over the four months of testing is mostly in the range of 10°C-35°C which is a modest range and does not impose accelerated degradation. Therefore, the observed degradation could be attributed to normal cycling and a life model could be calibrated accordingly.

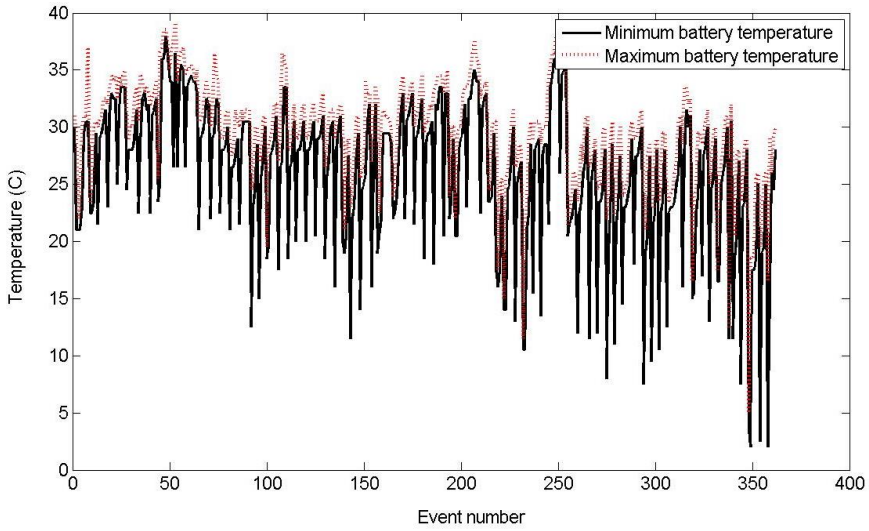


**Figure 4-47 Battery pack maximum and minimum temperature during each event (Over July-October)**

Battery Degradation Modeling and calibration

To model the battery degradation over a drive cycles or charge cycles, a life model is required which is able to capture the effect of different variables such as SOC, C-rate, temperature. The extended Ning's model provides such capabilities and was used for the current studies. Ning's model models the higher currents present in vehicle powertrain applications, and also takes into account the degradation under constant voltage charging operation [114]. Ning's model incorporates porous electrode theory, concentrated solution theory, Ohm's law, intercalation/deintercalation kinetics, and transport in both the solid phase and electrolyte phase [114]:

$$j_{para} = j_{para}^{0} exp\left(\frac{\alpha_c F}{RT}\eta\right) \quad (4\text{-}8)$$

Where, $j_{para}$, is the local parasitic reaction current density. More details about this model can

be found in the paper published by Ning et al. [114]. The model was extended by Stevens [115] to include considerations for DOD and discharge rate, and calibrated using the results of the very high discharge/charge rate (> 4C-rate) tests. The modified model is presented in Table 4-19. There are two tuning parameters in the model, $z_1$ and $z_2$; which account for accelerated degradation due to temperature and SOC.

**Table 4-19 Extended Ning life model [115]**

| |
|---|
| $j_{para} = \propto_{Temp}^{n,ave} \propto_{SOC}^{n,ave} j_{para}^{0} exp\left(\frac{\alpha_c F}{RT}\eta\right)$ |
| $\propto_{Temp}^{n,ave} = 0.01 * \left(\propto_{Temp}^{n}\right)^{z_1} + 0.99 * \propto_{Temp}^{n-1,ave}$<br>$\propto_{SOC}^{n,ave} = 0.01 * (1 + \beta_1 * \propto_{SOC}^{n})^{z_2} + 0.99 * \propto_{SOC}^{n-1,ave}$ |
| $\propto_{Temp}^{n} = exp\left(\frac{-40498}{RT}\left(\frac{1}{T} - \frac{1}{T^o}\right)\right)$<br>$\propto_{SOC}^{n} = exp\left(\frac{-100}{abs(60 - SOC)}\right)$ |

Based on this model, a degradation Simulink block was developed and added to the battery model in PSAT. Also, the voltage and SOC calculations were modified to include the modeled degradation effect (capacity fade affects the SOC, and power fade affects the voltage). Simulations with the original model and the battery profiles showed to be overestimating the capacity fade. One reason is that this model was developed based on very high C-rate tests, which is the case in hybrid vehicles. Using the road tests results and a least square optimization algorithm in Matlab, the tuning parameters were recalibrated to get a better match between the capacity fade curves. Resulting capacity fade curve is shown in Figure 4-48. The model parameters are presented in Table 4-20. The model shows capability in following the general trend of capacity loss. One an extensive road test data, covering a broader range of battery SOH (e.g. 2-3 years of vehicle operation), were available, it would be possible to further evaluate and validate the model.

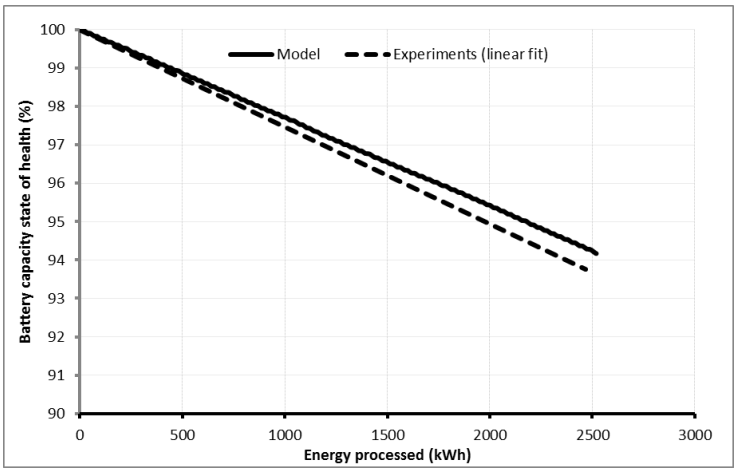


**Figure 4-48 Simulated capacity fade using the calibrated life model**

**Table 4-20 Model parameters calibrated with road test data**

| Parameter | Value |
|---|---|
| $\beta_1$ | 2 |
| $Z_1$ | 0.1 |
| $Z_2$ | 2 |
| $J^o_{para}$ | $8x10^{-9}$ |
| $\alpha_c$ | 0.5 |

## 4.4 Conclusion

In this chapter, results of Li-ion battery field test were presented. A converted Ford Escape powered by Li-ion battery packs was instrumented by a data logger and the powertrain and battery data under driving and charging was collected through the CANBus. A model of the EV powertrain was developed in PSAT and calibrated based on the road test data. The battery OCV and internal resistance were estimated and a simple battery model including a voltage source and charge/discharge resistance was developed accordingly. It was shown that the battery OCV can be estimated with an acceptable accuracy from the driving data. The model was then validated against several drive cycles and profiles of SOC, charge and discharge energy and battery temperature were nicely compared with the experimental data. The reversible heat showed to have a portion of 10% in the total heat during a sample driving event in a summer day. The

collected data from the EV were also used to identify the degradation trend sin the battery. Power fade, capacity fades and charge efficiency were studied through the data as three degradation metrics. A battery life model was also calibrated using the observed capacity degradation over a four-month testing period. Validation of the model will be possible once more data points are available. It was initially intended to develop an empirical life model of the battery. Due to the limited data, the degradation study did not meet its targeted goal. However, sample analysis was presented as a pathway for future studies.

# Chapter 5

# Modeling of Battery Lifetime in Hybrid Vehicle Operation

This chapter presents a study on the Li-ion battery operation in a PHEV through simulations. The objective is to evaluate impacts of climate control load as well as thermal preconditioning of the battery under different drive cycles on the vehicle range and battery life.

The following section is mainly based on the paper titled "Evaluation of Air Conditioning Impact on the Electric Vehicle Range and Li-Ion Battery Life" by "Samadani et.al" published by the Society of automotive Engineer (SAE). This thesis author specific contribution to this paper is to: "conduct the modeling, prepare the graphics and results and the final manuscript. This paper is co-authored by Dr. Fowler and Dr. Fraser as supervisors.

## 5.1 Range Anxiety and Auxiliary loads in PEVs

HEVs have already been introduced into the market as an alternative to conventional vehicles. However, to move away from fossil fuel energy sources, a demand for PHEV systems with all-electric range (AER) is increasing [116]. However, when it comes to making a purchase decision, consumers express concerns; anxiety about the range capability of the EVs (especially in harsh climates) besides initial costs and charging issues lies on the top of the list. The range of an EV or charge depleting range (CD) in a PHEV, is limited by the available capacity of the on-board battery, and directly related to the battery size and restricted by the vehicle weight and cost constraints.

In this regard, climate control loads are known to strongly aggravate the EV range. In a PHEV equipped with electric climate control system, the battery provides the driving power as well as auxiliary loads demands. The vehicle climate control system, i.e. air conditioning (A/C) and

heating, is responsible for providing sufficient thermal loads to quickly regulate a comfortable cabin temperature requested by the vehicle occupants. Such requirement would be more critical in case the vehicle has passed a period of hot or cold thermal soak. A/C is believed to be the main accessory requiring the largest quantity of power from the traction source resulting in a reduced AER and increased dependence on fossil fuel. It is reported that in an EV, A/C may reduce the driving range up to 35%, depending on the AC usage frequency [37]. Associated with the charge-depleting (CD) range reduction, there would be increased battery wear for the same distance driven when AC/heater system is operating, thanks to the higher C-rates imposed on the battery. As a solution, thermal preconditioning of the cabin and battery using off-board power (e.g. grid power) has been introduced to alleviate these impacts [117]. Regulating the battery initial temperature and reducing the higher transient thermal loads, preconditioning also helps the battery operate in its optimum temperature range (~20-35$^{o}$C) and yield best capacity and power performance [95], which would result in an optimized battery life and AER.

In this chapter, EV range capability, and battery performance and life of a PHEV are studied under different climate scenarios and operating conditions. A thermal model of cabin temperature is developed that simulates the interior temperature profile of the cabin. The model incorporates the ambient conditions, solar load, and the vehicle speed and is able to predict the required cooling (heating) load to cool down (warm up) the cabin from an initial state to a desired state. A model of a series PHEV and a parallel PHEV developed in Autonomie are used for the simulations. The thermal model is coupled with the vehicle models to yield the battery SOC at the end of the simulation, resulting AER and battery life degradation.

## 5.2 Cabin Thermal Model

To estimate the extra power required by the AC (heating) system, first the temperature profile of the cabin during a driving event needs to be determined. Therefore, a thermal model of the cabin was developed. The model incorporates the effect of solar radiation on the outer surface of the vehicle body, forced convection between the ambient and the outer body, conduction heat transfer through the body, natural heat transfer between the interior body and the cabin air, heat

transfer between the internal cabin components and the cabin air and also the load added by the passengers. A schematic of the thermal loads acting on the vehicle cabin is illustrated in Figure 5-1. Afterwards, the cooling power required by the compressor is calculated. Finally, the cooling power will be translated to the additional current (load) on the battery using the compressor performance look-up tables.

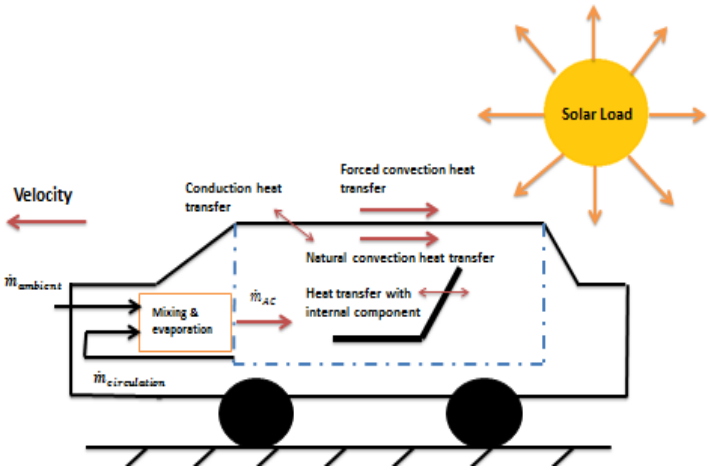


**Figure 5-1 Vehicle cabin and thermal loads acting on the cabin air**

Figure 5-2 illustrates a diagram of a typical vehicle AC system. The compressor is the main components in terms of energy consumption.

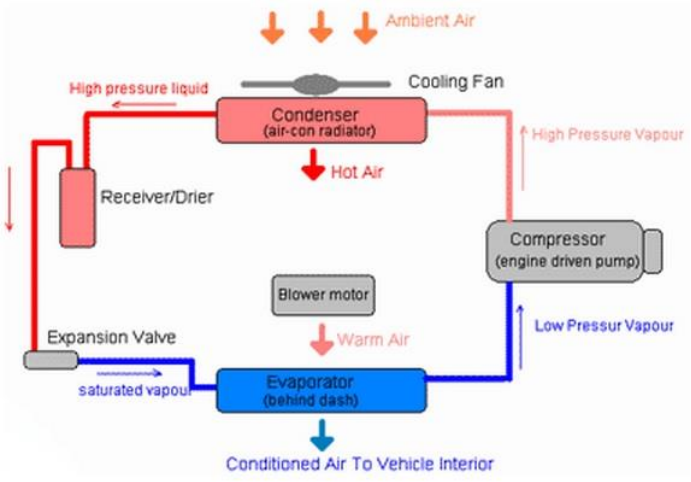


**Figure 5-2 schematic of the AC system [118]**

A variable speed electric compressor with the specifications presented in Table 5-1 and an electric fluid heater [119] installed on the research EV (presented in Chapter 4) are assumed for the simulations.

**Table 5-1 Specifications of the variable speed electric compressor [120]**

| | |
|---|---|
| Compressor type | Brushless DC Variable Speed |
| Refrigerant | R134a |
| Voltage Range | 135-315V DC |
| Evaporator Temperature Range | -23.3°C to 12.8°C |
| Maximum Compression Ratio | 8:1 |

A brief description of the thermal model is presented here. Detailed explanations can be found at [121]. Equation (5-1) summarizes the thermal loads on the cabin internal air:

$$\text{Thermla loads} = \dot{Q}_{\text{natural conv}} + \dot{Q}_{\text{components}} + \dot{Q}_{\text{passenger}} + \alpha\dot{Q}_{\text{solar}} \quad (5\text{-}1)$$

Where, $\dot{Q}_{\text{natural conv}}$ is the natural convection heat transfer between the inner side of the cabin and the cabin air; $\dot{Q}_{\text{components}}$ is the heat transfer between the cabin internal components and the cabin air; $\dot{Q}_{\text{passenger}}$ is the heat transfer between the passengers and the cabin air; $\alpha\dot{Q}_{\text{solar}}$ is the solar load which is absorbed by the cabin air and $\alpha$, is the weighting factor to account for the part of the solar load which is absorbed by the cabin air (the rest absorbed by the cabin internal component). Detailed description of the thermal loads can be obtained from [121, 122]. Considering a steady state for the dry air mass in the cabin;

$$\dot{m}_{\text{AC}} + \dot{m}_{\text{inf}} = \dot{m}_{\text{cir}} \quad (5\text{-}2)$$

Where, $\dot{m}_{\text{AC}}$ is the air mass flow through the evaporator, $\dot{m}_{\text{cir}}$ is the recirculated air mass flow from the cabin to the evaporator and $\dot{m}_{\text{inf}}$ is the infiltration air through the door and windows gaps. Assuming a wind speed of 6 km/h, the cabin air change per hour (ACH) for an ordinary sedan is 1.2 [123] and the value of $\dot{m}_{\text{inf}}$ is calculated accordingly. Also, the water vapor mass changes inside the cabin are calculated from the following equation:

$$\frac{dW_{air}}{dt} = (\dot{m}_{air}W)_{AC} + (\dot{m}_{air}W)_{inf} - (\dot{m}_{air}W)_{cir} + \dot{m}_{vap,\ passenger} \quad (5\text{-}3)$$

Where, W: absolute humidity, (kg water/ kg dry air). $\dot{m}_{vap,\ passenger}$: Vapor added from the passengers exhale. According to the Equation (5-3), cabin vapor mass changes as a result of the humidity addition by the air flowing through the AC blower, infiltration air flow, passengers exhale and the vapor leaving the cabin through the recirculated air (from the cabin to the AC cycle). The instantaneous cabin temperature is estimated based on the cabin air enthalpy, which is calculated from the energy balance:

$$\frac{dH_{air}}{dt} = \frac{\text{thermal loads} + (\dot{m}H)_{AC} + (\dot{m}H)_{inf} - (\dot{m}H)_{cir}}{m_{air}} \quad (5\text{-}4)$$

Where: $H_{air}$: Enthalpy of moist air. $(\dot{m}H)_{AC:}$ Enthalpy flow through the evaporator to the cabin

$(\dot{m}H)_{inf}$: Enthalpy flow from the ambient to the cabin through the unsealed doors & windows

$(\dot{m}H)_{cir}$: Enthalpy flow from the cabin to the AC cycle through recirculation

And finally the cabin air temperature is calculated based on the moist air enthalpy & temperature relation:

$$T_{air} = \frac{H_{air} - 2501W_{air}}{1.006 + 1.805W_{air}} \quad (5\text{-}5)$$

Several parameters are required to be set before running the thermal model, such as the dimensions and thermodynamic properties of the vehicle cabin (as well as the windows and doors), weather conditions (solar load, humidity and temperature) and the AC running mode (i.e. circulation coefficient). For the current analysis, those parameters that are not easily measurable from the vehicle are borrowed from the literature for a regular sedan. The cabin dimensions and thermodynamic properties used for the simulations are also presented in Table 5-2.

**Table 5-2 Baseline vehicle dimensions and thermodynamic properties assumed for simulation**

| | |
|---|---|
| Cabin | 3 ($m^3$) |
| Wind shield | 1.2x0.6x0.01 ($m^3$)<br>Thermal conductivity: 1.4 ($\frac{W}{mK}$) |
| Rear shield | 1 x0.6x0.01 ($m^3$)<br>Thermal conductivity: 1.4 ($\frac{W}{mK}$) |
| Side wind | 0.4x0.4x0.01 ($m^3$)<br>Thermal conductivity: 1.4 ($\frac{W}{mK}$) |
| Cabin internal component | Equivalent area: 7 ($m^2$)<br>Equivalent mass: 210 kg<br>Convective heat transfer coefficient: 100 ($\frac{W}{m^2K}$)<br>Specific heat capacity: 1.67 ($\frac{kJ}{kgK}$) |

A fuzzy controller, shown in Figure 5-3 is also designed to control the AC (blower) air mass flow rate to the cabin based on the instantaneous cabin temperature difference with the set point. Due to the lack of field test data on the AC system components and to simplify the calculations, it was assumed that the AC system is running under steady state condition and the air temperature at the evaporator exit is 5 ℃ . However, once such data is available, a model of the AC could be developed to account for the transient loads. For the heating scenarios, a temperature of 22 ℃ is assumed at the inlet vent.

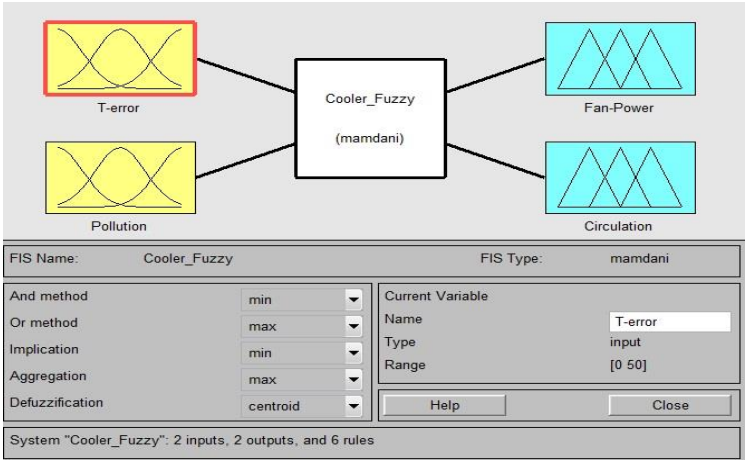


**Figure 5-3 Fuzzy controller to determine the blower mass flow rate**

## 5.3 Climate Scenarios

Three climate scenarios are assumed; each incorporating an ambient temperature condition and initial battery pack temperature (Table 5-3). Scenario1 represents the average ambient conditions in Toronto, Canada during June month with an average temperature of 25 (℃). Scenario 2 represents a summer day in Arizona, the hottest area in the US. In scenario 3, a winter day of Toronto in February month with an average ambient temperature of −8 (℃) is assumed. Although ambient conditions have daily and annual variations, the present work neglects temperature variation due to variable ambient conditions.

**Table 5-3 Scenarios considered for simulating the temperature profile of vehicle cabin**

| Scenario | 1-June, Toronto, | 2-July, Arizona | February, Toronto |
|---|---|---|---|
| Number of passengers | 2 | 2 | 2 |
| Solar irradiation | 0.6 $(\frac{\text{kW}}{\text{m}^2})$ | 1.1 $(\frac{\text{kW}}{\text{m}^2})$ | 0.2 $(\frac{\text{kW}}{\text{m}^2})$ |
| Ambient temperature | 23 (℃) | 35 (℃) | −5 (℃) |
| Ambient Relative humidity | 80 (%) | 35 (%) | 80(%) |
| Initial battery temperature | 23 (℃) | 35 (°C) | −5 (℃) |
| | | 25 (°C) (Preconditioning) | 5(℃) (Preconditioning) |
| Initial cabin air temperature | 42 (℃) | 55 (℃) | −5 (℃) |
| Initial cabin components temperature | 47 (℃) | 60 (℃) | −5 (℃) |
| Initial cabin air humidity | 60 (%) | 30 (%) | 60(%) |
| Drive cycle | Test drive cycle | | |

## 5.4 Results- Thermal model and A/C impacts

For the purpose of demonstration, the corresponding cabin temperature profile for scenario 1 and scenario 2 is plotted in Figure 5-4. The fuzzy controller determines the blower air flow rate based on the difference observed between the cabin air temperature and the desire point. Therefore, in the beginning of the simulation, the blower is set on maximum flow rate and the cabin temperature experiences a sudden decrease in the first 100 second and converges to a

steady state afterwards. Figure 5-5 illustrates the profile of cabin air absolute humidity during this simulation. As expected, decreasing the cabin air temperature results in a decrease in humidity content of the air until a certain value is reached. Scenario 3 is used for degradation studies in the next sections.

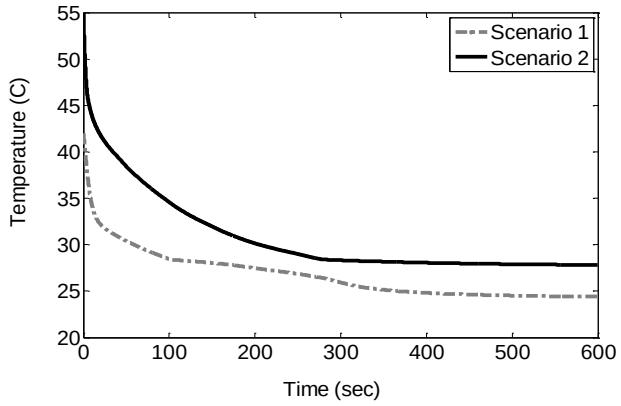


**Figure 5-4. Cabin temperature profile- Test derive cycle**

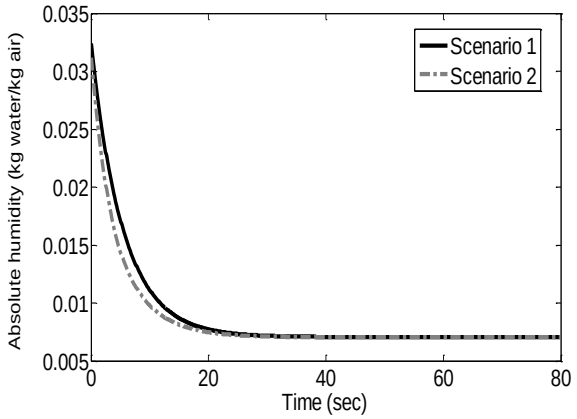


**Figure 5-5. Profile of cabin absolute humidity under test drive cycle**

Profile of the blower flow rate and the compressor current are plotted in Figure 5-6.Assuming an ideal evaporator, the enthalpy change of air passing through the evaporator is equal to the enthalpy change of the refrigerant and is assumed as the required cooling capacity (watt) from the compressor. This cooling capacity is then translated into the required current by the compressor. This is actually the extra load on the battery, which is shown in Figure 5-7.

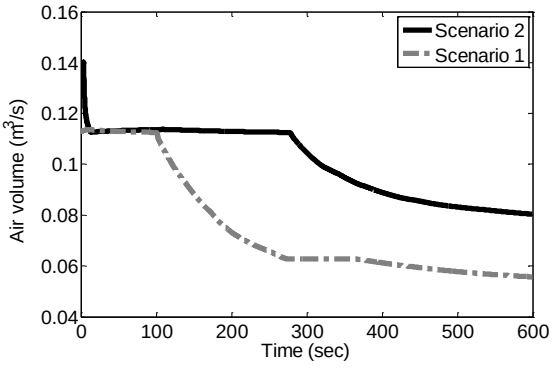


**Figure 5-6. Profile of air flow through the blower**

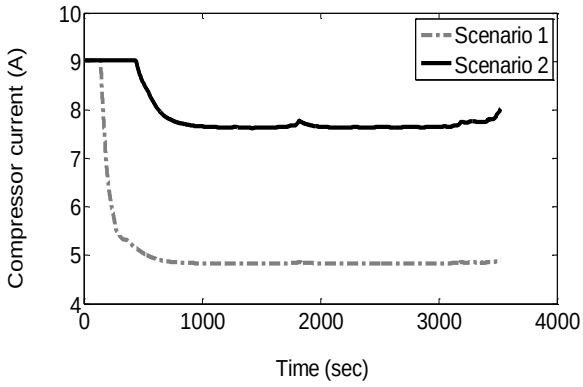


**Figure 5-7. Profile of compressor current under test**

**drive cycle**

## 5.5 Vehicle Simulations

For the current study, vehicle models initially developed by UWAFT [96] in Autonomie are used. The models include an E85 series extended range EV (EREV) as the baseline, and a pre-transmission parallel architecture. Both models are conversions of Malibu 2013. These architectures are illustrated in Figure 5-8 and Figure 5-9. Model inputs and the main powertrain components (which are assumed similar in all configurations) are described in Table 5-4. Each of these configurations creates a unique environment for the battery by allowing a different SOC range and power demand on the battery. Unlike the NiMH batteries of the current CS hybrids, which are operated over a small window (around 50% SOC), the batteries used in PHEVs operate over a large SOC window. Starting from a certain high SOC (e.g. 90%), the vehicle operates in a charge-depleting (CD) or an EV mode until a low SOC is reached. The battery manufacturer sets the lower SOC operation limit for the battery based on life considerations. For the PHEV cases SOC window of 90%-30% is assumed which is equivalent to a 40 mile AER. Each configuration contains a battery model consisting of the equivalent circuit model and the thermal ramp rate model presented earlier in Chapter 3. The battery pack is modeled by a linear scale up of a cell neglecting the effect of cell to cell variation and unbalancing.

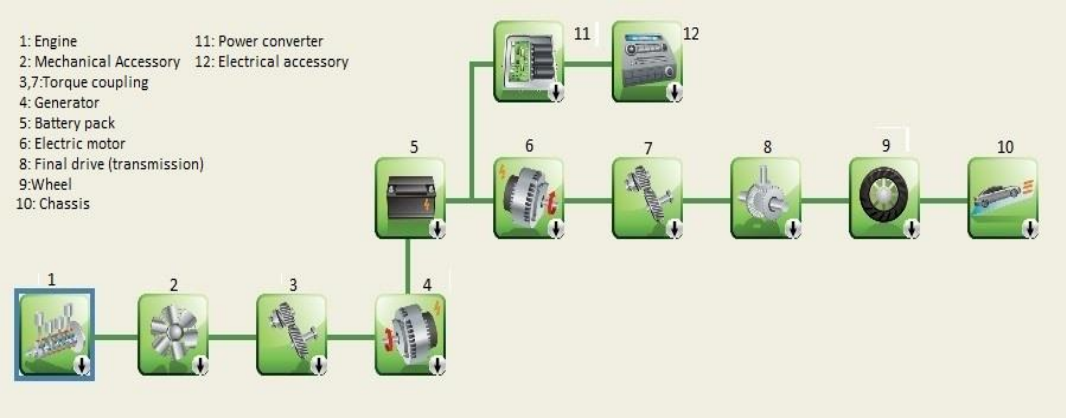


**Figure 5-8 Graphical presentation of the EREV series architecture**

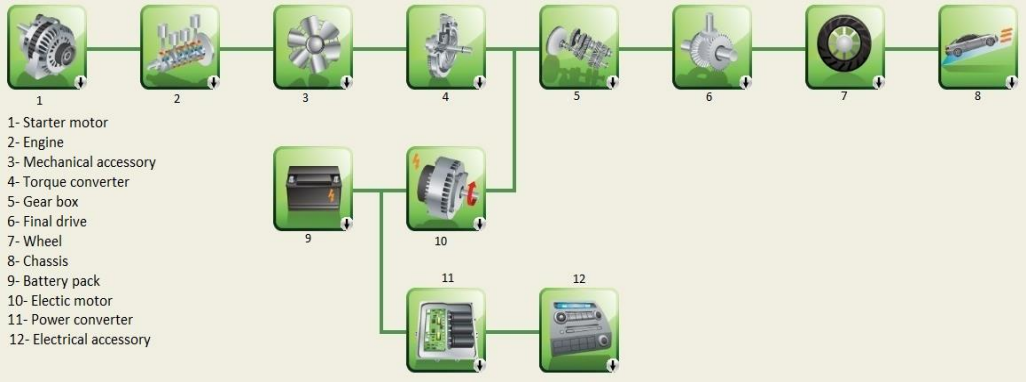


**Figure 5-9 Graphical presentation of the pre-transmission parallel architecture**

**Table 5-4 Component specifications and model inputs used in the Autonomie model of EREV [96]**

| **Component** | **Option** |
|---|---|
| Engine | GM LE9 Engine (E85)<br>2.4L E85 engine provided by GM. |
| Generator | TM4 Motive (105kW) |
| ESS (Battery) | A123 Battery Pack, (19.7kWh @ 346V) |
| Electric motor | TM4 Motive (206kW) |
| Final drive | Borg Warner eGearDrive |
| Chassis | 2013 Malibu |
| Power convertor | New Eagle DCDC Converter |
| Electrical accessory | The average power draw from accessories was assumed to be 1500W |
| Frontal area | 2.06 ($m^2$) |
| Vehicle mass | 2003.7 (kg) |
| Battery SOC window | 90%-30% |
| Battery thermal management | Natural air cooling |
| Drag coefficient, Cd | 0.25 |

### 5.5.1 CD range and Fuel consumption

CD range and fuel consumption of each configuration were simulated considering the effect of climate control loads and battery thermal preconditioning. Results show that the climate control loads has a relatively large impact on CD range reduction; on the other hand, battery thermal preconditioning plays a significant role on minimizing on range reduction due to the

climate control loads. The EV operation (CD mode) also represents the maximum battery usage and is a good indicator of the maximum temperature rise that the battery would undergo during vehicle operation.

Figure 5-10 and Figure 5-11 represent the CD range and battery temperature rise as a function of minimum SOC in the baseline model (Series PHEV) (operating under UDDS drive cycle) assuming no additional loads or preconditioning. The initial module temperature is set at five levels (-5°C to 35°C). It is observed that the EV range and final module temperature have a semi-linear correlation with ΔSOC.

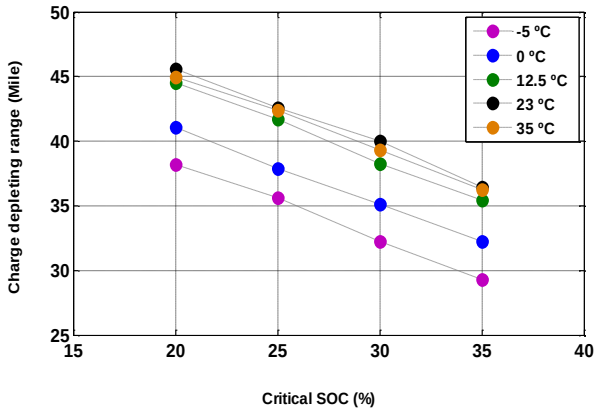


**Figure 5-10 AER results for different minimum SOC**

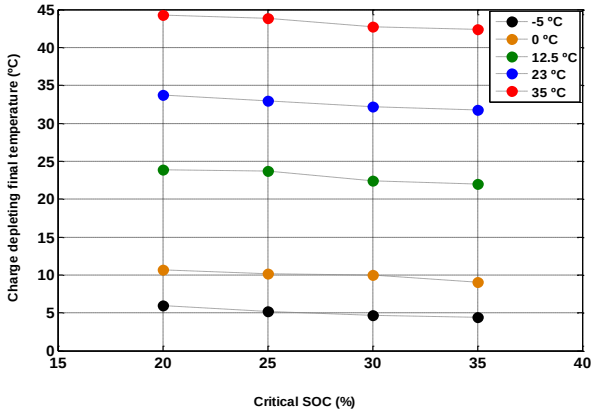


**Figure 5-11 Battery temperature at the end of AER**

Figure 5-12 through Figure 5-15 presents the effect of climate control loads and preconditioning on CD range and fuel economy. For fuel economy calculations, a utility factor (UF) of 0.75 was assumed and the fuel consumption was calculated based on Equations (2-3) through (2-5). Also, a 30% critical SOC was assumed.

In the series PHEV, fuel consumption is increased due to heating loads by 39% and the CD range is reduced by 20%. Also, applying A/C reduces the fuel economy by 65% and the CD range by 12%. Thermal preconditioning improves the situation by reducing the initial climate control system load. In case of heating, thermal preconditioning improves the fuel economy by 6% and the CD range by 11%; where, in case of A/C, the corresponding values are 1.5 % and 2%.

In case of parallel PHEV, using heat increases fuel consumption by 25% and decreases the CD range by 19%. Using A/C increases fuel consumption by 40% and decreases the CD range by 18%. Compared to no thermal preconditioning, thermal preconditioning with heat decreases fuel consumption by 4% and increases the CD range by 9%. and thermal preconditioning with A/C decreases fuel consumption by 3% and increases the CD range by 7%.

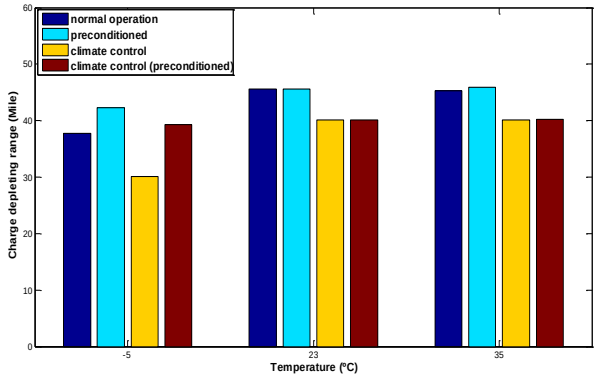


**Figure 5-12 Series PHEV (EREV) CD range assumming 30% critical SOC**

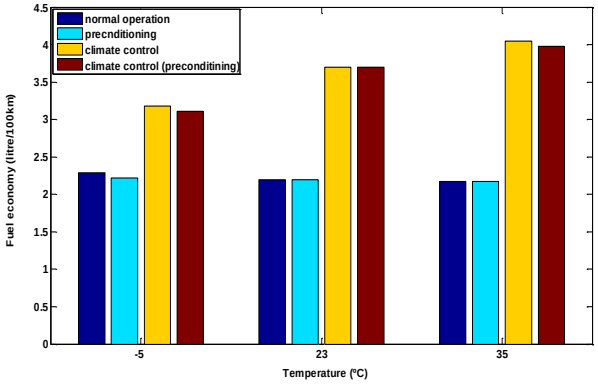


**Figure 5-13 Series PHEV (EREV) fuel consumption assumming 30% critical SOC**

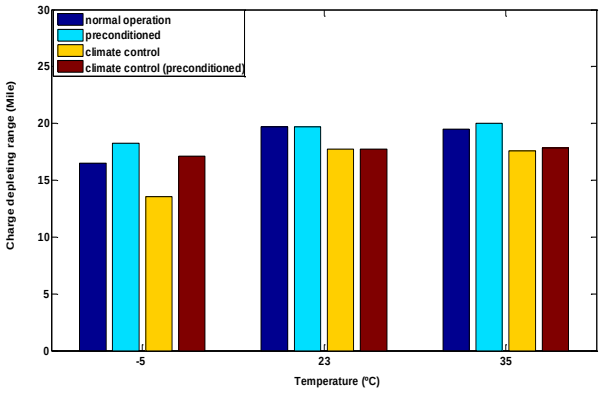


**Figure 5-14 Parallel PHEV CD range assumming 30% critical SOC**

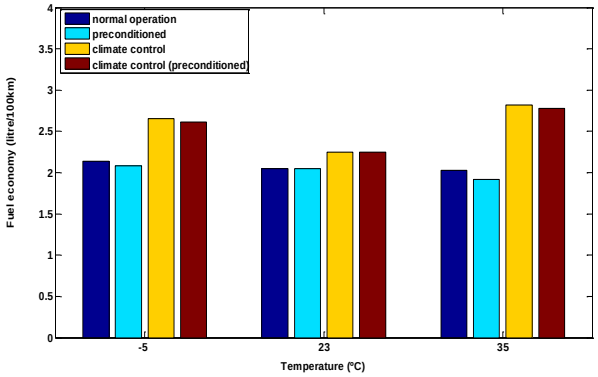


**Figure 5-15 Parallel PHEV fuel consumption assumming 30% critical SOC**

## 5.5.2 Degradation simulation

In this section, battery capacity fade is simulated under several operating conditions. The common definition for battery end-of-life (EOL) is when battery remaining capacity has reached

70% to 80% of beginning-of-life capacity. As an example, a 5% capacity loss per year results in 80% remaining capacity after 4 years. For the current analysis, a daily duty cycle is assumed as shown in Figure 5-16 that includes a morning trip starting at 8:00 AM with a distance of 30 km followed by a rest period till 4:30 PM and same driving back to the garage and finally a charge cycle and rest up to the next day. For scenarios with thermal preconditioning, the battery is assumed to be warmed up or cooled down over a 25-minute period. The test drive cycle used for current analysis consists of a city and highway driving and is illustrated in Figure 5-17.

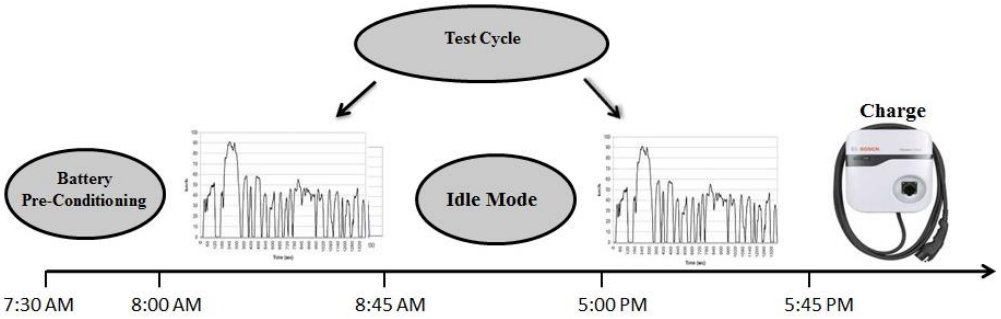


**Figure 5-16 Vehicle daily duty cycle assumed for simulations**

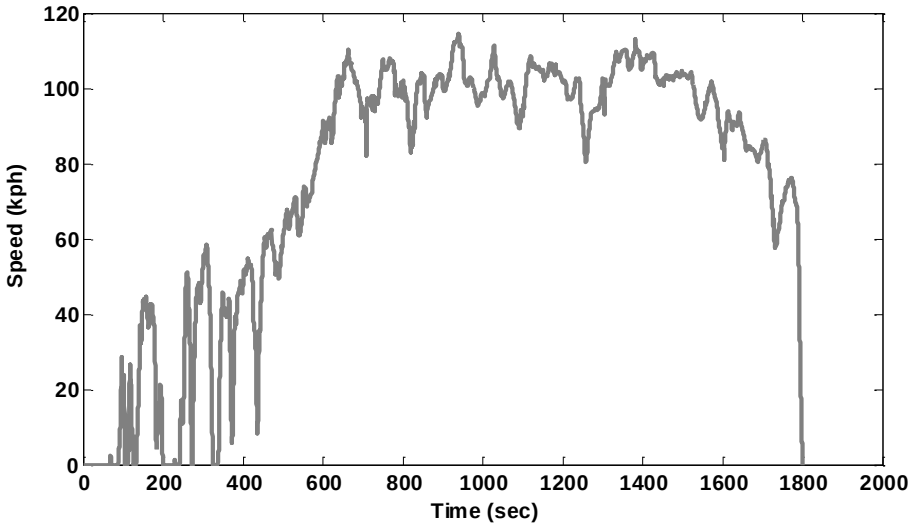


**Figure 5-17 The test drive cycle collected from the converted EV road tests**

Charging is assumed to happen at nights and between the two trips with a level two charging with 30A current and 240V voltage and the battery is fully charged at the beginning of each trip. The degradation model presented in Chapter 4 is used to simulate the decrease in the ability of

the battery to hold charge. Impact of climate control loads and preconditioning is incorporated in the simulations. When the battery is preconditioned, it is exposed to a different temperature range; therefore, the degradation rates will be different compared to a non-preconditioned case. Also, in case of preconditioning, due to the temperature dependent available capacity, the battery will experience a different depth of discharge (DOD) each day, which results in a different degradation rate. Battery temperature rise results from multiple factors, namely battery thermal mass, heat generation rate while driving, and rate of active cooling. A general comment on preconditioning could be as follows: Battery packs with small battery thermal mass, high heat generation rates, and limited or no active cooling while driving, likely to experience a large temperature rise while driving and benefit most from pre-cooling will be those. In Figure 5-18 , the yearly percent of capacity loss for the series PHEV is presented at various ambient temperatures, with and without climate control loads and preconditioning. Following observation could be made:

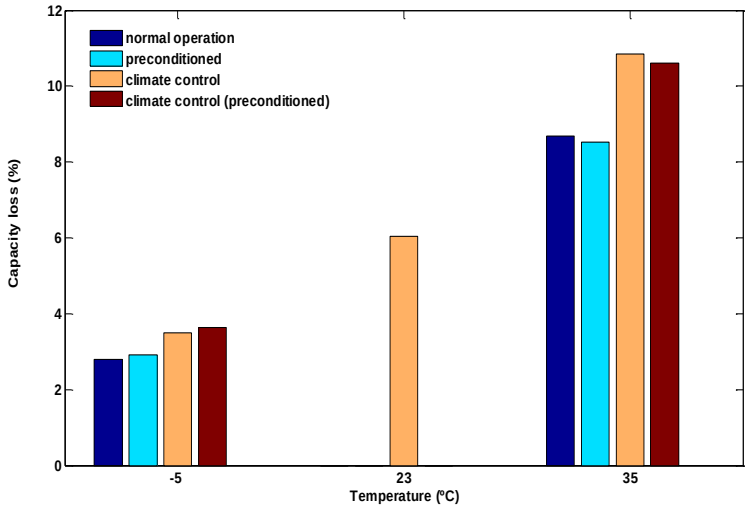


**Figure 5-18 Annual battery capacity loss rate in the series PHEV**

- The −5°C ambient case reduces fade by 53% relative to 23°C ambient. Thermal pre-heating at -5°C ambient increases battery capacity loss by almost 5%. However at such low temperatures, the small fade rates are relatively insignificant.

- The 35°C ambient case with no preconditioning increases capacity fade rates by 43% (relative to 23°C ambient).
- At hot ambient conditions (35°C), the most benefit from thermal pre-cooling is obtained; which the capacity-fade rate is decreased by ~2%.
- Heating and cooling load show a significant impact on the battery health. At −5°C, heating load result in ~25% increased degradation and at 35°C, ~22% capacity loss rate is accelerated.

Figure 5-19 shows battery degradation rates for the parallel PHEV. Generally, similar trends are observed. At 35°C ambient, thermal preconditioning reduces capacity-loss rate by 3% and the A/C loads adds a 17% on the capacity loss rate while heating results in a ~25% extra capacity loss rate. The two vehicle platforms each derive slightly different benefits from pre-cooling, partly due to the size of each vehicle's battery and partly due to the control strategies each layout employs.

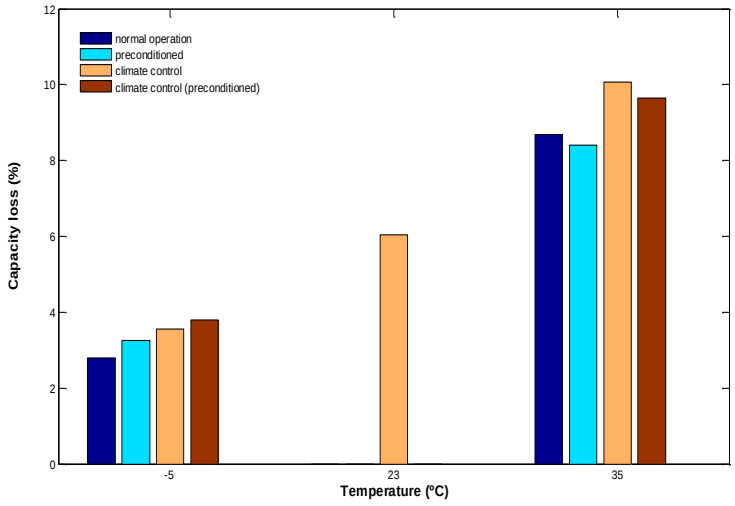


**Figure 5-19 Battery capacity loss rate in the Parallel PHEV**

## 5.6 Conclusions

In this chapter, impact of AC and heating loads on the Li-ion battery performance and

degradation and vehicle electric range and fuel consumption was studied. A Thermal model of the vehicle cabin was developed to predict the cabin temperature profile and required cooling/ heating load according to the set point. A model of Li-ion battery consisting of an equivalent circuit and a regressive thermal model presented in Chapter 3 was coupled with the cabin thermal model. The integrated model enables predicting the additional required power by the A/C or heating system from the battery. It was observed that climate control loads significantly increase fuel consumption and decrease CD range in PHEVs. To reduce these negative impacts, off-board powered thermal preconditioning of the battery and vehicle cabin was shown to be an efficient way.

# Chapter 6

# Conclusions and Recommendations

## 6.1 Conclusions and Contributions

In this thesis, Li-ion battery performance was studied through lab tests and in-situ vehicle field measurements. Experiments included EIS tests and cycling tests at cell level and also in-situ measurements from a converted electric vehicle (EV). Following conclusions could be made:

### 6.1.1 Thermal studies

Two commercially available battery cells were tested under a comprehensive set of charge and discharge cycling tests and different ambient temperatures (-10$^{o}$C to 35$^{o}$C). The battery cells were put in a jig to simulate battery pack condition in a vehicle. The energy efficiency and columbic efficiency of the cells were determined for each testing condition. Results agreed with the belief that the Li-ion cells have a better performance at higher temperatures. The temperature distribution of the cells was also found to be approximately uniform across the cell thickness. Heat generation of the cells was calculated assuming a natural convection mechanism for heat rejection to the ambient air. A thermal ramp rate model was then developed for each cell and operating mode using linear regression method. The model is able to predict the heat generation rate and the cell temperature rise according to the cell SOC, load (current) profile and ambient temperature. The model can be easily integrated with the battery model in Autonomie and is very useful in powertrain design and drive cycle simulations, as it eliminates the need for a detailed fundamental model with high computing cost.

### 6.1.2 EIS Tests and Modeling

A major objective in this research was to develop a battery performance model that could be used for real-time applications, such as vehicle on-board BMS. For this purpose, the battery cells were studied under a set of electrochemical impedance spectroscopy (EIS) tests. The cells' response was measured over a frequency range of 10 μHz to 1 MHz at different temperatures and SOCs. Based on the observed phenomenon from the frequency plots, an equivalent circuit model was proposed and developed for both cells. The proposed model offers an improvement of up to 6% in terms of average and maximum error in voltage predictions; which is still significant for EV applications in terms of extending the allowable battery discharge window and the vehicle range. In addition, the model capability in predicting HPPC test charge and discharge resistances was verified. It was observed that this model could be used as an alternative to the HPPC test within 20% error. The model shows the best performance at high temperatures which could be due to experimental errors at lower temperatures as a result of cell self-heating. This model is fast and easy to implement and is useful for hybrid powertrain design.

### 6.1.3 Field tests

Field tests were conducted with an electrified Ford Escape 2009 (EV-ACX2.5), belonging to Burlington Hydro Company. The objectives of the field testing included three phases as follows.

#### Energy analysis

A study was conducted on the feasibility and advantages of replacing the conventional (gasoline) fleet vehicles with the converted research EV. For this purpose, a data management system was programmed and installed to collect and analyze operation data of baseline fleet vehicles and EV-ACX2.5. Data of interest included charging and discharging events of EV-ACX2.5 and drive cycles of the fleet vehicles. Each vehicle was instrumented with a data logger that recorded and transmitted the data to a server. Having analyzed the data, detailed monthly reports were generated for EV-ACX2.5 over a five-month period, which enabled tracking of the vehicle's total distance travelled, energy consumption, efficiency, and charging times. The main

results are summarized as follows:

- Over five months of operation (October 2011-February 2012), the EV-ACX2.5 travelled 792.6 kilometers and used 222.6 kWh of grid electricity during charging, which yielded an average energy efficiency of 281 Wh/km.
- In comparison with fleet vehicles, it was found that the EV-ACX2.5 is more than 50% cheaper to operate in terms of energy economy (km/$).

### Powertrain Modeling and Fleet Analysis

The collected data were used to develop a powertrain model for the EV-ACX2.5 using PSAT software. The model was then validated using real-life drive cycles collected during the vehicle operation. Powertrain efficiency was also calculated through this model. It was observed that the EV-ACX2.5 was operating with 77% energy efficiency on average, which confirms the superiority of EVs to the conventional vehicles. The performance of the EV-ACX2.5 was also evaluated as a fleet vehicle. This task was performed by running the EV-ACX2.5 PSAT model under the HEVs' drive cycles to find out the EV-ACX2.5 energy requirement for the same trips. Results showed the EV-ACX2.5 can save almost 60% energy compared to the fleet vehicle.

### Degradation studies

The collected data from the EV were also used to identify the degradation trends in the battery pack. Power fade, capacity fade and charge efficiency fade were identified through the data as three degradation metrics. A battery life model was also calibrated using the observed capacity degradation over a four-month testing period. Validation of the model will be possible once more data points are available. It was initially intended to develop an empirical life model of the battery. Due to the limited data, the degradation study did not meet its targeted goal. However, the analysis presented could be used as a pathway for future studies.

### 6.1.4 Vehicle lifetime studies

Chapter 5 described a battery life analysis under a different scenario, which included climate control loads and battery preconditioning. Two PHEV powertrain architectures, including a series and a parallel design, were developed in Autonomie. Assuming a similar battery pack for both layouts, it was found that climate control system loads have a considerable impact on fuel consumption (up to a 65% increase) and charge depletion (CD) range (up to a 20% decrease) in PEVs. Off-board powered thermal preconditioning of a vehicle cabin and battery pack is an effective way to reduce the negative impact of climate control system loads. It was observed that thermal preconditioning can provide a moderate reduction in fuel consumption (up to 6%) and partially restores CD range (up to 11%) which translates to several kilometers of CD range. Also, in hot (35°C) ambient conditions, a pre-cooling of electric-drive vehicle batteries was observed to reduce capacity fade by 3% and climate control loads accelerated the capacity fade by 22% to 25%. All in all, off-board powered thermal preconditioning benefits both the consumer (via CD range extension) and vehicle manufacturers (via improved battery life and reduced warranty services).

Overall, this thesis contribution was to address the performance of the Li-ion battery in electrified vehicles and the direct and indirect impact of temperature on the battery performance and degradation. Fast and accurate models of battery performance and heat generation were developed for use in powertrain design and a degradation study through field tests was attempted. The indirect impact of temperature, i.e. climate control loads and preconditioning impacts, on the vehicle range and battery life, was modeled through coupling these models with a thermal model of a vehicle cabin.

## 6.2 Recommendations

The presented study provides a framework for model based design of PHEVs focusing on Li-ion battery. There are a number of potential extensions and recommendations that could be considered for future research:

### 6.2.1 Thermal testing

In the current analysis, the convective heat transfer coefficient was assumed to be at its natural convection value. However, the chamber fan turns on and off to control the chamber, which results in a varying convective heat transfer coefficient during cycling. Therefore, it would be beneficial to use a calorimeter to measure the cell heat transfer coefficient with a higher accuracy at different states (natural and forced convection).

The regression models are limited to the parameters' range in the tests. In the thermal characterization tests, C-rates were chosen to vary from 0.5 to 4.5 in discharge. In a real case of battery operation on a PHEV, C-rate could vary from values very close to zero up to 5. Therefore, it would be desirable to add more testing points to further widen the range as well as increase the homogeneity of the test domain.

The analysis and validation were based on cell level. However, single cell characteristics may not be linearly scaled to a module or pack level system. For example, the resistance observed from a single cell would include contact resistance where the cell tabs are bolted to the test cables. In a production battery pack, the tabs would be welded to a bus bar, thereby changing the resistance characteristics. Evaluating the internal resistance of a full battery pack would improve the fidelity of the model and yield more accurate vehicle simulation results. Therefore, pack level testing should be planned and carried out in future research.

It would be also desirable to repeat the thermal tests with different boundary conditions; i.e. a water cooling case versus forced air cooling and no cooling to enable the analysis of different battery thermal management strategies.

### 6.2.2 EIS testing

In the presented analysis, the regression models developed for each of the equivalent circuit model parameters are based on a limited number of test points, which would affect the regression capability in predicting the points that are far from the test points. Considering that the Li-ion

battery has a highly nonlinear dynamic, it is recommended that the EIS tests be repeated at more SOCs (especially between 30%-60%). In addition, as the battery ages, its electrochemical impedance spectra undergoes a shifts to the right and expansion resulting in the circuit parameters (resistance and capacitor values) to change [30]. Therefore, it would be necessary to consider the aging in the model development to reflect a more realistic perspective of the battery behavior in vehicle simulations.

The proposed model was based on the data of three positive temperatures (12.5ºC, 23.75ºC and 35ºC). Due to the limited availability of the EIS machine at the time of this research and uncertainty in the collected data, the low temperatures (1.25ºC and -10ºC) were ignored in the model development. It would be reasonable to repeat the tests at these temperatures to incorporate the low temperature battery response in the model development.

### 6.2.3 Field testing

While field testing provides a valuable opportunity to analyze the battery pack behavior under real-life operation, it is highly associated with uncertainty. There are several uncontrolled parameters while the vehicle is in operation or even in idle mode. In such situations, relying on a single vehicle for developing a battery life model adds more limitations to the analysis. Therefore, if circumstances permit, it is recommended to get a number of electrified vehicles instrumented and data logged. Additionally, as the battery aging happens over a 5-10 year period (battery manufacturer set point) and considering the nonlinear nature of battery degradation, data logging should be conducted over a wide time span so that the battery experiences different stages of aging. This way, model development and calibration tasks could be carried out with a higher accuracy. To improve the fleet study, the following studies are suggested:

- Develop a validated model of a baseline fleet vehicle in PSAT (once the powertrain data through CAN Bus is accessible).
- Comparison between the EV-ACX2.5 and the fleet vehicle, in terms of emissions and energy consumption over standard and real-life drive cycles.

Suggested improvements to the EV PSAT model are:

- For vehicle level simulations, temperature-dependent models for other major powertrain components, such as electric motors, should be created to more accurately model how total vehicle efficiency changes with temperature. Accurate representation of the entire vehicle is required to accurately predict vehicle range, performance, and overall energy consumption. As the vehicle model matures, it will also serve as a platform for developing vehicle control systems, torque splitting strategies and other optimization algorithms.

### 6.2.4 Battery lifetime modeling

In the presented study of auxiliary loads' impact on the battery, lack of experimental data made the author make some simplifying assumptions. Among these assumptions, the evaporator exit temperature was assumed a constant conveying steady state operation. However, to better quantify the loads imposed by the climate control system, a model of A/C system and heating system would be necessary, provided that technical data is available. In addition, validation of the climate control model requires a wind tunnel and an instrumented vehicle would be necessary for measuring the cabin temperature profile under different ambient conditions.

It is suggested that the battery degradation be analyzed under different control strategies. There is always a trade-off between the fuel replacement and battery degradation; i.e. high battery discharge results in better fuel economy but accelerates the battery capacity loss. There is different control strategies proposed for PHEVs, so far. Among these strategies, thermostat control, load-following control and cost based on control are three popular methods, which each provide a unique environment and load profile for the battery [39].

# References


[1] M. Ehsani, Y. Gao, A. Emadi, Modern Electric, Hybrid Electric, and Fuel Cell Vehicles: Fundamentals, Theory, and Design, second ed., CRC Press, 2009.

[2] D. Howell, Annual Progress Report for Energy Storage R&D, Vehicle Technologies Program, Energy Efficiency and Renewable Energy, Washington, DC, 2011.

[3] S. Dhameja, Electric Vehicle Battery Systems, Butterworth-Heinemann, 2002.

[4] G. Duleep, H.V. Essen, B. Kampman, M. Grünig, Impacts of Electric Vehicles - Deliverable 2 Assessment of Electric Vehicle and Battery Technology, CE Delft, 2011.

[5] Pollution Probe, Driving Electric: Understanding Electric Vehicle Technology and Environmental Benefits, 2015.

[6] W. Liu, Introduction to Hybrid Vehicle System Modeling and Control, John Wiley & Sons Inc., 2013.

[7] A.W. Stienecker, An Ultracacitor-Battery Energy Storage System for Hybrid Electric Vehicles, Electrical engineering, University of Toledo, 2005.

[8] D. Stotingco, A Simulation-Based Assessment of Plug-in Hybrid Electric Vehicle Architectures, Mechanical engineering, Massachusetts Institute of Technology, 2010, pp. 85.

[9] F.R. Kalhammer, B.M. Kopf, D.H. Swan, V.P. Roan, M.P. Walsh, Status and Prospects for Zero Emissions Vehicle Technology, Report of the ARB Independent Expert Panel, 2007.

[10] D. Kodjak, Consumer Acceptance of Electric Vehicles in the US, Mobile Source Technical Review Subcommittee International Council of Clean Transportation (ICCT), EPA, Washington DC, 2012.

[11] Accenture, Final Report:Plug-in Electric Vehicles Changing Perceptions, Hedging Bets, 2011.

[12] B. Pattipati, C. Sankavaram, System Identification and Estimation Framework for Pivotal Automotive Battery Management System Characteristics, IEEE Transaction on Vehicular Technology, 4 (2011) 869-884.

[13] Y. Xing, Ma, E., Tsui, K. L. , Pecht, M., Battery Management Systems in Electric and Hybrid Vehicles, Energies, 4 (2011) 1840-1857.

[14] M. Doyle, T.F. Fuller, J. Newman, Modeling of Galvanostatic Charge and Discharge of the Lithium/Polymer/Insertion Cell, J. Electrochemical Society, 140 (1993) 1526–1533.

[15] X. Hu, S. Li, H. Peng, A Comparative Study of Equivalent Circuit Models for Li-ion Batteries, J. Power Sources, 198 (2012) 359-367.

[16] B. Martin, A Dynamic Battery Model Considering the Effects of the Temperature and Capacity Fading, Elektrotechnika, (2012).

[17] H. Zhang, Chow, M-Y. , Comprehensive Dynamic Battery Modeling for PHEV Applications, Power and Energy Society General Meeting, 2010, pp. 1-6.

[18] J. Zhang, C. Song, H. Sharif, M. Alahmad, An Enhanced Circuit-Based Model for Single-Cell Battery, Applied Power Electronics Conference and Exposition (APEC), 25th Annual IEEEPalm Springs, CA, 2010, pp. 672 - 675.

[19] S.S. Zhang, Xu, K., Jow, T.R., Electrochemical Impedance Study on the Low Temperature of Li-ion Batteries, Electrochim. Acta, 49, no. 7 (2004) 1057-1061.

[20] F. Baronti, G. Fantechi, E. Leonardi, R. Roncella, Enhanced Model for Lithium-Polymer Cells Including Temperature Effects, 36th Annual Conference on IEEE Industrial Electronics Society, IEEE, Glendale, AZ, 2010, pp. 2329 - 2333.

[21] Y. Hu, S. Yurkovich, Y. Guezennec, B.J. Yurkovich, Electro-Thermal Battery Model Identification for Automotive Applications, J. Power Sources, 196 (2011) 449-457.

[22] W. Waag, Kabitz, S.,Sauer, D. U., Experimental Investigation of the Lithium-ion Battery Impedance Characteristic at Various Conditions and Aging States and its Influence on the Application, Applied Energy, 102 (2013) 885-897.

[23] C.H. Chen, J. Liu, K. Amine, Symmetric Cell Approach and Impedance Spectroscopy of High Power Lithium-ion Batteries,, J. Power Sources, 96 (2001) 321-328.

[24] R.E. Williford, Viswanathan, V. V., Zhang, J., Effects of Entropy Changes in Anodes and Cathodes on the Thermal Behavior of Lithium-ion Batteries, Journal of Power Sources, 189 (2009).

[25] k. Parsons, Design and Simulation of Passive Thermal Management System for Lithium-ion Battery Packs on an Unmanned Ground Vehicle, Mechanical Engineering, California Polytechnic State University, 2012.

[26] S. Al Hallaj, H. Maleki, J.S. Hong, J.R. Selman, Thermal Modeling and Design Considerations of lithium-ion Batteries, J. Power Sources, 83 (1999) 1–8.

[27] W.B. Gu, C.Y. Wang, Thermal and Electrochemical Coupled Modeling of a Lithium-Ion Cell, J. Electrochemical Society, 99 (2000) 748 - 762.

[28] P. Taheri, M. Bahrami, Temperature Rise in Prismatic Polymer Lithium-Ion Batteries:An Analytic Approach, SAE International, , SAE, 2012.

[29] P. Rong, Pedram, M., An Analytical Model for Predicting the Remaining Battery Capacity of Lithium-ion Batteries, Very Large Scale Integration (VLSI) Systems, IEEE Transactions, 14 (2006) 441-451.

[30] Y. Zhanga, C.Y. Wanga, X. Tang, Cycling Degradation of an Automotive LiFePO4 Lithium-ion Battery, Journal of Power Sources, 196 (2011) 1513–1520.

[31] E. Prada, D. Di Domenicoa, Y. Creffa, J. Bernarda, V. Sauvant-Moynota, F. Huetb, A Simplified Electrochemical and Thermal Aging Model of LiFePO4-Graphite Li-ion Batteries: Power and Capacity Fade Simulations, J. Electrochemical Society, 160 (2013) 616-628.

[32] M. Dubarry, V. Svoboda, R. Hwu, B.Y. Liaw, A Roadmap to Understand Battery Performance in Electric and Hybrid Vehicle Operation, J. Power Sources, (2007) 366–372.

[33] V. Klass, M. Behm, G. Lindbergh, Evaluating Real-Life Performance of Lithium-Ion Battery Packs in Electric Vehicles Electrochemical Society, 41 (2012).

[34] A. Barré, F. Suard, M. Gérard, M. Montaru, D. Riu, Statistical Snalysis for Understanding and Predicting Battery Degradations in Real-life Electric Vehicle Use, Journal of Power Sources, 245 (2014).

[35] H. Khayyam, S. Nahavandi, E. Hu, A. Kouzani, A. Chonka, J. Abawajyd, V. Maranoe, S. Davisf, Intelligent Energy Management Control of Vehicle Air Conditioning via Look-ahead System, J. Applied Thermal Engineering, 31 (2011) 3147-3160.

[36] J. Larminie, Lowry, J., Electric Vehicle Technology Explained, John Wiley and John Lowry2003.

[37] NREL, NREL Reveals Links Among Climate Control, Battery Life, and Electric Vehicle Range, 2012.

[38] E. Samadani, Gimenez, L., Scott, W., Farhad, S., Fowler, M., Fraser, R. A., Thermal Behavior of Two Commercial Li-Ion Batteries for Plug-in Hybrid Electric Vehicles 2014, SAE World Congress, Detroit, MI, 2014.

[39] E. Samadani, S. Farhad, W. Scottc, M. Mastalia, L.E. Gimenezc, M. Fowlerc, R.A. Frasera, Empirical Modeling of Lithium-ion Batteries Based on Electrochemical Impedance Spectroscopy Tests, Electrochimica Acta, 160 (2015) 169–177.

[40] E. Samadani, S. Panchal, M. Mastali, R.A. Fraser, Battery Life Cycle Management for Plug-in Hybrid Electric Vehicle (PHEVs) and Electric Vehicles (EVs), Transport Canada Final Report, Transportation Development Centre Of Transport Canada, University of Waterloo, 2012, pp. 88.

[41] S.S. Zhang, A Review on the Separators of Liquid Electrolyte Li-ion Batteries, Journal of Power Sources, 164 (2007) 351-364.

[42] M. Dubarry, V. Svoboda, R. Hwu, B.Y. Liaw, Capacity Loss in Rechargeable Lithium Cells during Cycle Life Testing: The Importance of Determining State of Charge, J. Power Sources, 174 (2007) 1121-1125.

[43] I.N. Laboratory, Battery Test Manual for Plug in Hybrid Electric Vehicles, September 2010.

[44] M.D.a.B.Y. Liaw, Identify Capacity Fading Mechanisms in a Commercial LiFePO4 Cell, J. Power Sources, 194 no.1 (2009) 541-549.

[45] E. Samadani, Lo, J., Fowler,M., Fraser, R. A., Gimenez,L., Impact of Temperature on the A123 Li-Ion Battery Performance and Hybrid Electric Vehicle Range, SAE Detroit, 2013.

[46] S. Pillar, Perrin, M., Jossen, A. , Methods for State-of-Charge Determination and their Applications, Journal of Power Sources, 96 (2001) 113-120.

[47] W. Tahil, How Much Lithium Does a Li-ion EV Battery Really Need?, Meridian International Research, (March 2010).

[48] V. Viswanathan, D. Choi, D. Wang, W. Xu, S. Towne, E. Williford, G. Zhang, J. Liu, Z. Yang, Effect of Entropy Change of Lithium Intercalation in Cathodes and Anodes on Li-ion Battery Thermal Management, J. Power Sources, 195, no. 11 (2010) 3720-3729.

[49] H.G. Schweiger, O. Obeidi, O. Komesker, A. Raschke, M. Schiemann, C. Zehner, M. Gehnen, M. Keller, P. Birke, Comparison of Several Methods for Determining the Internal Resistance of Lithium Ion Cells, J. Sensors, 10 (2010) 5604-5625.

[50] D. Linden, T.B. Reddy, Handbook of Batteries, 3rd ed., McGraw-Hill2001.

[51] G.A. Nazri, G. Pistaoie, Lithium Batteries, Science and Technology, Kluwer Academic Publishers2004.

[52] M. Shnayerson, The Car That Could. The Inside Story of GM's Revolutionary Electric

Vehicle, 1996.

[53] V. Srinivasan, J. Newman, A Model-based Comparison of Various Li-ion Chemistries, (2006).

[54] W. Mehrens, P. Axmann, M. Wachtler, Electrochemical Energy Storage Systems for Car Applications, Pres. HySA Systems Business Seminar, (November 2009).

[55] R. Lache, P. Nolan, D. Galves, G. Toulemonde, J. Gehrke, K. Sanger, V. Ha, S. Rao, J. Crane, Electric Cars: Plugged In. Batteries Must Be Included, Deutsche Bank AG, 2008.

[56] Battery University, Types of Lithium-ion, 2015.

[57] P. Arora, Z. Zhang, Battery Separators, J. Chem. Rev, 104 (2004) 4419-4462.

[58] M. Brain, How Lithium-ion Batteries Work, Howstuffworks

[59] O. Erdinc, B. Vural, M. Uzunoglu, A dynamic Lithium-ion Battery Model Considering the Effects of Temperature and Capacity Fading, Clean Electrical Power, 2009 International Conference, IEEE, 2009, pp. 383–386.

[60] L. Lam, Bauer, P., Kelder, E., A Practical Circuit-Based Model for Li-ion Battery Cells in Electric Vehicle Applications, in Telecommunications Energy Conference (INTELEC), IEEE 33rd International, 2011, pp. 1–9.

[61] A. Ostadi, M. Kazerani, S.-K. Chen, Optimal Sizing of the Energy Storage System (ESS) in a Battery-Electric Vehicle, Transportation Electrication Conference and Expo (ITEC), IEEE, IEEE, 2013, pp. 1–6.

[62] J. Newman, W. Tiedemann, Porous-Electrode Theory with Battery Application, AIChE, 21 (1975) 25-41.

[63] T.F. Fuller, M. Doyle, J. Newman, Simulation and Optimization of the Dual Lithium Ion Insertation Cell, J. Electrochemical Society, 141 (1994) 1-10.

[64] C.Y. Wang, W.B. Gu, B.Y. Liaw, Micro-Macroscopic Coupld Modeling of Batteries and Fuel Cells: Part II: Applications to Ni-Cd and Ni-MH Cells, J. Electrochemical Society, 145 (1998) 3418 - 3427.

[65] H. He, R. Xiong, J. Fan, Evaluation of Lithium-Ion Battery Equivalent Circuit Models for State of Charge Estimation by an Experimental Approach, J. Energies, 4 (2011) 582-598.

[66] C. Lin, B. Qiu, Q. Chen, Comparison of Current Input Equivalent Circuit Models of Electrical Vehicle Battery, Chinese J. Mech. Eng., 41 (2005) 76-81.

[67] B.Y. Liaw, M. Dubarry, From Driving Cycle Analysis to Understanding Battery Performance in Real-life Electric Hybrid Vehicle Operation, J. Power Sources, (2007) 76–88.

[68] I. Buchmann, How to Store Batteries, Battery University, 2015.

[69] Q. Zhang, White, R.E., Capacity Fade Analysis of a Lithium-ion Cell, J. Power Sources, 179, no. 2 (2008) 793-798.

[70] R. Spotnitz, Simulation of Capacity Fade in Lithium-ion Batteries, J. Power Sources, 113, no. 1 (2003) 72-80

[71] Electropaedia, Cell Chemistries-How Batteries Work, 2015.

[72] K. Edström, T. Gustafsson, J.O. Thomas, The Cathode–Electrolyte Interface in the Li-ion Battery, J. Electrochim. Acta, 50 (2004) 397–403

[73] J. Vetter, P. Novák, M.R. Wagner, C. Veit, K.-C. Möller, J.O. Besenhard, M. Winter, M. Wohlfahrt-Mehrens, C. Vogler, A. Hammouche, Ageing Mechanisms in Lithium-ion Batteries, J. Power Sources, 147, (2005) 269-281.

[74] S.B. Peterson, J. Apt, J.F. Whitacre, Lithium-ion Battery Cell Degradation Resulting from Realistic Vehicle and Vehicle-to-Grid Utilization, J. Power Sources, 195, no. 8 (2010) 2385-2392.

[75] C. Rosenkranz, Plug In Hybrid Batteries, Pres EVS20, (November 2003) 14.

[76] A. Pesaran, M. Keyser, G. Kim, S. Santhanagopalan, K. Smith, Tools for Designing Thermal Management of Batteries in Electric Drive Vehicles, Large Lithium Ion Battery Technology & Application Symposia Advanced Automotive Battery ConferencePasadena, CA, 2013.

[77] T.D. Tran, J.H. Feikert, R.W. Pekala, Rate Effect on Lithium-ion Graphite Electrode

performance, J. Appl. Electrochem, 26, no. 11 (1996) 1161-1167.

[78] K. Anime, J. Liu, I. Belharouak, High-temperature Storage and Cycling of CLiFePO4/ graphite Li-ion Cells, J. Electrochem. Com, 7 (2005) 669-673.

[79] M. Broussely, Aging Mechanisms and Calendar Life Predictions in Lithium-ion Batteries, J. Advances in Li-ion batteries, (2002) 293-432.

[80] P. Arora, R.E. White, M. Doyle, Capacity Fade Mechanisms and Side Reactions in Lithium-ion Batteries, J. Electrochem. Soc., 145 (1998) 3647-3666.

[81] H. Maleki, J.N. Howard, Effects of Overdischarge on Performance and Thermal Stability of a Li-ion Cell, J. Power Sources, 160 (2006) 1395-1402.

[82] C. Kishiyama, M. Nagata, T. Piao, J. Dodd, P. Lam, H. Tsukamoto, Improvement of Deep Discharge Capability for Lithium Ion Batteries, 205th Electrochemical Society Fall Meeting, 2003, pp. 252-259.

[83] J. Gonder, A. Simpson, Measuring and Reporting Fuel Economy of Plug-In Hybrid Electric Vehicles 22nd International Battery, Hybrid and Fuel Cell Electric Vehicle Symposium and Exhibition, NREL, Yokohama, Japan, 2006.

[84] J. Gonder, A. Brooker, J. Smart, Deriving In-Use PHEV Fuel Economy Predictions from Standardized Test Cycle Results, 5th IEEE Vehicle Power and Propulsion Conf., IEEE, Dearborn, Michigan, 2009.

[85] L. Drew, S. Jim, M. Raffaello, O. Francisco, B. Colin, A High Performance Aircraft Wind Tunnel Test Using Response Surface Methodologies, 2005 U.S. Air Force T&E Days, American Institute of Aeronautics and Astronautics2005.

[86] MathWorks Documentation Center, Skewness, 2015.

[87] Wolfram Mathworld, Skewness, 2015.

[88] C.K. Dyer, P.T. Moseley, Z. Ogumi, D.A. Rand, B. Scrosati, Encyclopedia of Electrochemical Power Sources, Elsevier Science2013.

[89] C. Vincent, B. Scrosati, Modern Batteries: An Introduction to Electrochemical Power Sources, 2 ed., Butterworth-Heinemann1997.

[90] N.R. Draper, H. Smith, Applied Regression Analysis, Wiley-Interscience1998.

[91] M. Chen, G.A. Rincón-Mora, Accurate Electrical Battery Model Capable of Predicting Runtime and IV Performance, Energy Conversion IEEE Trans., 21 (2006) 504-511.

[92] C. Mi, B. Li, D. Buck, N. Ota, Advanced Electro-Thermal Modeling of Lithiumion Battery System for Hybrid Electric Vehicle Applications, Vehicle Power and Propulsion Conference (VPPC), IEEE, IEEE, Arlington, TX, 2007, pp. 107–111.

[93] J. Shen, S. Dusmez, A. Khaligh, An Advanced Electro-Thermal Cycle-Lifetime Estimation Model for LiFePO4 Batteries, Transportation Electrification Conference and Expo (ITEC), IEEE, 2013, pp. 1–6.

[94] A. Pesaran, Battery Thermal Models for Hybrid Vehicle Simulations, J. Power Sources, 110 (2002) 377–382.

[95] A. Pesaran, S. Santhanagopalan, G. Kim, Addressing the Impact of Temperature Extremes on Large Format Li-Ion Batteries for Vehicle Applications, National Renewable Energy Laboratory, 2013.

[96] University of Waterloo alternative fuel Team (UWAFT), Design Report 5, University of Waterloo

Waterloo, 2012.

[97] S. Buller, M. Thele, E. Karden, R.W. Doncker Impedance-Based Non-Linear Dynamic Battery Modeling for Automotive Applications, J. Power Sources, 113 (2003) 422-430.

[98] N. Lotfi, P. Fajri, S. Novosad, J. Savage, Development of an Experimental Testbed for Research in Lithium-Ion Battery Management Systems, J. Energies, 6 (2013) 5231-5258.

[99] M.E. Orazem, B. Tribollet, Electrochemical Impedance Spectroscopy, Angew. Chem. Int. Ed.2009.

[100] D.V. Do, C. Forgez, K. El Kadri Benkara, G. Friedrich, Impedance Observer for a Li-Ion Battery Using Kalman Filter, Vehicle Tech. IEEE Trans., 58 (2009) 3930-3937.

[101] Zmantechnologies, Zman User's Manual, WonATech Co. LTD, Seoul, Korea, 2014.

[102] I.N. Laboratory, Battery Test Manual for Plug-In Hybrid Electric Vehicles Rev. 1, U.S. Dept. of Energy Vehicle Technologies Program, 2010.

[103] S. Yuan, H. Wu, C. Yin, State of Charge Estimation Using the Extended Kalman Filter for Battery Management Systems Based on the ARX Battery Model, J. Energies, 6 (2013) 444-470.

[104] E. Samadani, J. Lo, M. Fowler, R. Fraser, L. Gimenez, Impact of Temperature on the A123 Li-Ion Battery Performance and Hybrid Electric Vehicle Range, SAE World Congress,, SAE, Detroit, MI, 2013.

[105] Y. Zheng, M. Ouyang, L. Lu, J. Li, X. Han, L. Xu, H. Ma, T.A. Dollmeyer, V. Freyermuth, Cell State-of-Charge Inconsistency Estimation for LiFePO4 Battery Pack in Hybrid Electric Vehicles Using Mean-Difference Model, J. Applied Energy, 111 (2013) 571-580.

[106] K.S. Hariharan, V.S. Kumar, A Nonlinear Equivalent Circuit Model for Lithium-ion Cells, J. Power Sources, 222 (2013) 210-217.

[107] M. Greenleaf, H. Li, J.P. Zheng, Modeling of LixFePO4 Cathode Li-Ion Batteries Using Linear Electrical Circuit Model, IEEE Trans., 4 (2013) 1065-1070.

[108] H. Abu-Rub, M. Malinowski, K. Al-Haddad, Power Electronics for Renewable Energy Systems, Transportation and Industrial Applications, Wiley2014.

[109] Burlington Hydro, GridSmartCity® – Providing a Forum for Dialogue and Discovery.

[110] M. Giannikouris, Battery Lifecycle Management for PHEVs: Transport Canada Final Report, University of Waterloo, 2010, pp. 44.

[111] S.P. E. Samadani, M. Mastali, and R. A. Fraser, Battery Life Cycle Management for Plug-in Hybrid Electric Vehicle (PHEVs) and Electric Vehicles (EVs), University of Waterloo, 2012.

[112] Argonne National Laboratory, PSAT (Powertrain System Analysis Toolkit), Argonne, Transportation Technology R&D Center.

[113] D. Montgomery, Determining the Specific Heat Capacity of a Battery Pack; Illustrative Example and Description of Method.

[114] G. Ning, R.E. White, B.N. Popov, A Generalized Cycle Life Model of Rechargeable Li-ion Batteries, J. Electrochimica Acta, 51 (2006) 2012-2022.

[115] M.B. Stevens, Hybrid Fuel Cell Vehicle Powertrain Development Considering Power Source Degradation, University of Waterloo, 2008.

[116] Y. Li, Scenario-Based Analysis on the Impacts of Plug-In Hybrid Electric Vehicles' (PHEV) Penetration into the Transportation Sector, IEEE International Symposium on Technology and SocietyLas Vegas, NV, 2007, pp. 1-6.

[117] R.A. Barnitt, A.D. Brooker, L. Ramroth, J. Rugh, K.A. Smith, Analysis of Off-Board Powered Thermal Preconditioning in Electric Drive Vehicles, 25th World Battery, Hybrid and Fuel Cell Electric Vehicle Symposium & ExhibitionShenzhen, China, 2010.

[118] BlueDevil Product, How Do I Repair My Car’s AC?

[119] Metric Mind Corporation (MMC), EV Fluid Heaters, Metric Mind Corporation.

[120] Masterflux, Compressor Data Sheet, Master Flux Products.

[121] C.D. Haung, A Dyanamic Computer Simulation Model for Automobile Passenger Compatment Climate Control and Evaluation, Mechanical Engineering, Michigan Technological University, 1998.

[122] S. Sanaye, M. Dehghandokht, A. Fartaj, Temperature control of a Cabin in an Automobile using thermal Modeling and Fuzzy Controller, J. Applied Energy, 97 (2012) 860-868.

[123] L. Knibbs, R. de Dear, S. Atkinson, Field Study of Air Change and Flow Rate in Six Automobiles, J. Indoor Air,, 19 (2009) 303-313.

# Appendix-A

## Statistical Analysis of Cell Temperature Distribution

Investigating the coefficients of skew for each of the examined readings reveals different distribution behavior for each cell (A 1and A 2).

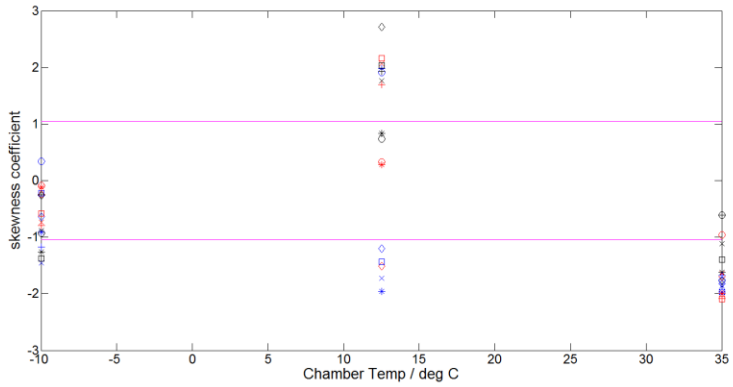


**A 1: Skew coefficient for experiments performed with Cell 1. The color code indicates SOC (blue=0%, red=50%, black=100%) and marker code indicates discharge and charge c-rate (charge: x=0.25, *=1.25, o=2.25; discharge: diamond=0.5, square=2.5, +=4.5)**

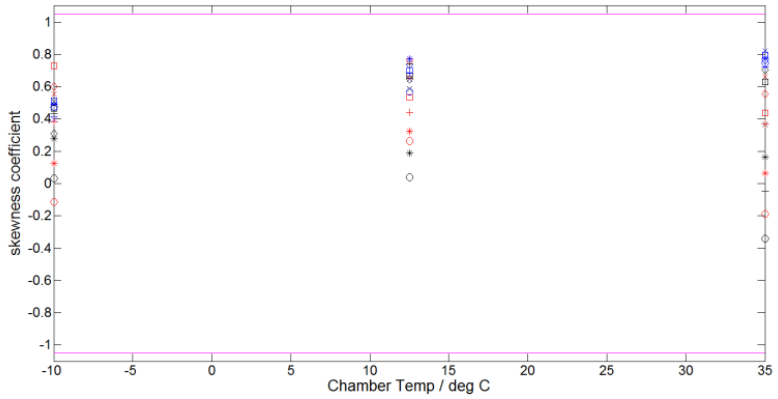


**A 2: Skew coefficient for experiments performed with Cell 2. The color code indicates SOC (blue=0%, red=50%, black=100%) and marker code indicates discharge and charge c-rate (charge: x=0.25, *=1.25, o=2.25; discharge: diamond=0.5, square=2.5, +=4.5**

For cell 1, over half of the sampled points there is evidence of a skewed distribution as the coefficient values fall outside the 90% confidence interval bounds with n=12. These confidence bounds are ±1.049 (in both batteries) and were obtained by fitting and extrapolating a table of 90% confidence bounds for

the skewness coefficient [20]. In contrast, all of the coefficients for cell 2 fall between the bounds suggesting the presence of a centered distribution.

Given that a large number of beginning-, middle-, and end-of-step skew coefficients fall outside the confidence bounds, and that these skew coefficients are neither consistently positive nor negative, it can be assumed that the observed skew in the temperature distributions is caused by factors other than the heat generation of the cell. Since cell 1 was on the bottom shelf of the chamber, it was a further distance from the chamber circulation fan. It is therefore possible that the location increases the likelihood of non-uniform temperature variations. This hypothesis is endorsed by the low difference between the mean and the median for cell 1.

The average difference between the mean and median of the temperature readings (A 3 and A 4) is −0.014K/−0.0075K for the charge and discharge steps of cell 1 and 0.089K/0.030K for the same steps of cell 2, respectively. The difference between mean and median rarely exceeded ±0.15K at the end or middle of step for both cells. This difference was consistently of greater magnitude for cell 2, centered at 0.05K, but this is still well within the margin of error. Further, the analysis of skew coefficients suggests there is no skewed distribution at any point for this cell. The standard deviation (σ) of the temperatures shows no consistent effect of chamber temperature or charge/discharge C-rate on the temperature spread. This suggests evenly distributed heating of the cell. The average σ was calculated to be 0.227 K/0.368 K for charge/discharge of cell 1 and 0.221K/0.302K for the charge/discharge of cell 2. While this temperature spread is higher than the error in the thermocouples, it is not greater than the chamber temperature control range (±0.5K). Further, the larger values of σ (above 0.5K) almost all correspond to the initial SOC of the charge or discharge step, with the value decreasing as the step is carried out (with two minor exceptions). This suggests the influence of environmental factors on the temperature distribution causes greater spread than any internal differences in the heat generation rate.

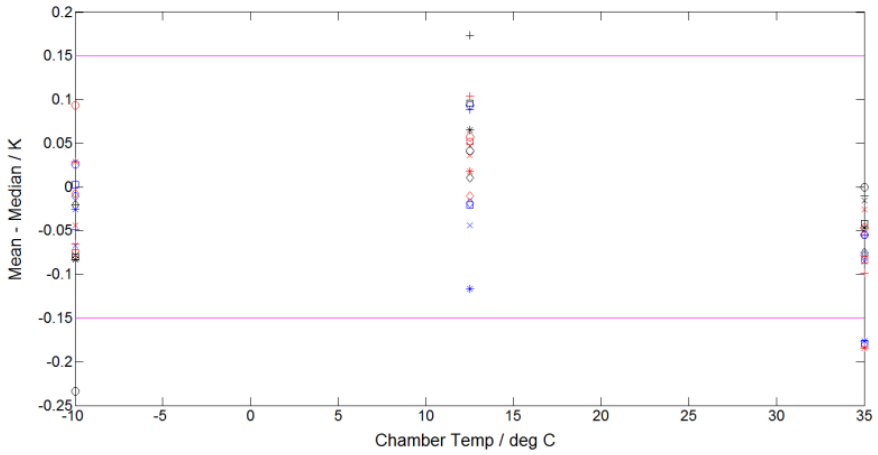


**A 3: $LiFePO_4$ cell temperature mean-median difference throughout the experiments. The color code indicates SOC (blue=0%, red=50%, black=100%) and marker code indicates discharge and charge c-rate (charge: x=0.25, *=1.25, o=2.25; discharge: diamond=0.5, square=2.5, +=4.5)**

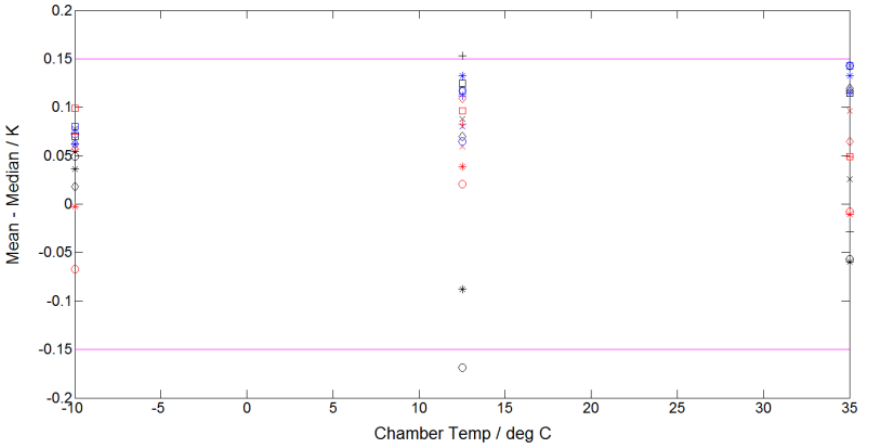


**A 4: $LiMn_2O_4$ cell temperature mean-median difference throughout the experiments. The color code indicates SOC (blue=0%, red=50%, black=100%) and marker code indicates discharge and charge c-rate (charge: x=0.25, *=1.25, o=2.25; discharge: diamond=0.5, square=2.5, +=4.5)**

# Appendix-B

## Derived Regression Models for the Circuit Parameters

## Battery #1 (LFP Cathode):

```
if (8.5<=temp)&&(temp<16.5)
    R1= -1.1924E-11*SOC^4 + 3.4367E-09*SOC^3 - 2.9815E-07*SOC^2 + 8.3662E- 06*SOC^1 + 9.0340E-04;
    R2=-7.3164E-12*SOC^4 + 5.8531E-10*SOC^3 - 2.0011E-09*SOC^2 - 7.9285E-07*SOC^1 + 1.6792E-03;
    C1= -7.2415E-07*SOC^4 + 1.9663E-04*SOC^3 - 1.6592E-02*SOC^2 + 4.7056E-01*SOC^1 + 1.8084E+01;
    C2= -9.3682E-05*SOC^4 + 2.2157E-02*SOC^3 - 1.7448E+00*SOC^2 + 5.1351E+01*SOC^1 + 3.6988E+01;
    R3=-2.8547E-09*SOC^3 + 4.0633E-07*SOC^2 - 1.6189E-05*SOC^1 +    9.2442E-04;
    R4=7.6329E-11*SOC^4 - 1.4614E-08*SOC^3 + 9.3078E-07*SOC^2 - 2.1735E-05*SOC^1 + 5.0689E-04;
    C3= -1.3139E-03*SOC^4 + 2.8153E-01*SOC^3 - 2.1037E+01*SOC^2 + 5.9944E+02*SOC^1 + 9.4176E+03;
    R5=-8.2231E-09*SOC^3 + 1.3670E-06*SOC^2 - 7.0295E-05*SOC^1 + 4.6949E-03;
    C4=-1.3881E-02*SOC^4 + 2.7501E+00*SOC^3 - 1.8106E+02*SOC^2 + 4.5201E+03*SOC^1 + 2.5236E+04;
elseif (16.5<=temp)&&(temp<32)
    R1=-7.3624E-12*SOC^4 + 9.8197E-10*SOC^3 - 5.5139E-08*SOC^2 + 3.4816E-06*SOC^1 + 6.9355E-04;
    R2=5.3921E-12*SOC^4 - 1.1286E-09*SOC^3 + 1.1558E-07*SOC^2 - 8.4552E-06*SOC^1 + 8.7765E-04;
    C1= -1.2508E-06*SOC^4 + 1.9713E-04*SOC^3 - 1.1057E-02*SOC^2 + 4.6085E-01*SOC^1 + 1.8513E+01;
    C2=2.3234E-05*SOC^4 - 6.0979E-03*SOC^3 + 4.0664E-01*SOC^2 + 1.8484E+00*SOC^1 + 4.4622E+02;
    R3=4.8039E-12*SOC^4 - 1.4603E-09*SOC^3 + 1.6947E-07*SOC^2 - 9.1099E-06*SOC^1 + 4.5446E-04;
    R4=-4.4560E-12*SOC^4 + 6.4079E-10*SOC^3 + 9.0600E-10*SOC^2 - 2.5548E-06*SOC^1 + 2.5477E-04;
    C3=2.9485E-03*SOC^4 - 6.5496E-01*SOC^3 + 4.5311E+01*SOC^2 - 9.8769E+02*SOC^1 + 2.1574E+04;
    R5=2.7156E-10*SOC^4 - 6.5474E-08*SOC^3 + 5.6005E-06*SOC^2 - 1.9843E-04*SOC^1 + 4.7122E-03;
    C4=-4.4313E-04*SOC^4 + 1.2049E-01*SOC^3 - 1.5526E+01*SOC^2 + 9.4699E+02*SOC^1 + 5.4311E+04;
 elseif (31<=temp)&&(temp<45)
    R1= 1.3499E-09*SOC^3 - 2.6207E-07*SOC^2 + 1.5019E-05*x + 6.5366E-04;
    R2= -8.2144E-10*SOC^3 + 1.5712E-07*SOC^2 - 9.7821E-06*x + 2.9033E-04;
    R3= 1.2436E-10*SOC^3 - 2.5186E-08*SOC^2 + 1.5903E-06*x + 1.1561E-04;
    R4= 9.2859E-09*SOC^3 - 8.4466E-07*SOC^2 + 1.8849E-05*x + 1.5014E-04;
    R5= -3.2258E-08*SOC^3 + 4.6544E-06*SOC^2 - 2.1509E-04*x + 5.3658E-03;
    C1= 3.2702E-04*SOC^4 - 5.7252E-02*SOC^3 + 2.8252E+00*SOC^2 - 1.4737E+01*x + 7.3334E+01;
```

```
        C2= 5.5117E-02*SOC^3 - 1.0919E+01*SOC^2 + 6.4710E+02*x + 3.8183E+02;
        C3= 2.4611E-01*SOC^3 - 2.3601E+01*SOC^2 + 6.6653E+02*x + 6.7549E+04;
        C4= -2.2639E-01*SOC^3 + 1.9599E+01*SOC^2 - 1.6303E+02*x + 9.9379E+04;
end
```

## Battery #2, (LMO & NMC Cathode):

```
if (temp>=8)&&(temp<=18)
            R1= 7.0808E-08*SOC^2 - 5.8329E-06*x + 1.3915E-03;
            R2= 4.2228E-08*SOC^2 - 3.7060E-06*x + 8.5987E-04;
            C1= 1.1364E-02*SOC^2 - 9.1497E-01*x + 4.4608E+01;
            C2 = -1.8337E-03*SOC^3 + 2.3421E-01*SOC^2 - 7.1334E+00*x + 2.7454E+02;
            R3=-8.0898E-09*SOC^3 + 1.5283E-06*SOC^2 - 1.0322E-04*x + 2.9054E-03;
            R4=-3.1205E-09*SOC^3 + 5.6908E-07*SOC^2 - 3.1298E-05*x + 6.9424E-04;
            C3= 1.2041E-01*SOC^3 - 2.6735E+01*SOC^2 + 1.5754E+03*x - 2.4632E+03;
            R5= -4.3900E-08*SOC^3 + 6.5245E-06*SOC^2 - 2.7019E-04*x + 6.5161E-03;
            C4= 5.3293E-01*SOC^3 - 8.0547E+01*SOC^2 + 3.3463E+03*x + 2.5908E+04;
else if (temp>=18)&&(temp<=28)
           R1= -2.6762E-10*SOC^4 + 5.1171E-08*SOC^3 - 3.2003E-06*SOC^2 + 7.5197E-05*x + 4.8916E-04;
           R2=-1.8426E-11*SOC^4 + 1.2486E-09*SOC^3 + 1.1699E-07*SOC^2 - 9.4292E-06*x + 6.9954E-04;
           C1=-1.6493E-05*SOC^4 + 3.1013E-03*SOC^3 - 1.8869E-01*SOC^2 + 4.4103E+00*x - 1.0525E+01;
           C2=-9.2389E-05*SOC^4 + 1.6293E-02*SOC^3 - 9.6568E-01*SOC^2 + 2.3868E+01*x + 1.9789E+01;
           R3=-4.1093E-09*SOC^3 + 8.7954E-07*SOC^2 - 6.1557E-05*x + 1.4540E-03;
           R4=8.3556E-11*SOC^4 - 1.7391E-08*SOC^3 + 1.2093E-06*SOC^2 - 3.1617E-05*x + 3.9427E-04;
           C3=1.5092E-02*SOC^4 - 2.9776E+00*SOC^3 + 1.9159E+02*SOC^2 - 4.5309E+03*x + 6.5452E+04;
           R5=-1.4079E-10*SOC^4 - 9.9293E-09*SOC^3 + 3.5492E-06*SOC^2 - 1.5901E-04*x + 4.5593E-03;
           C4=-6.2102E-02*SOC^4 + 1.2514E+01*SOC^3 - 8.4189E+02*SOC^2 + 2.1587E+04*x - 1.0310E+05;
else if (temp>28)
           R1= -3.1405E-09*SOC^3 + 4.6714E-07*SOC^2 - 1.8254E-05*x + 1.2772E-03;
           R2= 2E-10*SOC^4 - 4E-08*SOC^3 + 3E-06*SOC^2 - 8E-05*x + 0.0008;
           C1= -1.5376E+00*SOC^2 + 3.1609E+02*x - 2.8505E+03;
           C2= 5.2240E-03*SOC^3 - 3.7153E+00*SOC^2 + 5.5959E+02*x + 1.4230E+03;
           R3=-4.4305E-09*SOC^3 + 6.6673E-07*SOC^2 - 2.5507E-05*x + 3.9728E-04;
```

```
R4= -7.1244E-08*SOC^3 + 8.8381E-06*SOC^2 - 2.6090E-04*x + 4.4370E-03;
C3=1.7719E-01*SOC^3 - 3.5050E+01*SOC^2 + 1.7530E+03*x + 7.3067E+04;
R5=1.6885E-09*SOC^3 + 5.3492E-07*SOC^2 - 4.3545E-05*x + 1.0523E-03;
C4= 1.0117E+00*SOC^3 - 1.1603E+02*SOC^2 + 3.5250E+03*x + 3.7591E+04;
End
```

# Appendix-C

## Modification on the driver model in Autonomie to take in the power demand as input

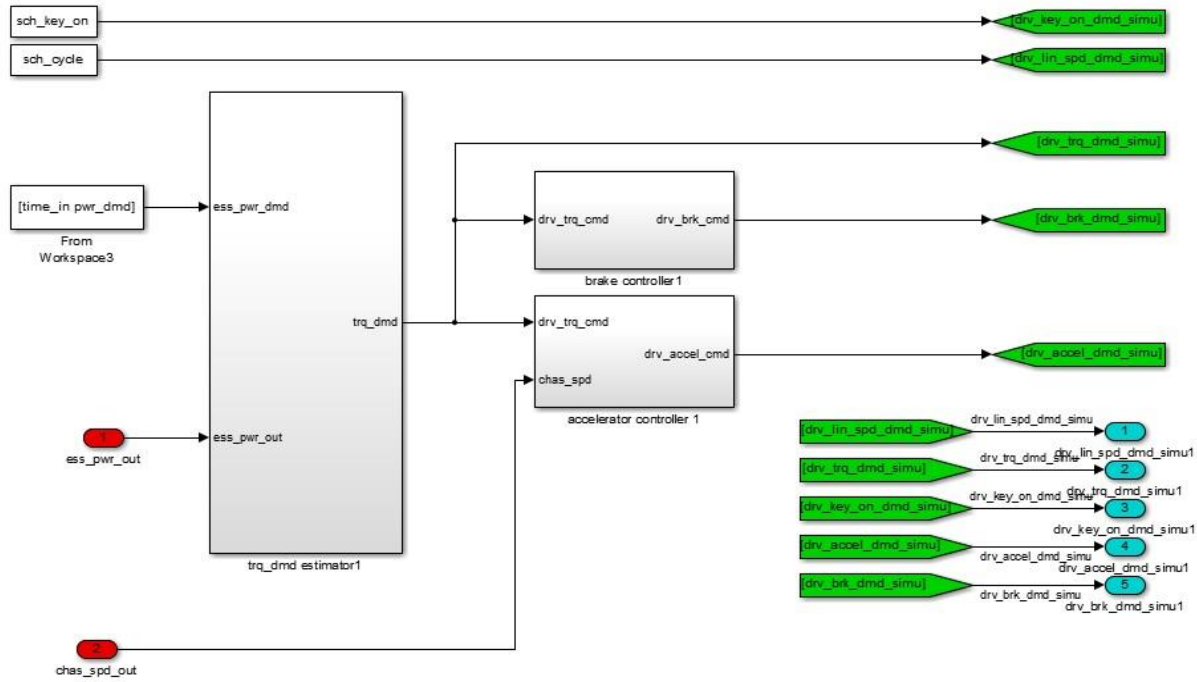


**C 1: driver sub-model- top level**

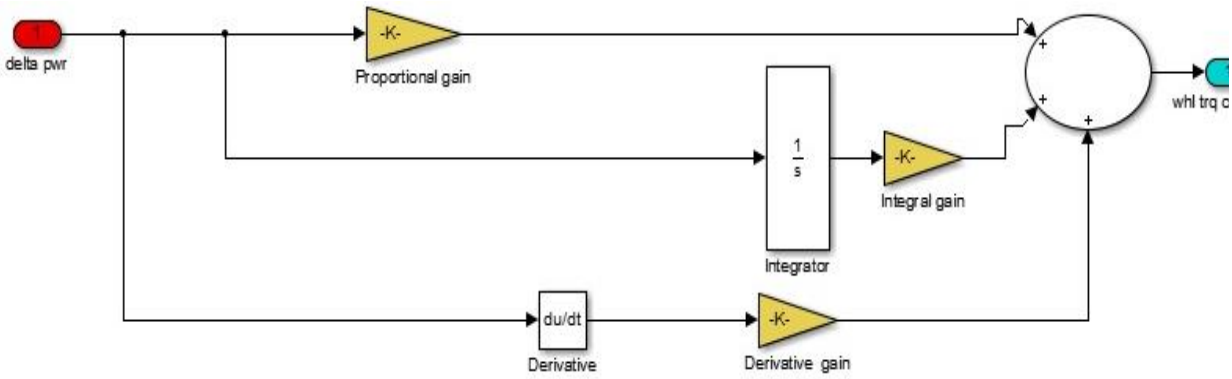


**C 2: Torque demand estimator**

# Appendix-D

## Monthly Report of EV-ACX2.5

**October 2011**

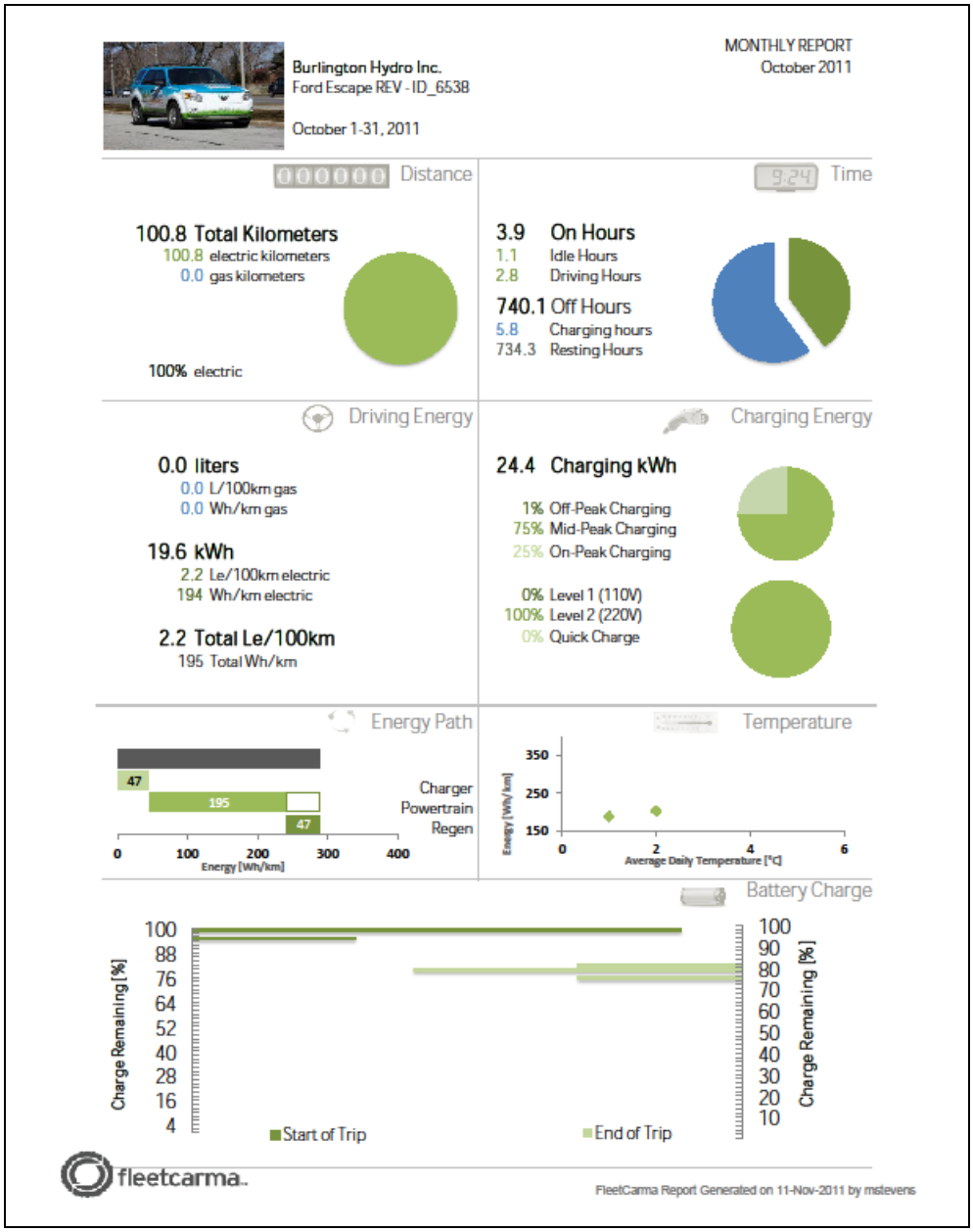

**December 2011**

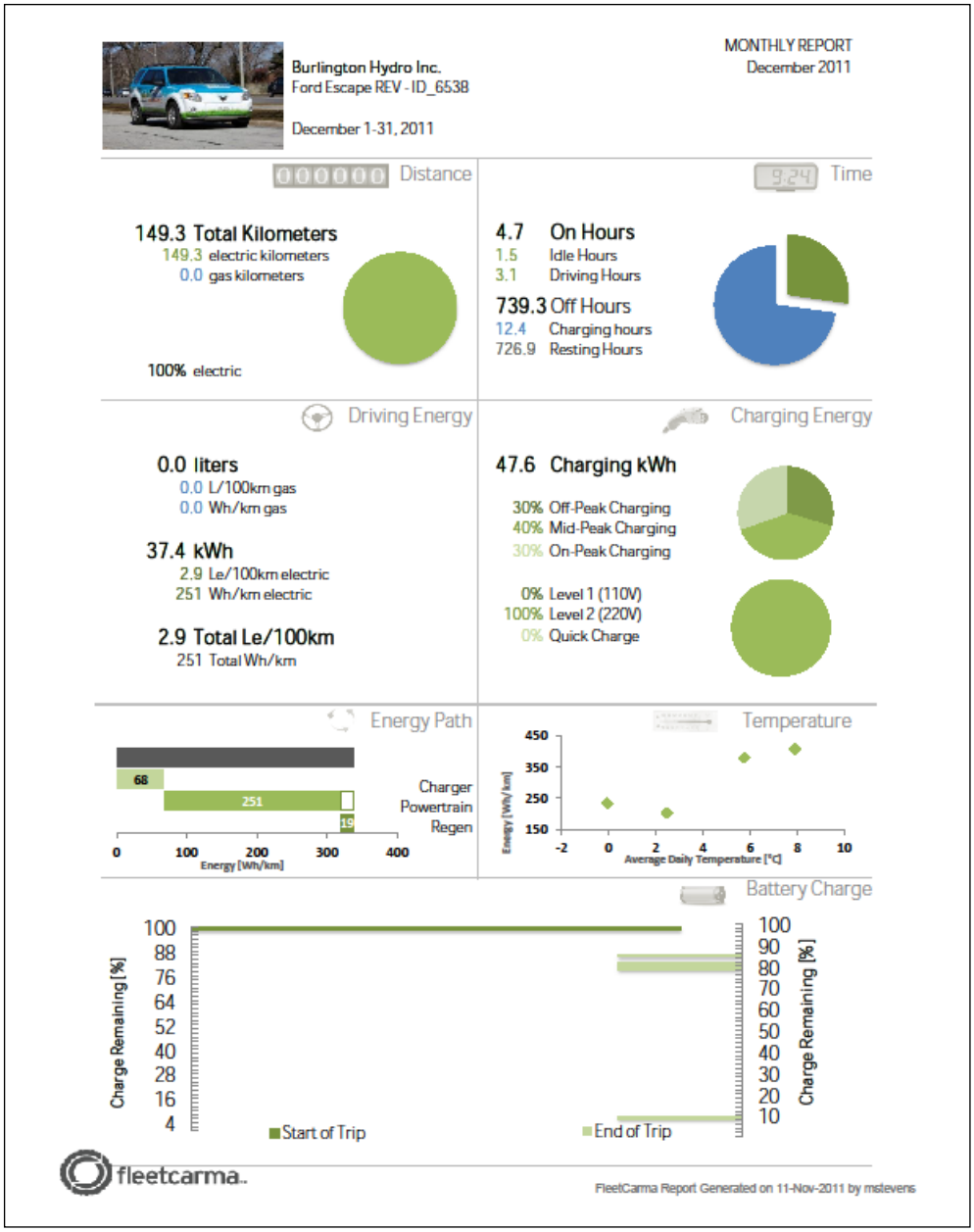

**January 2012**

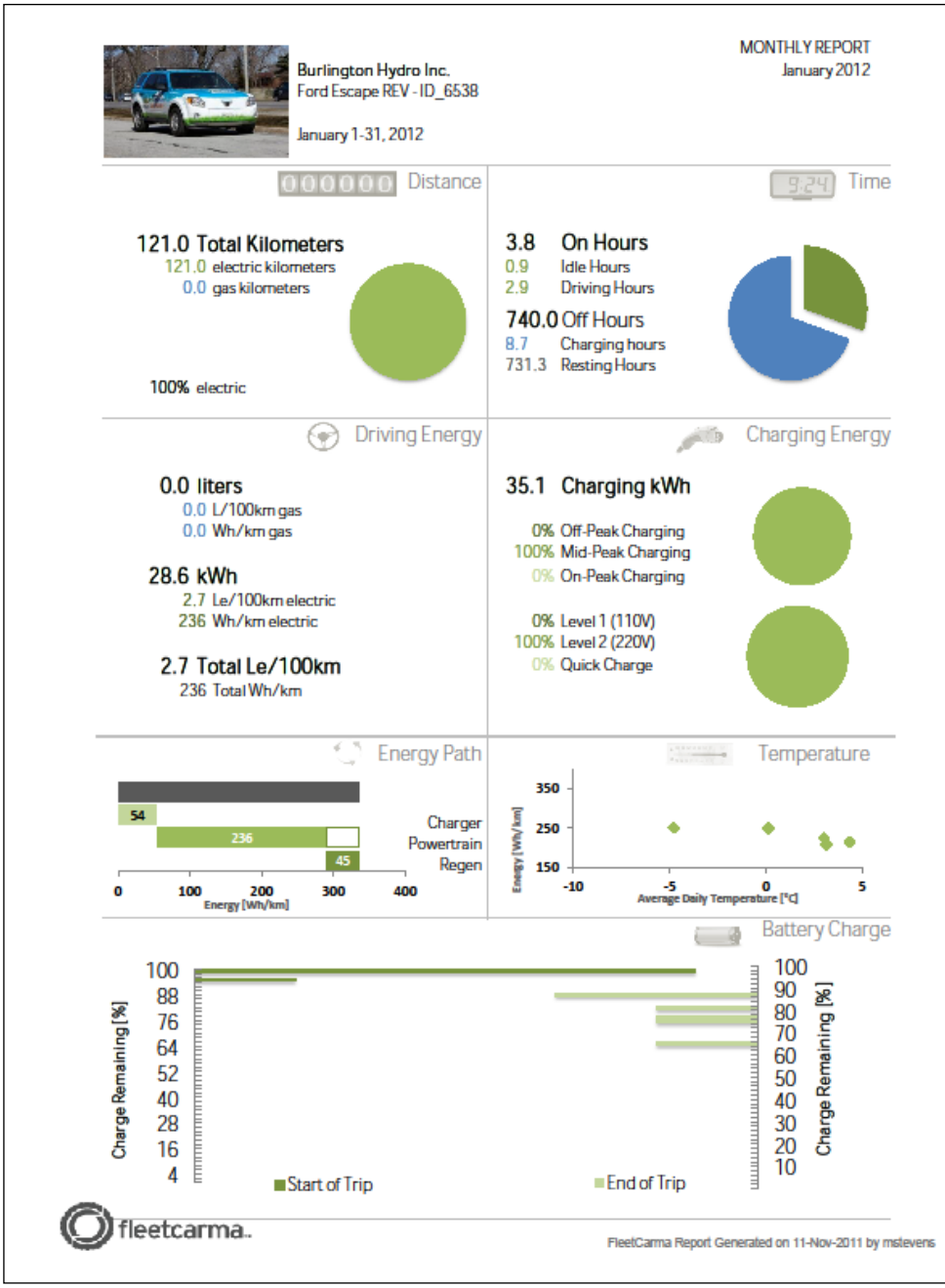

**February 2012**